UNIVERSITY OF CALIFORNIA

Santa Barbara

Design and Tribological Characterization of Stimuli-Responsive Hydrogels

A dissertation submitted in partial satisfaction of the

requirements for the degree Doctor of Philosophy

in Materials

by

Allison Leigh Chau

Committee in charge:

Professor Angela A. Pitenis, Chair

Professor Craig J. Hawker

Professor Megan T. Valentine

Professor Christopher M. Bates

December 2023

The dissertation of Allison Leigh Chau is approved.

_____

Craig J. Hawker

_____

Megan T. Valentine

_____

Christopher M. Bates

_____

Angela A. Pitenis, Committee Chair

December 2023

Design and Tribological Characterization of Stimuli-Responsive Hydrogels

To my grandparents:

Baw-Baw, Ang-Ang, Ma-Ma, and Ye-Ye

Who left behind everything they knew to come to America in hopes of a better future for their family

ACKNOWLEDGEMENTS

If I were to thank everyone who has helped me reach this point, the acknowledgements would be as long as this dissertation. I will try to be concise. To all of my elementary, middle and high school teachers and undergraduate professors but especially Mr. Faust and Mrs. Rundle: thank you for encouraging my curiosity and helping to nurture my love of science. I have continued to "embrace perplexity" throughout my academic journey.

To Prof. Chelsea Davis and the Davis Research Group, specifically Dr. Mitchell Rencheck, Dr. Hyeyoung Son, and Dr. Naomi Deneke: thank you for helping me grow as a researcher. My time in your group gave me a glimpse into what grad school was like and how fun research could be. Chelsea: thank you for patiently answering my list of questions every week, for challenging me as a researcher, and for your mentorship. Mitch, Hyeyoung, and Naomi: thanks for answering all my questions about grad school and for your encouragement.

To my advisor: Angela, thank you for taking the time to train and mentor me – especially during the early years – despite being on *thousands* of committees. You have taught me everything I know (*e.g.,* pipetting, using the tribometer, making hydrogels, using Illustrator, etc…), and I have truly learned from the expert. Thank you for spending countless hours helping me perfect my presentations and for teaching me how to effectively communicate science in an engaging way. I will always be amazed at how fast you can find a typo or error in a figure. Thank you for cultivating a positive lab culture of mentorship,

collaboration, and puns (so many puns). Because of your enthusiasm for collaborations, my one-month side project morphed into a two-year project that became a large portion of my thesis. Thank you for believing in me when I doubted myself and for giving me the opportunity and support to travel to 4 different countries and 3 states to present at 11 conferences. Words cannot express how grateful I am for your encouragement over the past 4.25 years. Your constant enthusiasm, positivity, and passion for research inspires me and motivates me to be a better scientist. You were the main reason why I decided to come to UCSB to pursue my doctorate, and I am so thankful for that decision.

To the members of the Interfacial Engineering Lab, past and present – Jonah, Lisa, Andrew, Dixon, Ahmed, Katie, Joey, Rachel, Cecelia, Conor, Madeleine, Kevin, Akshay, Nima, George, Megan, Jonathan, Ricardo: thank you for making my time in grad school so fun. I enjoyed our lab get togethers, the cramped office space and the musical chairs that we had to play when everyone happened to be in the office at the same time, and the chaos of having multiple meetings occurring at once. I'm so thankful to have such a supportive lab group and will miss you all when I leave.

Jonah: Thank you for building the lab with me. I look back fondly at all the ordering and unboxing of supplies, pipe bending, drilling into walls to put up shelving, almost breaking the sink by pouring dry ice down it, etc… I am so thankful to have been able to work alongside you throughout my Ph.D, and I

hope that some of the oratory and presentation skills that you naturally possess have rubbed off on me. Your sarcasm certainly has.

Andrew: I've thoroughly enjoyed our impromptu research discussions and whiteboarding sessions. Your stories always make me laugh, and as you are the resident chemist in the group, I appreciate that I can always bug you with chemistry questions.

Dixon: Your knowledge about random topics and your ability to balance being a researcher and excellent triathlete will always amaze me. Thanks for patiently answering all my basic biology questions.

Conor: Thank you for keeping me on my toes, for asking me all the hard questions I don't know how to answer, and for your enthusiasm about research (which really helps as a tired 5th year). You are amazing, and I can't wait to see where you will go next.

Lisa: Thank you for being my biking/surfing/SCUBA buddy, labmate, housemate, and friend. Thanks for introducing us to fika and for encouraging me to take more breaks and enjoy lunch outdoors. Your positivity, kindness, and love of party games is contagious, and I'm looking forward to many more adventures!

Juan: Thank you for all your support and assistance whenever I needed help. Our lab still probably wouldn't be fully built without you.

To my committee members – Prof. Craig Hawker, Prof. Chris Bates, Prof. Megan Valentine: thank you for all your advice on polymer chemistry and

mechanics. Your suggestions have improved and advanced my projects further. I also appreciate your support in helping me expand my professional network.

To my collaborators – Prof. Claus Eisenberg, Prof. Javier Read de Alaniz, Dr. Yongkui Tang, Younghoon Kwon, Pat Getty, Dr. Chelsea Edwards, Kseniia Karnaukh, and everyone in the IRG: I have thoroughly enjoyed working with you all. Thank you for all your advice and suggestions. You have made me a better scientist and have helped improve and push my projects forward.

To the wonderful outreach staff at CSEP and MRL – Dr. Arica Lubin, Ofelia Aguirre Paden, Sofi Sanabria-Guillen, Wendy Ibsen, Dr. Frank Kinnaman, Dr. Dotti Pak, and Dr. Julie Standish: thank you for your dedication to scientific outreach and for letting me be a part of it. Arica, Sofi, Ofi, and Wendy: I've truly enjoyed working with you all for the past year. Your passion and support of undergrads and graduate students is inspiring. I will strive to be involved in outreach wherever I go next.

To the Materials Department administrative staff: thank you for keeping the department running and for doing all the crucial jobs behind the scenes.

To my Purdue friends – Alice Li, Rebecca Chow, Esther Sun, Winnie Lo, Rong Xue, Dr. Karam Cho, Dr. Nhu Pham, Dr. Phu Vo, Dr. Nyansafo Aye-Addo, Prof. Town Oh: thank you for keeping me sane during undergrad and during the long years of COVID – for all the late night Zoom study sessions and long talks about research, life, and our faith. I am so grateful and thankful that we have been able to stay connected past graduation even though we live in 8 different states now.

Nyansafo: I will always admire your humility, work ethic, and passion for your research. Thank you for all your advice about grad school and for answering my endless questions. Rebecca: Your enthusiasm and passion for everything you do is contagious. Thank you for always hyping me up. Alice: Thank you for your constant support and encouragement. I know that I can always turn to you for advice and am so grateful for our friendship.

To my family – Mom, Dad, Maddie, Baw-Baw, Yee-Ma, Ko-Foo: thank you for your unwavering love and support. I know I don't say this enough but thank you for everything that you have done for me. I am the person I am today because of you all. I promise that I am done with school now and will get a "real" job.

And finally, I would like to thank God for His faithfulness and for providing such wonderful people in my life. By His grace, I have been saved.

2 Corinthians 4:7-9

"But we have this treasure in jars of clay, to show that the surpassing power belongs to God and not to us. We are afflicted in every way, but not crushed; perplexed, but not driven to despair; persecuted, but not forsaken; struck down, but not destroyed."

VITA OF ALLISON LEIGH CHAU
December 2023

EDUCATION

University of California, Santa Barbara 2019 – 2023
Doctor of Philosophy in Materials

Purdue University 2015 - 2019
Bachelor of Science in Materials Engineering with Highest Distinction

EMPLOYMENT

Graduate Student Researcher, Advisor: Prof. Angela Pitenis 2019 – 2023
Materials Department, University of California, Santa Barbara

Center for Science & Engineering Partnerships 2023
Mentor Leadership Fellow, University of California, Santa Barbara

Microscopy and Microanalysis Facility SEM Superuser 2022 – 2023
University of California, Santa Barbara

Early Undergraduate Research Experience & Knowledge Acquisition 2023
Research Mentor, University of California, Santa Barbara

Summer Institute in Mathematics and Science Research Mentor 2022, 2023
University of California, Santa Barbara

Undergraduate Research, Advisor: Prof. Chelsea Davis 2017 – 2019
Department of Materials Engineering, Purdue University

Summer Undergraduate Research Fellow 2018
Department of Materials Engineering, Purdue University

Undergraduate Teaching Assistant 2018 – 2019
Department of Materials Engineering, Purdue University

Product Development Intern, Organic Materials Engineering Dept. 2017
Stellantis (formerly Fiat Chrysler Automobiles), Auburn Hills, MI

Peer Teaching Assistant 2016 - 2017
First Year Engineering, Purdue University

PUBLICATIONS

13. Kwon, Y., Singh, S., Rodriguez, D., **Chau, A.L.**, Pitenis, A.A., De Tomaso, A.W., and Valentine, M.T., Mechanical resilience of the sessile tunicate *Botryllus schlosseri*. *Journal of Experimental Biology,* 2023. Doi: 10.1242/jeb.245124
12. **Chau, A.L.**, Pugsley, C.D., Miyamoto, M.E., Tang, Y., Eisenbach, C.D., Mates, T.E., Hawker, C.J., Valentine, M.T., and Pitenis, A.A., pH-Dependent Friction of Polyacrylamide Hydrogels. *Tribology Letters,* 2023, 71, Doi: 10.1007/s11249-023-01779-4
11. **Chau, A.L.*,** Edwards, C.E.R.*, Helgeson, M.E., and Pitenis, A.A., Designing Superlubricious Hydrogels from Spontaneous Peroxidation Gradients. *ACS Applied Materials and Interfaces,* 2023, 15, Doi: 10.1021/acsami.3c04636 (*equal contribution)
10. Atkins, D.J., **Chau, A.L.**, Rosas, J.M., Chen, Y-T., Chan, S., Urueña, J.M., and Pitenis, A.A., Silicone Implant Roughness, Friction, and Wear. *Surface Topography: Metrology and Properties,* 2022, 11, 014010, Doi: 10.1088/2051-672X/ac9f5a
9. Rosas, J.M., Atkins, D.J., **Chau, A.L.**, Chen, Y-T., Bae, R., Cavanaugh, M.K., Espinosa Lima, R.I., Bordeos, A., Bryant, M.G., and Pitenis, A.A., *In Vitro* Models of Soft Tissue Damage by Implant-Associated Frictional Shear Stresses. *Proceedings of the Institution of Mechanical Engineers, Part J: J Engineering Tribology,* 2022, 237, Doi: 10.1177/13506501221132897
8. **Chau, A.L.,** Getty, P.T., Rhode, A.R., Bates, C.M., Hawker, C.J., and Pitenis, A.A., Superlubricity of pH-Responsive Hydrogels in Extreme Environments. *Frontiers in Chemistry,* 2022, 10, 891519, Doi: 10.3389/fchem.2022.891519
7. **Chau, A.L.**, Urueña, J.M., and Pitenis, A.A., Load-independent hydrogel friction. *Biotribology,* 2021, 26, 100183, Doi: 10.1016/j.biotri.2021.100183
6. McGhee, E.O., **Chau, A.L.,** Cavanaugh, M.K., Gabriel Rosa, J., Davidson IV, C.L.G., Kim, J., Urueña, J.M., Sumerlin, B.S., Pitenis, A.A., and Sawyer, W.G., Amphiphilic Gel Lubrication and the Solvophilic Transition. *Biotribology,* 2021, 26, 100170, Doi: 10.1016/j.biotri.2021.100170
5. **Chau, A.L.**, Cavanaugh, M.K, Chen, Y-T., and Pitenis, A.A., A Simple Contact Mechanics Model for Highly Strained Aqueous Surface Gels. *Experimental Mechanics,* 2021, 61, 699-703, Doi: 10.1007/s11340-021-00699-5
4. Deneke, N.*, **Chau, A.L.***, and Davis, C.S., Pressure tunable adhesion of rough elastomers. *Soft Matter,* 2020, 17, 863-869, Doi: 10.1039/D0SM01754J (*equal contribution)
3. Degen G.D., Chen, Y-T., **Chau, A.L.**, Månsson, L.K., and Pitenis, A.A., Poroelasticity of highly confined hydrogel films measured with a surface

forces apparatus. *Soft Matter*, 2020, 16, 8096-8100, Doi:10.1039/d0sm01312a

2. **Chau, A.L.**, Rosas, J., Degen, G.D., Månsson, L.K., Chen, J., Valois, E., and Pitenis, A.A., Aqueous Surface Gels as Low Friction Interfaces to Mitigate Implant-Associated Inflammation. *Journal of Materials Chemistry B,* 2020, 8, 6782-6791, Doi: 10.1039/D0TB00582G
1. Son, H., **Chau, A.L.**, and Davis, C.S., Polymer thin film adhesion utilizing the transition from surface wrinkling to delamination. *Soft Matter,* 2019, 15, 6375-6382, Doi: 10.1039/C9SM01052A

ORAL PRESENTATIONS

10. **Chau, A.L.**, Karnaukh, K., Maskiewicz, I., Månsson, L.K., Pugsley, C.D., Miyamoto, M., Bailey, S.J., Read de Alaniz, J., and Pitenis, A.A., Lubricity of Light-Tunable Hydrogels. *ITC Fukuoka.* 2023. Fukuoka, Japan.
9. **Chau, A.L.**, Karnaukh, K., Månsson, L.K., Pugsley, C.D., Miyamoto, M., Bailey, S.J., Read de Alaniz, J., and Pitenis, A.A., Photoresponsive Hydrogel Lubricity. *STLE Annual Meeting & Exhibition.* 2023. Long Beach, CA.
8. **Chau, A.L.**, Karnaukh, K., Månsson, L.K., Bailey, S.J., Read de Alaniz, J., and Pitenis, A.A., Photoswitchable Hydrogel Friction. *MRS Spring Meeting.* 2023. San Francisco, CA.
7. **Chau, A.L.**, Karnaukh, K., Månsson, L.K., Bailey, S.J., Read de Alaniz, J., and Pitenis, A.A., Light-tunable hydrogel friction. *ACS Spring Meeting.* 2023. Indianapolis, IN.
6. **Chau, A.L.**, Edwards, C.E.R., Helgeson, M.E., and Pitenis, A.A., Hydrogel Superlubricity from Gradient Surface Structures. *Adhesion Society.* 2023. Orlando, FL.
5. **Chau, A.L.**, Getty, P.T., Rhode, A.R., Pugsley, C.D., Bates, C.M., Hawker, C.J., and Pitenis, A.A., Lubricity of Stimuli-Responsive Hydrogels (oral presentation). *Materials Research Outreach Program Symposium.* 2023. Santa Barbara, CA.
4. **Chau, A.L.**, Getty, P.T., Rhode, A.R., Bates, C.M., Hawker, C.J., and Pitenis, A.A., Superlubricity of pH-Responsive Hydrogels in Extreme Environments. *World Tribology Congress.* 2022. Lyon, France.
3. **Chau, A.L.**, Getty, P.T., Rhode, A.R., Bates, C.M., Hawker, C.J., and Pitenis, A.A., Superlubricity of pH-Responsive Hydrogels in Extreme Environments. *STLE Annual Meeting & Exhibition.* 2022. Orlando, FL.
2. **Chau, A.L.** and Davis, C.S., Polymer Thin Film Dewetting for Precisely Controlled Patterning. *MSE Summer Soft Matter Symposium.* 2019. West Lafayette, IN.
1. **Chau, A.L.,** Son, H., and Davis, C.S., Thin Film Adhesion through Wrinkling to Delamination Transition. *Purdue Undergraduate Research Conference*. 2018. West Lafayette, IN. (1st place award)

POSTER PRESENTATIONS

5. **Chau, A.L.**, Getty, P.T., Rhode, A.R., Bates, C.M., Hawker, C.J., and Pitenis, A.A., Superlubricity of pH-Responsive Hydrogels in Extreme Environments. *Gordon Research Conference on Tribology.* 2022. Lewiston, ME.
4. **Chau, A.L.**, Getty, P.T., Rhode, A.R., Bates, C.M., Hawker, C.J., and Pitenis, A.A., Superlubricity of Poly(acrylamide-*co*-acrylic acid) Hydrogels in Extreme Conditions. *Adhesion Society Annual Meeting.* 2022. San Diego, CA.
3. **Chau, A.L.**, Edwards, C., Helgeson, M., and Pitenis, A.A., Structure-Property Relationships of Gradient Hydrogels. *STLE Tribology Frontiers Virtual Conference*. 2020. (2nd place award)
2. **Chau, A.L.,** Son, H., and Davis, C.S., Thin Film Adhesion Between Glassy Thin Films and Compliant Substrates through Surface Buckling Instability. *Surface Engineering and Advanced Materials Processing Conference.* 2019. West Lafayette, IN.
1. **Chau, A.L.,** Son, H., and Davis, C.S., Validation of Wrinkling-to-Delamination Adhesion Measurement Technique. *Summer Undergraduate Research Fellowship Research Symposium.* 2018. West Lafayette, IN.

AWARDS & FELLOWSHIPS

University of California President's Dissertation Fellowship	2023
72nd Lindau Nobel Laureate Meeting (Physiology & Medicine) Delegate	2023
Doctoral Student Travel Grant	2023
Connie Frank Medical Fellowship	2023
Heeger Travel Fellowship	2023
STLE Early Career Award	2023
STLE Jeanie S. McCoy Scholarship	2023
MRL/Dow Travel Fellowship	2022
Northern California STLE Section Research Scholarship	2022
Bright Horizon Global Foundation Materials Dept. Service Award	2021, 2023
NSF Graduate Research Fellowship	2020 – 2023

ABSTRACT

Design and Tribological Characterization of Stimuli-Responsive Hydrogels

by

Allison Leigh Chau

Aqueous, low friction interfaces are ubiquitous in biology – from articular cartilage that coats synovial joints to mucin layers that act as a lubricating barrier for epithelial surfaces throughout the body – and have exceptional tribological properties. Hydrogels, three-dimensional networks of crosslinked hydrophilic polymer chains swollen in water, are often utilized as synthetic mimics for these biological systems due to their high water content, lubricity, and tunable mechanical properties. There is a great need to investigate the structure-property relationship of hydrogels to elucidate the lubrication mechanisms driving their behavior in order to design hydrogels with tunable friction coefficients.

In this dissertation, I provide a framework to study stimuli-responsive hydrogels and describe multiple methods to engineer hydrogel friction coefficients. Herein, we explore the tribological behavior of four systems: polyacrylamide (PAAm), poly(2-hydroxyethyl methacrylate) (pHEMA),

poly(acrylamide-*co*-acrylic acid) (P(AAm-*co*-AA)), and poly(*N*-isopropylacrylamide-*co*-spiropyran) (pNIPAAm-*co*-SP). By controlling environmental oxygen during polymerization, we synthesized non-ionic PAAm hydrogels with gradient surface structures. Using a reaction-kinetics model, we predicted the thickness and concentration of this surface gradient layer and investigated the impact of surface structure on the tribological behavior of these hydrogels. The amphiphilic nature of pHEMA hydrogels was explored and their solvophilic transition was exploited to control friction by regulating the ratio of water and ethanol. Charged P(AAm-*co*-AA) hydrogel friction was controlled by altering solution pH and AA concentration, and we demonstrated two orders of magnitude tunability of the friction coefficient. The surprising pH-dependent friction behavior of PAAm in response to extreme pH was also examined. Light tunable pNIPAAm gels were synthesized through the incorporation of spiropyran-methacrylate, a photoswitchable molecule. By manipulating the swelling and deswelling of the pNIPAAm-*co*-SP-MA gels with light, friction was tuned an order of magnitude. The investigations herein offer new insight into designing hydrogels with tunable tribological behavior and contribute to a deeper understanding of hydrogel lubricity.

TABLE OF CONTENTS

LIST OF FIGURES

LIST OF TABLES

LIST OF SCHEMATICS

LIST OF EQUATIONS

1 CHAPTER 1: BIOLOGICAL INSPIRATION

Table of Contents

1.1 Dissertation Overview

This dissertation discusses the design and tribological characterization of stimuli-responsive hydrogels. Chapter 1 establishes the biological motivation and need for understanding the structure-property relationship of hydrogel systems with tunable friction coefficients. Chapter 2 reviews the characteristics properties and microstructure of hydrogels. Chapter 3 gives an overview of tribology as a field, the deviation of hydrogel tribology from typical lubrication systems, and the proposed hydrogel lubrication mechanisms. Chapter 4 briefly describes the hydrogel systems analyzed in this dissertation along with the methods used to characterize their mechanical and tribological behavior. Chapters 5 – 8 discuss three different hydrogel systems: Chapter 5 focuses on the design of superlubricious hydrogels through controlling environmental oxygen, Chapter 6 discusses tuning friction by leveraging the amphiphilic and solvophilic nature of polymers, and Chapters 7 – 8 demonstrate the tribological tunability of pH-responsive hydrogels. The dissertation concludes with Chapters 9 – 10, which introduce the development of photoresponsive gels, which hold great promise for friction control and tunability, and summarize the important findings and future directions.

1.2 Biological Lubrication

Aqueous, heterogeneous hierarchical systems are ubiquitous in biology – from articular cartilage that coats synovial joints[1] to mucin layers that act as a lubricating barrier for epithelial surfaces throughout the body (*e.g.* eyes, ears, reproductive tract, gastrointestinal tract, and respiratory tract).[2–4] These systems are of interest to the soft matter tribological community due to their exceptional lubricating properties and low friction coefficients in a wide range of challenging sliding conditions.

Articular cartilage is a 2 – 4 mm thick connective tissue that coats the surfaces of joints and exhibits extremely low friction coefficients (μ ~ 0.001) despite high contact pressures (~ MPa) and high sliding speeds (~ cm/s).[5,6] There have been many studies investigating the mechanisms behind this low friction, [5,7–9] and the biphasic gradient structure of cartilage is thought to play an important role in its tribological behavior (*e.g.*, friction, lubrication) (**Figure 1.1**). Cartilage is 70 – 80 wt.% fluid with a dense extracellular matrix (ECM) secreted by embedded chondrocytes. The ECM is primarily composed of collagen fibers and proteins (*e.g.* aggrecan, lubricin, hyaluronic acid) that form a heterogeneous brush-like entangled network capable of withstanding enormous amounts of pressure and sliding speeds.[10] These components work synergistically together – collagen is thought to provide tensile strength to the network while proteins

maintain hydration, leading to osmotic swelling that provides compressive load support.[5]

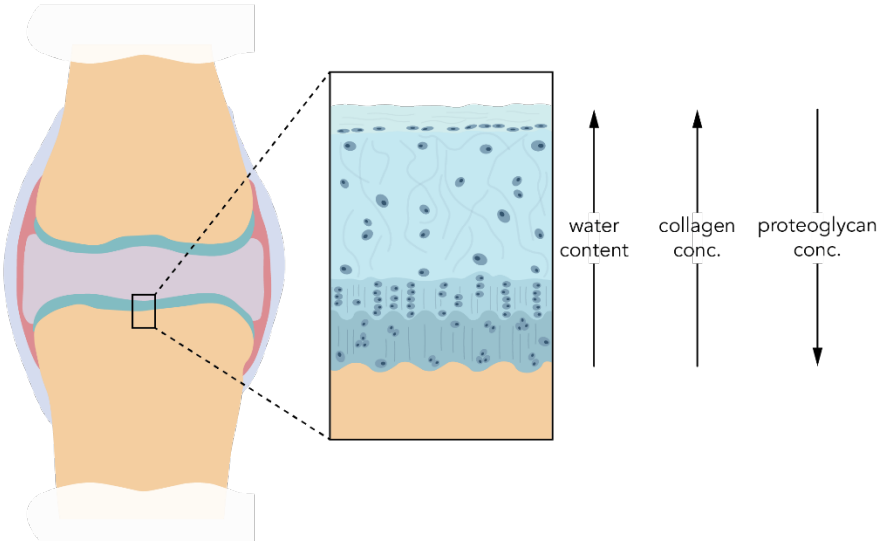

Figure 1.1 Schematic of articular cartilage with inset demonstrating the hierarchical, gradient structure of its extracellular matrix. Water content increases further from the bone. Adapted with permission from Y. Wang et al., *Adv. NanoBiomed. Res.*, **2**, 2022 under the Creative Commons license (http://creativecommons.org/licenses/by/4.0/).[11]

The distribution of these components within the ECM is heterogeneous, with water content and collagen concentration increasing and proteoglycan concentration decreasing closer to the cartilage surface. The low friction of cartilage is attributed to this high water content surface layer, although its exact composition is still debated.[5,12]

Similarly, mucus is a biological hydrogel composed primarily of water and glycoproteins (*i.e.*, mucins) that protects epithelial surfaces throughout the body.[2] In addition to acting as a barrier to foreign debris, mucus is a natural lubricant, shielding these surfaces from shear forces.[4] The lubricating properties

of mucus are particularly interesting due to the intricate structure of the mucin molecules that allow them to form both covalent (disulfide) and physical (aggregation and hydrophobic interactions) bonds.[3,4] This combination of crosslinks leads to interesting rheological behavior, as the physical crosslinks can break and reform under shear stress.[13,14] The ocular tear film, which coats the corneal epithelium, is one commonly studied mucus network (**Figure 1.2a**). This 2 – 5.5 μm thick film is composed of three layers (mucin, aqueous network, lipid) and protects the cornea and eyelid interface.[15] When this film is disrupted, as is the case when a foreign object such as a contact lens is inserted, interfacial friction can increase, leading to greater discomfort.[16,17]

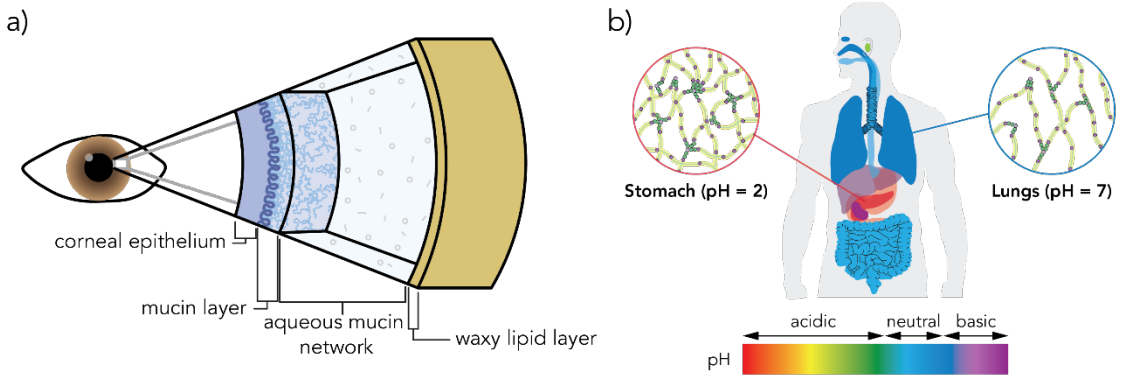

Figure 1.2 (a) Schematic of the ocular tear film. Adapted with permission from A. Kayal, "The Physiology of Tear Film", *Dry Eye Syndrome*, 2021 under the Creative Commons license (http://creativecommons.org/licenses/by/3.0/).[15] **(b)** Schematic of epithelial surfaces throughout the body and the pH of the surrounding environment. Adapted with permission from C. Wagner *et al.*, *Annu. Rev. Cell Dev. Biol.*, **34**, 2018 (Copyright © 2018 Annual Reviews)[2] and C. Werlang *et al.*, *Nat. Rev. Mater.*, **4**, 2019 (Copyright © 2019 Springer Nature).[4]

Additionally, depending on the pH of its surroundings, mucus adopts different physical and mechanical properties. In acidic environments, such as in

the stomach, the storage modulus of mucus increases due to increased crosslinking of hydrophobic domains.[13] In contrast, mucus in environments with neutral pH, such as the lungs, are less dense with fewer crosslinks (Figure 1.2b). Other studies have similarly demonstrated conformation changes in mucin with changing pH due to electrostatics.[18,19]

The structural and mechanical transformation of mucus in response to its environment and the heterogeneous, hierarchical structure of articular cartilage offer these biological systems remarkable tribological properties. However, it is difficult to directly study these systems due to their complexity. For instance, commercially available mucin does not have the same mechanical properties as native mucus due to the purification process, [20–22] making it very difficult to accurately study its behavior under various pH conditions. To circumvent this problem, hydrogels are often utilized as proxy materials.

1.3 Hydrogels as Synthetic Mimics

Hydrogels are excellent substitutions for articular cartilage [23–30] and similar aqueous, compliant biological systems[22,31–33] due to their high water content (> 80%), mechanical tunability, and lubricity.[25–27,34,35] Hydrogels are three-dimensional networks of crosslinked hydrophilic polymer chains swollen in water that possess characteristics of both liquids and solids, with the ability to maintain shape under stress while still allowing for fluid flow and diffusion.

Ever since the first published paper on hydrophilic gels by Wichterle and Lím in 1960,[36] hydrogel research has exponentially increased, from less than 1,000 total publications by the 1980s to more than 10,000 publications *per year* in 2020, accumulating to over 100,000 publications.[37] The rising interest in this intriguing material can be attributed to its versatility and application within the biomedical and commercial sectors through its use in contact lenses,[38,39] drug delivery systems,[40–44] tissue scaffolds,[26,45–47] and commercial products such as diapers and cosmetics.[48,49] Interest in soft matter within the research space has also gained popularity due to advancements in 3D printing,[50–52] soft robotics,[53,54] and biomimetics.[46,55,56]

The importance of the interfacial and tribological properties of hydrogels in these various applications cannot be understated. Understanding the fundamental structure-property relationships of hydrogels and elucidating the lubrication mechanisms behind their tribological behavior can help pave the way towards designing synthetic systems that interface with the human body in a more organic manner. In this dissertation, I provide a framework to study stimuli-responsive hydrogels and describe multiple methods to engineer hydrogel friction coefficient. Tunable friction coefficients are achieved via the regulation of environmental variables such as oxygen, solvent, pH, and light. These investigations offer insight into designing hydrogels with tunable tribological behavior and contribute to a deeper understanding of hydrogel lubricity.

2 CHAPTER 2: HYDROGEL OVERVIEW

To design hydrogels with tunable friction coefficients, understanding their structure-property relationship is essential. This chapter will briefly discuss polymers frequently used for hydrogel synthesis, the theoretical framework for hydrogel swelling, ways to tune the hydrogel microstructure, and the relationship between mesh size and hydrogel properties.

Table of Contents

2.1 Hydrogel Polymerization

Hydrogels are three-dimensional networks of crosslinked hydrophilic polymers swollen in water (**Figure 2.1**). They are comprised of synthetic polymers, natural polymers, or a combination of both. Some common synthetic polymers used to form hydrogels include polyacrylamide (PAAm),[57–62] poly(ethylene glycol) (PEG),[63–66] poly(2-hydroxyethyl methacrylate) (pHEMA),[67–69] poly(acrylic acid) (PAA),[70–75] poly(*N*-isopropylacrylamide) (pNIPAAm),[76–82] and poly(vinyl alcohol) (PVA)[28,83–85] (**Figure 2.1**). Natural polymers such as collagen,[86–88] gelatin,[89,90] agarose,[91,92] and alginate[85,93,94] are also frequently used.

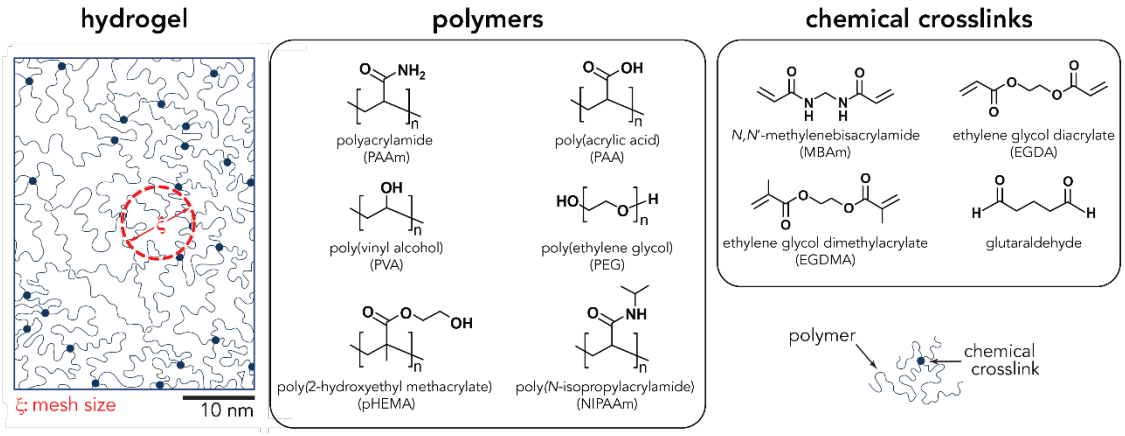

Figure 2.1 Idealized hydrogel schematic with chemical structures of the common polymers and chemical crosslinks used in hydrogel synthesis. Hydrogel mesh size, ξ, is indicated in red.

Crosslinks can either be chemical or physical in nature. Chemical crosslinks are covalent bonds that permanently link polymer chains together[95] while physical crosslinks are non-covalent in nature and include chain entanglements, hydrophobic bonding regimes, ionic complexes, hydrogen bonds, localized

crystallization, helix aggregation, and electrostatic interactions (**Figure 2.2**).[96,97] These bonds are often reversible in response to external stimuli, giving the hydrogel interesting mechanical and tribological properties. Some commonly utilized chemical crosslinks are *N,N'*-methylenebisacrylamide (MBAm),[35,98] glutaraldehyde,[99] ethylene glycol dimethacrylate (EGDMA),[100] and ethylene glycol diacrylate (EGDA) (**Figure 2.1**).[101]

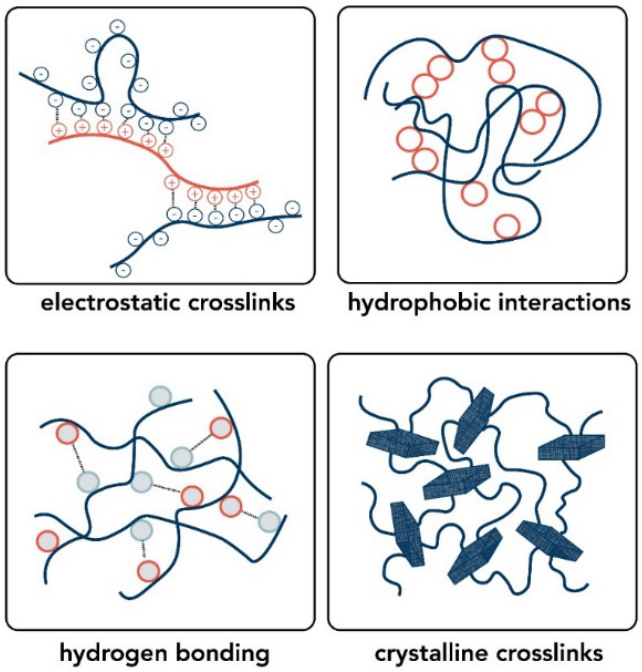

Figure 2.2 Schematic demonstrating different physical crosslinks in hydrogel systems, including electrostatic crosslinks, hydrophobic interactions, hydrogen bonding, and crystalline crosslinks.

One of the most common synthetic routes used to make hydrogels is free-radical polymerization, where water-soluble monomers are dissolved in solution with crosslinker molecules and an initiating system, which is typically redox or UV-initiated.[65] For redox-initiated systems, ammonium persulfate (APS) or

potassium persulfate (KPS) are often used as the initiator with *N,N,N',N'*-tetramethylethylenediamine (TEMED) or heat as the catalyst to speed up the reaction.[65,102,103] For UV-initiated systems, 2-hydroxy-1-[4-(2-hydroxyethoxy) phenyl]-2-methyl-1-propanone] (Irgacure 2959) and lithium phenyl-2,4,6-trimethylbenzoylphosphinate (LAP) are two of the most common water soluble photoinitiators.[104] While there have been several studies demonstrating that initiator concentration and selection can impact polymerization kinetics and hydrogel structure, this factor is often ignored.[65,102,105,106] For more information about the polymerization process and kinetics, see **Section 5.7**.

To quantify total polymer (%T) and crosslinker (%C) concentration within hydrogel networks, the following convention is often utilized:[35,73,107]

$$\%T\ (w/v) = \frac{monomer\ (g) + crosslinker\ (g)}{total\ volume\ (mL)} x100 \qquad \text{Eqn. 2.1}$$

$$\%C\ (w/w) = \frac{crosslinker\ (g)}{monomer\ (g) + crosslinker\ (g)} x100 \qquad \text{Eqn. 2.2}$$

where %T encompasses both monomer and crosslinker mass and %C quantifies the percentage of polymer that is crosslinker. Sometimes, the amount of crosslinker is considered negligible in the total polymer (%T) calculation due to its small quantity in comparison to the amount of monomer. With this convention, the total polymer concentration (%T) is calculated based solely on monomer mass, and the crosslinker concentration (%C) is just the ratio of

crosslinker to monomer mass.[107] Another common polymer and crosslinker quantification method is based on weight percent of the entire pre-polymerized mass, including water:[98,108,109]

$$mononer\ wt\% = \frac{monomer\ (g)}{total\ mass\ (g)} x100 \qquad \text{Eqn. 2.3}$$

$$crosslinker\ wt\% = \frac{crosslinker\ (g)}{total\ mass\ (g)} x100 \qquad \text{Eqn. 2.4}$$

Occasionally, monomer and crosslinker mole percent (mol%)[110] or monomer-to-crosslinker molar ratio is used instead.[111,112] In this dissertation, polymer and crosslinker concentration will be discussed in wt.% and calculated with Eqn. 2.3 and Eqn. 2.4. Monomer-to-crosslinker molar ratio will also be utilized occasionally. Monomer concentration, crosslinker concentration, and their ratio impact gel swelling, structure, and mechanics, as will be discussed further in Section 2.6.

2.2 Theoretical Framework for Hydrogel Swelling

Hydrogel swelling can be theoretically predicted by the Flory-Rehner model, which combines Gaussian chain elasticity and the Flory-Huggins solution theory to describe network elasticity and polymer-solvent mixing, respectively.[113,114] Within this model, there are two assumptions.[115,116] The first is molecular incompressibility – the volume of the swollen gel is the sum of the volume of the dry network and the absorbed solvent. The second assumption is

known as the Frenkel-Flory-Rehner (FFR) hypothesis which states that there is a thermodynamic balance between the entropy of mixing of the polymer and solvent and the rubber elasticity associated with stretching the network.[115] Based on this assumption, the free energy of the gel (ΔG_{tot}) can be written as the sum of the entropy of mixing of the polymers and solvent molecules (ΔG_{mix}) and the elastic energy of the stretched polymer chains (ΔG_{el}):

$$\Delta G_{\mathrm{tot}} = \Delta G_{\mathrm{mix}} + \Delta G_{\mathrm{el}} \qquad \text{Eqn. 2.5}$$

The driving force behind hydrogel swelling is mainly entropic – without the elastic retractive force, gels would swell infinitely to increase configurational entropy. However, as gel volume increases with swelling, the polymer chains stretch and an elastic retractive force develops as the configurational entropy of the chains decreases. Equilibrium swelling is achieved once these opposing forces balance, and the hydrogel will no longer change volume. For polyelectrolyte hydrogels (*i.e.*, charged hydrogel networks composed of polymers with ionizable functional groups), ionic contributions to the free energy (ΔG_{ion}) due to the presence of ions within and outside the network also need to be considered in the total free energy of the gel.[117]

Based on this thermodynamic balance, the Flory-Rehner equation for non-ionic polymer networks was developed:[114]

$$-\left[\ln\left(1-v_{2,\mathrm{s}}\right)+v_{2,\mathrm{s}}+\chi v_{2,\mathrm{s}}^{2}\right]=\left(\frac{V_1}{\bar{v}\bar{M}_{\mathrm{c}}}\right)\left(1-\frac{2\bar{M}_{\mathrm{c}}}{\bar{M}_{\mathrm{n}}}\right)\left(v_{2,\mathrm{s}}^{1/3}-\frac{v_{2,\mathrm{s}}}{2}\right) \qquad \text{Eqn. 2.6}$$

which can be rewritten as:

$$\frac{1}{\bar{M}_{\mathrm{c}}}=\frac{2}{\bar{M}_{\mathrm{n}}}-\frac{\frac{\bar{v}}{V_1}\left[\ln\left(1-v_{2,\mathrm{s}}\right)+v_{2,\mathrm{s}}+\chi v_{2,\mathrm{s}}^{2}\right]}{\left(v_{2,\mathrm{s}}^{1/3}-\frac{v_{2,\mathrm{s}}}{2}\right)} \qquad \text{Eqn. 2.7}$$

where $v_{2,\mathrm{s}}$ is the polymer volume fraction of a hydrogel at equilibrium swelling, χ is the Flory polymer-solvent interaction parameter (which is dependent on temperature and polymer volume fraction), $\bar{v}$ is the specific volume of the dry polymer, V_1 is the molar volume of the solvent (*e.g.*, water), $\bar{M}_{\mathrm{c}}$ is the average molecular weight between crosslinks, and $\bar{M}_{\mathrm{n}}$ is the number average molecular weight of the uncrosslinked polymer. From **Eqn. 2.7**, the volumetric swelling ratio, Q_v, can be determined:[114]

$$Q_{\mathrm{v}}^{5/3}=\frac{2\bar{M}_{\mathrm{c}}\frac{\bar{v}}{V_1}\left(\frac{1}{2}-\chi\right)}{v_{2,\mathrm{r}}^{2/3}\left(1-\frac{3\bar{M}_{\mathrm{c}}}{\bar{M}_{\mathrm{n}}}\right)} \qquad \text{Eqn. 2.8}$$

where $v_{2,\mathrm{r}}$ is the polymer volume fraction of a hydrogel immediately after polymerization (*i.e.*, before swelling). This equation can be simplified to:[118]

$$Q_{\mathrm{v}}^{5/3}\cong\frac{\bar{v}\bar{M}_{\mathrm{c}}}{V_1}\left(\frac{1}{2}-\chi\right) \qquad \text{Eqn. 2.9}$$

While the Flory-Rehner model sometimes follow experimental results, it arguably doesn't fit the data well and requires many fitting parameters.[115,119] Because of

this, other theoretical models have been developed to describe the equilibrium swelling behavior of hydrogels.[115,120–122]

2.3 Quantifying Hydrogel Swelling

There are several equations used in literature to quantify swelling, as demonstrated in **Table 2.1**. For the most part, the swollen hydrogel mass (m_s) and volume (V_s), dried hydrogel mass (m_d) and volume (V_d), and as polymerized mass (m_p) and volume (V_p) are the only variables needed. However, the terminology used to describe each method is ambiguous and inconsistent. For instance, the term "swelling ratio" has at least 10 different calculation methods across published literature (**Table 2.1**). Therefore, when comparing swelling data across different sources, it is important to examine the method used rather than just rely on terminology.

Table 2.1 Comparing equations in literature used to quantify swelling. The nomenclature used for variables are as follows: m – mass, V – volume, D – diameter. The nomenclature used for the subscripts are as follows: s – swollen, d – dry, p – as polymerized.

Terminology	Equation	Ref.
Equilibrium swelling ratio Degree of swelling Weight swelling ratio	$\frac{m_s}{m_d}$	123–125
Polymer weight fraction	$\frac{m_d}{m_s}$	126
Weight swelling ratio after preparation	$\frac{m_p}{m_d}$	125
Fluid absorption capacity	$\frac{m_s - m_d}{m_s}$	73

Water weight percent Water content Degree of swelling	$\left(\frac{m_s - m_d}{m_s}\right) x100$	44,111,124
Equilibrium swelling ratio Degree of swelling Weight swelling ratio	$\frac{m_s - m_d}{m_d}$	122,127,128
Weight swelling ratio	$\left(\frac{m_s - m_d}{m_d}\right) x100$	128,129
Mass swelling percent	$\left(\frac{m_s - m_p}{m_p}\right) x100$	130
Volume degree of swelling	$\frac{V_s}{V_d}$	107,124,131
Swelling ratio	$\frac{V_s}{V_p}$	132
Swelling ratio	$\frac{V_p}{V_s}$	133
Volume change	$\left(\frac{V_s - V_p}{V_p}\right) x100$	69
Swelling ratio	$\left(\frac{D_s}{D_p}\right)^3$	132
Swelling ratio	$\left(\frac{D_p}{D_s}\right)^3$	133
Linear swelling ratio	$\lambda = \left(1 + \left(\frac{m_{hydrogel}}{m_{polymer}} - 1\right) \cdot \frac{\rho_{polymer}}{\rho_{water}}\right)^{1/3}$	134
Equilibrium swelling ratio	$Q_v = 1 + \frac{\left(\frac{m_s}{m_d} - 1\right)\rho_{polymer}}{\rho_{water}}$	135

The volume change for polyacrylamide hydrogels with varying acrylamide concentration but constant monomer-to-crosslinker molar ratio (54:1) was

examined (Figure 2.3). Surprisingly, the swelling behavior was not monotonic – the volume initially decreased with acrylamide concentration, reached a minimum, and then increased. This behavior does not follow the Flory-Rehner model, which predicts a monotonic decrease with increasing monomer concentration.

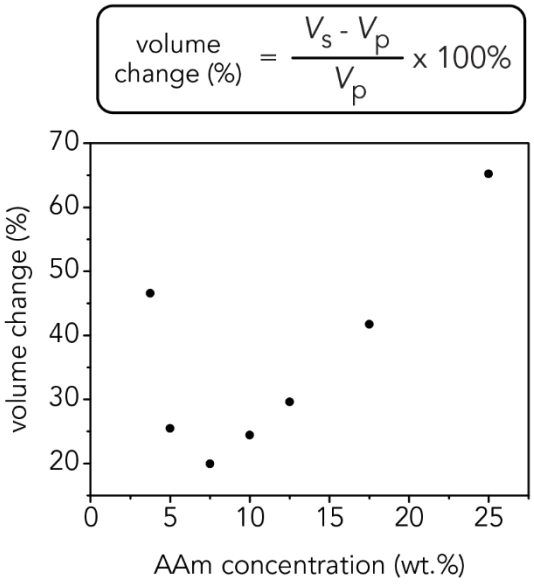

Figure 2.3 Volume change as a function of acrylamide (AAm) concentration (wt.%) for polyacrylamide hydrogels with the same monomer-to-crosslinker molar ratio (54:1). Surprisingly, the swelling behavior was not monotonic.

One potential reason for this deviation is the swelling metric chosen. Since the volume change equation utilizes the volume of the hydrogel as polymerized (V_p) and fully swollen (V_s), it only accounts for the excess water absorbed by the hydrogel after polymerization and overlooks the existing water from the pre-polymerized solution. Conversely, the Flory-Rehner model accounts for the total amount of water in the gel by considering the polymer volume fraction at

equilibrium swelling, $v_{2,s}$ (see **Eqn. 2.18**). If another swelling metric such as the equilibrium swelling ratio (m_s/m_d) or volume degree of swelling (V_s/V_d) was used, the swelling behavior would most likely decrease as predicted by the Flory-Rehner model since these metrics account for the total amount of water in the hydrogel. However, it is still interesting to note that the minimum swelling occurred at an intermediate acrylamide concentration (7.5 wt.%). While this phenomenon has not been fully explored, it demonstrates the impact that different swelling metrics can have in the interpretation of the data (see **Section 8.3.1** and **Figure 8.3**) and further validates the importance of being cognizant about the selected swelling metric.

2.4 Hydrogel Mesh Size

Mesh size is a structural parameter that is often used to characterize the hydrogel network structure. It controls hydrogel mechanics and many other macroscopic properties and can be thought of as a measure of polymer chain mobility.[95,136–138] The following section will describe two common methods used to estimate mesh size based on the characteristics of the polymer chain.

2.4.1 Correlation Length

In his seminal work, de Gennes viewed hydrogels as polymer solutions that existed at the critical overlap concentration, *c**, where polymer chains in solution

just begin to overlap and transition from the dilute regime (c < c*) to the semi-dilute regime (c > c*) (Figure 2.4).

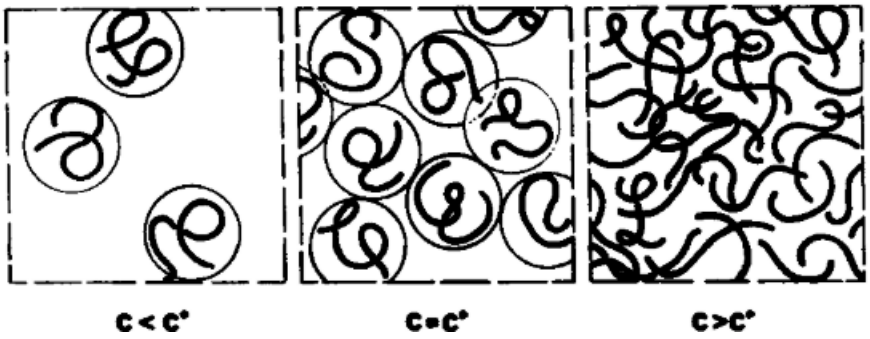

Figure 2.4 Schematic of polymer chains in solution in the dilute (c < c*) and semi-dilute regimes (c* > c). According to de Gennes, hydrogels exist at the critical overlap concentration (c = c*), where the polymer chains just begin to overlap. From *Scaling Concepts in Polymer Physics,* by P-G de Gennes. Copyright © 1979 by Cornell University Press. Used by permission of the publisher, Cornell University Press.[137]

In this framework, mesh size, ξ, is defined as the correlation length between monomers in the hydrogel network.[137] This occurs within polymer segments known as "blobs", where the correlation length is the distance between two points of entanglement in which the polymer chain does not interact with any other polymers (Figure 2.5).[139]

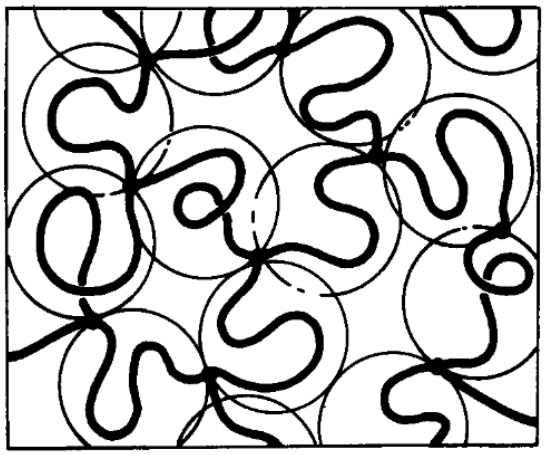

Figure 2.5 Schematic of hydrogel network existing at the critical overlap concentration, *c**. The chain is segmented into "blobs" composed of *N* monomers. Within each blob, the chain does not interact with any other polymer chains. The blob diameter is also known as the mesh size, ξ. From *Scaling Concepts in Polymer Physics*, by P-G de Gennes. Copyright © 1979 by Cornell University Press. Used by permission of the publisher, Cornell University Press.[137]

Therefore, the mesh size scales with blob diameter and can be estimated with the following equation:[137,139]

$$\xi = R_{\mathrm{g}} \left(\frac{c^*}{c} \right)^m \qquad \text{Eqn. 2.10}$$

where R_{g} is the radius of gyration of a polymer chain and scales with the number of repeat units within the blob (*e.g.*, $R_{\mathrm{g}} \sim N^{3/5}$ in a good solvent), c is the polymer concentration, c^* is the critical overlap concentration, and m is a scaling coefficient dependent on water-polymer interactions. For non-ionic polymers in a good solvent, m = 0.76.[140] The critical overlap concentration can be calculated from **Eqn. 2.11**, where N is the number of repeat units, M_{w} is the weight-average molecular weight of the polymer and N_{A} is Avogadro's number.[139]

$$c^* = \frac{N}{R_{\mathrm{g}}^3} = \frac{3M_{\mathrm{w}}}{4\pi N_{\mathrm{A}} R_{\mathrm{g}}^3} \qquad \text{Eqn. 2.11}$$

Within this framework, the mesh size can be thought of as the conformational space (*i.e.*, blob) in which polymer chains can thermally fluctuate without interacting with any other polymer chains. This correlation mesh size often scales with the average distance between chemical crosslinks in network and is frequently defined as such.[141,142]

2.4.2 End-to-End Distance

Peppas *et al.* defined mesh size as the end-to-end distance of a polymer chain between chemical crosslinks:[131]

$$\xi = \nu_{2,s}^{-1/3}(\bar{r}_0^2)^{1/2} \qquad \text{Eqn. 2.12}$$

where $\nu_{2,s}$ is the polymer volume fraction of a hydrogel at equilibrium swelling and $(\bar{r}_0^2)^{1/2}$ is the end-to-end distance of a freely rotating polymer chain, which can be calculated as:

$$(\bar{r}_0^2)^{1/2} = lC_n^{1/2}\left(\frac{2\bar{M}_c}{M_r}\right)^{1/2} \qquad \text{Eqn. 2.13}$$

where M_r is the molecular weight of the repeat unit, C_n is the Flory characteristic ratio, $\bar{M}_c$ is the effective molecular weight between crosslinks, and l is the length of a C-C bond along the monomer backbone. Based on the equilibrium swelling theory developed by Flory and Rehner (see **Eqn. 2.7**),[113,143] Peppas *et al.* developed three equations for $\bar{M}_c$ depending on the crosslink density of the network.[131] For loosely crosslinked networks where the molecular weight between crosslinks is large enough that the chains can be represented by a Gaussian distribution, **Eqn. 2.14** should be used. **Eqn. 2.15** and **Eqn. 2.16** were developed for highly crosslinked networks (*i.e.*, in which the chains are too short for Gaussian statistics) polymerized without and with solution, respectively.

$$\frac{1}{\bar{M}_c} = \frac{2}{\bar{M}_n} - \frac{\frac{\bar{v}}{V_1}\left[\ln\left(1-\nu_{2,s}\right)+\nu_{2,s}+\chi\nu_{2,s}^2\right]}{\nu_{2,r}\left[\left(\frac{\nu_{2,s}}{\nu_{2,r}}\right)^{\frac{1}{3}}-\frac{1}{2}\left(\frac{\nu_{2,s}}{\nu_{2,r}}\right)\right]} \qquad \text{Eqn. 2.14}$$

$$\frac{1}{\bar{M}_c} = \frac{2}{\bar{M}_n} - \frac{\frac{\bar{v}}{V_1}\left[\ln\left(1-\nu_{2,s}\right)+\nu_{2,s}+\chi\nu_{2,s}^2\right]\left[1-\frac{1}{N}\nu_{2,s}^{2/3}\right]^3}{\left(\nu_{2,s}^{1/3}-\frac{1}{2}\nu_{2,s}\right)\left(1+\frac{1}{N}\nu_{2,s}^{1/3}\right)^2} \qquad \text{Eqn. 2.15}$$

$$\frac{1}{\bar{M}_c} = \frac{2}{\bar{M}_n} - \frac{\frac{\bar{v}}{V_1}\left[\ln\left(1-\nu_{2,s}\right)+\nu_{2,s}+\chi\nu_{2,s}^2\right]\left[1-\frac{1}{N}\nu_{s,r}^{2/3}\right]^3}{\nu_{2,r}\left(\left(\frac{\nu_{2,s}}{\nu_{2,r}}\right)^{1/3}-\frac{1}{2}\left(\frac{\nu_{2,s}}{\nu_{2,r}}\right)\right)\left(1+\frac{1}{N}\left(\frac{\nu_{2,s}}{\nu_{2,r}}\right)^{1/3}\right)^2} \qquad \text{Eqn. 2.16}$$

For these equations, $\bar{M}_n$ is the number average molecular weight of the uncrosslinked polymer, $\nu_{2,r}$ is the polymer volume fraction of the hydrogel right after polymerization and before swelling, χ is the Flory polymer-solvent interaction parameter (which is dependent on temperature and polymer volume fraction), $\bar{v}$ is the specific volume of the repeat unit, V_1 is the molar volume of the solvent (*e.g.*, water), and $N = \frac{2\bar{M}_c}{M_r}$, the number of repeat units between crosslinks. The 2 prefactor in *N* is assuming vinyl repeat units. For pHEMA hydrogels, Peppas *et al.* found that increasing the crosslinking ratio decreased the molecular weight between crosslinks, thereby decreasing mesh size.[131]

2.5 Mesh Size Measurements

Determining hydrogel mesh size is a difficult task. Despite the idealized schematics that are often drawn, most gels are not homogeneous and often have

a heterogeneous distribution of mesh sizes.[109] Therefore, reported mesh sizes are typically averages, and swelling is often utilized as an indirect way to predict mesh size by calculating the polymer volume fraction of the hydrogel after polymerization ($v_{2,\mathrm{r}}$) and after swelling ($v_{2,\mathrm{s}}$): [131]

$$v_{2,\mathrm{r}} = \frac{V_{\mathrm{d}}}{V_{\mathrm{p}}} \qquad \text{Eqn. 2.17}$$

$$v_{2,\mathrm{s}} = \frac{V_{\mathrm{d}}}{V_{\mathrm{s}}} \qquad \text{Eqn. 2.18}$$

where V_{d} is the volume of the dry polymer, V_{p} is the volume of the hydrogel after polymerization, and V_{s} is the hydrogel volume at equilibrium swelling. Once $v_{2,\mathrm{r}}$ and $v_{2,\mathrm{s}}$ are known, **Eqn. 2.12 – Eqn. 2.16** can be utilized to estimate mesh size by calculating $\bar{M}_{\mathrm{c}}$. Oftentimes, $\bar{M}_{\mathrm{n}}$ is unknown and needs to be approximated.

Mechanical characterization is also used to indirectly estimate mesh size using the rubber elasticity theory and the linear elastic storage modulus, *G'*: [114,137,144,145]

$$G' = Ak_BT\rho_{\mathrm{el}} = Ak_BT\frac{\rho N_{\mathrm{A}}}{\bar{M}_{\mathrm{c}}} \qquad \text{Eqn. 2.19}$$

where ρ_{el} is the number density of elastically active polymer chains in the network, ρ is density of the dry polymer network, N_{A} is Avogadro's number, and A is a pre-factor whose value changes depending on the network model. For

affine networks, $A = 1$ while $A = 1 - \frac{2}{f}$ for phantom networks, where f is the functionality of the monomer. To account for swelling, the polymer volume fraction of the swollen gel, $v_{2,s}$, can be included:

$$G' = Ak_BT\rho_{\mathrm{el}}v_{2,s}^{1/3} = Ak_BT\frac{\rho N_{\mathrm{A}}}{\bar{M}_{\mathrm{c}}}v_{2,s}^{1/3} \qquad \text{Eqn. 2.20}$$

However, both **Eqn. 2.19** and **Eqn. 2.20** are assuming defect-free networks, which is not the case in real systems. Since defects can negatively impact network elasticity, as shown in **Figure 2.6**, Flory developed **Eqn. 2.21** to account for dangling chain defects that do not contribute to network elasticity.

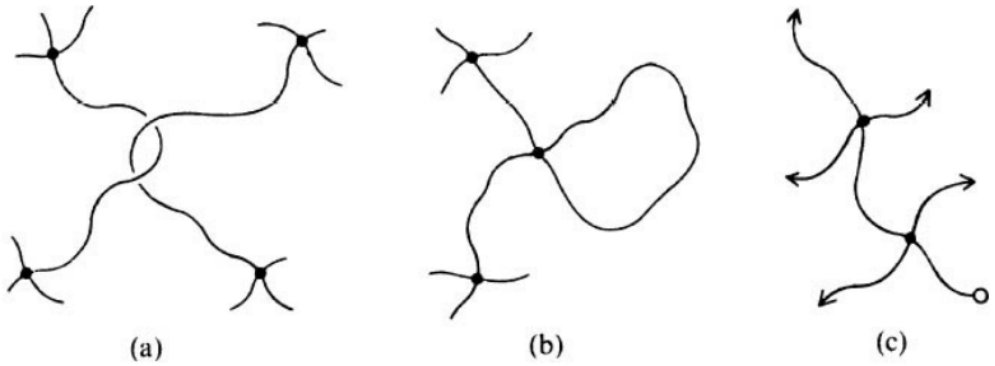

Figure 2.6 Possible hydrogel network defects. Filled circles represent crosslinks while open circles represent points of chain termination. **(a)** Physical entanglements between chains still contribute to network elasticity despite being considered a defect. **(b)** Closed loop, where both ends of the chain are connected to the same crosslink point, do not contribute to the elasticity of the network. **(c)** Dangling/loose chains that are only connected to the network at one end also do not contribute to network elasticity. Reproduced with permission from L. Treloar, *The Physics of Rubber Elasticity*, 1975.[145] Copyright © 1975 Oxford University Press.

$$G' = Ak_BT\rho_{\mathrm{el}}\left(1 - \frac{2\bar{M}_{\mathrm{c}}}{M_{\mathrm{r}}}\right) = Ak_BT\frac{\rho N_{\mathrm{A}}}{\bar{M}_{\mathrm{c}}}\left(1 - \frac{2\bar{M}_{\mathrm{c}}}{M_{\mathrm{r}}}\right) \qquad \text{Eqn. 2.21}$$

Mesh size can be estimated by measuring the storage modulus and using the relationship $\rho_{\mathrm{el}} \approx \xi^{-3}$ to solve for ξ.[137,146] With this relationship, mesh size scales inversely with storage modulus as $\xi \sim G'^{-1/3}$. Alternatively, **Eqn. 2.19** - **Eqn. 2.21** can be rearranged to solve for $\bar{M}_{\mathrm{c}}$ and then plugged into **Eqn. 2.13** to solve for mesh size.[147] With this method, mesh size scales with storage modulus as $\xi \sim G'^{-1/2}$.

Mesh size can also be measured through various measurement techniques, such as particle diffusion,[147,148] differential dynamic microscopy (DDM),[149] small angle x-ray scattering (SAXS),[109,150,151] small angle neutron scattering (SANS),[152,153] dynamic light scattering (DLS),[144,154–156] and scanning electron microscopy (SEM).[35,148,154] Mesh sizes for various hydrogels are listed in **Table 2.2** to demonstrate the order of magnitude difference for synthetic hydrogels in comparison to natural hydrogels— synthetic hydrogels typically have much smaller mesh sizes than natural hydrogels. It is important to note that these values are highly variable and dependent on acquisition method as well as polymer concentration, crosslinking density, and swelling conditions as will be discussed in the following section.

Table 2.2 Mesh size compilation for common hydrogels. Ranges are given to account for varying polymer and crosslinking concentrations.

	Hydrogel	Mesh Size Range (nm)	Acquisition Method	Ref.
Synthetic hydrogels	Poly(acrylamide) (PAAm)	1-10	SAXS	[150]
	Poly(ethylene glycol) (PEG)	2-8 6-16	DLS SAXS	[144] [151]
	Poly(2-hydroxyethyl methacrylate) (pHEMA)	3-9	Storage modulus	[147]
	Poly(N-isopropylacrylamide) (pNIPAAm)	10-46	Storage modulus Swelling	[157]
Natural hydrogels	Hyaluronic acid (HA)	7-60 200	Swelling Shear modulus	[118] [149]
	Collagen (COL)	2000-3000	Shear modulus	[149]

2.6 Tuning Mesh Size & Hydrogel Properties

The hydrogel network is a function of the molecular weight of polymer chains, crosslinking density, and external factors such as polymerization conditions, solvent, pH, and temperature.[95] By varying the total polymer and crosslinker concentrations, network structure and mechanical properties can be tuned. For polyacrylamide hydrogels, Denisin and Pruitt concluded that total polymer concentration had the greatest impact on the mechanical properties.[35] Using the convention of **Eqn. 2.1** and **Eqn. 2.2**, when the crosslinker concentration (%C) was fixed and total polymer concentration (%T) was varied, mesh size decreased with increasing %T, leading to an increase in elastic modulus.[35,107] However, for a given polymer concentration (%T) when the

crosslinker concentration (%C) was varied, mesh size decreased with increasing %C up to a certain point, where it then plateaued, and then increased again.[35,107] This phenomenon was explained by crosslink clustering when bisacrylamide (MBAm) was used as the crosslinker. Due to its higher reactivity ratio, MBAm ($r_{MBAm} > 1$) is more likely to react with itself than with acrylamide ($r_{AAm} < 1$), leading to the formation of MBAm-rich clusters within the hydrogel network.[58,59,61] This structural inhomogeneity has been confirmed by scanning electron microscopy.[35,109] Network structure can also be modified by varying both the monomer to crosslinker ratio and total polymer concentration. With this method, gels with similar elastic moduli but different mesh sizes can be formed.[148] External factors such as temperature, solvent conditions, and pH can also impact mesh size by influencing swelling. This will be discussed further in Chapters 5 – 8.

The rubber elasticity model (**Eqn. 2.19** - **Eqn. 2.21**) can also be used to estimate the theoretical elastic modulus. However, employing a slightly modified version of the rubber elasticity equation (**Eqn. 2.22**), Kizilay and Okay demonstrated that this model overpredicted the modulus for polyacrylamide hydrogels due to crosslinker inefficiency and clustering:[158]

$$G' = Ak_BT\frac{2\rho N_{\mathrm{A}}X}{M_{\mathrm{r}}}v_{2,\mathrm{r}} \qquad \textbf{Eqn. 2.22}$$

where $v_{2,\mathrm{r}}$ is the polymer volume fraction after polymerization, ρ is the polymer density, X is the crosslinker molar ratio (molar ratio of bisacrylamide to acrylamide), and M_{r} is the molecular weight of the repeat unit.[158]

2.7 Mesh Size Scaling Relationships

Using de Genne's scaling arguments, the relationship between mesh size and various macroscopic properties such as elastic modulus, shear stress, and friction coefficient have been determined for hydrogels composed of flexible, semi-dilute polymer chains (**Table 2.3**).[137,150,159]

Table 2.3 Compilation of scaling principles relating hydrogel mesh size to a variety of different macroscopic properties, assuming flexible, semi-dilute polymer chains.

Property	Relationship	Ref.
Intrinsic permeability	$k \sim \xi^2$	107,159
Draining time	$t_{\mathrm{d}} \sim \xi^2$	159
Polymer relaxation time	$t_{\mathrm{r}} \sim \xi^3$	150
Elastic modulus	$E \sim \xi^{-3}$	137
Friction coefficient	$\mu \sim \xi^{-1}$	150
Shear stress	$\tau \sim \xi^{-3}$	159
Osmotic pressure	$\Pi \sim E \sim \xi^{-3}$	160

Based on these scaling relationships, with increasing mesh size, hydrogel permeability increases, draining time increases, polymer relaxation time increases, elastic modulus decreases, friction coefficient decreases, and shear stress decreases. Unsurprisingly, water content also increases with increasing mesh size.[159,161]

2.8 Time-Dependent Hydrogel Properties

Because hydrogels are a combination of polymer and solvent, they can exhibit viscoelasticity and poroelasticity, both of which are time-dependent behaviors that can be difficult to decouple.[162,163] Viscoelasticity describes the time-dependent relaxation that polymers experience under deformation while poroelasticity describes the time-dependent flow of solvent under deformation. Poroelasticity was first introduced by Biot in 1941 and is used to describe the interaction between fluid and a porous medium under deformation.[164] The timescale of poroelasticity is related to the diffusion of the solvent in the network and is dependent on the lengthscale of observation.[163,165] Viscoelasticity, on the other hand, is a material property, and its value is not dependent on the lengthscale over which it is being observed.[163] For hydrogels, its viscoelastic properties comes from the polymer network. Polyacrylamide is often considered a linear elastic material (*i.e.*, viscoelasticity can be disregarded) within a certain range of strains due to its constant storage modulus.[35]

Because viscoelastic relaxation does not depend on the deformation lengthscale, the poroelastic and viscoelastic behavior of polyacrylamide hydrogels can be decoupled.[166] However, poroelasticity or viscoelasticity (or both) are often ignored when characterizing the mechanical properties of hydrogels.[167] Schulze *et al.* argued that hydrogel poroelasticity can be neglected if the applied pressure is less than the osmotic pressure of the hydrogel network,

which scales with elastic modulus (Table 2.3).[160] For non-ionic hydrogels, osmotic pressure can be viewed as the pressure of the solvent within the hydrogel,[121] whereas for ionic hydrogels, osmotic pressure is due to a concentration gradient of counterions inside and outside the hydrogel network. In this dissertation, we consider poroelasticity and viscoelasticity as negligible effects since the contact pressures that we are applying are typically less than the elastic moduli of the hydrogels and our timescales of deformation are shorter than viscoelastic timescales.

3 CHAPTER 3: HYDROGEL TRIBOLOGY

Tribology is the study of the lubrication, adhesion, friction, and wear of materials in relative motion.[168] For hydrogels, most of the tribological literature is focused on kinetic friction (the force that opposes motion) and investigating the friction dissipation mechanisms within these systems rather than static friction (the force required to instigate motion between objects at rest). This chapter will briefly discuss the friction mechanisms for hard materials, demonstrate how hydrogel friction deviates from these models, and touch upon several proposed lubrication mechanisms for hydrogel. We will end the chapter with design principles for low friction hydrogel interfaces.

Table of Contents

3.1 Friction in Engineering Systems

The first recorded friction experiments were conducted by Leonardo da Vinci against wooden surfaces and form the basis for what is now known as Amontons' three laws of friction, with the third law being credited to Coulomb:[168–170]

1) Friction force is linearly proportional to the applied normal force
2) Friction force is independent of apparent contact area
3) Kinetic friction force is independent of sliding velocity

The first law can be summarized by the familiar equation:

$$\mu = \frac{F_{\mathrm{f}}}{F_{\mathrm{n}}} \qquad \text{Eqn. 3.1}$$

where F_{f} is the resultant friction force, F_{n} is the applied normal force, and μ is the proportionality constant better known as the friction coefficient. In dry conditions, many hard materials follow Amonton's laws despite their empirical basis.

For solid materials with fluid lubricants, the Stribeck curve was developed to encompass the various factors that affect friction. It utilizes a dimensionless parameter known as the Sommerfeld number (S), which is proportional to the viscosity (η), sliding speed (v), and applied normal force (F_{n}) as $S\,\alpha\,\frac{\eta v}{F_{\mathrm{n}}}$ (**Figure 3.1**).[98,171]

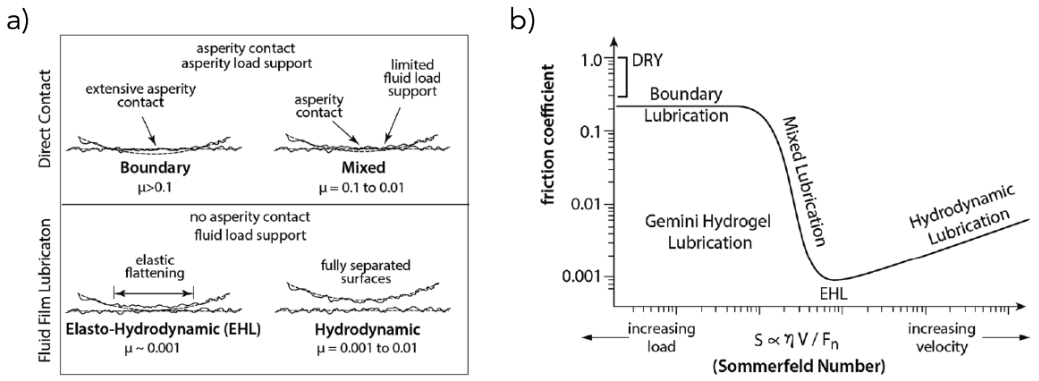

Figure 3.1 (a) Schematics demonstrating the contact modes for the four regimes of the Stribeck curve – boundary, mixed, elastohydrodynamic (EHL), and hydrodynamic (full fluid film) lubrication – and the typical friction coefficient range. **(b)** Representative Stribeck curve for two lubricated surfaces. Aqueous gel lubrication in self-mated contact does not follow this curve but rather stays between μ = 0.001 – 0.01 across a wide range of sliding speeds. Adapted with permission from A. Pitenis *et al.*, *Soft Matter,* **10**, 2014.[98] Copyright © 2014 Royal Society of Chemistry.

The Stribeck curve plots the friction coefficient between two sliding interfaces as a function of the Sommerfeld number and partitions it into four lubrication regimes – boundary, mixed, elastohydrodynamic lubrication (EHL), and hydrodynamic lubrication – which are highly dependent on applied force and sliding speed. During boundary or mixed lubrication, the two sliding interfaces are in direct contact. These lubrication modes typically occur at low sliding speeds or high applied loads and exhibit either speed independent (boundary lubrication) or speed-dependent (mixed lubrication) behavior. At high sliding speeds or low loads, a fluid film forms and separates the interfaces from direct contact, leading to EHL and hydrodynamic lubrication. Within these fluid film lubrication regimes, friction coefficients are minimized and a weak speed-dependence emerges due to increasing fluid film thickness with increasing

Sommerfeld number (*i.e.*, increasing sliding velocity and decreasing force).[172] Within fluid film lubrication, energy dissipation is due to heat loss as the fluid film is sheared.

For low elastic modulus materials, Hamrock and Dowson developed an equation to predict the minimum fluid film thickness, h_{min}, needed to obtain soft-EHL:[173]

$$h_{\min} = 2.8R^{0.77}(\eta_o v)^{0.65}E'^{-0.44}F_n^{-0.21} \qquad \text{Eqn. 3.2}$$

where R is the probe radius of curvature, $\eta_o$is the viscosity of the fluid, v is the sliding velocity, F_n is the applied normal load, and $E' = 2E^*$ where E^* is the reduced elastic modulus of the sample. For fluid film lubrication to occur, h_{min} needs to be larger than the surface roughness of the substrate.[172,174,175]

3.2 Hydrogel Lubricity

Amonton's laws and the Stribeck curve were developed with hard, engineering materials, such as metals and ceramics, in mind. Unsurprisingly, hydrogels exhibit more complex tribological behavior and often deviate from these lubrication mechanisms. **Table 3.1** details several experimental factors that affect hydrogel friction, including but not limited to applied normal load, sliding speed, temperature, and contact area between the probe and substrate.

Table 3.1 Compilation of previous hydrogel studies examining testing parameters and their effect on the measured friction coefficient. The responses vary depending on the chemical composition of the hydrogel, making it difficult to predict their tribological behavior.

Parameter	Hydrogel	Effect on Friction Coefficient (μ)
Applied normal load, F_n	Polyacrylamide (PAAm)[176] Poly(vinyl alcohol)[30,177] Poly(*N*-isopropylacrylamide) (pNIPAAm)[178]	$\mu \downarrow$ as $F_n \uparrow$
	Poly(2-acrylamido-2-methylpropanesulfonic acid) sodium salt (pNaAMPS)[177]	$\mu \leftrightarrow$ as $F_n \uparrow$
	Nano-hydroxyapatite reinforced poly(vinyl alcohol) (Nano-HA/PVA)[29]	$\mu \uparrow$ as $F_n \uparrow$
Sliding speed, v	Poly(vinyl alcohol) (PVA)[29] Polyacrylamide (PAAm)[179]	$\mu \downarrow$ as $v \uparrow$
	Poly(acrylamide) (PAAm)[98]	Below a critical transition speed: $\mu \leftrightarrow$ as $v \uparrow$
	Poly(*N*-isopropylacrylamide) (pNIPAAm)[179] Poly(acrylamide) (PAAm)[98]	Above a critical transition speed: $\mu \uparrow$ as $v \uparrow$
Temperature, T	Poly(acrylamide) (PAAm)[136]	$\mu \downarrow$ as $T \uparrow$
Contact area, A	Poly(vinyl alcohol) (PVA) [170]	$\mu \downarrow$ as $A \uparrow$

In addition to these testing parameters, the sliding configuration needs to be considered. Dunn *et al.* investigated the differences between migrating, stationary, and Gemini contact.[180] Migrating contact occurs when an impermeable probe (such as glass) slides against a hydrogel substrate, allowing contact between the probe and substrate to migrate across the hydrogel surface during sliding (**Figure 3.2a**). During stationary contact (**Figure 3.2b**), a hydrogel probe slides against an impermeable substrate. The hydrogel is under persistent

load for the duration of the sliding experiment and contact moves with the hydrogel as it slides. Gemini or "self-mated" contact (Figure 3.2c) transpires when a hydrogel probe slides against a hydrogel substrate.

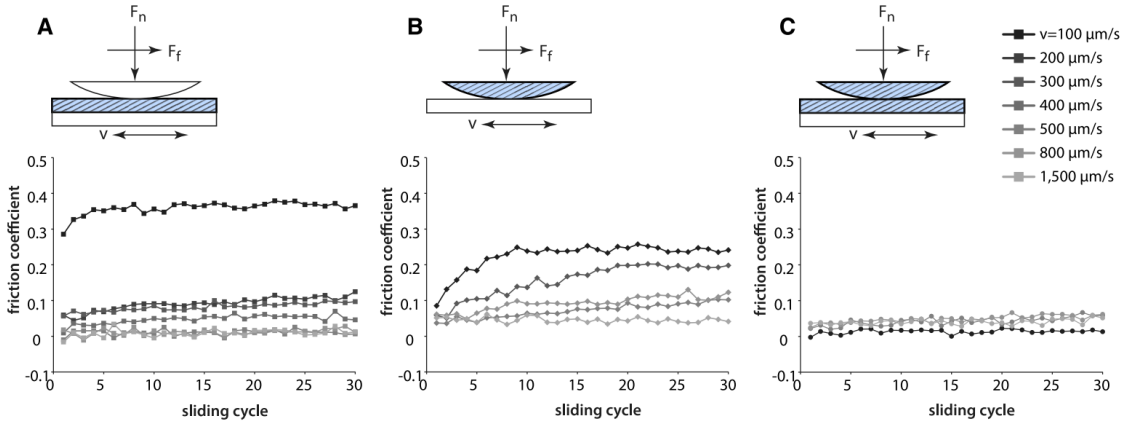

Figure 3.2 Friction coefficient as a function of sliding cycle with different sliding configurations: (a) glass probe on hydrogel substrate (migrating contact), (b) hydrogel probe on glass substrate (stationary contact), and (c) hydrogel probe on hydrogel substrate (Gemini contact). Friction is speed-dependent for both migrating and stationary contact but speed independent for Gemini contact. Reproduced with permission from A. Dunn *et al.*, *Tribology Letters*, 54, 2014.[180] Copyright © 2014 Springer Nature.

Dunn *et al.* found that migrating and stationary contact were speed-dependent, but Gemini contact was speed independent. This difference was attributed to the impermeability of the countersurface, limiting fluid flow and pressure to one side of the interface.

Similarly, Simič *et al.* examined the effects of hydrogel surface structure and the impact of contact configuration on friction (Figure 3.3) Hydrogels with a "brushy" loosely crosslinked surface structure have different friction behavior than those with a homogeneously crosslinked network despite being composed of the same material (as will be discussed further in Chapter 5), and the contact

mode (*e.g.*, stationary vs. migrating) impacted the speed-dependence of the system.

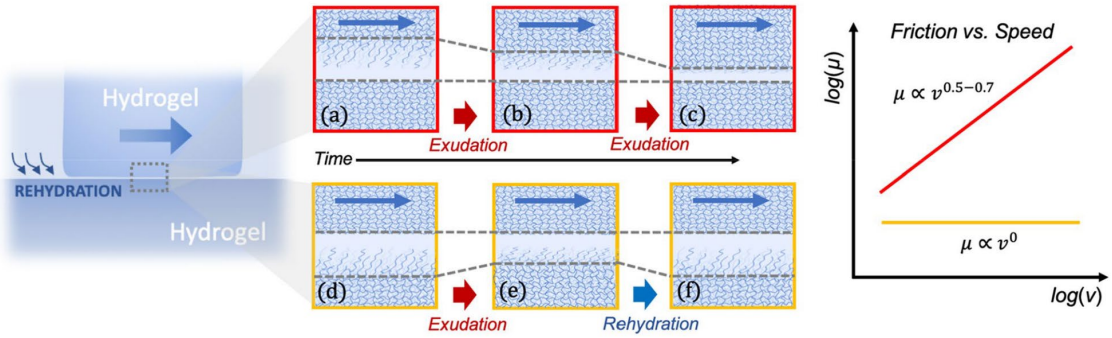

Figure 3.3 Schematic demonstrating different tribological behavior depending on probe configuration. **(a – c)** For brushy hydrogel probes in stationary contact with a crosslinked hydrogel surface, water exudation dominates, leading to increasing friction with sliding speed due to dehydration. **(d – f)** For crosslinked hydrogel probes in migrating contact with a brushy surface, water exudation was balanced by rehydration, maintaining a thin fluid film layer between interfaces. Reproduced with permission from R. Simič *et al.*, *Tribology Letters*, **68,** 2020 under the Creative Commons license (http://creativecommons.org/licenses/by/4.0/).[181]

When a brushy hydrogel probe was in stationary contact with a crosslinked hydrogel substrate (**Figure 3.3a-c**), dehydration at the contact point occurred, leading to speed-dependent friction behavior. However, when the brushy hydrogel was in migrating contact with a crosslinked hydrogel probe, a thin fluid film layer was maintained, and the friction coefficient was speed independent.

These results demonstrate that friction coefficient is a systems property and is highly influenced by testing parameters and hydrogel structure.[176] Therefore, hydrogel material properties need to be considered, such as the chemical makeup of the polymer chains (*e.g.*, their hydrophilicity), crosslinking density, water content, elasticity, and surface structure. All these factors impact the

interactions between the hydrogel and sliding countersurface but are often difficult to decouple due to their interdependence. Despite these complexities, researchers have attempted to provide a unifying theory and develop scaling laws that can predict the tribological behavior of hydrogels based on microstructure and mechanics. To date, no such theory exists. Nonetheless, several hydrogel lubricity mechanisms have been proposed and will be explored in the following section.

3.3 Proposed Mechanisms of Hydrogel Lubricity

There have been many proposed mechanisms for friction dissipation within hydrogel systems. This section will summarize several of them conceptually and is not meant to be an exhaustive list. For a more in-depth analysis and overview of the mathematical derivations for the lubrication models, see the review articles by Shoiab *et al.*[182] and Bonyadi *et al.*[183] The lubrication mechanisms discussed in this section were mainly developed for non-ionic hydrogels and not necessarily applicable for charged hydrogels, which have the added complexity of electrostatic interactions. Discussions of charged hydrogel lubricity can be found in Chapters 7 and 8. Additionally, most of these models focus on kinetic friction – there are very few that emphasize static friction, although it is an important factor in biological wear. Sections 3.3.1 – 3.3.3 focus on models developed for gel-on-substrate or probe-on-gel tribological pairings (*i.e.*,

stationary or migrating contact, respectively), where the substrate or probe are impermeable hard materials such as glass. Section 3.3.4 and Section 3.3.5 emphasize models developed for self-mated ("Gemini") gel-on-gel sliding configurations. As discussed in the following sections and summarized in Table 3.2, many of the lubrication models have a critical velocity, where the mechanism for friction dissipation transitions with increasing sliding speed.

Table 3.2 Comparison of various hydrogel lubrication models and the proposed frictional dissipation mechanisms at different sliding velocities. Blue highlighted boxes represent microtribological measurements while green highlighted boxes represent nanotribological measurements. Hydrogel abbreviations: PAAm- polyacrylamide, PDMA- poly(dimethylacrylamide), PNaAMPS - poly(2-acrylamido-2-methylpropanesulfonic acid) sodium salt, pNIPAAm- poly(*N*-isopropylacrylamide).

Lubrication Model	Hydrogel System	Counter surface	Low velocity	Transition velocity	High velocity
Poroelastic Lubrication	Bulk PAAm[184]	Glass	**Poroelastic lubrication:** pressure driven fluid flow		
	PDMA films[185]	Glass	**Poroelastic lubrication:** constant contact area	$Pe \sim \frac{poroelastic\ relaxation\ time}{dwell\ time} = 1$	**Poroelastic lubrication:** changing contact area
Hydrodynamic Lubrication	Bulk PAAm, PAA, and agarose[138]	PMMA Glass	**Hydrodynamic flow:** fluid shearing through hydrogel network	Interfacial shear thinning of polymer chains	**Hydrodynamic lubrication:** viscous dissipation within fluid film layer
Repulsion-Adsorption Model	Bulk PNaAMPS and PVA[170, 174, 187]	Glass PNaAMPS	<u>Adsorption regime</u> **Elastic deformation:** stretching of polymer chains adsorbed onto surface	$v_f \sim \frac{mesh\ size}{adsorption\ time}$	<u>Repulsive regime</u> **Hydrodynamic lubrication:** viscous dissipation within a fluid film layer
Baumberger's Adhesive Model	Bulk gelatin[189]	Glass	**Elastic deformation:** stick-slip model of adhesive polymer chains	Dependent on hydrogel composition, concentration, and viscosity	**Non-hydrodynamic dissipation mechanism:** shear thinning of hydrogel film with the thickness on the order of a mesh size
Viscous-Adhesive Model	Thin PAAm[154, 179]	Glass	<u>Adhesive regime</u> **Elastic deformation:** stick-slip model of adhesive polymer chains	Dependent on the viscoelasticity of the hydrogel, viscosity, and polymer relaxation	<u>Viscous regime</u> **Non-hydrodynamic dissipation mechanism:** shear thinning of the hydrogel surface
Hydration Lubrication	Charged hydrogels[191,192]	Charged surface	**Hydration lubrication:** fluid film due to repulsive interactions between sliding interfaces (not due to hydrodynamic lubrication)		
Polymer Fluctuation and Relaxation Lubrication	Bulk pNIPAAm and PAAm[98]	pNIPAAm PAAm	<u>Thermal fluctuation lubrication</u> **Thermal fluctuations:** polymer chain fluctuations	$v_f \sim (mesh\ size)^{-2}$	<u>Polymer relaxation lubrication</u> **Non-Newtonian shear:** relaxation of strained polymer chains

3.3.1 Poroelastic Lubrication

Several models have been developed for poroelastic lubrication, which occurs when there is pressure-driven fluid flow.[184–186] The Péclet number (*Pe*) is a dimensionless parameter comparing advective components (sliding) to diffusive components (fluid flow). In other words, it is the ratio of the poroelastic relaxation time to dwell time. A hallmark of poroelastic lubrication is decreasing friction with increasing sliding speed (**Figure 3.4 and Figure 3.5**).

Delavoipière *et al.* investigated poroelastic lubrication for micron-thin poly(dimethylacrylamide) (PDMA) films and attributed friction dissipation to fracture mechanics and poroelastic fluid flow (**Figure 3.4**).[185] Below a critical velocity, the friction force increased with sliding speed with a constant contact area. Above the critical velocity, the contact area decreased and became asymmetrical. This asymmetry was due to a poroelastic driven fluid flow pressure imbalance between the leading and trailing edge of contact that created a net lift force, decreasing the contact area and friction force. The leading and trailing edges were viewed as cracks opening and closing with friction dissipating due to poroelastic fluid flow.

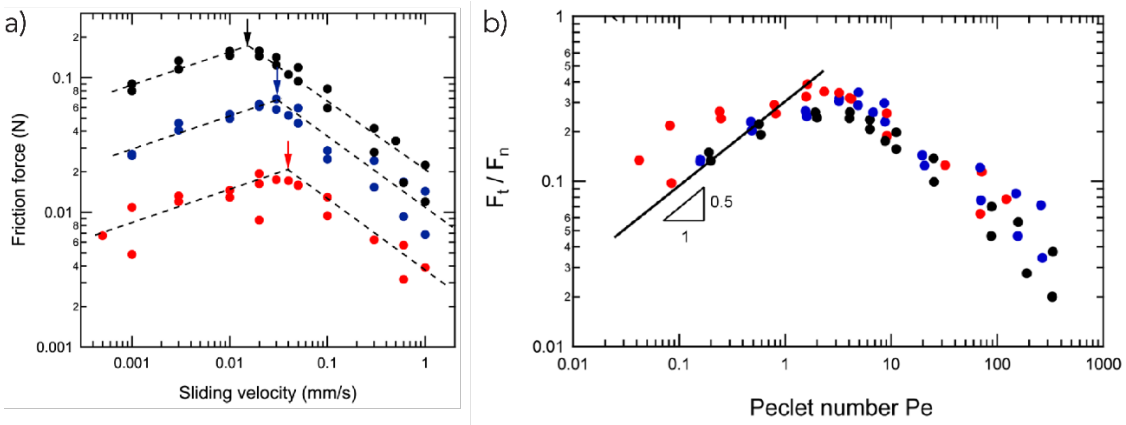

Figure 3.4 (a) Friction force as a function of sliding velocity at three applied loads: F_n = 50 mN (red), F_n = 200 mN (blue), and F_n = 600 mN (black). The critical velocity shifts to lower sliding speeds with increasing applied load. **(b)** Friction coefficient as a function of Péclet number at three applied loads. Reprinted with permission from J. Delavoipière *et al.*, *Langmuir*, **34**, 2018.[185] Copyright © 2018 American Chemical Society.

Unlike Delavoipière *et al.* (**Figure 3.4b**), Reale and Dunn saw a monotonic decrease in friction coefficient with increasing *Pe* (*i.e.*, velocity) for polyacrylamide bulk hydrogels (**Figure 3.5**).[184] At low *Pe* values, there was more time for poroelastic fluid flow, which increased adhesion between the hydrogel and countersurface due to dehydration of the contact area, leading to greater friction.

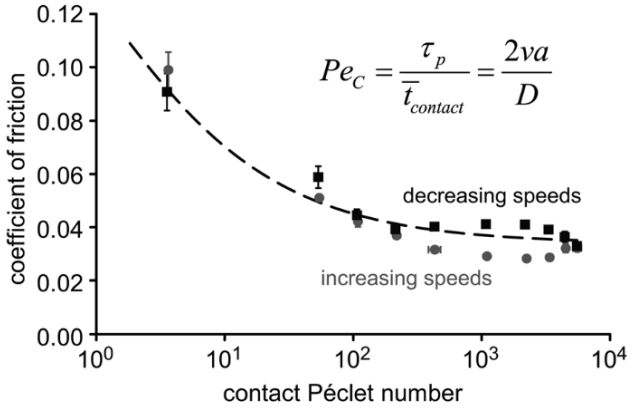

Figure 3.5 Friction coefficient as a function of Péclet number. Reproduced with permission from E. Reale and A. Dunn, *Soft Matter*, **13**, 2017.[184] Copyright © 2017 Royal Society of Chemistry.

This lubrication mechanism is only valid in the instances where applied pressure exceeds the osmotic pressure of the hydrogel, which scales with elastic modulus (Table 2.3).[160] If the applied pressure is not greater than the osmotic pressure, fluid flow is not possible.

3.3.2 Hydrodynamic Lubrication

Cuccia *et al.* proposed that hydrodynamic lubrication was the main friction dissipation mechanism for hydrogels.[138] At low and high sliding speeds, they observed increasing friction coefficients with increasing velocity (Figure 3.6). They postulated that this increase was due to hydrodynamic flow as fluid sheared through the polymer network at low velocities and hydrodynamic lubrication as a result of fluid film formation at high velocities. At intermediate velocities, there was a time-dependent transition where friction decreased due to interfacial shear thinning of polymer chains aligning in the shear direction.

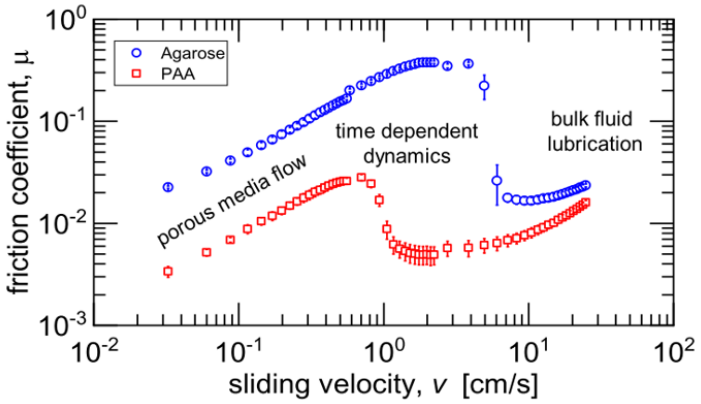

Figure 3.6 Friction coefficient as a function of sliding velocity for agarose (blue circles) and poly(acrylic acid) (PAA) (red squares) hydrogels. Three lubrication regimes can be identified. At low velocities, hydrodynamic flow through the hydrogel network is the dominating friction dissipation mechanism. At high velocities, viscous dissipation due to the formation of a fluid film layer (*i.e.*, hydrodynamic lubrication) is the dominant mechanism. The transition velocities are dependent on the interfacial shear thinning of the hydrogel network. Reproduced with permission from N. Cuccia *et al., Proc. Natl. Acad. Sci.,* **117**, 2020.[138] Copyright © 2020 National Academy of Sciences.

3.3.3 Adhesive Models

The repulsion-adsorption model, developed by Gong in 1998, divides hydrogel lubrication into two regimes – adsorption and repulsion.[170,174,187] Below the critical velocity, polymer chains adsorb onto the countersurface due to attractive interactions. As shear stress is applied, these connection points break and reform as the two interfaces slide past one another. The elastic deformation of these adsorbed polymer chains and the viscous friction between the solvent and substrate are the contributing factors to friction forces within this regime (**Figure 3.7**).

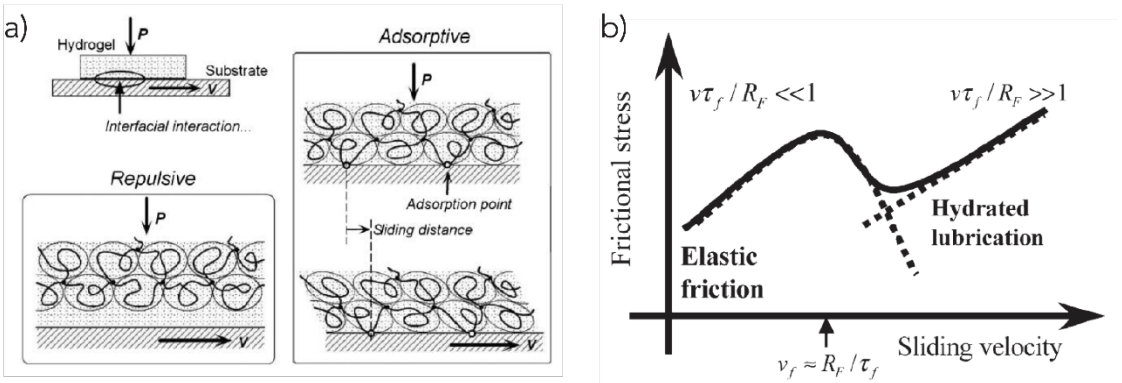

Figure 3.7 (a) Schematic of the adsorption-repulsive model for hydrogels interacting with a solid substrate. **(b)** Frictional stress as a function of sliding velocity, with the transition velocity, $\boldsymbol{v_f}$, labeled demonstrating the speed at which the friction mechanism transitions from elastic deformation of polymer chains to viscous dissipation within the fluid film. In this figure, R_F represents the hydrogel mesh size (ξ). Adapted with permission from J.P. Gong, *Soft Matter*, **2**, 2006.[170] Copyright © 2006 Royal Society of Chemistry.

The critical sliding velocity (v_f) is dependent on the hydrogel mesh size (ξ) and the relaxation time of polymer attachment and detachment from the countersurface (τ_f) as $v_f \approx \frac{\xi}{\tau_f}$. Once sliding speed exceeds v_f, the polymer chains cannot relax fast enough to adsorb onto the substrate and a fluid layer forms at the hydrogel surface. Friction dissipation is now dominated by hydrodynamic lubrication, with friction increasing with sliding speed as the fluid layer thickness increases.[188]

Like the repulsion-adsorption model, Baumberger suggested an adhesive model based on Schallamach's rubber theory[189] that attributed friction to stick-slip and adhesive interactions between the polymer network and countersurface at low velocities.[89,190] In this model, stick-slip occurs as shear is applied and the polymer chains abruptly attach and detach from the substrate. However, at high

velocities Baumberger proposed that the dominating friction dissipation mechanism was the shear thinning of a hydrogel film with the thickness on the order of a mesh size rather than hydrodynamic lubrication as the repulsion-adsorption model postulated.

The viscous-adhesive model[154,179] proposed by Espinosa-Marzal *et al*. is similar to the adhesive model developed by Baumberger. In the low velocity regime, energy dissipation was attributed due to stick-slip and the formation and breakage of temporary adhesive bonds. At high velocities, the dominating mechanism was credited to viscous dissipation within the hydrogel network due to shear thinning of the hydrogel surface. However, the viscous-adhesive model expanded upon the previous models by considering polymer network confinement, poroelastic relaxation, the effects of load on polymer relaxation, and non-Newtonian shear when determining the critical transition velocity.[179] As demonstrated in Figure 3.8, the critical transition velocity is very composition-dependent.

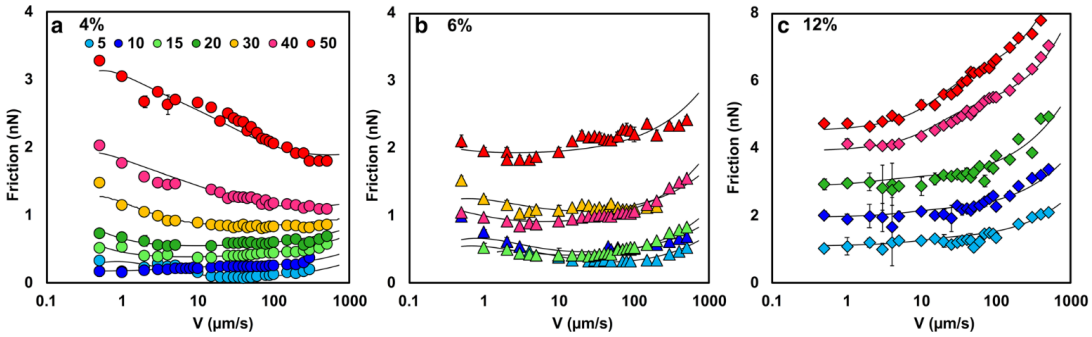

Figure 3.8 Friction force as a function of sliding velocity for **(a)** 4 wt.%, **(b)** 6 wt.%, and **(c)** 12 wt.% polyacrylamide hydrogels. Depending on the composition and mechanics of the hydrogel, the frictional behavior with respect to sliding velocity changed. Adapted with permission from T. Shoiab and R.M. Espinosa-Marzal, *Tribol. Lett.*, **66**, 2018.[179] Copyright © 2018 Springer Nature.

3.3.4 Hydration Lubrication

The hydration lubrication model was developed to describe the lubrication of two brushy and/or charged hydrogel surfaces, although this mechanism can be applicable for charged hard surfaces as well.[191,192] In this model, lubrication is due to the formation of a fluid film layer produced by elastic and osmotic pressure (for hydrogel brushes) or repulsive electrostatic interactions and hydration repulsion between hydration shells (for charged hydrogels) that separate the two surfaces from contact. Viscous dissipation occurs within this fluid film layer, leading to extremely low, superlubricious ($\mu \leq 0.005$) friction coefficients.[191] This lubrication mechanism will be further discussed in **Chapter 7** and is thought to be one of the mechanisms behind the low friction exhibited by articular cartilage.[191,193]

3.3.5 Mesh Size Control Models

For hydrogels in self-mated ("Gemini") contact, Pitenis *et al.* proposed that the dissipation mechanism was dependent on polymer chain fluctuations.[98] At low sliding speeds below a critical sliding velocity, the friction coefficient was found to be speed independent due to random thermal chain fluctuations that created a blurred interface and relaxed shear stress generated during sliding (Figure 3.9).

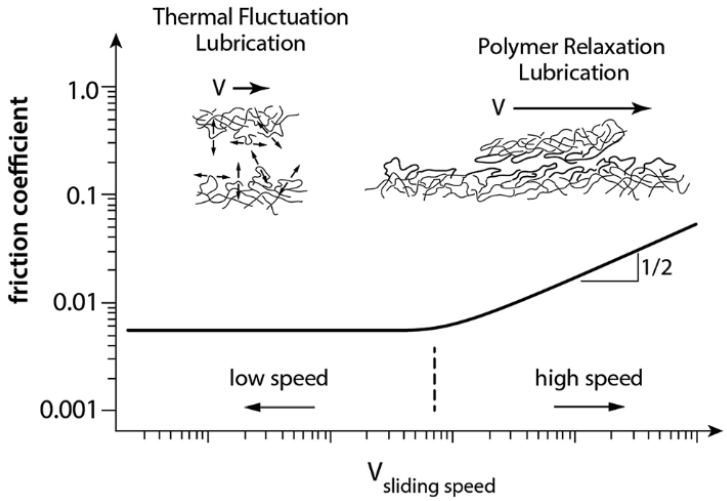

Figure 3.9 Proposed lubrication mechanism for self-mated ("Gemini") hydrogel sliding interfaces. At low sliding speeds, the friction coefficient is speed independent due to thermal fluctuations of the polymer chains that create a blurred interface. Past a critical velocity, friction coefficient increases with sliding speed due to the inability of the polymer chains to relax and dissipate shear stress. Reproduced with permission from A. Pitenis *et al., Soft Matter,* **10,** 2014.[98] Copyright © 2014 Royal Society of Chemistry.

Above the critical sliding velocity, there is a speed-dependent regime (*i.e.*, polymer relaxation lubrication) where non-Newtonian shear occurs at the sliding interface. The polymer chains do not have time to relax and fully dissipate shear stress at higher sliding speeds, leading to a build-up of stress. This polymer

fluctuation lubrication model has recently been supported by molecular dynamic simulations that demonstrated that polymer chains reorient and stretch in the direction of shear, leading to entropic stress.[194]

Urueña *et al.* investigated the lubrication of Gemini polyacrylamide hydrogels and found that the critical sliding velocity was achieved when polymer relaxation time corresponded to the time it took to move one mesh and scaled with hydrogel mesh size as $v_f \sim \xi^{-2}$.[150] With this scaling, the critical velocity increased with polymer concentration. The mesh sizes for polyacrylamide hydrogels of varying polymer concentration were experimentally determined with small angle x-ray scattering (SAXS), and it was postulated that the friction coefficient in the speed independent regime scaled with mesh size as $\mu \sim \xi^{-1}$ (Table 2.3). This one structural parameter was hypothesized to control the lubrication behavior for hydrogels in Gemini configuration. Further studies by Pitenis and Sawyer defined the critical transition velocity by the Weissenberg number (*Wi*) – the characteristic time in the experiment (polymer relaxation time) multiplied by the characteristic deformation rate (shear rate over a single mesh).[159] They argued that the critical transition occurred earlier around *Wi* ~ 0.1 rather than *Wi* ~ 1 as Urueña had proposed.[150]

Work by McGhee *et al.* postulated that energy dissipation in Gemini hydrogel systems occurs by solvent shearing through the hydrogel network at a hydrodynamic penetration depth that is on the order of a mesh size.[136] This

dissipation mechanism is similar to the hydrodynamic dissipation mechanism proposed by Cuccia *et al.* at low sliding speeds.[138]

3.4 Designing Hydrogel Friction

While friction is a systems property that is highly dependent on testing parameters (*e.g.*, sliding speed and applied contact force) and probe configuration (*e.g.*, stationary, migrating, Gemini), the interfacial properties of the hydrogel network must also be considered as demonstrated by Simič *et al.* (Figure 3.3). In this dissertation, I aim to tune hydrogel friction through intentional design of the surface and bulk structure for four different systems: polyacrylamide (PAAm), poly(2-hydroxyethyl methacrylate) (pHEMA), poly(acrylamide-*co*-acrylic acid) (P(AAm-*co*-AA)), and poly(*N*-isopropylacrylamide-*co*-spiropyran) (pNIPAAm-*co*-SP). For PAAm, the surface structure was controlled with environmental oxygen during polymerization. The amphiphilicity and solvophilic nature of pHEMA was exploited to tune friction with solvent conditions. The stimuli-responsive behavior of charged P(AAm-*co*-AA) hydrogels was investigated by controlling solution pH and acrylic acid content, and pNIPAAm hydrogels were engineered to respond to light through the incorporation of photoswitchable moieties that changed hydrophilicity when irradiated with light.

There is much to explore in the field of hydrogel lubricity, and this dissertation work focuses on the structure-property relationships of hydrogel friction rather than exploring the effects of sliding speed and applied force. To that end, typically only one sliding speed and normal force were utilized during tribological sliding experiments and were carefully chosen to avoid soft-EHL, as will be discussed further in the following chapter.

4 CHAPTER 4: MATERIALS & METHODS

In this dissertation, four hydrogel systems were investigated: polyacrylamide (PAAm), poly(2-hydroxyethyl methacrylate) (pHEMA), poly(acrylamide-*co*-acrylic acid) (P(AAm-*co*-AA)), and poly(*N*-isopropylacrylamide-*co*-spiropyran) (pNIPAAm-*co*-SP). In this chapter, hydrogel synthesis conditions are briefly discussed as well as the assembly of the custom-built tribometer. The parameters used for mechanical and tribological testing are also explored.

Table of Contents

4.1 Hydrogel Synthesis

Free-radical polymerization was utilized to synthesize four different hydrogel networks (polyacrylamide (PAAm), poly(2-hydroxyethyl methacrylate) (pHEMA), poly(acrylamide-co-acrylic acid) (P(AAm-*co*-AA)), and poly(*N*-isopropylacrylamide) (pNIPAAm)) with varying monomer and crosslinker concentrations. Further synthesis details for each network can be found at the beginning of each of the subsequent chapters.

4.2 Tribometer Assembly

Friction coefficients are typically measured with tribometers, although rheometers can also be used.[124] For our experiments, a linear reciprocating tribometer was utilized and built as described by Urueña *et al.*[195] A titanium double-leaf cantilever was mounted to a piezoelectric stage (P-629.1CD) with a 1.5 mm range that controlled displacements in the z direction. Capacitance probes (Lion Precision Elite Series, C5R-0.8-2.0 with CPL190 driver, 5 μm/V sensitivity, 20 V range) mounted in the normal and tangential directions were used to measure cantilever displacements in the normal and tangential directions. These displacements were converted into forces using the cantilever spring constants. Samples were placed on a motorized stage (Physik Instrumente, L-509.20DG10, 52 mm travel range) that provided linear

reciprocation (**Figure 4.1**). The noise floor, or minimum detectable friction coefficient, for the tribometer was estimated with the following equation:

$$\mu = \frac{F_{\mathrm{f}}}{F_{\mathrm{n}}} = \frac{K_{\mathrm{f}} \cdot x}{F_{\mathrm{n}}} \qquad \text{Eqn. 4.1}$$

where K_f is the tangential spring constant of the double-leaf cantilever, x is the minimum detectable displacement by the capacitance probes, and F_n is the applied normal force. The capacitance probes used herein have a 5 nm resolution (x = 5 nm).

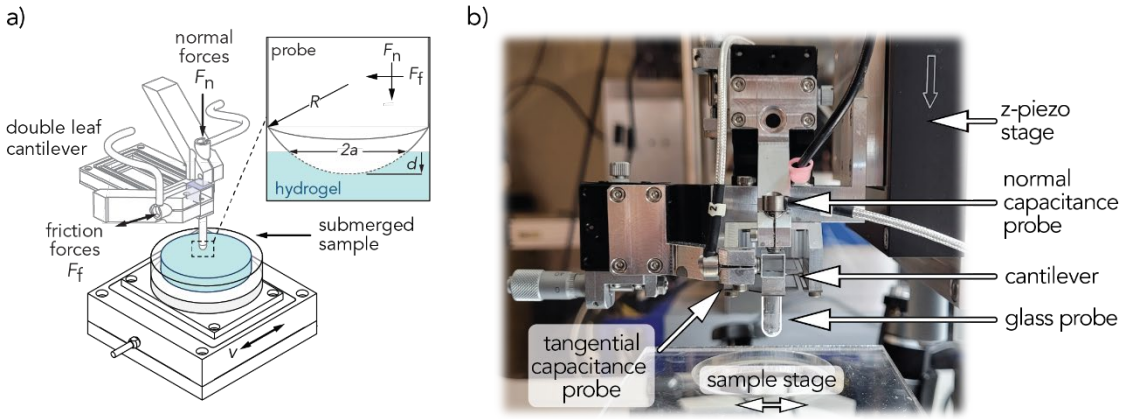

Figure 4.1 (a) Schematic and **(b)** image of the linear reciprocating tribometer. A probe is attached to the double-leaf cantilever that deflects in the normal and tangential directions. Capacitance probes are used to measure these displacements, which are converted to forces using the cantilever spring constants.

4.3 Tribological Characterization

Tribological experiments were performed with the linear reciprocating tribometer. Hydrogels were either secured in a polystyrene petri dish or custom polyetheretherketone (PEEK) dish and submerged in solution for the entirety of

the experiment. Hemispherical borosilicate glass or polytetrafluoroethylene (PTFE) probes were used as sliding countersurfaces (see Table 4.1 for specific probe radii).

Table 4.1 Testing parameters used for each hydrogel system.

	Probe	Spring constants	Friction Parameters	Indentation Parameters
Chapter 5 PAAm	Glass R = 3.1 mm	K_n = 221 μN/μm K_f = 100 μN/μm	F_n = 1 mN v = 500 μm/s x = 3 mm μ_{min} = 0.0005 $P \approx$ 9 – 11 kPa	F_n = 1.5 mN v = 10 μm/s
Chapter 6 pHEMA	pHEMA R = 2 mm		F_n = 1 mN v = 100 μm/s x = 2, 5 mm	F_n = 1.5 mN v = 1 μm/s
Chapter 7 P(AAm-co-AA)	Glass R = 2 mm R = 3.1 mm	K_n = 150 μN/μm K_f = 100 μN/μm	F_n = 4 mN v = 100 μm/s x = 4 mm μ_{min} = 0.000125	F_n = 1.5 mN v = 10 μm/s $P \approx$ 10 kPa
Chapter 8 PAAm	Glass R = 2.6 mm PTFE R = 3.2 mm	K_n = 220 μN/μm K_f = 100 μN/μm	F_n = 4 mN v = 100 μm/s x = 4 mm μ_{min} = 0.0002 $P \approx$ 13 – 15 kPa	F_n = 1.5 mN v = 10 μm/s $P \approx$ 10 kPa
Chapter 9 p(NIPAAm-co-SP-MA)	Glass R = 2.6 mm	K_n = 220 μN/μm K_f = 92 μN/μm	F_n = 2 mN v = 500 μm/s x = 4 mm	F_n = 1.5 mN v = 10 μm/s

Samples were mounted to the motorized stage, which traveled at a sliding velocity ranging from v = 100 μm/s to 500 μm/s across a sliding path ranging between 2 to 5 mm (1/2) cycle. An applied normal load ranging from F_n = 1 to 4 mN was maintained for at least 30 cycles. Eqn. 4.2 was used to calculate the friction coefficient for each individual cycle, μ_{cycle}.

$$\mu_{\text{cycle}} = \frac{\langle F_{\text{f,forward}} \rangle - \langle F_{\text{f,reverse}} \rangle}{2\langle F_{\text{n}} \rangle} \qquad \text{Eqn. 4.2}$$

The friction forces in the forward ($F_{f,forward}$) and the reverse ($F_{f,reverse}$) directions were averaged across the free sliding regime in the middle 25% of the sliding path along with the normal force (F_n). The average friction coefficient for a hydrogel sample, μ_{sample}, was determined by averaging μ_{cycle} over the last 25 – 30 cycles in the steady state friction regime. The reported friction coefficients are the averages and standard deviations of μ_{sample} from three separate hydrogels.

Figure 4.2 illustrates a representative friction force loop. Testing parameters for each hydrogel system can be found in Table 4.1. Sliding path distance was at least four times the contact diameter (see Eqn. 4.6) to ensure that the probe moved out if its initial contact footprint when sliding. Applied normal force and sliding speed were chosen to ensure that the minimum fluid film thickness (Eqn. 3.2) was less than the hydrogel surface roughness to avoid soft-EHL.

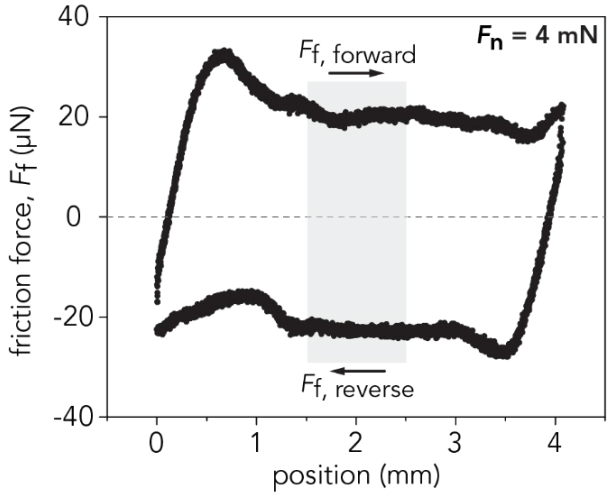

Figure 4.2 Representative friction force loop with the middle 25% of the loop highlighted in gray. Data was taken from P(AAm-*co*-AA) hydrogel with 12 wt.% AA (see Chapter 7). The following sliding parameters were used: F_n = 4 mN, v = 100 μm/s, x = 4 mm.

4.4 Mechanical Characterization

Microindentations were conducted with the tribometer to determine the reduced elastic modulus, E^*, of the hydrogels. Indentation depth, d, was calculated by accounting for the compliance of the cantilever as $d = z - x$, where z is the vertical piezo displacement and x is the cantilever displacement. A hemispherical borosilicate glass probe was used to apply a maximum normal force of F_n = 1.5 mN at an indentation velocity ranging between 1 to 10 μm/s to three separate positions along the gel. Five to six indentation measurements were performed at each location, and the approach curves were fit up to F_n = 1 mN using Hertzian contact mechanics theory (**Eqn. 4.3**) by minimizing the sum of squared errors (**Eqn. 4.4**) to solve for E^*:

$$F_n = \frac{4}{3} E^* R^{1/2} d^{3/2} \qquad \text{Eqn. 4.3}$$

where R is the probe radius of curvature, d is the indentation depth, and $E^* = E/(1 - \nu^2)$, where E is the compressive elastic modulus and ν is the Poisson's ratio of the hydrogel. To minimize the sum of squared errors, the lsqcurvefit Matlab function was used. This function employs the squared 2-norm of the residual (**Eqn. 4.4**), and minimizes this value to find the desired variable, x.

$$\sum (f(x, x_{\text{data}}) - y_{\text{data}})^2 \qquad \text{Eqn. 4.4}$$

In this case, the desired variable x is the reduced elastic modulus, E^*, x_{data} are the indentation depths d, y_{data} are the normal forces F_n, and the function f is $F_n = \frac{4}{3}E^*R^{1/2}d^{3/2}$ (Eqn. 4.3).

Representative indentation curves are displayed in Figure 4.3a. The reported elastic moduli are the averages and standard deviations of 45 – 54 total indentations spanning three separate gels. Representative Hertzian fits of the approach curve can be found Figure 4.3 (a) Representative indentation curve with the point of contact labeled along with the approach and retraction curves. (b) Representative Hertzian fit of the approach curve with the Hertz fit labeled in red. Data was taken from 17.5 wt.% PAAm hydrogel polymerized in 0.01 mol.% O2 (see Chapter 5). The following indentation parameters were used: *Fn* = 1 mN and *v* = 10 μm/s.Figure 4.3b. Testing parameters for each hydrogel system can be found in Table 4.1.

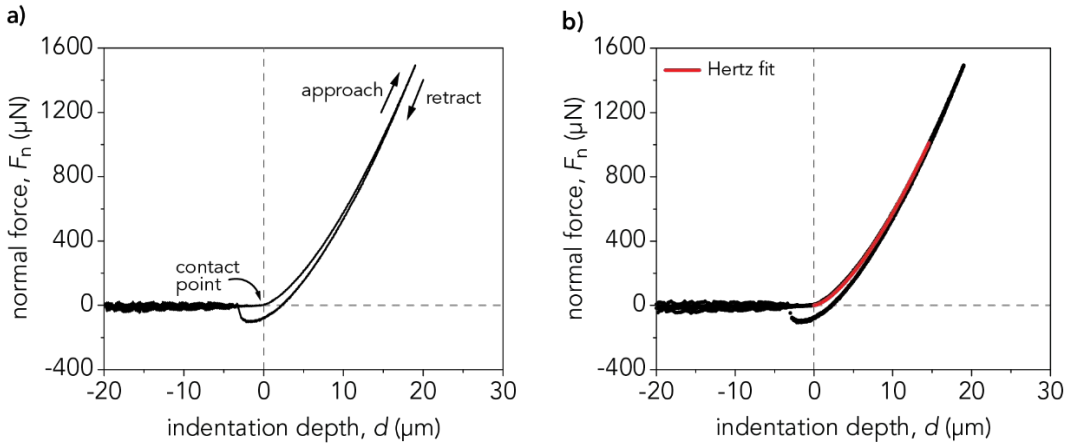

Figure 4.3 (a) Representative indentation curve with the point of contact labeled along with the approach and retraction curves. **(b)** Representative Hertzian fit of the approach curve with the Hertz fit labeled in red. Data was taken from 17.5 wt.% PAAm hydrogel polymerized in 0.01 mol.% O_2 (see **Chapter 5**). The following indentation parameters were used: F_n = 1 mN and v = 10 μm/s.

Hertzian contact mechanics can also be used to estimate the contact radius, contact diameter, and maximum applied contact pressure. Contact radius, *a*, can be estimated with the following equation:

$$a = \sqrt{Rd} \qquad \text{Eqn. 4.5}$$

where *R* is the probe radius and *d* is the indentation depth. With this equation, the maximum contact radius is determined based on the maximum indentation depth reached at the applied normal force. Contact diameter, $D = 2a$, can also be calculated with **Eqn. 4.6**:

$$D = 2\left(\frac{3F_{\mathrm{n}}R}{4E^{*}}\right)^{1/3} \qquad \text{Eqn. 4.6}$$

where the maximum indentation depth is not needed. Maximum contact pressure can be estimated using **Eqn. 4.7**:

$$P = \frac{3F_{\mathrm{n}}}{2\pi a^{2}} \qquad \text{Eqn. 4.7}$$

5 CHAPTER 5: DESIGNING SUPERLUBRICIOUS INTERFACES

The surface structure of hydrogels polymerized through free-radical polymerization can be modified by controlling environmental oxygen concentrations, leading to the formation of a polymer concentration gradient. In this chapter, 17.5 wt.% polyacrylamide hydrogels are polymerized in low (0.01 mol% O_2) and high (20 mol% O_2) oxygen environments, and their mechanical and tribological properties are characterized through microindentation, nanoindentation, and tribological sliding experiments. Without significantly reducing the elastic modulus of the hydrogel ($E^* \approx 200$ kPa), we demonstrate an order of magnitude reduction in friction coefficient (from $\mu = 0.021 \pm 0.006$ to $\mu = 0.002 \pm 0.001$) by adjusting polymerization conditions (*e.g.*, oxygen concentration). A quantitative analytical model based on polyacrylamide chemistry and kinetics is developed to estimate the thickness and structure of the monomer conversion gradient, termed the 'surface gel layer'. We find that polymerizing hydrogels at high oxygen concentrations leads to the formation of a pre-swollen surface gel layer that is approximately five times thicker ($t \approx 50$ μm) and four times less concentrated (≈ 6% monomer conversion) at the surface prior to swelling compared to low oxygen environments ($t \approx 10$ μm, ≈ 20% monomer conversion). Our model can be readily modified to predict the pre-swollen concentration profile of the polyacrylamide gel surface layer for any reaction conditions – monomer and

initiator concentration, oxygen concentration, reaction time, and reaction media depth – or used to select conditions that correspond to a certain desired surface gel layer profile.

This chapter was reproduced in part with permission from:[196]

Chau, A.L.*, Edwards, C.E.R.*, Helgeson, M.E., and Pitenis, A.A., Designing Superlubricious Hydrogels from Spontaneous Peroxidation Gradients. *ACS Applied Materials & Interfaces,* **15** (36), 43075 – 43086, 2023. (*equal contributions)

Table of Contents

5.1 Introduction

As described in Chapter 2, the mechanical and transport properties of crosslinked hydrogel structures are controlled by the average spacing or correlation length between polymer chains, known as the mesh size, ξ. Polymer concentration and crosslink density control mesh size, which can also be tuned after polymerization by solvent quality, pH, and temperature.[95] Conventionally "homogeneous" hydrogels are assumed to have a characteristic microstructure and mesh size that does not dramatically differ between the surface and the bulk. However, previous studies have demonstrated microscale heterogeneities in homogeneous hydrogels despite exhibiting generally isotropic bulk properties.[109,152]

Investigations of the interplay between chemically-crosslinked, homogeneous hydrogel structure and mechanics have led to scaling relationships between mesh size and elastic modulus,[137] $E \sim \xi^{-3}$, and friction coefficient,[150] $\mu \sim \xi^{-1}$, in the semi-dilute regime for good solvents (Table 2.3). These scaling relationships indicate that increasing ξ reduces E and μ concurrently, resulting in a tradeoff between strength and lubricity. By contrast, biological hydrogels, such as the extracellular matrix surrounding cartilage (Figure 1.1), often possess both exceptional load-bearing capabilities and ultralow friction coefficients. For cartilage, these excellent mechanical properties

can be attributed to the hierarchical structure and compositional gradient of its extracellular matrix, an entangled network of collagen fibers and proteins.[7,197]

To achieve this difficult balance of stiffness and lubricity in synthetic systems, recent investigations have focused on synthesizing and characterizing hydrogels with spatial gradients, where there is a gradual transition in mesh size or crosslinking density with increasing depth (*z*) (**Figure 5.1a-c**) as opposed to discrete layers with abrupt, stepwise changes in structure (**Figure 5.1d**).[198–201] There are many established methods used to synthesize hydrogels with spatial gradients, including dip coating,[202] microfluidics,[199,203] fluid mixing,[204,205] controlling substrate thickness,[206] UV polymerization with photomasks,[198,207–209] and electrochemical gradients, although these are often time-consuming and low throughput due to their experimental complexity.[210,211]

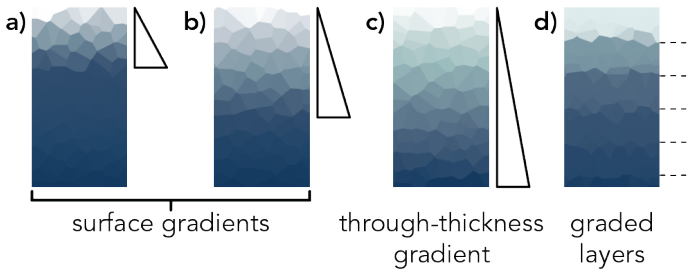

Figure 5.1 Illustration of hydrogels exhibiting relatively **(a)** shallow and **(b)** deep depth-wise surface gradients. **(c)** Depth-wise gradient through the entire hydrogel sample thickness. **(d)** Graded hydrogels with discrete layers of increasing polymer concentration.

The simplest method to create hydrogels with polymer concentration gradients at the surface (top 100s μm) does not require complex synthetic techniques. In 2001, Gong *et al.* discovered that hydrogels cast on hydrophobic

substrates polymerized heterogeneously, forming gels with gradients at the gel-substrate interface.[212,213] This "substrate effect" was attributed to high interfacial tension between the polymerizing solution and hydrophobic substrate, leading to a polymer concentration gradient that increased from the gel interface to the gel bulk.[214] Spencer *et al.* synthesized polyacrylamide hydrogels on substrates with varying surface energies and demonstrated that μ decreased with increasing substrate hydrophobicity; hydrogels cast on glass exhibited higher μ and E compared to those cast on polystyrene.[215] Recently, Simič and Spencer convincingly argued that oxygen permeability of the molding surface is responsible for this "mold effect" rather than surface energy.[216] This reasoning followed observations that oxygen inhibits free-radical polymerization and affects the interface exposed to air.[216,217]

Oxygen inhibition of free-radical polymerization reactions is a well-known phenomenon in polymer synthesis, particularly in thin films. Dissolved oxygen acts as a radical scavenger, terminating propagation of the polymerizing chain by reacting with polymerizing alky radicals to form stable, chain-terminal peroxyl radicals.[218–228] This inhibition significantly impedes polymerization where oxygen is abundant and leads to the formation of a liquid surface layer that never gels. There have been several studies examining the kinetics of this phenomenon in photoinitiated acrylate polymer thin film systems[218,220–222,224,226–231] to estimate the thickness of the unpolymerized layer, with estimates ranging between 1 μm and

50 μm, depending on the photoinitiator concentration, initiation rate, oxygen concentration, and initial film thickness (Table 5.1).[66,221,223,225,228,229]

Table 5.1 Comparison of the thickness of the unpolymerized oxygen inhibited layer for a variety of polymer thin film and hydrogel systems. (*dependent on photoinitiator concentration, initiation rate, film thickness, and oxygen concentration)

Acrylate System	Oxygen Inhibited Layer Thickness (μm)*	Characterization Technique	Ref.
Urethane-acrylate	1	Positron annihilation spectroscopy, x-ray photoelectron spectroscopy, microthermal analysis, nanoindentation	[223]
Urethane acrylate difunctional resin	4 – 34	Confocal Raman spectroscopy	[228]
Poly(ethylene glycol) diacrylate	4 – 35	Modeling (kinetics)	[221]
1,6-hexanediol diacrylate	5 – 50	Modeling (kinetics, heat transfer, mass transfer)	[229]
Dimethacrylate	10 – 20	Confocal Raman spectroscopy	[225]
Polyethylene glycol diacrylate hydrogel (40 wt.%)	20	Reaction-diffusion finite element model and experiments	[66]

In general, decreasing ambient oxygen concentration diminishes peroxyl formation and increases double bond conversion, reducing the thickness of the unpolymerized liquid layer.[218,221,228,229] Additionally, shortening the curing time by increasing the rate of radical initiation and propagation reduces the effects of oxygen inhibition by minimizing the diffusion time of oxygen.[218,221,228,229] However, these models did not investigate the structure or thickness of the gel surface that formed below this liquid layer due to oxygen diffusion within the film, despite clear demonstrations of a concentration gradient.[229]

For hydrogels synthesized via free-radical polymerization, the oxygen inhibition effect can result in a loosely crosslinked surface layer with a

crosslinking and polymer concentration gradient.[232–234] The thickness of this layer, denoted herein as the surface gel layer, is highly dependent on polymerization kinetics, crosslinker concentration, and oxygen diffusion and concentration (**Figure 5.2**).[232] Pitenis *et al.* demonstrated the superlubricity ($\mu \leq 0.005$) of 7.5 wt.% polyacrylamide hydrogels polymerized in ambient air (20 mol% O_2) in self-mated gel-on-gel contact, although the surface layer was not characterized.[235] Spencer and Simič controlled environmental oxygen (0 – 22% O_2) during the polymerization of 9.6 wt.% polyacrylamide hydrogels and demonstrated that with increasing oxygen, both the friction coefficient ($\mu \approx 0.1$ to $\mu \approx 0.002$) and elastic modulus ($E \approx 21$ kPa to $E < 1$ kPa) decreased.[236] They postulated that these decreases could be explained by an increase in thickness of the surface gel layer with increasing O_2 content, although the thickness was not directly measured.

While these studies and many others have demonstrated that high water content surface layers are critical for achieving a lubricious sliding interface,[39,181,234,237] it remains unclear what specific aspects of the surface gel layer structure (*e.g.*, polymer concentration, thickness) tune the lubricity of hydrogels. The relationship between surface structure and properties is complex for heterogeneous hydrogels, and current experimental methods for estimating the surface gel layer thickness involve indirect techniques such as microindentation,[238,239] nanoindentation,[108,181,216,234,236] development of new

contact mechanics models,[240,241] neutron reflectivity,[242] and confocal fluorescence microscopy.[211,232] Further, experiments cannot reliably distinguish the interplay between a surface gel layer's thickness, mesh size, polymer concentration, and concentration gradient (or lack thereof), particularly as they impact mechanical properties such as lubricity and elastic modulus. While reaction-diffusion models for polymerization kinetics can predict these intricacies of the surface gel layer structure, no such models have been developed to estimate the surface gel layer thickness for polyacrylamide chemistry, including the effects of oxygen inhibition, despite the many kinetics investigations of photopolymerized thin film systems. In this work, a combined experimental and modeling approach provides a complete picture of the surface gel layer structure, mechanics, and tribology in 17.5 wt.% polyacrylamide hydrogels synthesized in a controlled environment whose surface structure is tuned using oxygen concentration.

5.2 Materials & Methods

5.2.1 Hydrogel Synthesis

Acrylamide (AAm), *N,N'*-methylenebisacrylamide (MBAm), *N,N,N',N'*-tetramethylethylenediamine (TEMED), and ammonium persulfate (APS) were purchased from Sigma Aldrich. All reagents were used as received. Stock solutions of AAm (30 wt.%), MBAm (2 wt.%), TEMED (10 vol.%, corresponding to 7.9 wt.%), and APS (10 wt.%) were prepared in ultrapure deionized (DI) water

(18.2 MΩ·cm). Aliquots of each constituent were used to form a precursor solution of 17.5 wt.% AAm and 0.7 wt.% MBAm, following the methods by Urueña *et al.*[150] The final TEMED and APS concentrations were 0.12 wt.% and 0.15 wt.%, respectively. With a 54:1 molar ratio of monomer to crosslinker, most chain segments will incorporate at least one crosslinking group before reaching the entanglement molecular weight, which is 200 repeat units for 100 wt.% polyacrylamide. Thus, polymerizing chains of sufficient length to entangle in our 17.5 wt.% hydrogels are expected to have formed a crosslink instead; we anticipate potential entanglement effects to play a negligible role in our measurements.

The precursor solution (5 mL volume) was polymerized in a 35 mm diameter polystyrene mold with the top surface exposed to the atmosphere as a "free surface", creating an air-liquid interface. The pre-polymerized solution height was 5.2 mm. Polymerization was completed in a glove box, and an oxygen sensor (Alpha Omega Instruments, Trace Oxygen Analyzer, Series 3520 G) with a range of 0 – 10,000 ppm O_2 was used to monitor the oxygen content. Humidity was controlled with a commercial portable humidifier, and the relative humidity and temperature were monitored with a thermo-hygrometer (Omega Digital Thermo-Hygrometer, Model #RH411). Gels were polymerized in two oxygen concentrations targeting 100 ppm O_2 (glove box) and 200,000 ppm O_2 (atmospheric conditions), corresponding to 0.01 mol% O_2 and 20 mol% O_2

respectively, to alter the surface gel layer thickness (Figure 5.2). The reactions were quenched 15 min after the start of polymerization when the gels were submerged into a water bath at least 8x the gel volume. Hydrogel sections (24 mm diameter) were equilibrated in DI water at room temperature in a sterile environment at least 5 days before testing to ensure that equilibrium swelling was reached. We assume that oligomers that did not incorporate a crosslink prior to termination (*i.e.* free polymer) have been washed away by these steps and do not affect tribological results. For additional details on synthesis conditions, see Section 5.6.1.

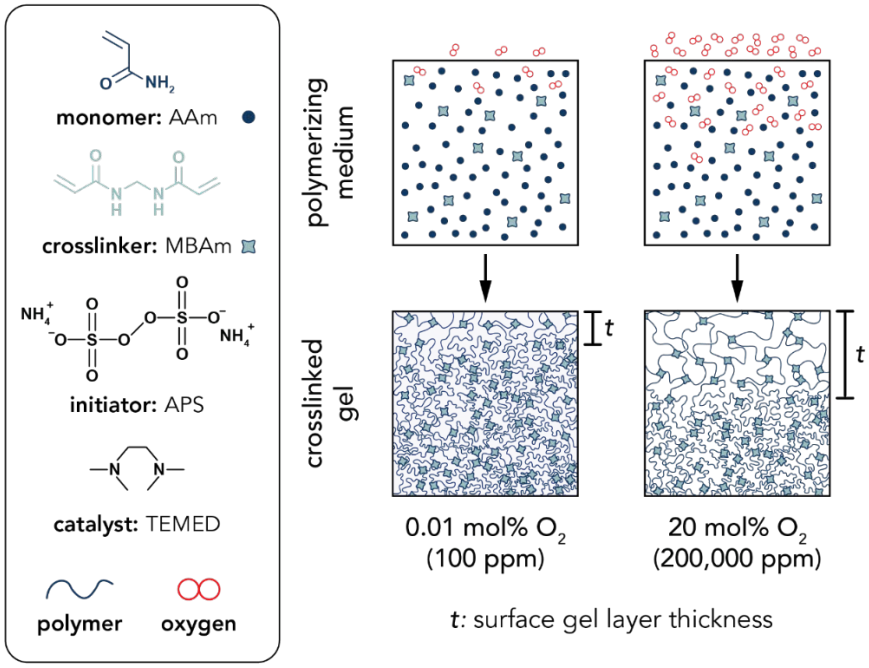

Figure 5.2 Chemical structures of the acrylamide (AAm) monomer (dark blue circle), *N,N'*-methylenebisacrylamide (MBAm) crosslinker (light blue cross), ammonium persulfate (APS) initiator, and *N,N,N',N'*-tetramethylethylenediamine (TEMED) catalyst with schematics of the hydrogel structures after 15 min polymerization in 0.01 mol% O_2 and 20 mol% O_2. The surface gel layer thickness, *t*, is denoted.

5.2.2 Nanoindentations

To characterize the stiffness of the surface gel layer, nanoindentations were performed using an atomic force microscope (AFM, Asylum MFP-3D Bio). A spherical borosilicate colloidal probe (Novascan) with a radius of R = 2.5 μm and normal spring constant of k = 0.25 nN/nm was calibrated via indentations against a glass slide. Force curves were generated at varying normal forces (F_n = 2 nN to 400 nN) with an indentation velocity of 2 μm/s. Measurements were completed at 25°C with the gels submerged in DI water. Hertzian contact mechanics (**Eqn. 4.3**) was used to estimate the reduced elastic modulus, E^*, of the surface gel layer by fitting the approach curves to an indentation depth of 0.55 μm, determined by the small angle approximation theory and probe radius of curvature (**Section 5.6.2**). This small indentation depth also ensured that the analysis stayed within the strains allowable for Hertzian contact mechanics.[243] The reported elastic moduli are the averages and standard deviations of 15 total indentations spanning three separate gels and 10 indentations spanning two separate gels for the 0.01 mol% O_2 and 20 mol% O_2 gels, respectively.

5.2.3 Microindentations & Friction Measurements

Tribological experiments and microindentations were conducted as outlined in **Section 4.3** and **Section 4.4.** Representative indentation curves are displayed in **Figure 5.3b**, and representative Hertzian fits of the approach curve

can be found **Section 5.6.3.** Representative friction force loops are displayed in **Figure 5.3c-d.** For additional details regarding contact area and pressure calculations, see **Sections 4.4 and 5.6.4.**

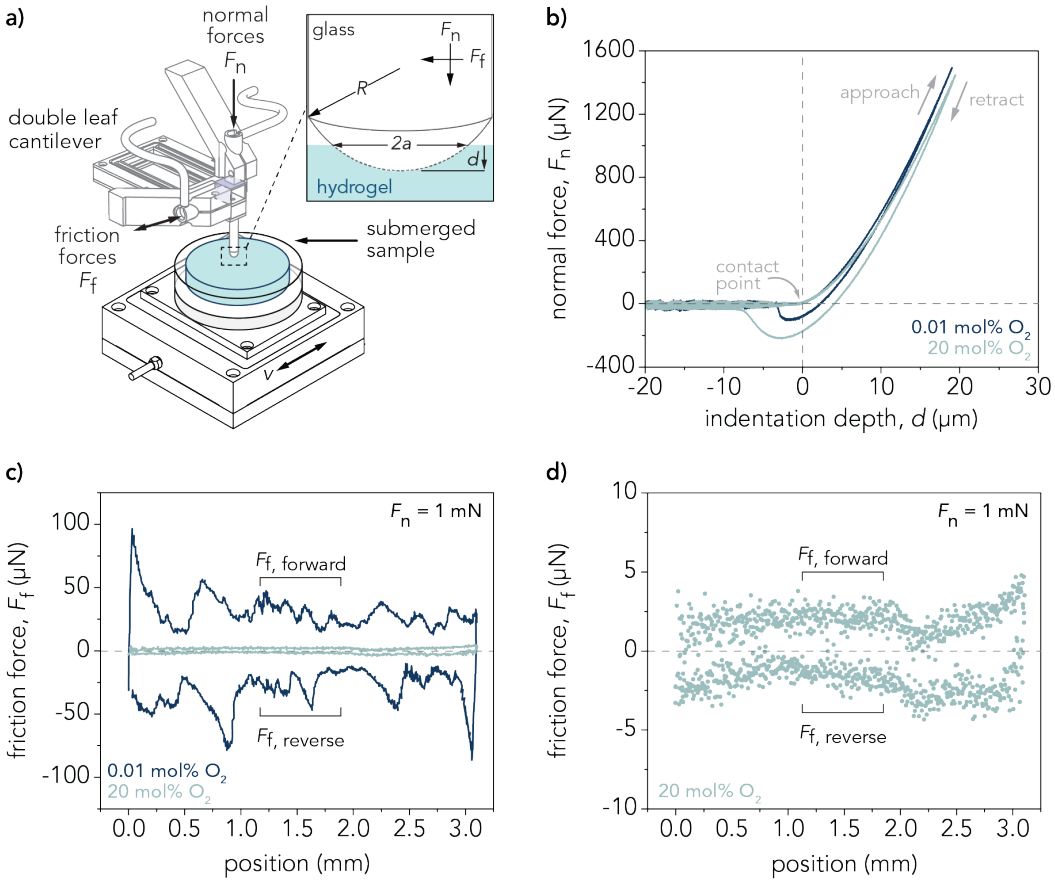

Figure 5.3 (a) Schematic of the linear reciprocating tribometer with inset demonstrating the contact diameter, *2a*, between the glass probe with radius of curvature, *R*, and hydrogel sample with an indentation depth, *d*. The applied normal forces, F_n, and resulting friction forces, F_f, are measured by capacitance probes, which convert the deflections of the double-leaf cantilever into forces. **(b)** Representative microindentation curves for the 17.5 wt.% polyacrylamide hydrogels polymerized at 0.01 mol% O_2 (dark blue) and 20 mol% O_2 (light blue). The reduced elastic modulus, *E**, is estimated by fitting the approach curves from the point of contact to F_n = 1 mN with Hertzian contact mechanics. **(c)** Representative friction force loops of the 17.5 wt.% polyacrylamide hydrogels polymerized at 0.01 mol% O_2 (dark blue) and 20 mol% O_2 (light blue) at an applied normal force of F_n = 1 mN and sliding velocity of *v* = 0.5 mm/s. Friction coefficients for each cycle are calculated by analyzing the middle 25% of the sliding path. **(d)** Enlarged friction force loop of the hydrogel polymerized at 20 mol% O_2 to highlight the extremely low friction forces.

5.2.4 Model Development

For detailed information about the reaction-kinetics model development, see Section 5.7.

5.3 Results & Discussion

In this work, 17.5 wt.% polyacrylamide hydrogels were polymerized at two oxygen concentrations (0.01 mol% and 20 mol% O_2) with one surface exposed as a "free surface" to the atmosphere to create hydrogels with surface gel layers of varying depth. Polymerization of this system occurred at the air-liquid interface, and it was expected that the hydrogels exposed to higher oxygen concentration during polymerization would have thicker gradient surface gel layers and therefore lower friction coefficients, μ, and reduced elastic moduli, E^*. Tribological sliding experiments were performed to measure the friction coefficients, and an analytical model based on polymerization kinetics was developed to estimate the surface gel layer thickness and its gradient. Nanoindentation was conducted to determine the surface mechanics accompanied by microindentation to probe deeper within the surface gel layer.

5.3.1 Friction Coefficients

The average friction coefficients for the 17.5 wt.% polyacrylamide hydrogels were calculated over 30 sliding cycles at an applied normal load of F_n = 1 mN (contact pressure, $P \approx$ 9 kPa to 11 kPa) and sliding velocity of v = 0.5

mm/s and averaged across three separate gels. Smooth, hemispherical glass probes were used as the countersurface. For gels prepared at 0.01 mol% O_2, the friction coefficient was $\mu = 0.021 \pm 0.006$. In contrast, the friction coefficient was an order of magnitude lower ($\mu = 0.002 \pm 0.001$) for samples prepared at 20 mol% O_2, which is within the superlubricity regime ($\mu \leq 0.005$) (**Figure 5.3c-d**). Low friction was maintained for these samples and the friction coefficients did not significantly change throughout the experiment (**Figure 5.4**), suggesting that the surface gel layer had sufficient time to recover before the next reciprocating cycle. If compression and local draining of the surface gel layer had occurred, we would have expected the friction coefficients of 20 mol% O_2 hydrogels to gradually increase over time to those exhibited by 0.01 mol% O_2 hydrogels.

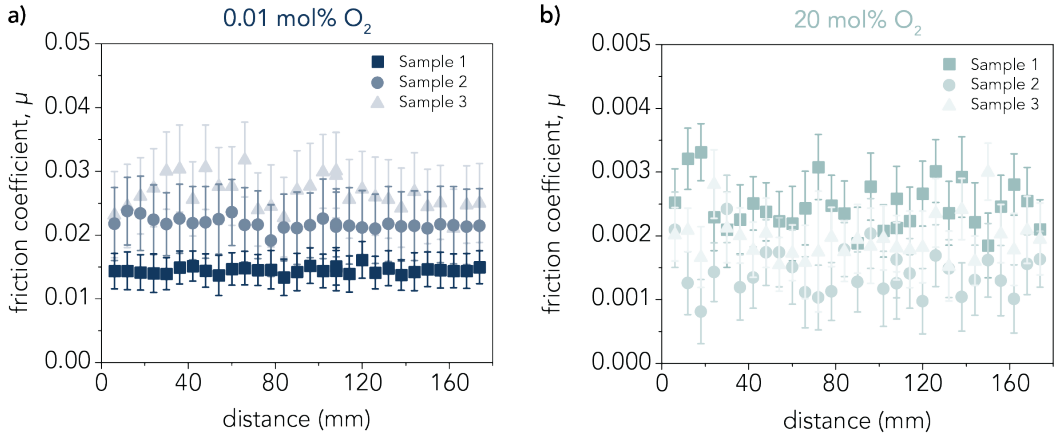

Figure 5.4 Friction coefficient as a function of sliding distance over 30 cycles for the **(a)** 0.01 mol% O_2 and **(b)** 20 mol% O_2 hydrogels. Friction does not significantly change over time. Note the difference in scale between the two plots.

With the testing conditions used herein, the minimum fluid film thickness, h_{min}, for soft-EHL lubrication is estimated to be between 33 – 36 nm using **Eqn. 3.2**. If h_{min} was significantly greater than the surface roughness of the 20% O_2 hydrogel, then the observed superlubricity would likely be due to a thick fluid film layer rather than the hydrogel surface. Since our hydrogels were cast in open air, it is difficult to estimate the surface roughness. However, using the scaling relationship $\mu \sim \xi^{-1}$ and following a Monte Carlo analysis outlined by Pitenis *et al.*,[235] the estimated surface mesh sizes for the hydrogels at 0.01 mol% and 20 mol% O_2 are $\xi = 2 \pm 0.4$ nm and $\xi = 32 \pm 15$ nm, respectively. Since h_{min} is on the same order of magnitude as the estimated mesh size of the 20 mol% O_2 gel, it is likely that there is still contact between the gel surface and probe, indicating that the measured superlubricity is not solely due to a fluid film layer.

The drastic reduction in friction coefficient by simply increasing the oxygen concentration during polymerization while maintaining the same initial monomer and crosslinker concentrations was also observed by Simič and Spencer with 9.6 wt.% polyacrylamide gels cast against polyethylene membranes in varying oxygen concentrations (0 – 22% O_2).[236] In self-mated gel-on-gel contact, the friction coefficient decreased from $\mu \approx 0.1$ at 0% O_2 to $\mu \approx 0.006$ at 22% O_2 at a sliding speed of $v = 0.5$ mm/s and contact pressures $P \approx 6 – 10$ kPa.[236] At 22% O_2, the authors estimated the thickness of the surface gel layer to be greater than 15 μm based on non-Hertzian responses during nanoindentations.

This decrease in friction with increasing oxygen concentration suggests that either the surface gel layer increased in thickness or potentially had a more loosely crosslinked structure at the surface, or some combination thereof.

Comparisons against other polyacrylamide hydrogels ranging in monomer (3.75 – 17.5 wt.%) and crosslinker (0.03 – 0.7 wt.%) concentrations (see **Figure 5.5**, **Table 5.5**) also highlight the extremely low friction coefficients exhibited by our 17.5 wt.% polyacrylamide hydrogels, despite high polymer concentrations and the use of an impermeable glass probe as the countersurface as opposed to another gel.

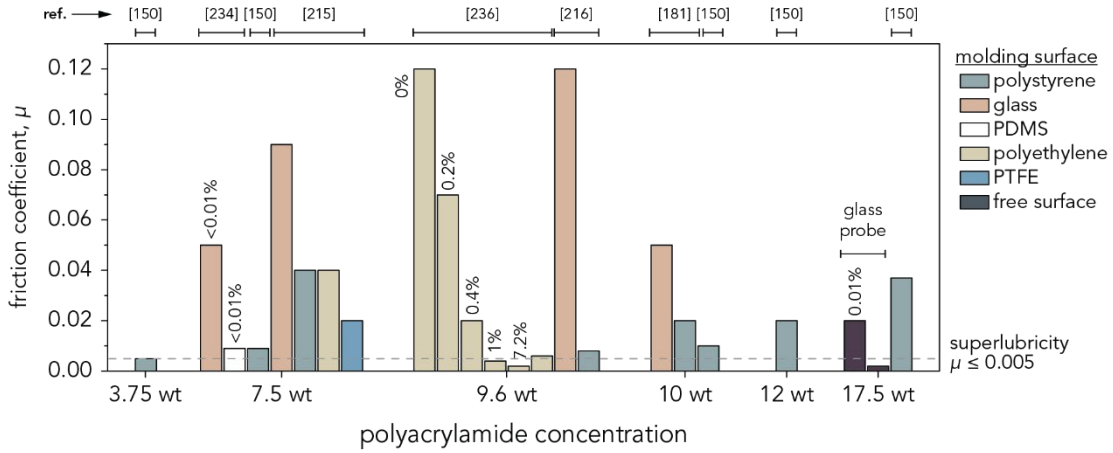

Figure 5.5 Comparison of friction coefficients of polyacrylamide hydrogels with varying monomer and crosslinker concentrations molded against different materials (polystyrene, glass, PDMS, polyethylene, PTFE, and air-liquid interface ("free")). All samples are cast at 20 mol% O_2 unless labeled otherwise. Sliding experiments were conducted with a self-mated gel-on-gel configuration unless otherwise stated. Tribological testing parameters are as follows: v = 0.5 mm/s and $P \approx$ 6-11 kPa.

Dunn *et al*. demonstrated that self-mated gel-on-gel sliding led to lower friction coefficients than glass-on-gel for 8 wt.% polyacrylamide hydrogels with

0.5 wt.% MBAm crosslinker at low sliding speeds (v = 0.1 mm/s), but this distinction lessened at higher sliding speeds.[180] They demonstrated that glass-on-gel friction coefficients were dominated by continuous polymer-glass interactions while the probability of polymer chain interactions in the gel-on-gel configuration was greatly reduced, leading to greater solvation and lower friction coefficients. Therefore, it is expected that sliding experiments conducted with glass probes as the countersurface would have larger friction coefficients. Yet, the friction coefficients measured herein for the hydrogels at 20 mol% O_2 are remarkably low, even lower than the friction coefficients for self-mated 3.75 wt.% polyacrylamide hydrogels (μ = 0.005),[150] which could be due to the absence of a molding surface since our hydrogel surfaces were exposed to the atmosphere and polymerized at this air-liquid interface.

Sliding experiments were also conducted at varying normal loads and sliding speeds to further interrogate the tribological behavior of the hydrogels. For self-mated gel-on-gel sliding configurations, friction coefficients typically decrease with increasing load due to nonlinear contact radius scaling.[176,244] Friction coefficients also tend to increase with sliding velocity past a critical transition velocity, v^*, due to the inability of the hydrogel to relax shear strain.[150,244] The 17.5 wt.% polyacrylamide gels herein deviated from previously observed tribological behavior – for the gels at 0.01 mol% O_2, μ slightly

increased with increasing load (**Figure 5.6**); for both oxygen conditions, μ decreased with increasing sliding speed (**Figure 5.7**).

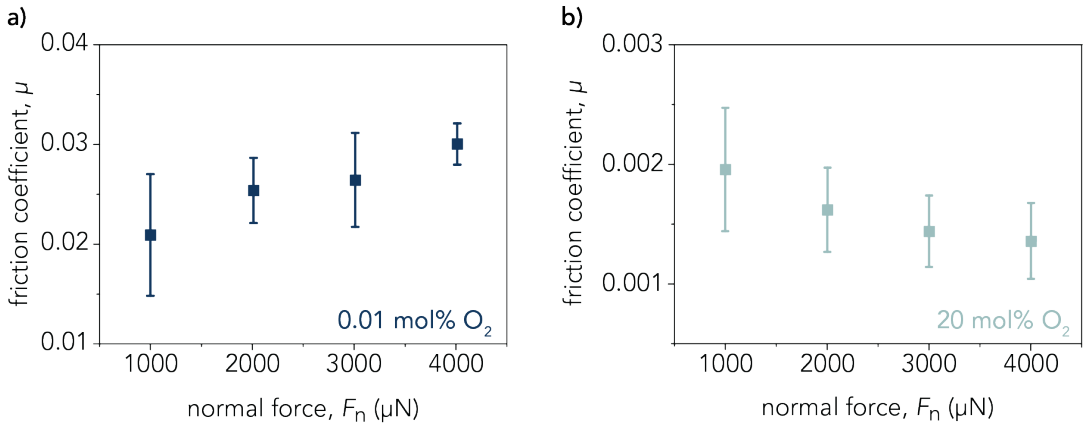

Figure 5.6 Friction coefficient as a function of applied normal force, F_n, for the 17.5 wt.% polyacrylamide hydrogels at 0.01 mol% O_2 and 20 mol% O_2. **(a)** Friction coefficient slightly increased with increasing normal force at 0.01 mol% O_2. **(b)** Friction coefficient slightly decreased with increasing normal force at 20 mol% O_2.

Shoaib *et al*. similarly observed decreasing μ with increasing v when below v^*, indicating that faster sliding velocities may be required to surpass v^* for these gels.[154] While further experimentation is warranted to understand these interesting tribological behaviors, they may be indicative of poroelastic effects due to the complex gradient surface gel layer. We leave the investigation of this complex behavior to future studies.

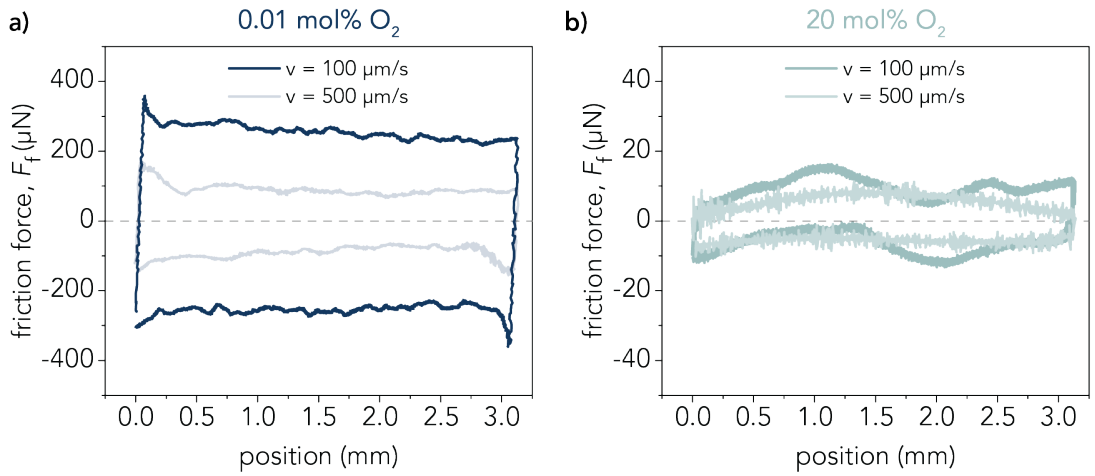

Figure 5.7 Friction force loops comparing the effects of sliding velocity for the 17.5 wt.% polyacrylamide hydrogels at **(a)** 0.01 mol% O_2 and **(b)** 20 mol% O_2. In both cases, the friction force decreased with increasing sliding velocity, which is the opposite of what is typically observed for hydrogels. This may indicate poroelastic effects that require further investigation.

5.3.2 Microindentation Measurements & Analysis

The reduced elastic modulus of the top 15 µm of the polyacrylamide hydrogels was obtained with microindentations along three different positions and averaged across three independent hydrogel samples at a constant indentation velocity of 10 µm/s. At 0.01 mol% O_2, E^* = 242 ± 11 kPa, with a slight decrease to E^* = 203 ± 38 kPa at 20 mol% O_2. Representative indentation curves and Hertzian contact mechanics fits can be found in **Figure 5.3b** and **Section 5.6.3.** At first glance, the slightly higher modulus reported for the 0.01 mol% O_2 could be explained by less peroxyl formation in the gel surface with dissolved oxygen at the start of the reaction leading to smaller predicted mesh sizes, as shown by the model in **Section 5.4.** However, there is no statistical significance between the experimentally determined E^*. Our results suggest that

the modulus of hydrogel surfaces at large indentation depths is insensitive to differences in oxygen content in real systems and is largely determined by the starting concentrations of reactant species; in our experiments, the starting dissolved oxygen concentration even in the 20 mol% O_2 case was an order of magnitude smaller than the APS (initiator) and TEMED (catalyst) concentration.

To examine the effects of indentation velocity on the measured elastic modulus, the hydrogels were indented at a lower velocity, v = 1 μm/s, which was comparable to the velocity used during nanoindentations (see **Section 5.3.3** and **Figure 5.8**).

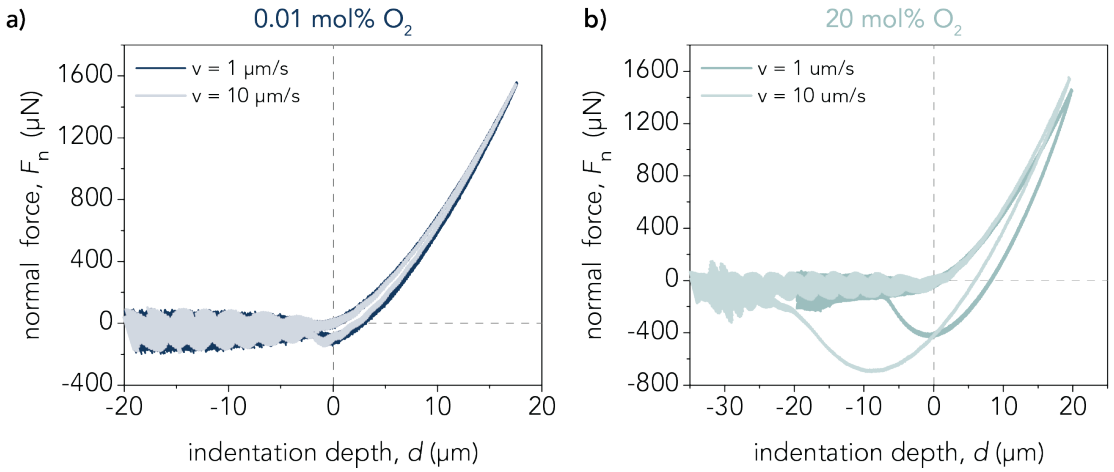

Figure 5.8 Representative microindentation curves for the 17.5 wt.% polyacrylamide hydrogels comparing indentation velocities. **(a)** For the 0.01 mol% O_2 hydrogels, the elastic modulus was not affected by indentation velocity. **(b)** For the 20 mol% O_2 hydrogels, there was a slight decrease (≈ 18%) in elastic modulus with decreasing indentation velocity.

Indentation velocity did not significantly impact the elastic modulus of the 0.01 mol% O_2 hydrogels, but the elastic modulus decreased by about 18% for

the 20 mol% O_2 hydrogels, suggesting poroelastic behavior due to the presence of a highly hydrated surface gel layer.

5.3.3 Surface Mechanics

Atomic force microscopy (AFM) was used to probe the mechanics of the superficial region of the surface gel layer across two to three independent hydrogel samples at a constant indentation velocity of 2 μm/s. Only the first 0.55 μm of the approach curve was analyzed with Hertzian contact mechanics to stay within the small angle approximation and allowable strain (**Section 5.6.2**). **Figure 5.9** displays representative nanoindentation approach curves for the polyacrylamide hydrogels cast at 0.01 mol% O_2 and 20 mol% O_2. Across three independent gel samples, the average reduced elastic modulus at 0.01 mol% O_2 was $E^* = 257 \pm 48$ kPa. At 20 mol% O_2, $E^* = 1.1 \pm 0.2$ kPa across two independent hydrogel samples. For additional representative nanoindentation curves, see **Figure 5.14.**

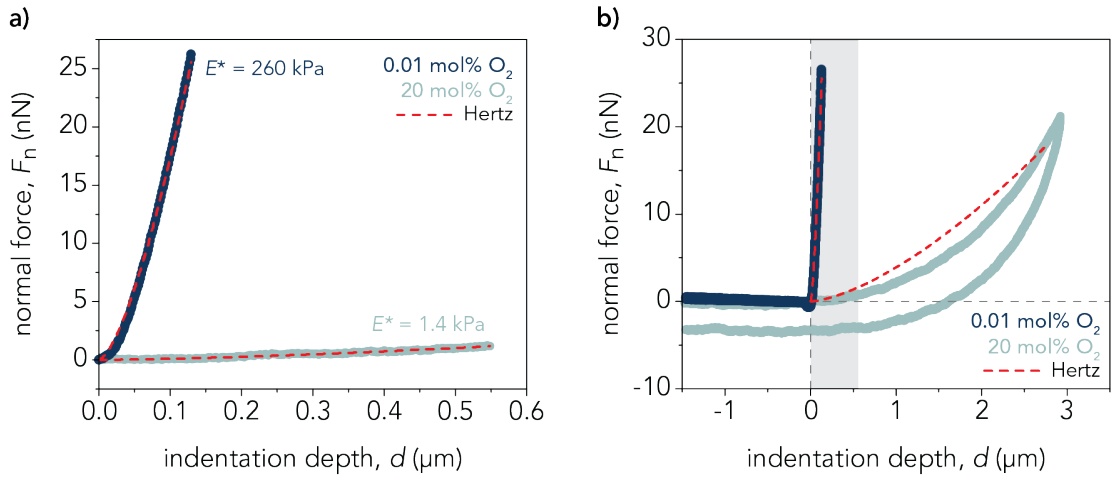

Figure 5.9 (a) Representative nanoindentation approach curves for the 17.5 wt.% polyacrylamide hydrogels at 0.01 mol% O_2 (dark blue) and 20 mol% O_2 (light blue). Hertzian contact mechanics (red dotted line) was used to fit the first 0.55 μm of the approach curve to determine the reduced elastic modulus, E^*. For the plotted curves, E^* = 260 kPa and E^* = 1.4 kPa at 0.01 mol% O_2 and 20 mol% O_2, respectively. **(b)** Full nanoindentation curves for the hydrogels demonstrating the deviation of the Hertz contact model past 0.55 μm (gray region) for the hydrogel at 20 mol% O_2.

The low reduced elastic modulus value for the hydrogels cast in 20 mol% O_2 indicate that the gel structure at the top 0.55 μm of the hydrogel surface is extremely soft. In both cases, the surface is directly exposed to the atmosphere as a "free" surface in local equilibrium with the atmospheric oxygen concentration and not cast against any solid material. This may explain why our 17.5 wt.% polyacrylamide hydrogels with 0.7 wt.% crosslinker cast in 20 mol% O_2 have similar reduced elastic moduli at the surface to literature gels cast against polyethylene membranes in 20 mol% O_2 (E < 1 kPa as measured by AFM), despite the previously-reported gels having a *lower* polyacrylamide and crosslinker concentration at 9.6 wt.% and 0.4 wt.%, respectively.[236] The 17.5 wt.% polyacrylamide hydrogel surfaces cast herein at an air-liquid interface

may be more loosely crosslinked than the literature reports for polyacrylamide hydrogels cast against molding surfaces despite higher polymer concentrations in the bulk (see **Table 5.5**).[108,112,150,181,215,216,234,236,238–240] These results highlight that the surface effects of oxygen inhibition are best observed and exploited at a free surface where oxygen can easily diffuse throughout the duration of the reaction, as demonstrated in more detail in **Section 5.4**. Moreover, increasing oxygen concentration results in a significantly different surface structure despite having a minimal effect on the mechanical properties of the gel at larger indentation depths.

Owing to its simplicity, the Hertz contact mechanics model has been broadly deployed to characterize heterogeneous materials, such as articular cartilage,[5] cells,[245] and hydrogels.[236] At low indentation depths within the small strain limit ($\leq$ 0.55 μm), the Hertzian contact model fits the data well (**Figure 5.9a**). However, the fit deviates from the approach curve at 20 mol% O_2 at higher indentation depths, indicating that this model may not be the most appropriate one to use (**Figure 5.9b, Figure 5.15**). Since the Hertz model assumes a homogeneous network, the observed deviations support heterogeneity of the network at the surface. Johnson and Dunn similarly observed non-Hertzian behavior for polyacrylamide hydrogels of varying concentration cast against polystyrene in ambient condition and used the Fredrickson high-penetration brush model and Winkler mechanics to fit the initial portions of indentation

curves to estimate the thickness of the surface gel layer.[108,238] For our 20 mol% O_2 hydrogels, the Fredrickson high-penetration brush model fit the entirety of the nanoindentation approach curve (**Figure 5.15**), suggesting a thick surface gel layer.

5.4 Modeling Gelation at the Surface

We postulate that the measured frictional decrease and lower surface elastic modulus for the hydrogels polymerized at 20 mol% O_2 compared to those at 0.01 mol% O_2 can be attributed to a thicker surface gel layer with larger mesh size. However, the relative impacts of oxygen content on surface gel layer thickness, polymer concentration, and crosslink density are difficult to distinguish in any further detail using experiments. Here, we developed a reaction-diffusion model for conversion of acrylamide and crosslinker monomers under various conditions as the polymerization progresses, both in the bulk and at the surface of the gel. We used this model to gain insight into the formation of the surface gel layer under the tested conditions, as well as its structure after 15 min of polymerization at 0.01 mol% and 20 mol% O_2. This model predicts conversion of monomers to polymers as a function of time and depth from the gel surface, which corresponds to concentration of polymer chains in the gel prior to swelling.

Since AAm and MBAm are treated equivalently in the model (see **Section 5.7.1**), the predicted crosslink density is directly proportional to the predicted monomer conversion. However, in the experimental system, bisacrylamide radicals are much more reactive with both acrylamide and bisacrylamide monomers than are acrylamide radicals.[59,109] The enhanced incorporation of bisacrylamide monomers at early reaction times in the real system leads to the well-known microscale heterogeneity of the polyacrylamide network, with formation of microdomains of large segmental density.[246] Our model cannot capture this heterogeneity due not only to the equivalence assumption discussed above but also because the composition is treated as a continuum across every calculated depth within the gel. Thus, while our model predictions suggest trends in crosslink density, we restrict our interpretation to average polymer concentration per depth from the surface in the pre-swollen gel.

Our model intends to provide a micrometer-scale description for gel structure from the surface to the gel bulk via the polymer concentration at each depth, rather than segmental-level structural detail. Therefore, we describe the observed trends in terms of mesh size to be purposefully agnostic to the molecular structure at the very surface of the gel. For example, both a "brushy" structure such as that postulated by Simič *et al.*[42] and one with very long connective chains between crosslinks could have a large mesh size. Regardless, our results demonstrate that considering 10s μm to 100s μm of gel layer

thickness at the surface is important because the oxygen conditions during polymerization affect polymer concentrations throughout this entire depth, which in turn governs the mechanical and tribological gel properties; any segmental-scale mechanistic explanations for surface polymer conformation in the lower friction oxygen-inhibited gels must be compatible with the reduced concentration of polymer at the gel surface predicted herein.

5.4.1 Gelation at Low Oxygen Concentration

During gelation at low oxygen concentration (0.01 mol% O_2), predicted monomer conversion proceeds uniformly throughout the depth of the gel, apart from the surface where oxygen continues to diffuse into the polymerizing medium (Figure 5.17). Consequently, dissolved oxygen is locally enhanced near the surface and reacts to form peroxides at an elevated rate. As the reaction proceeds, a gel is predicted to form quickly (Figure 5.10a), along with a surface gel layer whose distinction from the bulk gel becomes clearer over time. At this O_2 concentration, the thickness of the surface gel layer remains approximately constant once developed (Figure 5.10b). Meanwhile, the gradient in monomer conversion (*i.e.*, polymer concentration) from the surface of the gel to the bulk – as given by the slope of the conversion in the surface gel layer – becomes steeper with time (Figure 5.10c), since progression of the polymerization at the surface cannot keep up with the rate of conversion in the bulk. The methodology

for determining the point of gelation based on monomer conversion, the surface of the gel, and extracting surface layer thickness and gradient from the monomer conversion traces is provided in Section 0. The predicted apparent surface gel layer is very thick (>50 μm) early in the gelation process because the distinction between the surface layer and bulk gel is ill-defined at very early times. This indistinction is reflected in a larger error associated with the fit used to extract the surface layer thickness (Figure 5.19). However, two distinct regions are quickly established as the bulk gel formed, and the surface gel layer thickness quickly decreases to approximately 10 μm after which it remains almost constant. As polymerization proceeds past five minutes, the surface gel layer thickness decreases slightly (Figure 5.20a) and its gradient becomes more severe. The conversion of monomer to polymer narrowly outcompetes the peroxidation side-reaction from dissolved oxygen at the gel's surface, whereas in the gel bulk – where oxygen concentration remains negligible after the first few minutes of the reaction – polymerization strongly dominates any peroxidation. After 15 min of polymerization, a surface gel layer 10.8 μm thick with a monomer conversion gradient of approximately 4 %/μm are predicted, compared to a total gel thickness of 5.2 mm. Thus, before post-polymerization swelling, the polyacrylamide hydrogel samples polymerized at 0.01 mol% O_2 are predicted to have an ≈ 11 μm thick surface gel layer, and the polymer

concentration at the surface is about three times less than the bulk (Figure 5.11a) with a corresponding decrease in crosslink density.

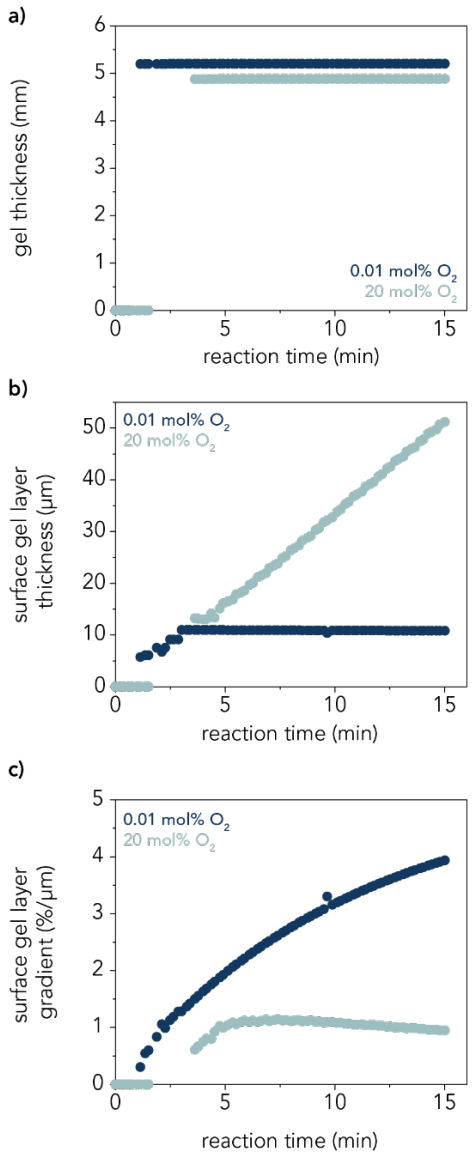

Figure 5.10 Predictions of the reaction-diffusion model at low and high oxygen conditions. **(a)** Bulk gel formation occurs within minutes of adding APS and TEMED to initiate the polymerization, reaching a thickness of 5.2 mm for the 0.01 mol% O_2 hydrogels (dark blue) and 4.9 mm for the 20 mol% O_2 hydrogels (light blue). **(b)** Surface layer thickness, extrapolated from fits of the monomer conversion in the surface gel layer as a function of polymerization time. At 0.01 mol% O_2 (dark blue), the surface gel layer thickness slowly decreases with reaction time after its initial formation. At 20 mol% O_2 (light blue), the surface gel layer thickness increases throughout the polymerization. **(c)** Severity of gradient in monomer conversion from the surface

of the gel to the bulk increases with polymerization time at 0.01 mol% O_2 (dark blue) but decreases slightly with time at 20 mol% O_2 (light blue). At 15 min polymerization, the surface gel layer conversion gradient is 4 %/μm and 1 %/μm at 0.01 mol% and 20 mol% O_2, respectively.

5.4.2 Gelation at High Oxygen Concentration

During gelation at higher ambient oxygen conditions (20 mol% O_2), predicted monomer conversion remains negligible at the surface of the polymerization medium due to significant oxygen inhibition. This upper layer never forms a gel and is presumably washed away when gels are plunged into water to quench the polymerization, causing the hydrogel to be about 325 μm thinner than the gel at 0.01 mol% O_2 (**Figure 5.21**). This unpolymerized liquid layer was similarly observed in studies of oxygen inhibition of acrylate thin films.[220,221,223,229] Below this un-gelled film, polymerization proceeds to reach conversions above 5%, forming a gel as soon as the oxygen is consumed (**Figure 5.18**). Like the 0.01 mol% O_2 case, oxygen consumption in the bulk takes about two minutes, after which a gel forms throughout the system (**Figure 5.10a**). As the polymerization proceeds, the distinction between the surface gel layer and bulk gel takes longer to establish than at 0.01 mol% O_2, and its thickness increases significantly with polymerization time once the distinction between layers is established (**Figure 5.10b**). At every time point after initial formation of the surface gel layer (≈ 2.5 min), the thickness of this layer is larger for 20 mol% O_2 than for 0.01 mol% O_2. Meanwhile, the severity of the gradient in monomer conversion in the surface gel layer remains relatively constant once it

is established (Figure 5.10c) and even decreases slightly according to fits of the monomer conversion at the surface of the gel (Figure 5.20b). After 15 min, a 51.2 μm thick surface layer is predicted compared to a total gel thickness of 4.9 mm, with 6.2% monomer conversion at the surface of the gel and a surface gel layer monomer conversion gradient of 1 %/μm (Figure 5.10c). The surface polymer concentration is almost ten times less than the bulk, whose monomer conversion is already slightly lower than that of the 0.01 mol% O_2 case, consistent with the small experimentally observed decrease in E^* of the hydrogel (Figure 5.3b).

5.4.3 Comparison of the Surface Gel Layer Profiles

The surface gel layer thickness predictions herein for the 17.5 wt.% polyacrylamide hydrogels cast in 20 mol% O_2 are within the same order of magnitude as those predicted by indentations and contact mechanics modeling for polyacrylamide hydrogels ranging in monomer (7.5 to 15 wt.%) and crosslinker (0.03 to 0.6 wt.%) concentrations (Table 5.5).[108,112,150,181,215,216,234,236,238–240] However, they are larger than previous estimates for the highest concentration hydrogel (15 wt.% AAm, 0.6 wt.% MBAm), which estimated a surface gel layer thickness of 13 μm for a hydrogel cast against a polystyrene surface in ambient air (20 mol% O_2),[108] as compared to our estimate of 51 μm. Gombert *et al.* used neutron reflectometry and infrared spectroscopy to

compare the surface structures of 7.5 wt.% polyacrylamide hydrogels cast against glass and PDMS surfaces in extremely low oxygen environments (<0.01 mol% O_2).[234] They concluded that polymer concentration gradients formed for the gels cast against PDMS due to its hydrophobicity and predicted the gradients to extend more than 50 μm. This may indicate the importance of an air-liquid interface for the formation of thick surface gel layers for high polymer concentration hydrogels.

Previous studies have not resolved the polymer concentration gradient within the surface gel layer. However, the model herein predicts conversion of monomers to polymers, which corresponds to the concentration of polymer chains in the gel prior to swelling. Over the course of polymerization, the severity of the monomer conversion gradient from the surface to the bulk increases with time for both oxygen concentrations (**Figure 5.11**). However, monomer conversion at the surface of the 0.01 mol% O_2 gels increased while conversion remained around 5% at 20 mol% O_2. During hydrogel polymerization at 20 mol% O_2, the monomer conversion profile in the surface layer remains constant in time, whereas the bulk increases in conversion over time (**Figure 5.11b**). Since oxygen is progressively consumed as it diffuses further into the film, a higher conversion is reached as less oxygen inhibition occurred deeper into the polymerizing medium. This effect is not observed at 0.01 mol% O_2, since the oxygen concentration was low enough that it is entirely consumed at short

depths into the gel, essentially forming a reaction-diffusion boundary layer. There is a steeper transition from the surface polymer concentration to the bulk over 11 μm (4%/μm) in comparison to the 20 mol% O_2 case in which the surface gel layer polymer concentration transitioned more gradually at 1%/μm over 51 μm (**Figure 5.11**), leading to a surface gel layer that is approximately five times thicker and four times less dense than the one at 0.01 mol% O_2 prior to swelling. While these conclusions assume that overall monomer conversion is related to polymer concentration, the large decrease in friction coefficient achieved in gels prepared at 20 mol% O_2 support our predictions that the 0.01 mol% O_2 and 20 mol% O_2 gels have entirely different surface characteristics. In particular, our predictions show that not only a thicker surface gel layer, but a combination of a thicker layer and less concentrated polymer at the surface structure give rise to superlubricity in polyacrylamide gels polymerized at higher oxygen concentrations.

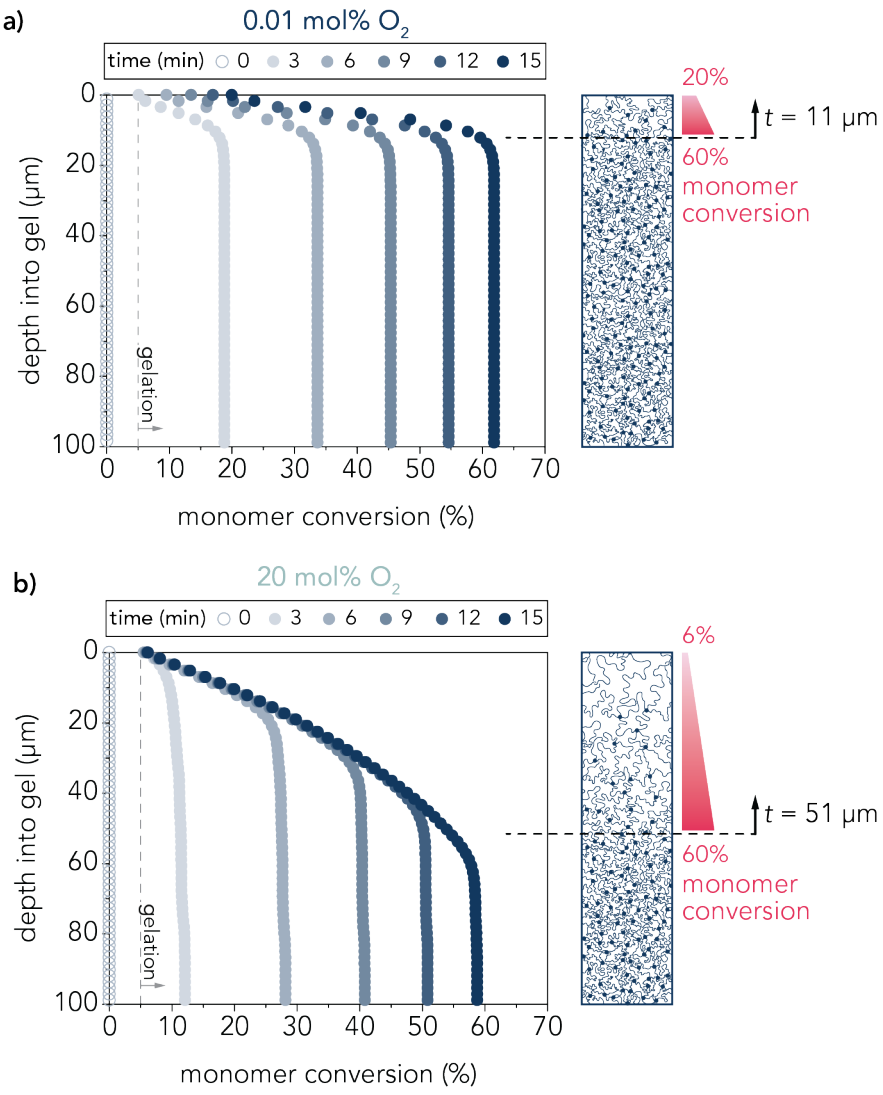

Figure 5.11 Monomer conversion at the surface of the gel at various polymerization times as a function of the depth from the gel surface for the **(a)** 0.01 mol% and **(b)** 20 mol% O_2 hydrogels. Gelation occurs at around 5% monomer conversion. At the surface of the 20 mol% O_2 hydrogels, the conversion remains just above the gel point at 5%. Schematic representation of the top 100 µm of the hydrogel structures at 0.01 mol% O_2 and 20 mol% O_2 demonstrate that the surface gel layer is thicker with a smaller monomer conversion gradient at higher O_2 compared to the surface gel layer at lower O_2. This indicates a more gradual transition in polymer concentration from the surface gel layer to the bulk at 20 mol% O_2, contrasting a more abrupt change in polymer concentration at 0.01 mol% O_2.

Overall, the model predicts qualitatively different structures and time-dependent formation behavior of the surface gel layer at the liquid-air interface for low versus high O_2. In **Figure 5.11**, we observe two shapes of surface gel layer as the polymerization proceeds in time. For 0.01 mol% O_2 at the interface, the model predicts that oxygen depletion in the bulk leads to the formation of a reaction-diffusion boundary layer at the air-liquid surface, resulting in a surface gel layer whose thickness remains relatively constant in time after its initial formation but with a gradient that sharpens over time due to the increasing conversion in the bulk gel. In contrast, for 20 mol% O_2 at the interface, the model predicts a gradient that remains relatively static but penetrates deeper into the gel as oxygen diffuses further, resulting in a thicker, more diffuse surface gel layer. In summary, at low O_2, the surface layer thickness is maintained, while the gradient and surface monomer conversion increase with time; at high O_2, surface layer thickness grows in time, while the gradient and concentration at the gel surface are maintained.

5.4.4 Model Predictions

To more generally understand the transition between the surface gel layer growth profiles, we predict monomer conversion and the corresponding profile of the surface gel layer after 15 min of polymerization for a wide range of O_2 concentrations (0.004 to 46.5 mol%) using our reaction-diffusion model (**Figure**

5.22). At very low O_2 concentrations below 0.1 mol% (~1,000 ppm), increasing the amount of O_2 also decreases the conversion at the surface of the gel, *i.e.* gives rise to a gel whose surface polymer concentration is lower (Figure 5.23a). In this regime, consistent with the surface gel layer profile of our low O_2 (0.01 mol%) case described above, increasing O_2 also increases the thickness of the surface gel layer (Figure 5.23b) though its gradient stays relatively constant (Figure 5.23c). Only very small amounts of O_2 (above 0.1 mol%) cause the surface of the reacting media to remain unpolymerized (Figure 5.23d), which results in the gel's surface polymer concentration being fixed at the gel point (about 5% monomer conversion). Further increasing O_2 above 0.1 mol% causes the surface gel layer thickness to grow, which in turn results in a shallower surface gel layer gradient (Figure 5.23c). These features are consistent with the surface gel layer profile of our high O_2 (20 mol%) case described above. Excessively high O_2 also impacts bulk conversion (Figure 5.23e), which will increase the mesh size in the gel bulk but may negatively affect the gel's strength. We expect the predicted trends to hold for other gel compositions (monomer, crosslinker, initiator, and catalyst concentrations) and polymerization media heights (H) as controlled by the dimensionless groups governing this reaction-diffusion model (Da_{M}, Da_{O_2}, and α), though the cutoff in O_2 concentration above which the surface is at the gel point will be composition- and H-dependent. The interplay between these variables and their impact on the gradient structure at the surface

of the gel is challenging to verify experimentally and represents a rich area for future study.

Moving beyond the analysis of the gelation process for the two oxygen conditions studied in this work, the results of the model provide practical principles for using oxygen- and time-dependent control of gelation reactions to control the formation of surface layers during hydrogel preparation, thereby enabling the design of superlubricity. The experiments and model reveal that superlubricity is achieved under high-oxygen polymerization conditions through the formation of a surface layer that is both thick and diffuse. These features could be enhanced by performing reactions in an oxygen-enriched atmosphere at the expense of polymer concentration in the bulk. In general, the model could be used to predict or design pre-swollen surface gel layer profiles for a wide range of monomer and oxygen compositions, reaction times, and polymerization media heights. Furthermore, it is interesting to consider how time variations in the atmospheric oxygen concentration could be used to sculpt the desired shape of the surface gel layer conversion profile for a particular gel composition and geometry, thereby providing added control in designing the structure and properties of the surface layer. Because such control can be difficult to achieve in practice, we leave a detailed study of this possibility using the model and experiments to future work.

5.5 Conclusion

Free-radical polymerization of hydrogels is an uncontrolled, random process that frustrates predictions of the precise microstructure at the surface and within the bulk. Here, we proposed that oxygen inhibition of acrylamide/*N*,*N*′-methylenebisacrylamide polymerization leads to superlubricity at the hydrogel surface, with the friction coefficient decreasing two orders of magnitude from $\mu = 0.021 \pm 0.006$ at 0.01% O_2 to $\mu = 0.002 \pm 0.001$ at 20 mol% O_2. To explain these results, we developed a parameter-free reaction-diffusion model using kinetic parameters for the exact chemistry and composition of the system. We found that polymerizing under high oxygen conditions (20 mol% O_2) increased the thickness of the surface gel layer but decreased the severity of the monomer conversion gradient between the surface and the bulk. This was indicated by a lower monomer conversion at the gel surface during the reaction, even though the gels cast at 0.01 mol% and 20 mol% O_2 had similar conversions in the bulk (corresponding to similar moduli). Prior to swelling the gels, we predicted that the gel at 0.01 mol% O_2 had a surface gel layer thickness of 11 μm with a monomer conversion gradient of 4%/μm while the gel at 20 mol% O_2 had a surface gel layer thickness of 51 μm with a 1%/μm gradient, indicating that surface gel layer at 20 mol% O_2 was approximately five times thicker and four times less concentrated at the surface prior to swelling. Simulations suggest that the surface layer thickness, polymer

concentration gradient, and elastic modulus at the surface can be tuned to achieve the lowest friction coefficient at a given monomer/crosslinker concentration, using a combination of O_2 concentration and the interplay between reaction time and initiator concentration. We leave a comprehensive study of the complex interplay between these variables, friction, and modulus, or their fine-tuning for specific applications, to further study. Overall, this work established that a thicker surface gel layer with lower polymer concentration led to superlubricity in the polyacrylamide system under oxygen inhibition and portends the use of more sophisticated time-dependent control of reaction conditions to sculpt the precise structure – and therefore properties – of the surface gel layer.

5.6 Appendix A: Mechanical Data

5.6.1 Hydrogel Synthesis

Table 5.2 Volume and mass of each component in the pre-polymerized hydrogel solution, along with the corresponding wt.% and mol.%.

Chemical	Stock Solution		Mass (mg)	Mole (mmol)	Concentration	
	Concentration	Volume (µL)			wt.%	mol.%
Acrylamide (AAm)	30 wt.%	2917	875	12.3	17.5	5.15
N,*N*'-methylene bisacrylamide (MBAm)	2 wt.%	1750	35	0.2	0.7	0.10
DI water	---	183	4077	226	81.5	94.7
N,*N*,*N*',*N*'-tetramethylethylene diamine (TEMED)	10 vol.% (7.9 wt.%)	75	6.0	0.05	0.12	0.02
Ammonium persulfate (APS)	10 wt.%	75	7.5	0.03	0.15	0.01

Table 5.3 Synthesis conditions for the 17.5 wt.% polyacrylamide hydrogels.

Target O_2 ppm	Actual O_2 ppm (mol%)	Relative Humidity	Temperature (°C)
100 ppm (0.01 mol% O_2)	30 – 500 ppm (0.003 – 0.05 mol%)	14 – 22%	19 – 20.5
200,000 ppm (20 mol% O_2)	Ambient air (20.95 mol%)	42 – 64%	19 – 20.5

5.6.2 Small Angle Approximation

Indentation depth, *d*, into the sample can be predicted via geometry and can be written as a function of probe radius, *R*, and cos(*θ*) as shown in **Figure 5.12**.

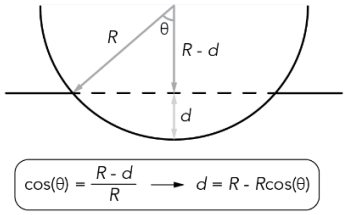

Figure 5.12 Schematic of probe with radius of curvature, *R*, indenting a sample with indentation depth, *d*.

The small angle approximation for the trigonometric function cos is as follows:

$$\boldsymbol{\cos(\theta) = 1 - \frac{\theta^2}{2}} \qquad \text{Eqn. 5.1}$$

Eqn. 5.1 can be substituted for cos(*θ*) so:

$$\boldsymbol{d = \frac{\theta^2}{2} R} \qquad \text{Eqn. 5.2}$$

To stay within 1% error for the small angle approximation, θ = 38°.

5.6.3 Microindentation Hertz Fits

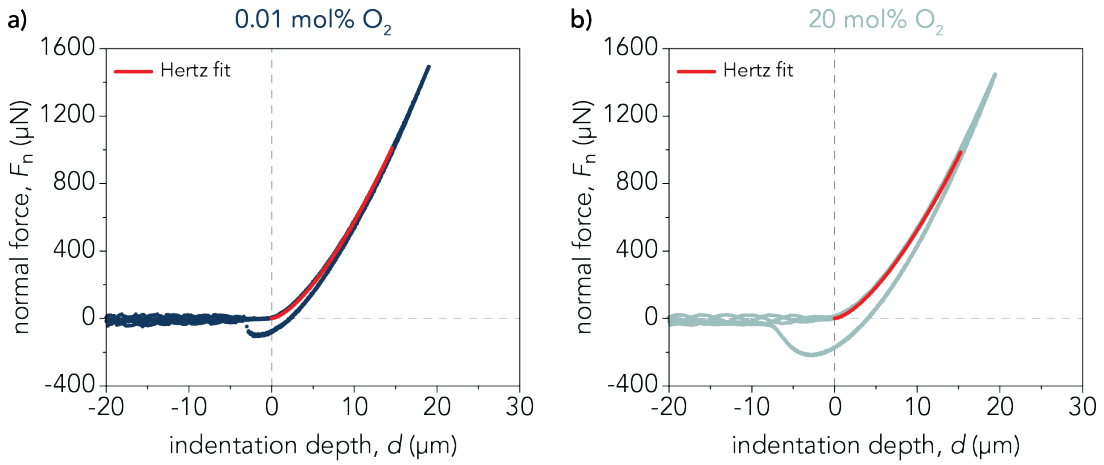

Figure 5.13 Representative microindentation approach curves with the Hertz contact mechanics model overlayed in red fitting from the point of contact to F_n = 1 mN for the gels cast at **(a)** 0.01 mol% O_2 (dark blue) and **(b)** 22 mol% O_2 (light blue).

5.6.4 Contact Area & Pressure Estimations

Table 5.4 Estimated contact radius, contact area, and maximum contact pressure based on Hertzian contact mechanics.

Hydrogel	Reduced Elastic Modulus, E^* (kPa)	Contact Radius, a (μm)	Contact Area, A (mm²)	Maximum Contact Pressure, P (kPa)
0.01 mol% O_2	**242 ± 11** (3 gels, n = 54)	**213 ± 3** (3 gels, n = 54)	**0.142 ± 0.004** (3 gels, n = 54)	**11 ± 0.3** (3 gels, n = 54)
20 mol% O_2	**203 ± 38** (3 gels, n = 54)	**226 ± 3** (3 gels, n = 54)	**0.161 ± 0.028** (3 gels, n = 54)	**9 ± 1** (3 gels, n = 54)

5.6.5 Literature Comparison

Table 5.5 Comparison of the elastic modulus, friction coefficient, and estimations of the surface gel layer thickness of polyacrylamide hydrogels cast with different monomer (acrylamide, AAm) and crosslinker (*N,N'*-methylenebisacrylamide, MBAm) concentrations and polymerization conditions. The listed friction coefficient values were determined by digitizing the data from literature at the listed testing parameters (sliding speed, v, and estimated contact pressure, P).[108,112,150,181,196,215,216,234,236,238–240] Unless otherwise stated, the tribological testing parameters are as follows: v = 0.5 mm/s and $P \approx$ 6-11 kPa. Gemini indicates a self-mated gel-on-gel configuration during tribological experiments (e.g., the probe material was composed of the same hydrogel material). *Testing parameters are as follows: v = 100 μm/s and $P \approx$ 1 kPa ** Poisson's ratio of 0.5 was used to estimate the elastic modulus for our data (17.5 wt.% polyacrylamide hydrogels).

concentrations (wt%)		mold material (O_2 mol)	elastic modulus (E) (kPa)			friction coefficient (μ)	surface gel layer		Ref.
AAm	MBAm		micro-rheology	AFM	micro tribometer		thickness (μm)	characterization technique	
2.25		**glass** (20%)	0.12						112
2.5		**glass** (20%)	0.16						
2.75		**glass** (20%)	0.21						
5	0.2	**PS** (20%)			7.3		21	contact mechanics	108
7.5	0.03				2.4		44	contact mechanics	
7.5	0.3				34		17	contact mechanics	
7.5	0.5				40		13	contact mechanics	
15	0.6				170		13	contact mechanics	
7.5	0.3	**PS** (20%)			31-33	**Steel***: $\mu = 0.026$ **Gemini***: $\mu \approx 0.01$	13-29	microindentations	238
7.5	0.3	**glass** (<0.01%)		11	29	**Gemini:** $\mu \approx 0.05$	crosslinked surface structure expected		234
		PDMS (<0.01%)		≈ 1	27	**Gemini:** $\mu \approx 0.009$	50	microindentations, FTIR	
7.5	0.3	**glass** (20%)		≈ 9		**Gemini**: $\mu \approx 0.09$	crosslinked surface structure expected		215
		PS (20%)		≈ 0.4		**Gemini**: $\mu \approx 0.04$	"brushy" surface structure expected		
		PE (20%)		≈ 0.7		**Gemini**: $\mu \approx 0.04$	"brushy" surface structure expected		
		PTFE (20%)		≈ 0.4		**Gemini**: $\mu \approx 0.02$	"brushy" surface structure expected		
7.5	0.39	**PS** (20%)		1.5	≈ 20 - 30	**Steel probe**: $\mu \approx 0.02$	"brushy" surface not characterized but observed		239
9.6	0.4	**glass** (20%)		30		**Gemini**: $\mu \approx 0.12$	crosslinked surface structure expected		216
		PS (20%)		0.3		**Gemini**: $\mu \approx 0.008$	10-20	nanoindentations	
9.6	0.4	**PE** (0%)		21		**Gemini**: $\mu \approx 0.12$	crosslinked surface structure expected		236
		PE (0.2%)		7		**Gemini**: $\mu \approx 0.07$	surface layer getting softer		
		PE (0.4%)		3		**Gemini**: $\mu \approx 0.02$	surface layer getting softer		
		PE (1%)		< 1		**Gemini**: $\mu \approx 0.004$	> 5	nanoindentations	
		PE (7.2%)		< 1		**Gemini**: $\mu \approx 0.002$	surface layer getting softer		
		PE (22%)		< 1		**Gemini**: $\mu \approx 0.006$	> 15	nanoindentations	

concentrations (wt%)		mold material (O_2 mol)	elastic modulus (E) (kPa)			friction coefficient (μ)	surface gel layer		Ref.
AAm	MBAm		micro-rheology	AFM	micro tribometer		thickness (μm)	characterization technique	
10	0.4	**glass** (20%)		29		**Gemini**: μ ≈ 0.05	crosslinked surface structure expected		181
		PS (20%)		< 0.1		**Gemini**: μ ≈ 0.02	10-20	nanoindentations	
10	0.4	**PS** (20%)		0.03			12	poroelastic contact mechanics model	240
3.75	0.15	**PS** (20%)				**Gemini**: μ ≈ 0.005			150
7.5	0.3					**Gemini**: μ ≈ 0.009			
10	0.4					**Gemini**: μ ≈ 0.01			
12.5	0.5					**Gemini**: μ ≈ 0.02			
17.5	0.7					**Gemini**: μ ≈ 0.037			
17.5	0.7	**free** (0.01%)		193**	182**	**Glass:** μ ≈ 0.02	11	reaction-kinetics model	196
		free (20%)		0.8**	152**	**Glass**: μ ≈ 0.002	51	reaction-kinetics model	

5.6.6 Atomic Force Microscopy

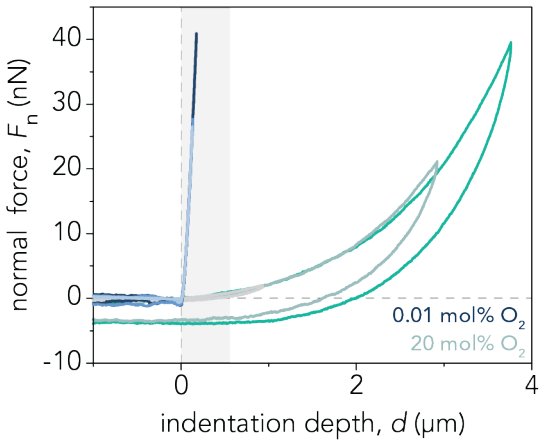

Figure 5.14 Full nanoindentation curves for the 17.5 wt.% polyacrylamide hydrogels at 0.01% O_2 (dark blue) and 20% O_2 (light blue) for varying applied normal forces (F_n = 2, 20, 25, 30, 40 nN) at an indentation velocity of 2 μm/s. The region of analysis (the first 0.55 μm) is indicated by the gray shaded box.

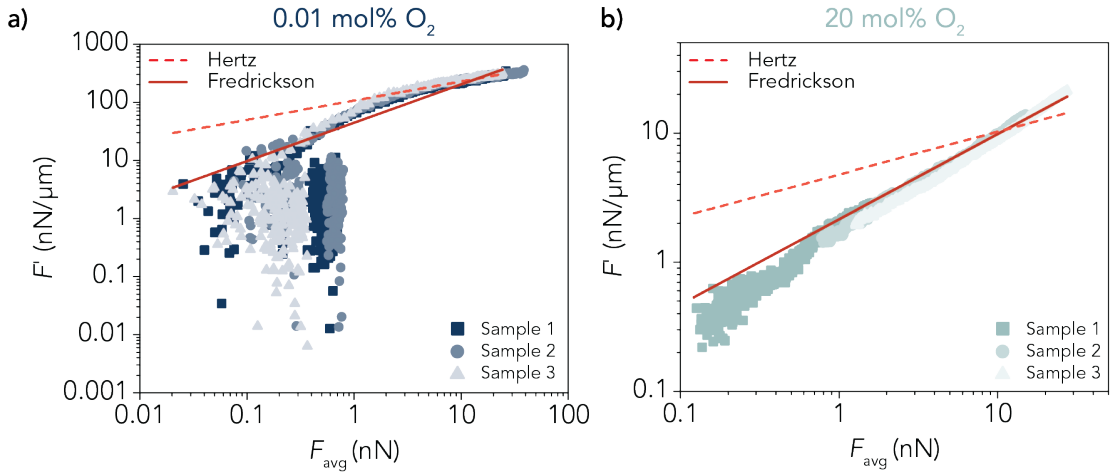

Figure 5.15 Representative log-log plots of the derivative (dF_n/dd) of the nanoindentation approach curves as a function of force following the methods outlined by Garcia *et al.*[247] The dashed red lines represent the Hertzian contact model while the solid red lines represent the Fredrickson high-penetration brush model.[108,248,249] **(a)** At 0.01 mol% O_2, the Hertz contact model fits the data better. **(b)** At 20 mol% O_2, the Fredrickson high-penetration brush contact model fits the data better.

5.7 Appendix B: Reaction-Kinetics Model

5.7.1 Model Development

Since the entire set of reaction mechanisms associated with polyacrylamide polymerization is known (**Schematic 5.1**), a reaction-diffusion model that accounts for the precise geometry and gel component concentration used herein (see **Section 5.2**) can be generated. Using reported values for reaction constants, this model is quantitative, without any adjustable parameters. Several analytical models have been put forth to understand the effect of oxygen inhibition in photopolymerizations of various acrylate monomers in thin films[219,229] or microfluidic geometries[221] and in other chemistries.[231] Despite the ubiquity of acrylamide polymerization in applications as commonplace as gel

electrophoresis, no similar models have been developed for the acrylamide chemistry. Additionally, prior modeling efforts have not investigated the free surface of the gel with oxygen inhibition in any chemistry or geometry.

Schematic 5.1 The reaction mechanism of a redox-initiated free-radical polymerizing system. In the present case, APS and TEMED are the initiator and catalyst, respectively. The rate constant, *k*, for each step is denoted with a subscript. *M* represents a reactive unit, *i.e.,* acrylamide or *N,N'*-methylenebisacrylamide monomers or crosslinkers, respectively, *M** is the oligomer-bound radical, *O** is the oxygen radical, and *I** is any possible initiation species. The dominant termination mechanism in polyacrylamide is not biomolecular termination but rather disproportionation,[250,251] in which one chain-terminal radical reacts with the hydrogen (*H*) neighboring a second chain-terminal radical to form a hydrogen-terminal chain and a new double bond (*M'*).

Initiation	$APS + TEMED \xrightarrow{k_i} 2\ I^*$	radical formation
Propagation		
	(i) $I^* + M \xrightarrow{k_f} IM^*$	polymer chain formation
	(ii) $IM_n^* + M \xrightarrow{k_p} IM_{n+1}^*$	polymer chain growth
Inhibition	$IM_n^* + O_2 \xrightarrow{k_s} IM_nOO^*$	peroxidation side-reaction
Termination	$IM_n^* + IM_{m+1}^* \xrightarrow{k_t} IM_nH + IM_mM'$	disproportionation

Our model builds on extensive prior work on free-radical polymerization with peroxidation side-reactions.[219,221,229,231] The polymerization is initiated by consumption of APS and TEMED, which produce radicals at a rate of initiation (r_i), given by:

$$r_i = 2k_i[APS][TEMED] \qquad \textbf{Eqn. 5.3}$$

In the second step, the primary radicals react with an unconverted double-bond (*M*), either on acrylamide or *N,N'*-methylenebisacrylamide monomers, and continue to propagate in chain growth at the rate r_p:

$$r_p = k_p[R^*][M] \qquad \text{Eqn. 5.4}$$

In this expression, *R** represents all reactive radicals, which are *I**, *IM**, and IM_n***; in other words, we assume that all radicals are equally reactive ($k_f \approx k_p$), as well as equivalent reactivity between AAm and MBAm monomers when reacting with growing polymer chains. Note that the IM_nOO^* radicals that form via the peroxidation side reaction are stable and do not further participate in the reaction after formation. Reactive radicals can also be consumed by various classical termination mechanisms. Here, we consider only termination by disproportionation, whose prevalence in polyacrylamide polymerization greatly surpasses all other termination modes, including conventional biomolecular termination.[250,251] In sum, the total rate of radical termination (r_t) from inhibition and termination is given by:

$$r_t = k_t[R^*]^2 + k_s[R^*][O_2] \qquad \text{Eqn. 5.5}$$

In the real system, MBAm is more reactive than AAm, causing early formation of MBAm-rich sequences that act as more compact subdomains in the gel as the composition of residual monomer drifts to further favor AAm as the reaction proceeds.[59] This and other causes of molecular-level inhomogeneity such as statistical chemical heterogeneity are excluded from the present model for simplicity. While the assumption of acrylamide and bisacrylamide reactive equivalence is limited, the local structure of the monomers is similar: the

bisacrylamide simply has two separate reactive groups that react independently with either oxygen or other moieties; each end reacts in a first order manner with the same mechanism as the acrylamide monomer.[252] **Figure 5.16** and associated discussion in **Section 5.7.2** provide in-depth details of the diversity of structures formed during polymerization. While kinetic constants for oxygen reactivity with bisacrylamide and its substituents have not been measured, the polymerization of both AAm and MBAm will be inhibited more at higher local oxygen concentration in the real system. This is the main effect our model aims to probe, and its microscale impacts are captured without differentiating AAm and MBAm reactivity individually.

To develop the model equations, we seek an expression for the monomer conversion, X, at various depths z in the polymerizing medium and as a function of reaction time t, $X(t) = \frac{1-[\mathrm{M}](t)}{[\mathrm{M}](t=0)}$. Monomer conversion reveals the progress of the gelation reaction at every depth from the surface (z = 0) to the bottom of the casting mold ($z = H$). The rate of monomer consumption, $-\frac{d[\mathrm{M}]}{dt}$, is equivalent to r_p. Therefore, to extract $X(t,z)$, we require an expression for [R^*] in terms of known variables – reaction constants and initial concentrations of $[\mathrm{APS}]_{\mathrm{init}}$, $[\mathrm{TEMED}]_{\mathrm{init}}$, and $[\mathrm{O_2}]_{\mathrm{init}}$ (see **Table 5.6** and **Table 5.7**) – as well as variables accessible by differential equations: the time-dependent concentrations of APS, TEMED, and O_2. We assume the bottom and sides of the gel casting mold are

impermeable to oxygen so that net diffusion of oxygen is symmetric in *x*-*y*. Thus, reactivity is a function of depth only, and the model is one-dimensional. In addition to the rate laws above, achieving the expression for [*R**] requires a species balance describing the reaction-diffusion of oxygen in the z-direction into the polymerizing medium:

$$\frac{\delta[\mathrm{O_2}]}{\delta t} = D_{\mathrm{O_2}} \frac{d^2[\mathrm{O_2}]}{dz^2} - k_{\mathrm{s}}[\mathrm{R}*][\mathrm{O_2}] \qquad \text{Eqn. 5.6}$$

The dissolved oxygen content at the upper surface of the reacting medium is assumed to remain in equilibrium with the surrounding atmosphere throughout the polymerization for each O_2 concentration (0.01 mol% and 20 mol% O_2). We estimate this constant dissolved oxygen content at the upper surface using Henry's Law constant H^{cc} = 0.032 at standard temperature and pressure for oxygen dissolution into water.

The mathematical steps and nondimensionalization required to derive $X(\tau, \eta)$, the final expression for monomer conversion as a function of dimensionless depth, $\eta = \frac{z}{H}$, and time, $\tau = \frac{D_{\mathrm{O_2}}}{H^2} t$, are provided in **Section 5.7.4**. The solution assumes a net zero production rate of radical species, *i.e.*, that *R** are consumed as soon as they are generated, and that the temperature remains constant so that the rate constants and oxygen diffusivity, $D_{\mathrm{O_2}}$, are constant throughout the reacting medium. $X(\tau, \eta)$ is given by:

$$\frac{d(1-X)}{d\tau} = -Da_{\mathrm{M}}(1-X)\left[-\theta + (\theta^2 + \alpha AT)^{1/2}\right] \qquad \text{Eqn. 5.7}$$

where $\theta(\tau,\eta) = \frac{[\mathrm{O_2}]}{[\mathrm{O_2}]_{init}}$ is the dimensionless oxygen concentration, *A* and *T* are the dimensionless APS and TEMED concentrations, $\alpha = \frac{8k_{\mathrm{i}}k_{\mathrm{t}}\,[\mathrm{APS}]_{\mathrm{init}}[\mathrm{TEMED}]_{\mathrm{init}}}{(k_{\mathrm{s}}[\mathrm{O_2}]_{\mathrm{init}})^2}$ is a dimensionless group representing the rate of initiation of the polymerization relative to the rate of oxygen side-reactions, and $Da_{\mathrm{M}} = \frac{k_{\mathrm{p}}k_{\mathrm{s}}H^2[\mathrm{O_2}]_{\mathrm{init}}}{2k_{\mathrm{t}}D_{\mathrm{O_2}}}$ is the monomer Damköhler number that relates the reaction and diffusive transport rates of the monomer. Evaluating this expression requires solutions for θ, *A*, and *T* as functions of τ and η. APS and TEMED concentrations are solved using the coupled differential equations:

$$\frac{dA}{d\tau} = -\frac{k_{\mathrm{i}}H^2[\mathrm{TEMED}]_{\mathrm{init}}}{D_{\mathrm{O_2}}}AT \qquad \text{Eqn. 5.8}$$

$$\frac{dT}{d\tau} = -\frac{k_{\mathrm{i}}H^2[\mathrm{APS}]_{\mathrm{init}}}{D_{\mathrm{O_2}}}AT \qquad \text{Eqn. 5.9}$$

$\theta(\tau,\eta)$ is obtained by the nondimensionalized reaction-diffusion equation for O_2:

$$\frac{\delta\theta}{\delta\tau} = \frac{\delta^2\theta}{\delta\eta^2} - Da_{\mathrm{O_2}}\theta[-\theta + [\theta^2 + \alpha AT]^{1/2}] \qquad \text{Eqn. 5.10}$$

where $Da_{\mathrm{O_2}} = \frac{k_{\mathrm{s}}^2H^2[\mathrm{O_2}]_{\mathrm{init}}}{2k_{\mathrm{t}}D_{\mathrm{O_2}}}$ is the oxygen Damköhler number.

5.7.2 Propagation & Inhibition Mechanisms for AAm and MBAm

The vast structural dispersity arising from polyacrylamide propagation mechanisms, including MBAm crosslinker incorporation and reaction pathways, is explored in this section and summarized in **Figure 5.16**. All individual radicals (highlighted in teal) are assumed to have equivalent reactivity in all of these reactions in the model to avoid accounting for the vast dispersity of local polyacrylamide chain radical structures. These radicals would all have an equivalent – but different – reactivity with oxygen, as denoted by the difference in k_p and k_s in **Table 5.6**. While **Figure 5.16** shows a number of possible reaction pathways after incorporation of a crosslinker into a growing oligomer, note that MBAm could also be the first monomer incorporated, and that the monomers can be incorporated in any sequence.

One of these reaction pathways is intramolecular cyclization, wherein the other end of an MBAm monomer already incorporated into the polymer polymerizes into the chain. While a ring formed between radicals and crosslinks within the same MBAm crosslinker was shown here, note that this process can occur for much larger cycles. Cycles are more likely to form at lower monomer concentration and are considered defects because they render the crosslinker elastically ineffective.

When the other end of an incorporated MBAm monomer does not experience cyclization, it is likely that growth of a second polyacrylamide chain

will be initiated at that double-bond, establishing MBAm as an elastically effective crosslink. Note that the depiction in Figure 5.16 shows the example of this initiation prior to the continued growth of the existing chain, but due to the short radical lifetimes it is likely that this initiation event occurs at a later time. Aside from cyclization, the incorporation of each end of MBAm into the gel matrix is decoupled.

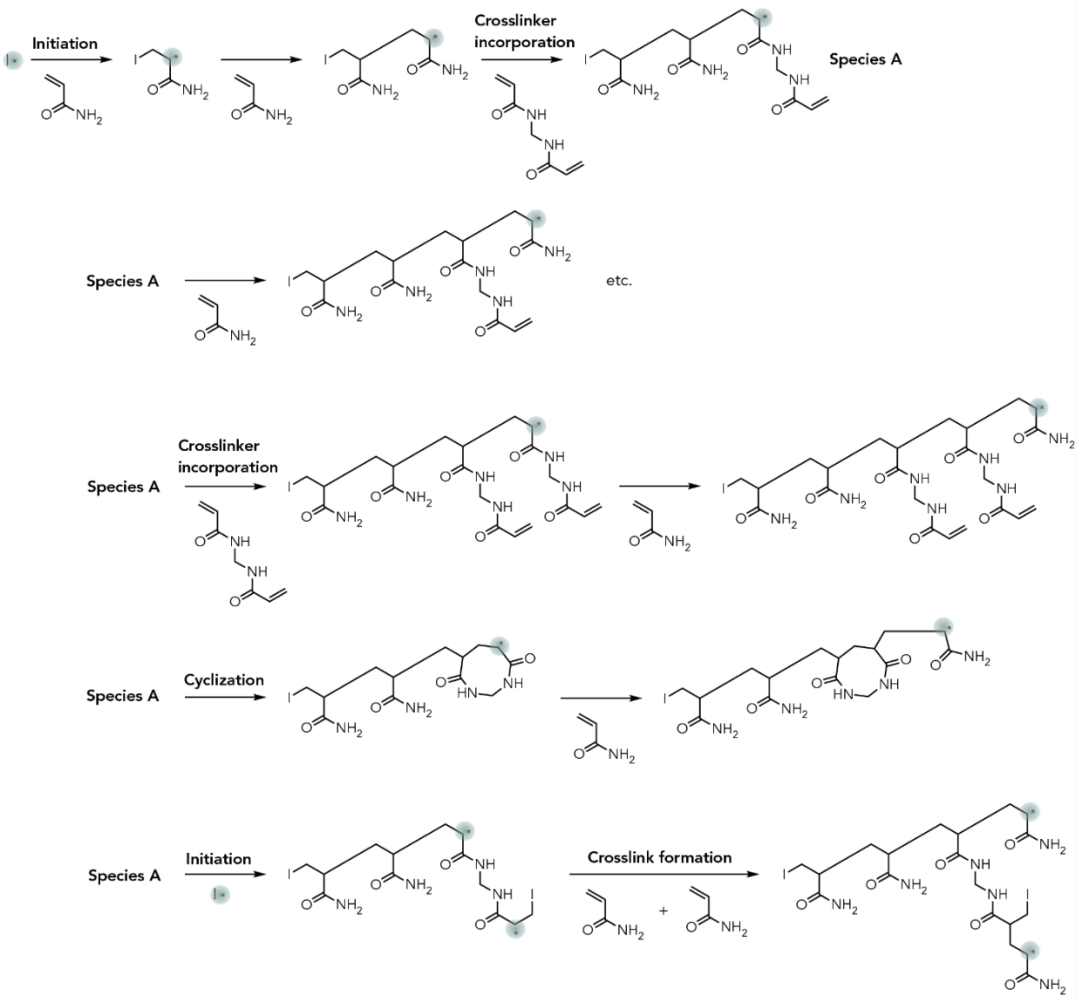

Figure 5.16 Structures formed during initiation and propagation of polyacrylamide; radicals are highlighted in teal for easy visualization. On initiation, the chain grows with AAm until incorporation of a crosslinker, denoted by example oligomer Species A. Once incorporated into a chain, the resulting radical structure can either react with AAm or MBAm monomer or react

with the double bond at the other end of the MBAm crosslinker to form a cyclic defect. Additionally, the other double bond may come in contact with another radical initiator instead, resulting in polyacrylamide chains continuing to grow simultaneously and independently at both ends of the crosslinker, and thus the establishment of a crosslink.

5.7.3 Reaction-Diffusion Constants & Concentrations

Table 5.6 Kinetic constants from literature and experimental reaction conditions used in our model.

Parameter	Value Used	Units	Ref.
Initiation rate constant, k_i	2.5×10^{-5}	$m^3/(mol\ s)$	253
Propagation rate constant, k_p	1	$m^3/(mol\ s)$	227
Termination rate constant, k_t	3×10^3	$m^3/(mol\ s)$	227
Inhibition rate constant, k_s	10^5	$m^3/(mol\ s)$	253
Diffusivity of O_2 in water, D_{O2}	8×10^{-10}	m^2/s	254
Depth of the reacting medium, H	0.0052	m	Calculated with 5 mL solution and 35 mm diameter mold
$[O_2]_{init,\ 0.01\%}$	0.00013088	mol/m^3	Calculated with 100 ppm O_2 at standard temperature and pressure (STP) is 0.00409 mol/m^3 (air is 40.9 mol/m^3 at STP); and Henry's constant as $H^{cc} = 0.032$.
$[O_2]_{init,\ 20\%}$	0.26176	mol/m^3	Calculated with 200,000 ppm O_2 in air is 8.18 mol/m^3; and $H^{cc} = 0.032$.
$[TEMED]_{init}$	12.90	mol/m^3	Calculated with 17.5 wt.% gel protocol
$[APS]_{init}$	6.57	mol/m^3	Calculated with 17.5 wt.% gel protocol
$[M]_{init}$	2552	mol/m^3	$[M]_{init} = [AAm]_{init} + 2[MBAm]_{init}$ Calculated with 17.5 wt.% gel protocol

Using the values listed in **Table 5.6**, the following constants were calculated with **Eqn. 5.11 - Eqn. 5.15**:

$$APS_{\text{const}} = \frac{k_{\text{i}} H^2 [\text{TEMED}]_{\text{init}}}{D_{\text{O}_2}} \qquad \text{Eqn. 5.11}$$

$$TEMED_{\text{const}} = \frac{[\text{APS}]_{\text{init}}}{[\text{TEMED}]_{\text{init}}} \qquad \text{Eqn. 5.12}$$

$$Da_{\text{O2}} = \frac{k_{\text{s}}^2 H^2 [\text{O}_2]_{\text{init}}}{2 k_{\text{t}} D_{\text{O}_2}} \qquad \text{Eqn. 5.13}$$

$$Da_{\text{M}} = \frac{k_{\text{p}} k_{\text{s}} H^2 [\text{O}_2]_{\text{init}}}{2 k_{\text{t}} D_{\text{O}_2}} \qquad \text{Eqn. 5.14}$$

$$\alpha = \frac{8 k_{\text{i}} k_{\text{t}} [\text{APS}]_{\text{init}} [\text{TEMED}]_{\text{init}}}{(k_{\text{s}} [\text{O}_2]_{\text{init}})^2} \qquad \text{Eqn. 5.15}$$

Table 5.7 Constants calculated for the 0.01 mol% O_2 and 20 mol% O_2 polyacrylamide hydrogels.

Constants	0.01 mol% O_2	20 mol% O_2
APS_{const}	10.9005	10.9005
$TEMED_{\text{const}}$	0.5093	0.5093
Da_{O2}	7.3729 x 10^{6}	1.4746 x 10^{10}
Da_{M}	73.729	147460
α	0.2967	7.4216 x 10^{-8}

We note that in simulation, the dimensionless time τ is significantly larger than the equivalent numerical value of real time t. When t = 1 sec, this corresponds

to dimensionless time $\tau = \frac{t\, D_{O_2}}{H^2} = 2.96 \times 10^{-5}$. Therefore, t = 15 min corresponds to τ = 0.0266272.

5.7.4 Reaction-Diffusion Model Derivation

Consumption of APS and TEMED follow $\frac{dC}{dt} = -k_i[\mathrm{APS}][\mathrm{TEMED}]$, where C represents [APS] or [TEMED]. Introducing dimensionless APS concentration as $A = \frac{[\mathrm{APS}]}{[\mathrm{APS}]_{init}}$, dimensionless TEMED concentration as $T = \frac{[\mathrm{TEMED}]}{[\mathrm{TEMED}]_{init}}$, and dimensionless time as $\tau = \frac{t\, D_{O_2}}{H^2}$, we obtain the following dimensionless equation for APS consumption:

$$\frac{dA}{d\tau}\frac{D_{O_2}[\mathrm{APS}]_{\mathrm{init}}}{H^2} = -k_i AT[\mathrm{APS}]_{\mathrm{init}}[\mathrm{TEMED}]_{\mathrm{init}} \rightarrow$$

$$\frac{dA}{d\tau} = -\frac{k_i H^2[\mathrm{TEMED}]_{\mathrm{init}}}{D_{O_2}} AT \qquad \text{Eqn. 5.16}$$

Similarly, the dimensionless consumption of TEMED follows:

$$\frac{dT}{d\tau}\frac{D_{O_2}[\mathrm{TEMED}]_{\mathrm{init}}}{H^2} = -k_i AT[\mathrm{APS}]_{\mathrm{init}}[\mathrm{TEMED}]_{\mathrm{init}} \rightarrow$$

$$\frac{dT}{d\tau} = -\frac{k_i H^2[\mathrm{APS}]_{\mathrm{init}}}{D_{O_2}} AT \qquad \text{Eqn. 5.17}$$

Next, nondimensionalize the reaction-diffusion equation for oxygen. Here, we introduce $\theta = \frac{[O_2]}{[O_2]_{init}}$ as dimensionless [O_2] and $\eta = \frac{z}{H}$ as dimensionless depth from the surface of the reacting medium:

$$\frac{\delta[\mathrm{O_2}]}{\delta t} = D_{\mathrm{O_2}}\frac{\delta^2[\mathrm{O_2}]}{\delta z^2} - k_\mathrm{s}[\mathrm{R}*][\mathrm{O_2}] \rightarrow$$

$$\frac{D_{\mathrm{o_2}}[\mathrm{O_2}]_\mathrm{init}}{H^2}\frac{\delta\theta}{\delta\tau} = \frac{D_{\mathrm{o_2}}[\mathrm{O_2}]_\mathrm{init}}{H^2}\frac{\delta^2\theta}{\delta\eta^2} - k_\mathrm{s}[\mathrm{R}*][\mathrm{O_2}]_\mathrm{init}\theta \qquad \text{Eqn. 5.18}$$

$$\frac{\delta\theta}{\delta\tau} = \frac{\delta^2\theta}{\delta\eta^2} - \frac{k_\mathrm{s}[\mathrm{R}*]H^2}{D_{\mathrm{O_2}}}\theta \qquad \text{Eqn. 5.19}$$

The concentration of reactive radicals [R*] is given by:

$$[\mathrm{R}*] = \frac{-k_\mathrm{s}[\mathrm{O_2}] + ((k_\mathrm{s}[\mathrm{O_2}])^2 + 8k_\mathrm{i}k_\mathrm{t}[\mathrm{APS}][\mathrm{TEMED}])^{1/2}}{2k_\mathrm{t}} \qquad \text{Eqn. 5.20}$$

or in terms of dimensionless variables,

$$[\mathrm{R}*] = \frac{-k_\mathrm{s}[\mathrm{O_2}]_\mathrm{init}\theta + ((k_\mathrm{s}[\mathrm{O_2}]_\mathrm{init})^2\theta^2 + 8k_\mathrm{i}k_\mathrm{t}[\mathrm{APS}]_\mathrm{init}[\mathrm{TEMED}]_\mathrm{init}AT)^{1/2}}{2k_\mathrm{t}} \qquad \text{Eqn. 5.21}$$

Plug this expression into the partial differential equation for θ and simplify to obtain:

$$\frac{\delta\theta}{\delta\tau} = \frac{\delta^2\theta}{\delta\eta^2} - \frac{{k_\mathrm{s}}^2H^2[\mathrm{O_2}]_\mathrm{init}}{2k_\mathrm{t}D_{\mathrm{O_2}}}\theta(-\theta + (\theta^2 + \frac{8k_\mathrm{i}k_\mathrm{t}[\mathrm{APS}]_\mathrm{init}[\mathrm{TEMED}]_\mathrm{init}}{(k_\mathrm{s}[\mathrm{O_2}]_\mathrm{init})^2}AT)^{1/2}) \qquad \text{Eqn. 5.22}$$

By defining the constants $Da_{\mathrm{O_2}}$ and α (see **Section 5.7.1**), the final expression for oxygen diffusion is:

$$\frac{\delta\theta}{\delta\tau} = \frac{\delta^2\theta}{\delta\eta^2} - Da_{\mathrm{O_2}}\theta(-\theta + [\theta^2 + \alpha AT]^{1/2}) \qquad \text{Eqn. 5.23}$$

Next, the reaction-diffusion equation for monomer follows $\frac{d[\mathrm{M}]}{dt} = -k_\mathrm{p}[\mathrm{R}*][\mathrm{M}]$. This expression can be nondimensionalized to find $\xi = \frac{[\mathrm{M}]}{[M]_{init}}$, the dimensionless monomer concentration at a given depth in the reaction medium. Note that the conversion of monomer, X, satisfies $X = 1 - \xi$.

$$\frac{D_{\mathrm{O}_2}[\mathrm{M}]_\mathrm{init}}{H^2}\frac{d\xi}{d\tau} = -k_\mathrm{p}[\mathrm{R}*][\mathrm{M}]_\mathrm{init}\xi \;\rightarrow\; \frac{d\xi}{d\tau} = \frac{-k_\mathrm{p}H^2}{D_{\mathrm{O}_2}}[\mathrm{R}*]\xi \qquad \text{Eqn. 5.24}$$

Plug in [R*] to obtain:

$$\frac{d\xi}{d\tau} = \frac{-k_\mathrm{p}k_\mathrm{s}H^2[\mathrm{O}_2]_\mathrm{init}}{2k_\mathrm{t}D_{\mathrm{O}_2}}\xi(-\theta + (\theta^2 + 8\frac{k_\mathrm{i}k_\mathrm{t}}{{k_\mathrm{s}}^2}\frac{[\mathrm{APS}]_\mathrm{init}[\mathrm{TEMED}]_\mathrm{init}}{{[\mathrm{O}_2]_\mathrm{init}}^2}AT)^{1/2}) \qquad \text{Eqn. 5.25}$$

Using the same definition of α and defining a new Damköhler number,$Da_\mathrm{M} = \frac{k_\mathrm{p}k_\mathrm{s}H^2[\mathrm{O}_2]_\mathrm{init}}{2k_\mathrm{t}D_{\mathrm{O}_2}}$, the final differential equation for monomer conversion is obtained:

$$\frac{d\xi}{d\tau} = -Da_\mathrm{M}\xi\left(-\theta + (\theta^2 + \alpha AT)^{1/2}\right) \qquad \text{Eqn. 5.26}$$

5.7.5 Extracting Surface Layer Thickness & Gradient

A series of studies by Baselga *et al*. in the late 1980s sought to determine the process of network formation for AAm/MBAm gelation with APS and TEMED initiator under various conditions.[61] One such study determined that a sample with initial $[\mathrm{AAm}]_{init}$ = 1.28 mol/L and $[\mathrm{MBAm}]_{init}$ = 0.074 mol/L reached the gel

point at 6% monomer conversion based on digitization of graphical data provided in that paper.[61] In a separate study, Baselga *et al*. found that doubling the concentration of monomer and crosslinker, while halving the weight percent of crosslinker in the initial feedstock—similar to our experimental system with $[AAm]_{init}$ = 2.46 mol/L and $[MBAm]_{init}$ = 0.05 mol/L—approximately halved the conversion (by weight) at the gel point.[58] As a safe estimate, we assumed gelation occurred at 5% monomer conversion (rather than 3%) in this work. Thus, according to our model, the entirety of this surface gel layer reached gelation.

The first point where the monomer conversion exceeds 5% is taken to be the upper surface of the gel. To minimize error of fit while capturing surface shape, a depth of gel is chosen for fitting such that the surface gel layer represents about 10%. In other words, for the 0.01 mol% O_2 case, the top 100 μm of gel is fit to extract surface gel layer thickness and gradient, whereas the top 300 μm is fit for the 20 mol% O_2 case. Fitting is conducted on this cropped data at each time point using the MATLAB shape language modeling (SLM) engine. A degree 1 fit was conducted using 3 knots and free interior knots; *i.e.*, two line segments were fit to the data. The thickness of the surface gel layer was taken to be the depth corresponding to the intersection of these two line segments. The slope of the gradient layer was taken to be the slope of the line at the surface of the gel.

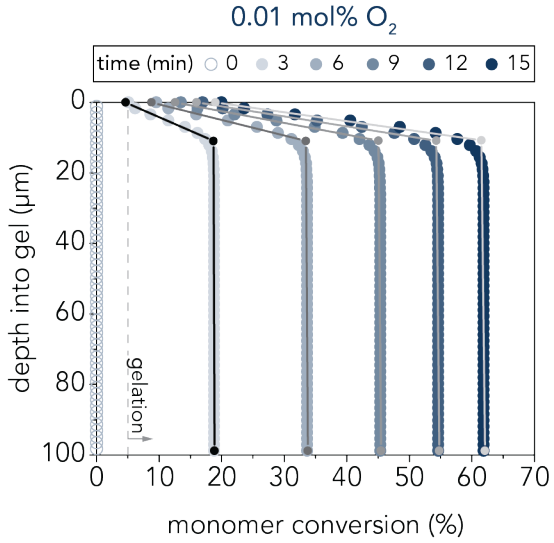

Figure 5.17 Fits of monomer conversion for the top 100 μm of gel for the hydrogels polymerized at 0.01 mol% O_2. The gray lines show the exact line segment fit of monomer conversion, with the intersection of the line segments denoting the transition from surface gel layer to the bulk gel. Fits are shown at various reaction times. SLM algorithm fits well at all time points.

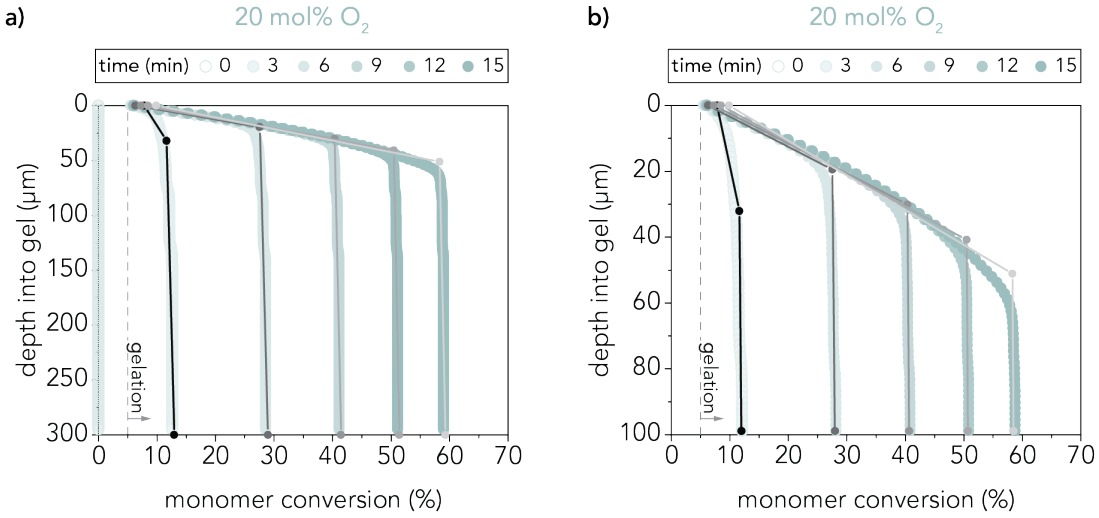

Figure 5.18 Fits of monomer conversion for the top **(a)** 300 μm and **(b)** 100 μm of gel for the hydrogels polymerized at 20 mol% O_2. The gray lines show the exact line segment fit of monomer conversion, with the intersection of the line segments denoting the transition from surface gel layer to the bulk gel. Fits are shown at various reaction times. The SLM algorithm fits well at all time points except 3 minutes, where the root mean square error (RMSE) value is above the cutoff; clearly the surface and bulk layers are not yet distinct at 3 minutes.

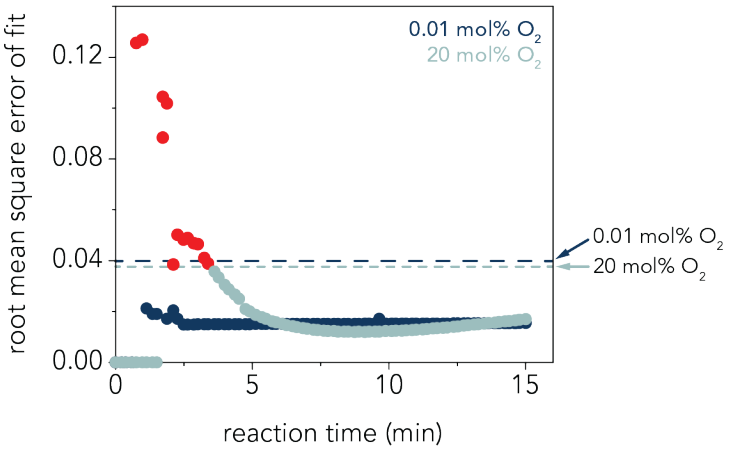

Figure 5.19 Root mean square error (RMSE) of the SLM fit for 0.01 mol% O_2 (dark blue) and 20 mol% O_2 (light blue). Horizontal lines indicate the RMSE cutoff value, one standard deviation above the average of the non-zero RMSE values at each O_2 concentration. Above the cutoff, the fits do not accurately reflect the shape of the surface layer, corresponding to an ill-defined distinction between the surface gel layer and bulk gel as the gel forms at early times. The red dots represent the reaction times in which the corresponding thickness and gradient of the surface gel layer were excluded from the main text.

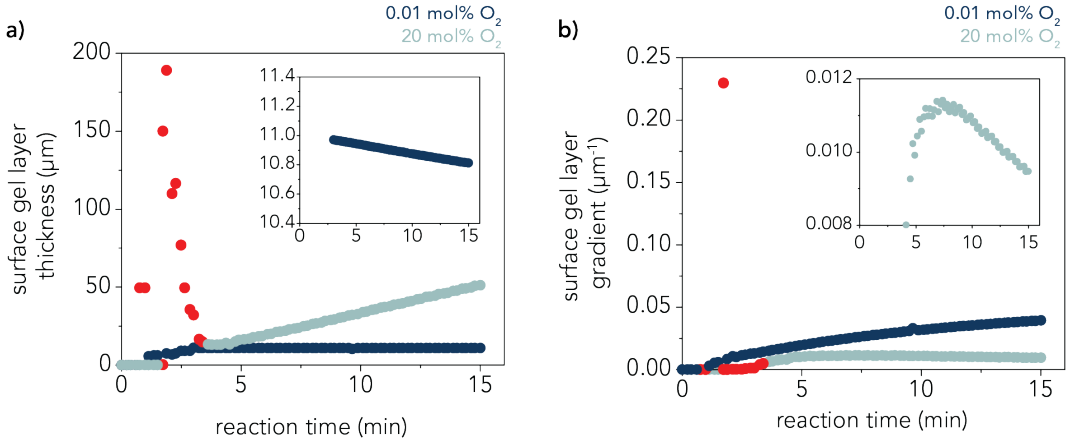

Figure 5.20 (a) Surface gel layer thickness and **(b)** surface gel layer thickness gradient as a function of reaction time with insets highlighting the decrease in surface gel layer thickness and gradient with increasing time. The red dots represent the reaction times in which the RMSE of the SLM fit was greater than the cutoff value and excluded from the main text.

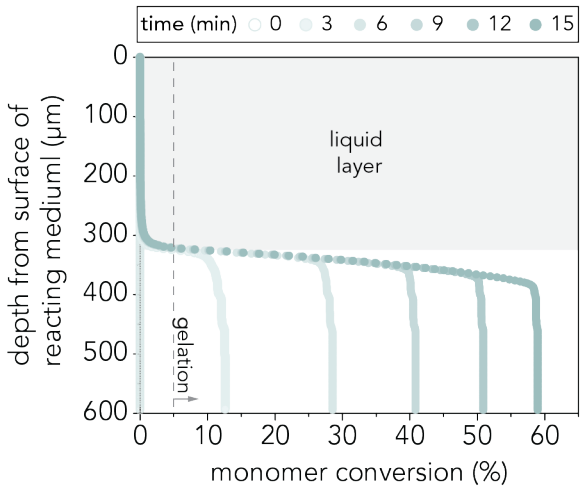

Figure 5.21 Unlike the 0.01 mol% O_2 case, in the 20 mol% O_2 polymerization shown here, oxygen inhibits the polymerization at the surface of the reaction so that even after 15 minutes, no significant monomer conversion or gelation occurs until about 300 μm into the reacting medium, resulting in a thinner gel.

5.7.6 Model Results for Varying Oxygen Concentration

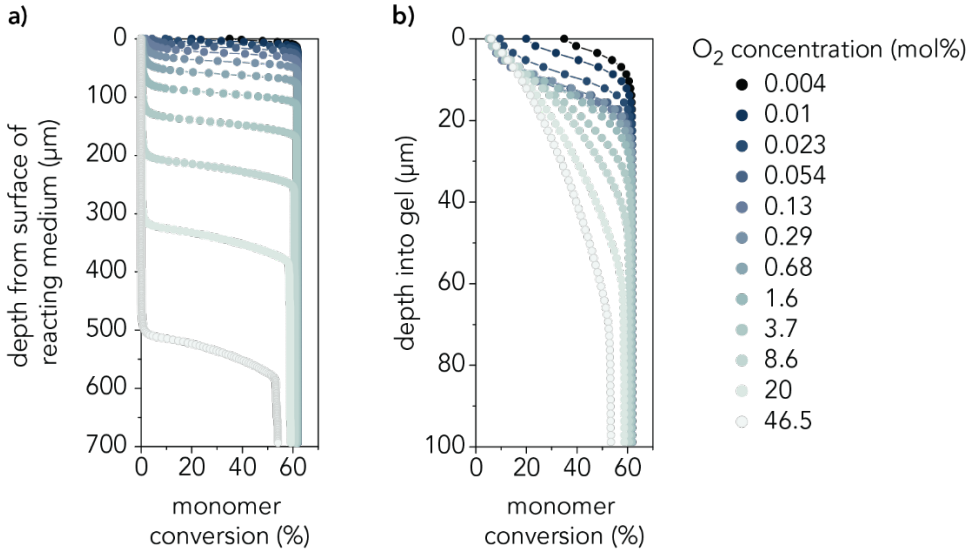

Figure 5.22 Monomer conversion fraction profiles after 15 minutes of polymerization at various oxygen concentrations (0.004 – 46.5 mol%), with all other parameters fixed (monomer, crosslinker, and initiator concentrations; reaction medium depth *H*; and kinetic constants). Profiles are shown **(a)** as a function of depth from the top surface of the reacting medium and **(b)** as a function of depth into the gel prior to swellings by removing any ungelled liquid layer (< 5% conversion) at the upper surface of the reacting medium.

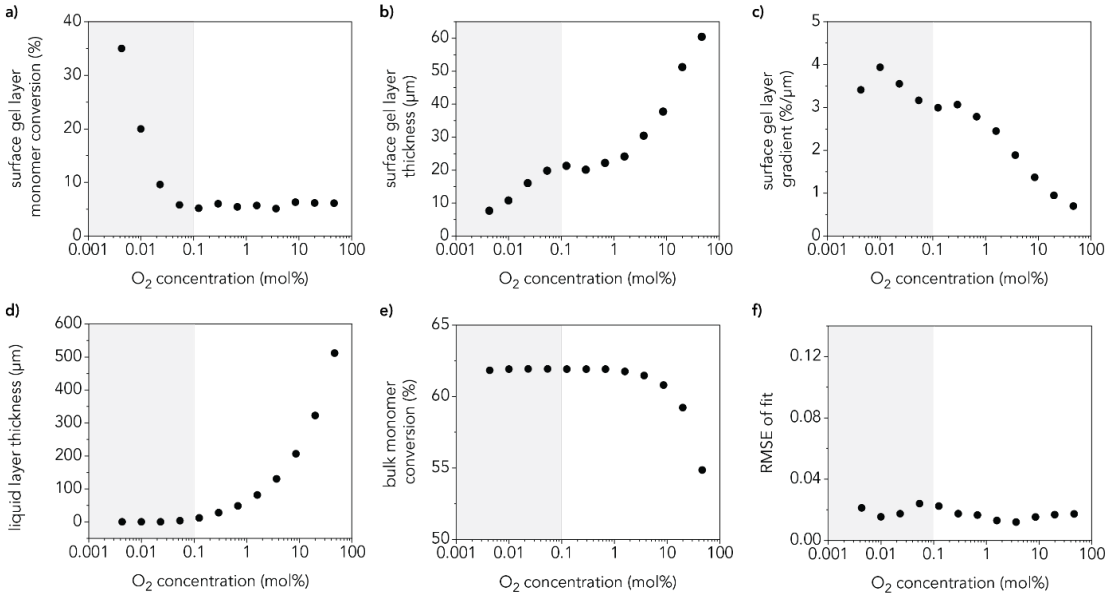

Figure 5.23 The following are plotted at varying oxygen concentrations corresponding to the various profiles plotted in **Figure 5.22**. **(a)** Conversion of monomer at the surface of the gel. **(b)** Thickness of the surface gel layer from SLM fit of the profiles. **(c)** Monomer conversion gradient in the surface gel layer, also extracted from the SLM fit of the profiles. **(d)** Thickness of the unpolymerized liquid layer at the upper surface of the reacting medium. **(e)** Monomer conversion in the gel bulk, as measured by the conversion deep into the gel, which is affected by oxygen diffusion only at early times during polymerization. **(f)** Root mean square error (RMSE) of fit corresponding to **(b)** and **(c)**. Note that the RMSE cutoff for the 0.01 mol% and 20 mol% O_2 data reported in the text is around 0.04, so all values reported here fit well.

6 CHAPTER 6: TUNABLE LUBRICITY THROUGH AMPHIPHILICITY

Amphiphilic polymers possess both hydrophobic and hydrophilic domains and are commonly used as drug delivery systems due to their ability to incorporate both nonpolar and polar moieties within the network.[255] They often have greater mechanical strength and adhesion than typical hydrophilic hydrogels due to their hydrophobic domains and also have the ability to phase-separate and form aggregates with specific architecture.[255,256] In the following chapter, the swelling and tribological behavior of amphiphilic poly(2-hydroxyethyl methacrylate) (pHEMA) will be explored. We propose that a solvent-induced transition of inter- and intra-gel associations occurs with the addition of ethanol, causing the polymer chains to orient themselves in a manner that promotes either their hydrophobic or hydrophilic domains to the surface. By controlling the polarity of the solvent, we were able to tune the friction coefficient and adhesion an order of magnitude from $\mu \approx 0.01$ to > 1 and $F_{adh} <$ 10 μN to 650 μN, respectively.

This chapter was reproduced in part with permission from: [69]

McGhee, E.O., Chau, A.L., Cavanaugh, M.C., Rosa, J.G., Davidson IV, C.L.G., Kim, J., Urueña, J.M., Sumerlin, B.S., Pitenis, A.A., and Sawyer, W.G., Amphiphilic gel lubrication and the solvophilic transition. *Biotribology,* **26**, 100170, 2021.

Table of Contents

6.1 Amphiphilicity in Biology

The lubrication mechanism of articular cartilage is the subject of much debate, but the current prevailing mechanism is a boundary lubrication model where confinement and fluid pressurization play an important role in the exhibited low friction. The synovial fluid surrounding cartilage has complex rheological behaviors[257] and its low viscosity at high shear rates may be responsible for the low shear stress, friction, and wear rate of the system.[186,258–260] Synovial fluid is composed of several macromolecules, including hyaluronic acid, lubricin, and phospholipids, which work together to maintain hydration and lubrication.[261] Many of these macromolecules are amphiphilic, and their amphiphilic nature allows them to interact synergistically in ways that may help promote lubrication.[262–264]

As discussed in Chapter 1, hydrogels are often used as synthetic mimics for biological systems such as articular cartilage. But tuning the solvent conditions to optimize lubrication for an amphiphilic gel has not yet been explored. To close this gap, we investigated poly(2-hydroxyethyl methacrylate) (pHEMA), a well-known amphiphilic gel, and swelled the gels in water/ethanol solutions with varying amounts of ethanol (Figure 6.1). The tribological properties of these gels were investigated in self-mated ("Gemini") configuration to mimic the typical sliding interfaces found in biology. Friction varied from low ($\mu \approx 0.01$) to high ($\mu > 1$) depending on ethanol concentration.

The lowest friction coefficient was achieved for the most swollen gels. It is postulated that ethanol is needed to passivate the hydrophobic domains within the pHEMA chain to reduce possible hydrophobic/hydrophobic interactions, thereby reducing friction.

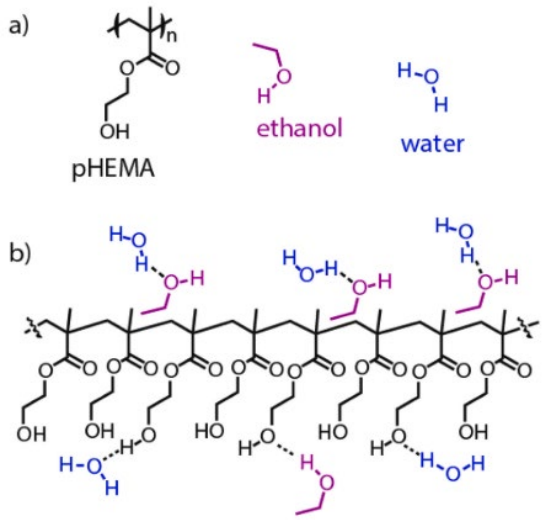

Figure 6.1 (a) Chemical structures of pHEMA, ethanol, and water. **(b)** Proposed intermolecular interactions between ethanol, water, and pHEMA network: (1) hydrogen bonding of pendent hydroxyl groups with water and ethanol, (2) hydrogen bonding between water and ethanol, and (3) hydrophobic interactions between ethanol and the pHEMA backbone.

6.2 Materials & Methods

6.2.1 Hydrogel Preparation

Stock solutions of *N,N'*-methylenebisacrylamide (MBAm), ammonium persulfate (APS), and *N,N,N,N'*-tetramethylethylenediamine (TEMED) were prepared in ultrapure water. Aliquots of each constituent were used to form a precursor solution of 67 wt% HEMA and 0.3 wt% MBAm. The final APS and TEMED concentrations were 0.15 wt%. Polymerization was completed in a nitrogen-rich environment to prevent oxygen inhibition. Poly(2-hydroxyethyl

methacrylate) (pHEMA) hemispherically-capped probes and flat discs were made by polymerizing the precursor solution in polyolefin molds with a 2 mm radius of curvature or between two parallel polystyrene plates with a gap height of 5 mm, respectively. Both molds had an average surface roughness of $R_a \approx 20$ nm. The probes and discs were equilibrated in individual containers with water/ethanol solutions (0, 12, 20, 25, 32, 35, 50, 75, and 100 vol.% ethanol) for at least 48 h prior to testing.

6.2.2 Swelling Experiments

Twenty-two pHEMA discs (10 mm diameter, 5 mm thickness) were prepared following the methods above and equilibrated in sealed vials of water/ethanol solutions (0 to 100 vol% EtOH) at room temperature. After swelling for 48 h, the final sample dimensions (V_s) were compared to initial volume measurements after polymerization (V_p), and the volume change was calculated using **Eqn. 6.1**.

$$volume\ change\ (\%) = \left(\frac{V_s - V_p}{V_p}\right) x100 \qquad \textbf{Eqn. 6.1}$$

6.2.3 Mesh Size Calculations

The mesh size was estimated using the model developed by Peppas *et al.* (**Eqn. 2.12,** reproduced below):[131]

$$\xi = \nu_{2,s}^{-1/3}(\bar{r}_0^2)^{1/2} \qquad \textbf{Eqn. 2.12}$$

As discussed in **Sections 2.4** and **2.5**, the mesh size can be calculated using the polymer volume fraction after swelling ($v_{2,s}$), which can be estimated from the volume change of the pHEMA gels during swelling as:

$$v_{2,s} = \frac{v_{2,\mathrm{r}}}{\left(V_\mathrm{s}/V_\mathrm{p}\right)} \qquad \text{Eqn. 6.2}$$

where $v_{2,\mathrm{r}}$ is the polymer volume fraction after polymerization and is the ratio of the dried polymer volume to the hydrogel volume after polymerization (**Eqn. 2.17**). Based on the crosslinking concentration of the pHEMA hydrogels herein (0.3 wt.%), the end-to-end distance, $(\bar{r}_0^2)^{1/2}$, can be estimated as ~ 15 Å. This value does not change with swelling, so the mesh size can be calculated by combining **Eqn. 2.12** and **Eqn. 6.2**:

$$\xi = v_{2,\mathrm{r}}^{-1/3}\left(V_\mathrm{s}/V_\mathrm{p}\right)^{1/3}(\bar{r}_0^2)^{1/2} \qquad \text{Eqn. 6.3}$$

6.2.4 Friction & Indentation Measurements

All tribological experiments of pHEMA hydrogels were performed in the self-mated ("Gemini") configuration with a hemispherically-capped pHEMA probe (radius of curvature, R = 2 mm) sliding against a flat pHEMA disc. An average normal load of F_n = 1 mN and sliding speed of v = 100 μm/s was applied. A stroke length of 2 mm was used for all experiments, except the 12 – 30 vol.% ethanol samples which required a stroke length of 5 mm due to excessive friction. For a more detailed description of the tribological

measurements, see **Section 4.3**. Indentation experiments were also conducted in the Gemini configuration. A maximum applied load of F_n = 1.5 mN and indentation velocity of 1 μm/s was used. The maximum force of adhesion, F_{adh}, was calculated following the method described by McGhee *et al.*[265] For more details about indentation measurements, see **Section 4.4**. All experiments were performed fully submerged in their respective water/ethanol solution.

6.3 Swelling

The swelling behavior of pHEMA is greatly impacted by the ratio of water and ethanol, as demonstrated by the volume change with increasing ethanol concentration (**Figure 6.2a**). As the gels swelled, polymer volume fraction decreased ($v_{2,s}$) (**Figure 6.2b**), solution volume fraction increased, and mesh size (ξ) increased (**Figure 6.2c**). Maximum swelling and solution viscosity[266] was achieved at 65 vol.% EtOH (**Figure 6.2d**).

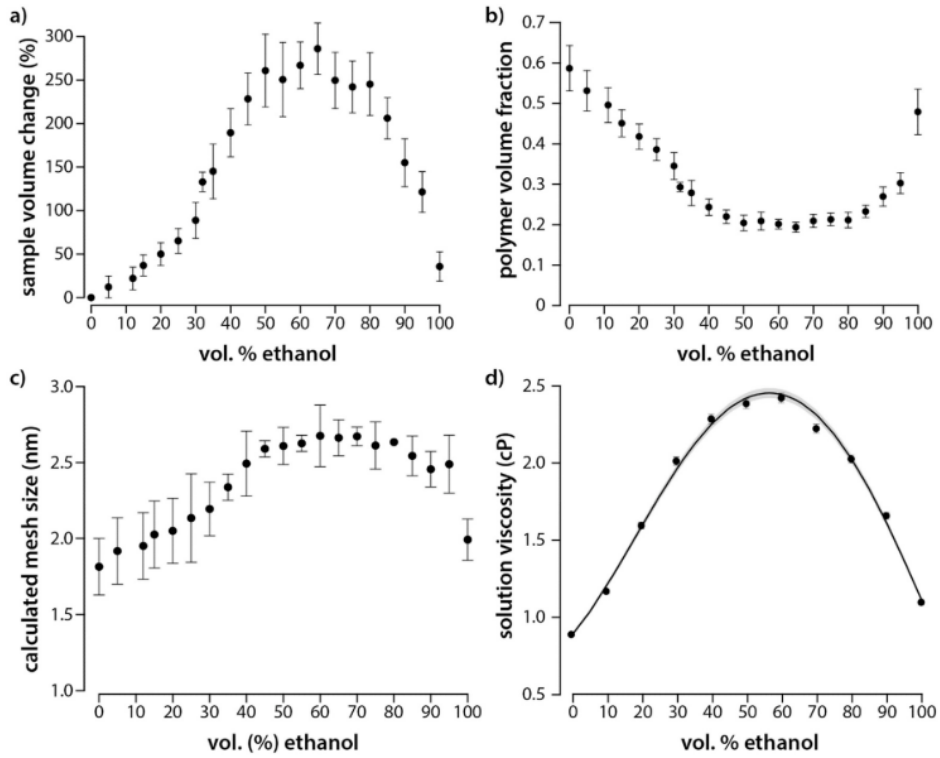

Figure 6.2 Swelling behavior of pHEMA gels after 48 h in water/ethanol solutions. **(a)** Volume change of pHEMA gels as a function of ethanol (EtOH) concentration and normalized such that there was no volume change at 0 vol.% EtOH. **(b)** Swollen polymer volume fraction, $\boldsymbol{\nu_{2,s}}$, as a function of ethanol concentration. **(c)** Calculated mesh size based on swelling measurements. **(d)** Solution viscosity for the water/ethanol solution as a function of ethanol concentration. Viscosity data was taken from L. Khattab *et al., Korean J. Chem. Eng.*, **29**, 2012.[266]

6.4 Friction & Adhesion

Friction coefficients of the amphiphilic pHEMA gels in Gemini contact were very sensitive to ethanol concentration (**Figure 6.3a**). In pure water (0 vol.% EtOH), $\mu \approx 0.35$. However, just increasing the ethanol concentration to 12 vol.% produced an order of magnitude jump in friction ($\mu > 4$). As ethanol concentration increased further, the friction coefficient decreased

monotonically, dropping to $\mu \approx 0.02$ at 50 vol.% EtOH and staying low up to 100 vol.% EtOH.

The high friction coefficients ($\mu > 1$) at low ethanol concentrations indicate that there may be adhesive contributions to the friction coefficient; therefore, the force of adhesion was measured in Gemini contact. Adhesion followed the same trend as the friction coefficient, with adhesion drastically increasing ($F_{adh} \approx 650$ μN) at 12 vol.% EtOH but then monotonically decreasing with higher ethanol concentrations and reaching a minimum at 50 vol.% EtOH (**Figure 6.3c**).

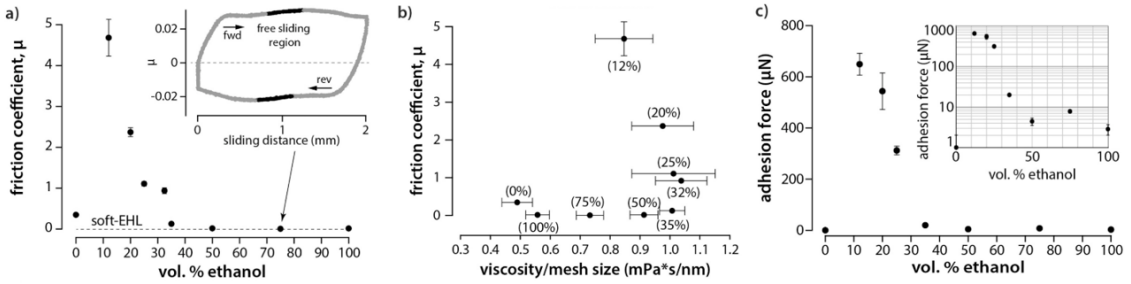

Figure 6.3 (a) Friction coefficient as a function of ethanol concentration for Gemini pHEMA hydrogels with inset displaying a loop for the lowest friction coefficient ($\mu \approx 0.025$) at 75 vol.% EtOH. Maximum friction was achieved at 12 vol.% EtOH with the lowest friction occurring at > 35 vol.% EtOH. Soft-EHL is denoted with a dotted line. **(b)** Friction coefficient as a function of viscosity/mesh size. The corresponding ethanol concentration is labeled above each data point. **(c)** Maximum force of adhesion as a function of ethanol concentration. Maximum adhesion of 650 μN was also achieved at 12 vol.% EtOH. The inset presents the maximum force of adhesion in a semi-log plot.

One possible dissipation mechanism for this system is fluid shearing and penetrating through both gel surfaces at a depth on the order of a mesh size, where shear stress (τ) scales with viscosity (η) and mesh size as $\tau \sim \eta v/(2\xi)$. However, when the friction coefficient is plotted as a ratio of the viscosity to mesh size, there is no clear correlation (**Figure 6.3b**). Another possible

mechanism is soft-elastohydrodynamic (soft-EHL) lubrication. As briefly mentioned in Section 3.1, soft-EHL was developed by Hamrock and Dowson to describe the lubrication of gels.[173] This model consistently predicted friction coefficients below μ = 0.002, shear stresses below 10 Pa, and film thicknesses on the order of 30 nm for the pHEMA gels, all of which are an order of magnitude lower than the experimentally observed friction coefficients for Gemini pHEMA gels in contact at low sliding speeds. Therefore, it is unlikely that the tribological behavior of the pHEMA gels herein can be explained by soft-EHL.

6.5 Proposed Solvophilic Transition

The pendent hydroxyl groups and polarity of the methacrylic ester groups provide pHEMA with its hydrophilic properties while the less polar aliphatic regions along the backbone make pHEMA inherently amphiphilic. Even as uncrosslinked polymer chains in solution, pHEMA is not fully water soluble due to the inter- and intramolecular hydrophobic associations of the aliphatic regions in the backbone of the polymer.[267] However the addition of water-miscible alkyl alcohol to solution can dissociate these hydrophobic interactions and lead to more swelling, as demonstrated in Figure 6.2a. We therefore propose that the solvent-induced transition in inter- and intra-gel associations are responsible for the swelling and tribological behavior of pHEMA gels.

In pure water (0 vol.% EtOH), moderate friction and very little adhesion was observed for the Gemini pHEMA gels, which is indicative of a highly hydrophilic surface. This implies that the pHEMA chains are orientated in such a way to selectively present the pendent hydroxyl groups at the interface while the hydrophobic aliphatic regions associate below the surface (**Figure 6.4a**).

When a small concentration of ethanol is added to the solution, both friction and adhesion drastically increase. The addition of ethanol leads to partial dissociation and plasticization of the hydrophobic-associated domains, which allows enough chain mobility for the hydrophobic domains to orient towards the gel surface (**Figure 6.4b**). This is consistent with the work of Li *et al.* who found that solvent interactions and chain segment motion impacted hydrogel adhesion.[268] We therefore propose that during contact, the exposed hydrophobic regions on both pHEMA surface will spontaneously de-wet[269] and form strong hydrophobic/hydrophobic interactions, leading to the observed high friction and adhesion. The maximum friction coefficient and adhesion for Gemini contacts of pHEMA were observed at 12 vol.% EtOH, which was the lowest concentration of ethanol tested above pure water. We hypothesize that there was just enough ethanol for the partial dissociation of the sub-surface hydrophobic domains but not enough to completely passivate these regimes.

As the ethanol concentration increased, friction and adhesion monotonically decreased. With increased concentration, the alkyl regions of the

ethanol can associate with the aliphatic regions of pHEMA and effectively coat the chains with a hydroxyl-presenting surface (Figure 6.4c), promoting hydrophilicity and leading to increased swelling and mesh size (Figure 6.3a and Figure 6.3c).

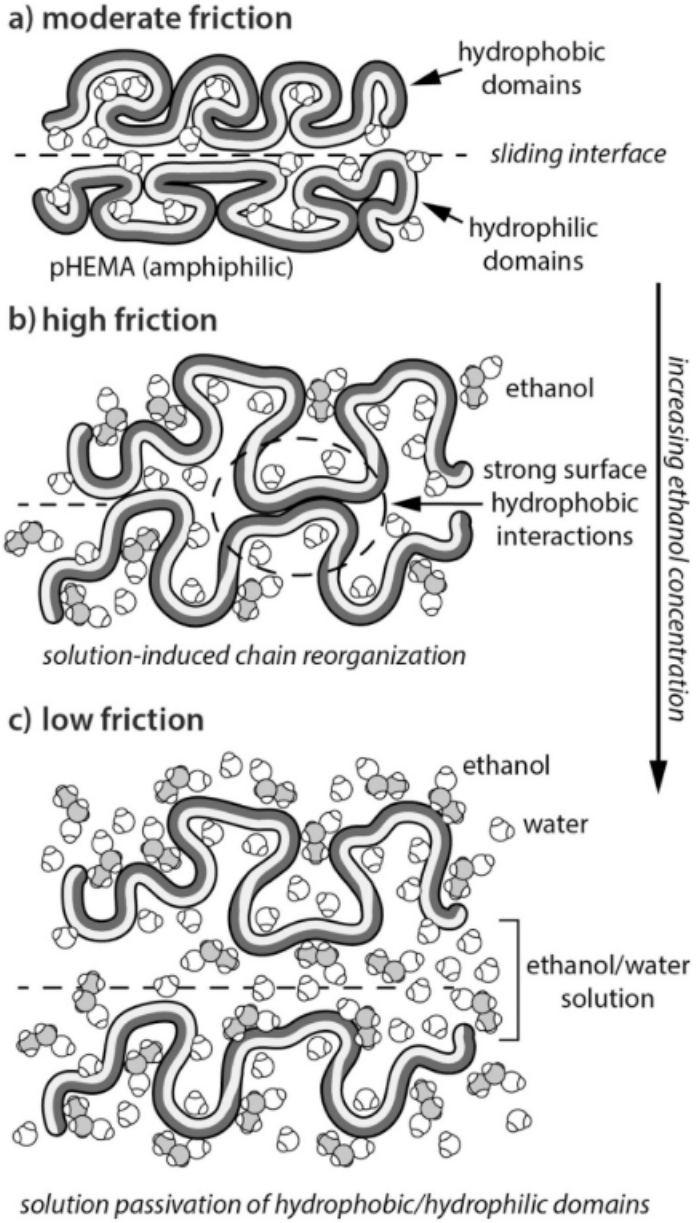

Figure 6.4 Proposed chain configurations for Gemini pHEMA hydrogels swollen in water/ethanol solutions. **(a)** In pure water (0 vol.% EtOH), the pHEMA chains selectively present the hydrophilic pendent hydroxyl groups to the aqueous solvent while the aliphatic hydrophobic backbones associate via inter- and intra-chain associations. **(b)** At intermediate concentrations of ethanol, the ethanol selectively solvates and plasticizes the hydrophobic domains of pHEMA. Due to low ethanol concentration, passivation is incomplete and leads to chain-chain interactions within the gel and across the interface, causing high friction and adhesion. **(c)** At high ethanol concentration, the remaining hydrophobic domains are passivated, lowering friction due to a reduction in interfacial interactions between polymer chains.

6.6 Timescale of Hydrophobic Association

The timescale of this functional group and chain reorientation is much longer than the short dynamics of friction and adhesion measurements and must have occurred during the long equilibration process (> 48 h). Therefore, when conducting friction and adhesion measurements, the surface chemistry and optimal chain orientation has already been locked in place, allowing us to observe this solvophilic transition.

While low friction and low adhesion and high friction and high adhesion were observed for the pHEMA gels equilibrated in high ethanol and low ethanol solutions, respectively, the gels equilibrated in pure water experienced moderate friction and low adhesion. This curious result may be explained through kinetics. To explore the role of kinetics directly, pHEMA gels in Gemini configuration were submerged in water and placed in contact for varying amounts of time ranging from ~1 s to ~100,000 s. The adhesion force increased monotonically with contact time as displayed in **Figure 6.5a**. For the pHEMA gels swollen in pure water, the polymer chains may be oriented in such a way

that the hydrophilic hydroxyl groups are exposed at the surface with the hydrophobic regions hidden in the interior. In order for new hydrophobic/hydrophobic interactions to form at the interface, the chains need to spontaneously break the interior hydrophobic associations and reorient so the hydrophobic domains are at the surface for a sufficient amount of time to match with a hydrophobic domain on the countersurface that has undergone the same process. Unsurprisingly, this process is slow and has a very low probability of success.

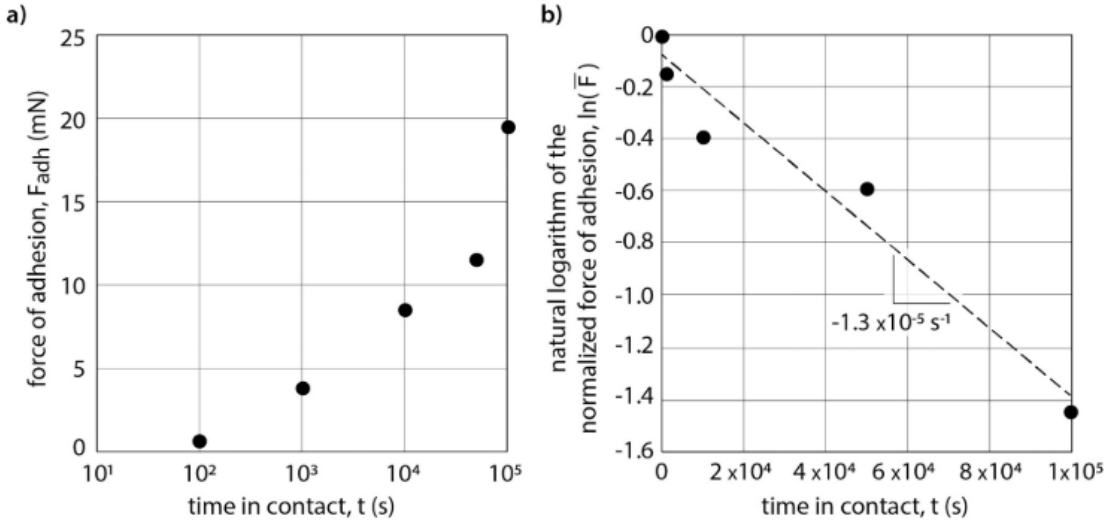

Figure 6.5 Force of adhesion for Gemini pHEMA gels submerged in water. **(a)** Force of adhesion as a function of contact time. At short contact times (< 10 s), the force of adhesion is less than 0.4 mN. As contact time increased, adhesion increased. **(b)** Linear fitting of the natural log of the normalized force of adhesion as a function of contact time to estimate the rate constant.

Assuming first order kinetics, the fractional coverage of hydrophobic interactions (θ) across the interface is zero at time zero ($\theta = 0$ at $t = 0$), and that once a hydrophobic/hydrophobic association is formed it will remain intact until the

force of adhesion separates the chains during unloading, the fractional coverage of bonds as a function of time can be written as:

$$\frac{d\theta}{dt} = k(1-\theta) \qquad \text{Eqn. 6.4}$$

$$\theta = 1 - e^{-kt} \qquad \text{Eqn. 6.5}$$

where k is an exponential decay constant. It can be assumed that each chain within a single mesh could be involved in one hydrophobic association. Therefore, the number of hydrophobic interactions, N, can be estimated by dividing the projected contact area (A_o) by the projected area of one mesh size ($\pi\xi^2$) and multiplying this by the fractional coverage of bonds (**Eqn. 6.6**).

$$N = \left(A_o/(\pi\xi^2)\,(1-e^{-kt})\right) \qquad \text{Eqn. 6.6}$$

The force of adhesion, F_{adh}, can be assumed to be proportional to the number of hydrophobic associations, N, and the time dependent force:

$$F_{adh} = F_o + (F_\infty - F_o)(1-e^{-kt}) \qquad \text{Eqn. 6.7}$$

where F_o is the adhesion force at time zero and F_∞ is the adhesion force for complete saturation of the hydrophobic interactions at the surface (*i.e.*, θ = 1). The force of adhesion can be normalized as:

$$\bar{F} = \frac{(F_{adh} - F_o)}{(F_\infty - F_o)} = (1-e^{-kt}) \qquad \text{Eqn. 6.8}$$

Eqn. 6.8 can be rearranged to plot the natural log of 1 minus the normalized force of adhesion, $\ln(1-\bar{F})$ as a function of contact time (t) to fit for the exponential decay constant, k. As shown in Figure 6.5b, k = -1.3 x 10^{-5} s, which suggests that the time constant for this process, 1/k, is on the order of ~80,000 s. This is consistent with the expected slow evolution of the gel surfaces that requires the hydrophobic regions of the surface chains to randomly reorient themselves and then associate with an opposing hydrophobic domain on the countersurface.

Based on the apparent area of contact, A_o ~ 0.5 mm^2, and the estimated area of one mesh size, $\pi\xi^2$ ~ 10 nm^2, the number of hydrophobic interactions could be on the order of N = 5 x 10^{10}. Assuming a saturation force of F_∞ = 25 mN, the force for each interaction is on the order of 0.5 pN, which is within the range of expected forces for weak bonds and short-ranged hydrophobic interactions.

6.7 Concluding Remarks

These experiments explore the solvophilic transition of amphiphilic pHEMA gels in Gemini contact swollen in water/ethanol solutions. Below the solvophilic transition, the Gemini pHEMA gels had high friction and high adhesion; above the solvophilic transition, the gels had low friction and low adhesion. We hypothesize that this transition is driven by the amphiphilic nature of pHEMA

and the mixture of polar and nonpolar solvent molecules. Below the solvophilic transition, the aliphatic ethanol selectively solvates and plasticizes some hydrophobic domains of pHEMA to allow for chain mobility and reorientation. But this incomplete passivation exacerbates chain-chain hydrophobic interactions across the Gemini interface, leading to high friction and adhesion. As the solution becomes more ethanol-rich, the alkyl regions of ethanol can associate with the aliphatic regions of pHEMA, effectively coating the chains with hydroxyl groups, which decreases hydrophobic interactions and promotes swelling, leading to a decrease in friction and adhesion. By controlling the polarity of the solvent, we were able to tune friction coefficient and adhesion an order of magnitude. In the next chapter, we will discuss tuning the friction of hydrogels with pH rather than solvent polarity.

7 CHAPTER 7: PH-RESPONSIVE HYDROGELS

Poly(acrylamide-*co*-acrylic acid) (P(AAm-*co*-AA)) hydrogels are highly tunable and pH-responsive materials frequently used in biomedical applications. The swelling behavior and mechanical properties of these gels have been extensively characterized and are thought to be controlled by the protonation state of the acrylic acid (AA) through the regulation of solution pH. Yet their tribological properties have been underexplored. In this chapter, we hypothesize that electrostatics and the protonation state of AA will also drive the tribological properties of these polyelectrolyte gels. P(AAm-*co*-AA) hydrogels were prepared with constant acrylamide (AAm) concentration (33 wt.%) and varying AA concentration to control the amount of ionizable groups in the gel. The monomer:crosslinker molar ratio (200:1) was kept constant. Hydrogel swelling, stiffness, and friction behavior were studied by systematically varying the acrylic acid (AA) concentration from 0 – 12 wt.% and controlling solution pH (0.35, 7, 13.8) and ionic strength (I = 0 or 0.25 M). The stiffness and friction coefficient of bulk hydrogels were evaluated using a microtribometer and borosilicate glass probes as countersurfaces. The swelling behavior and elastic modulus of these polyelectrolyte hydrogels were highly sensitive to solution pH and poorly predicted the friction coefficient (μ), which decreased with increasing AA concentration. P(AAm-*co*-AA) hydrogels with the greatest AA concentrations (12 wt.%) exhibited superlubricity (μ = 0.005 ± 0.001) when swollen in

unbuffered, deionized water (pH = 7, I = 0 M) and 0.5 M NaOH (pH = 13.8, I = 0.25 M) (μ = 0.005 ± 0.002). Friction coefficients generally decreased with increasing AA and increasing solution pH. We postulate that tunable lubricity in P(AAm-*co*-AA) gels arises from changes in the protonation state of acrylic acid and electrostatic interactions between the probe and hydrogel surface.

This chapter was reproduced in part with permission from:[111]

Chau, A.L., Getty, P.T., Rhode, A.R., Bates, C.M., Hawker, C.J., and Pitenis, A.A., Superlubricity of pH-Responsive Hydrogels in Extreme Environments. *Frontiers in Chemistry*, **10**, 891519, 2022.

Table of Contents

7.1 Introduction

The term "superlubricity" was first coined by Hirano and Shinjo in 1993 while studying the friction between two mica sheets.[270] They theorized that the friction forces between two crystalline materials could be eliminated through the cancellation of opposing forces created by atomic lattice mismatches. Over time, the term "superlubricity" was adopted to describe the tribological behavior of any material system where the friction coefficient (μ) was less than 0.01.[271–273] However, this value is not universally agreed upon. For soft materials, a more demanding threshold of $\mu \leq 0.005$ is often used to denote superlubricity,[235,274] which will be adopted herein.

Hydrogels are often used as anti-biofouling materials and coatings for biomedical devices that require low friction interfaces such as catheters.[275] In many of these cases, polyelectrolyte and polyzwitterionic polymer brush systems are used to achieve the desired ultra-low friction coefficients.[276–279] Gong *et al.* demonstrated that the length of surface-grafted polyelectrolyte polymer brushes can be varied to tune friction and achieve superlubricity[280] while Spencer *et al.* synthesized a superlubricious double-network hydrogel by grafting polyelectrolyte polymer chains from the surface, obtaining friction coefficients in the range of 0.001 – 0.004.[281] Rudy *et al.* covalently attached an entangled network of poly(acrylamide-*co*-acrylic acid) polymer chains to PDMS, achieving a friction coefficient of $\mu = 0.003 \pm 0.005$ in PBS solution.[282] Superlubricity has

also been demonstrated in bulk hydrogels. Bulk hydrogels with depth-wise mesh size gradients with $\xi \approx 50$ nm at the surface have exhibited superlubricity ($\mu \approx 0.001$) in sliding contact with hydrogel probes.[235] Wang *et al*. synthesized zwitterionic copolymer hydrogels that achieved superlubricity ($\mu \approx 0.002$) in water with sapphire countersurfaces and attributed the ultra-low frictional behavior to hydration lubrication caused by the formation of hydration layers surrounding the charges of the zwitterionic copolymers.[272]

The structural tunability of hydrogels through temperature- or pH-induced swelling is another attractive quality, especially in the design of sensors[54,283] and drug delivery capsules.[42,44] Poly(acrylic acid) (PAA) is a well-known pH-sensitive polyelectrolyte and is often copolymerized with other polymers such as poly(vinyl alcohol) (PVA)[284] or poly(acrylamide) (PAAm)[285,286] for greater mechanical strength. The effects of solution pH and ionic concentration on the swelling properties of PAA-based hydrogels have been thoroughly studied.[73,123,130,287–293] Swelling increases when the pH of the solution exceeds the pK_a of PAA (≈ 4.7) due to the deprotonation of the carboxylic acid groups in acrylic acid.[293]The formation of these negatively charged carboxylate ions (COO^-) leads to electrostatic repulsion between polymer chains, which increases the hydrogel swelling capacity and mesh size.[150,291,293] Conversely, when pH drops below the pK_a or if salt is added, swelling decreases.[123,288,289] This swelling, in turn, leads to changes in the stress relaxation behavior of the gel.[73]

Notably, there have been few investigations studying the impact of solution pH on the tribological properties of bulk polyelectrolyte gels. Han *et al.* showed that thin (~μm) multilayered devices composed of PAA and poly(allylamine hydrochloride) (PAH) swelled at low pH and exhibited lower friction as solution pH decreased.[294] Ma *et al.* recently controlled the friction coefficient of PAA nanohydrogel brush systems by changing the solution pH *in situ*.[295] Additionally, the pH range used to test the tunability of these polyelectrolyte systems is often limited between 1 and 12. To our knowledge, there have been no studies observing the effects of extremely acidic (pH < 1) or extremely basic (pH > 10) conditions on the mechanical characteristics of polyacrylamide-*co*-acrylic acid (P(AAm-*co*-AA)) hydrogels. Despite several in-depth studies examining the effects of pH on the swelling dynamics and mechanics of such polyelectrolyte gels, there are no systematic studies connecting solution pH and acrylic acid concentration to tribological properties. In this work, P(AAm-*co*-AA) hydrogels were synthesized with varying AA concentrations (0 – 12 wt.%) and swollen in solutions of varying pH (0.35, 7, 13.8) and ionic strength (I = 0 or 0.25 M) with the goal of tuning the friction coefficient and achieving superlubricity. The changes in swelling and stiffness in response to extreme pH were also studied for these polyelectrolyte gels. Superlubricity was achieved in the P(AAm-*co*-AA) hydrogels with highest AA concentration (12 w.%) in deionized water and NaOH.

7.2 Materials & Methods

7.2.1 Hydrogel Synthesis

Poly(acrylamide-*co*-acrylic acid) hydrogels (P(AAm-*co*-AA)) were synthesized via free-radical polymerization. Stock solutions of acrylamide (AAm) (1 g/mL), *N*,*N*′-methylenebisacrylamide (MBAm) (25 mg/mL), ammonium persulfate (APS) (50 mg/mL), and *N*,*N*,*N*′,*N*′-tetramethylethylenediamine (TEMED) (50 mg/mL) were prepared in ultrapure water (Ω = 18.2 MΩ·cm). The final AAm concentration of all P(AAm-*co*-AA) hydrogels was 0.5 g/mL (corresponding to 33 wt.%). The molar ratio of AAm:AA was controlled by adding uninhibited acrylic acid (AA) (neat) to the pre-polymerized solution. Six different molar ratios of AAm:AA (1:0, 100:1, 20:1, 15:1, 10:1, and 7.5:1) were synthesized, corresponding to 0, 1, 5, 6, 9, and 12 wt.% AA of the total monomer concentration. All hydrogels will be referenced as P(AAm-*co*-AA)-*x*, where *x* represents the wt.% of AA, or by the concentration of AA in wt%. The monomer:crosslinker molar ratio was maintained at 200:1 for all hydrogel samples (**Figure 7.1**). The pre-polymerized solutions were deposited between two flat polystyrene plates (surface roughness, $R_a \approx 20$ nm) in ambient air and polymerized at room temperature (23°C) for a maximum of 2 h. Hydrogel sections (16 or 24 mm diameter) were equilibrated in either unbuffered deionized (DI) water (18.2 MΩ·cm) (pH = 7, I = 0 M), 0.5 M HCl (pH = 0.35, I = 0.25 M), or 0.5 M NaOH (pH = 13.8, I = 0.25 M). The hydrogels equilibrated in

DI water for at least 72 h before testing while separate hydrogel samples equilibrated in either HCl or NaOH for at least one week (**Figure 7.6**). The molarity of the NaOH solution was chosen to ensure complete (100%) neutralization (deprotonation) of all AA units in the hydrogel using the following formula (**Eqn. 7.1**):[296]

$$DN = \frac{n\ (base)}{n\ (ionizable\ monomer)} \times 100\% \qquad \text{Eqn. 7.1}$$

where *DN* is the degree of neutralization (%) and *n* is the number of moles. The same principle was applied when determining the molarity of the HCl solution to ensure complete protonation of all AA.

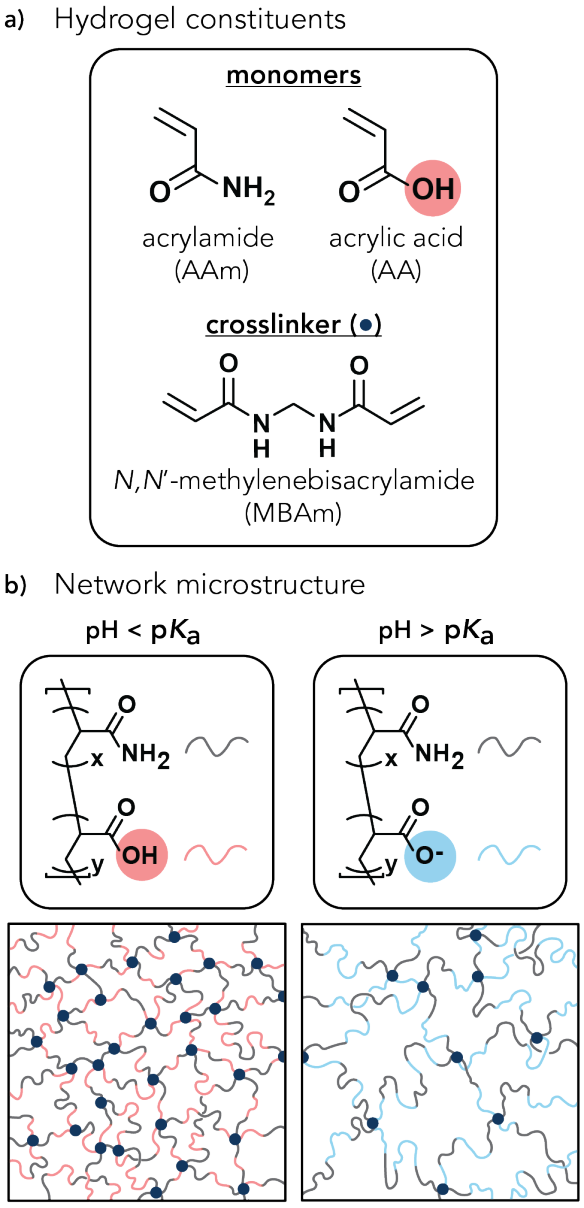

Figure 7.1 (a) Chemical structures of the monomers (acrylamide and acrylic acid) and crosslinker (*N*,*N*′-methylenebisacrylamide) (navy circle). The molar ratio of acrylamide to acrylic acid monomers varied from 1:0, 100:1, 20:1, 15:1, 10:1, and 7.5:1, corresponding to 0, 1, 5, 6, 9, and 12 wt.% AA of the total monomer concentration. The monomer-to-crosslinker molar ratio of 200:1 was kept constant across all AA concentrations. **(b)** Representative P(AAm-*co*-AA) hydrogel network microstructures depicting the expected protonation state and interaction between polymer chains within the network as a function of solution pH. When the pH of the solution is less than the pK_a of the hydrogel, the acrylic acid should be protonated (denoted by red). When the pH > pK_a, the acrylic acid should become deprotonated and negatively charged (denoted by blue), increasing electrostatic repulsion between polymer chains and increasing the mesh size.

7.2.2 Swelling Measurements

Hydrogels were equilibrated in unbuffered DI water (pH = 7, I = 0 M), 0.5 M HCl (pH = 0.35, I = 0.25 M), or 0.5 M NaOH (pH = 13.8, I = 0.25 M) for at least four weeks to ensure equilibrium swelling was reached. The gels were sectioned with a 6 mm diameter circular punch and then weighed (m_s) using a Mettler Toledo XPR105DR analytical balance (repeatability ± 15 µg). Lens paper was used to gently wipe away excess liquid from the hydrogel surface before weighing. Samples were then dried in a vacuum oven for 10 days at 60 °C and weighed to obtain their dry mass (m_d). The water content (%) was calculated using **Eqn. 7.2.**[124] The reported water contents are average values and standard deviation from three samples unless otherwise stated.

$$water\ content\ (\%) = \frac{m_s - m_d}{m_s} \times 100\% \qquad \text{Eqn. 7.2}$$

7.2.3 Microindentation & Friction Measurements

Tribological experiments and microindentations were conducted as outlined in **Section 4.3** and **Section 4.4.** An optical profilometry trace of the glass probe can be found in **Figure 7.7**. Representative indentation curves and friction force loops are displayed in **Figure 7.2b** and **Figure 7.2c**, and representative Hertzian fits of the approach curve can be found in **Figure 7.8.**

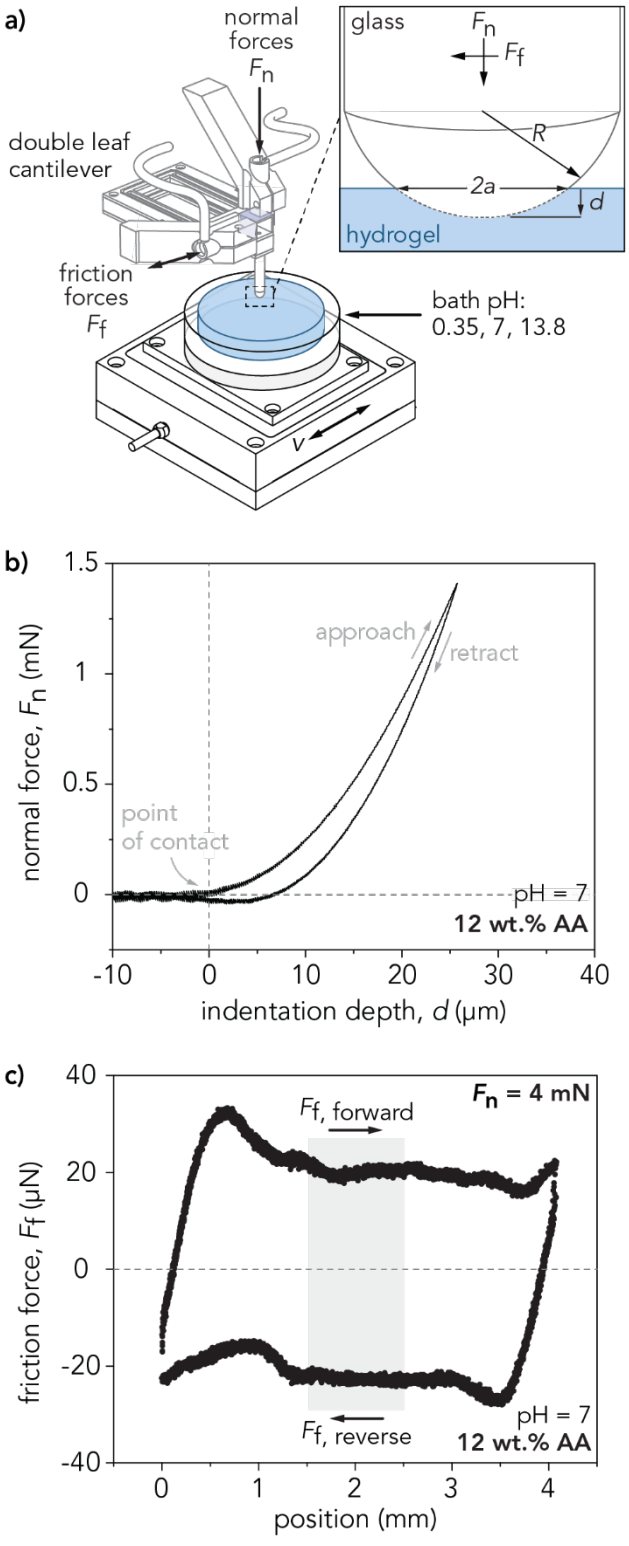
a)
normal forces
F_n
double leaf cantilever
friction forces
F_f
bath pH:
0.35, 7, 13.8
v
glass
F_n
F_f
R
2a
d
hydrogel
b)
normal force, F_n (mN)
1.5
1
0.5
0
approach
retract
point of contact
pH = 7
12 wt.% AA
-10
0
10
20
30
40
indentation depth, d (μm)
c)
friction force, F_f (μN)
40
20
0
-20
-40
F_n = 4 mN
F_f, forward
F_f, reverse
pH = 7
12 wt.% AA
0
1
2
3
4
position (mm)

Figure 7.2 (a) Schematic depicting the custom-built linear reciprocating tribometer used for indentation and sliding experiment. The glass probe, with a radius of curvature R, is mounted to a double-leaf cantilever, which deflects in response to indentation and sliding. Capacitance probes measure the normal and tangential displacements of the cantilever, converting them into normal and friction forces. For indentation experiments, a defined normal force, F_n, is applied to the sample at a specified indentation velocity, v_{ind}. During sliding experiments, the sample stage displaces linearly at a defined sliding velocity, v, while applying a normal force, F_n. The inset shows the area of contact between the probe and hydrogel, denoted by the contact area diameter, $2a$. The indentation depth of the probe into the gel is denoted by d. **(b)** Representative indentation curve for the P(AAm-*co*-AA)-12 hydrogel at pH = 7. A maximum applied normal force of F_n = 1.5 mN is applied to the hydrogel at an indentation velocity of v_{ind} = 10 μm/s. Using Hertzian contact mechanics, the reduced modulus, E^*, is estimated by fitting the slope of the approach curve from the point of contact to F_n = 1 mN. **(c)** Representative friction force loop for the P(AAm-*co*-AA)-12 hydrogel at pH = 7 for one reciprocating cycle at an applied normal force of F_n = 4 mN and sliding velocity of v = 100 μm/s. Friction forces for each cycle are calculated by analyzing the middle 25% of the sliding path (light gray area). The friction coefficient of this individual cycle is μ = 0.005. To calculate the average friction coefficient for each hydrogel, the friction coefficients from 25 cycles are averaged.

7.3 Results & Discussion

P(AAm-*co*-AA) hydrogels with varying AA concentrations (0 – 12 wt.%) were placed in three solutions (0.5 M HCl, unbuffered DI water, 0.5 M NaOH) with pH (0.35, 7, 13.8) ranging below and above the pK_a of the copolymer hydrogel (p$K_a \approx 4.5$)[123] to alter the protonation state of the AA. We expected that all the AA was protonated while in HCl and deprotonated while in NaOH (**Eqn. 7.1, Section 7.6.6**. Since unbuffered DI water has no added counterions, I = 0 M. Water content, reduced elastic moduli (E^*), and friction coefficients (μ) of the gels were compared as a function of AA concentration and pH. For all measurements, the averages and standard deviations were reported for three gels at each condition unless otherwise stated. **Figure 7.1b** schematically depicts the expected protonation state and interactions between polymer chains within the P(AAm-*co*-AA) hydrogel network as a function of the solution pH.

7.3.1 Swelling & pH

Swelling in hydrogels is often measured with different metrics (**Table 2.1**) as discussed in **Section 2.3**. Water content, which represents the amount of solution absorbed by the gel in its fully swollen state,[124] was used to quantify swelling in our work (**Figure 7.3a**). Previous swelling studies of P(AAm-*co*-AA) hydrogels have demonstrated that swelling increases with increasing pH and acrylic acid concentration due to an increase in electrostatically repelling carboxylate ions caused by AA deprotonation.[73,123,130,287,290,291]

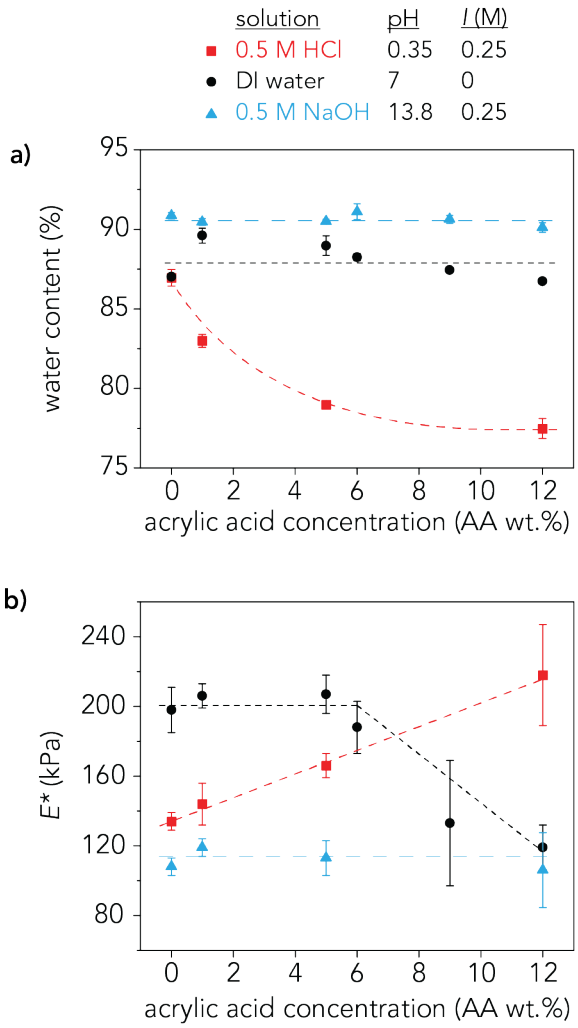

Figure 7.3 (a) Water content (%) and **(b)** reduced modulus, *E**, as a function of AA concentration at pH = 0.35 (red squares), pH = 7 (black circles), and pH = 13.8 (blue triangles). At pH = 0.35, the water content monotonically decreased and *E** increased with increasing AA as expected. In DI water, the swelling ratio increased with the addition of 1 wt.% AA and then slightly decreased with increasing AA wt.%. *E** followed the same trend, decreasing at higher AA concentrations. At pH = 13.8, the water content and *E** stays relatively constant with increasing AA concentration at 90 – 91% and 92 – 119 kPa respectively. The dashed lines are guidelines and not meant to indicate a fit. For *E**, each data point is an average of three samples (n = 3) with error bars as the standard deviation. For the water content measurements, n = 3 except for the following samples where n = 2: 9 wt.% AA in NaOH and 1 wt.% AA, 6 wt.% AA, 9 wt.% AA, and 12 wt.% AA in DI water.

As expected, water content increased with increasing pH for all AA concentrations except for the P(AAm-*co*-AA)-0 hydrogel, where water content

was 87% at both pH = 0.35 and pH = 7, indicating that in its fully swollen state, roughly 87% of the hydrogel mass was due to water while the remaining 13% was polymer. It is reasonable that the water content stayed constant for the P(AAm-*co*-AA)-0 hydrogels at these pH values because there were no ionizable carboxylic acid groups present in the gels. However, increasing AA concentration at pH > pK_a did not lead to an increase in water content as expected. The P(AAm-*co*-AA) hydrogels in DI water (pH = 7, I = 0 M) had a water content that fluctuated between 87 – 90% from 0 to 12 wt.% AA. Similarly, when swollen in NaOH (pH = 13.8, I = 0.25 M), the water content stayed relatively constant between 90 – 91%. In contrast, the water content decreased monotonically from 87 ± 0.5% to 79 ± 0.2% as AA concentration increased for the hydrogels swollen in HCl (pH = 0.35, I = 0.25 M), which was expected due to greater amounts of hydrogen bonding between the protonated carboxylic acid and amide groups.

One possible reason for this discrepancy for the gels in NaOH was the presence of excess sodium counterions (Na^+). Since the molarity of the NaOH solution was chosen to ensure complete deprotonation of all AA monomers, there was a stoichiometric excess of Na^+ counterions in solution. Polyelectrolyte gels swell due to osmotic pressure from the counterions trapped within the network that ensure network electroneutrality.[297,298] If there is an excess of counterions outside the network within the solution, this may reduce the osmotic

pressure driving swelling. Additionally, the ionic strength of the solution has been shown to decrease swelling due to charge screening, reducing repulsion between polymer chains.[123,124] One way to test this conjecture is to increase the ionic strength in DI water through the addition of a salt, such as NaCl, to observe any potential effects of charge screening on swelling. Another factor that may be influencing this AA concentration independence is crosslink degradation. Since MBAm is the crosslinker used in these P(AAm-*co*-AA) hydrogels, the amide is susceptible to attack in these extremely basic conditions. This could lead to the hydrolysis of the amide groups,[299] decreasing the effective crosslinking density and forming additional acrylic acid groups (**Figure 7.11** and **Figure 7.12**). If crosslinks are breaking, this could overpower any differences caused by increasing AA concentration. One confirmation of this hypothesis is the increase in water content of the P(AAm-*co*-AA)-0 hydrogel at pH = 13.8 (91 ± 0.2%), despite the lack of AA.

For the hydrogels in DI water, the slight decrease in swelling with increasing AA concentration may be explained by an increase in total polymer concentration with the addition of AA (**Section 7.6.8, Table 7.3**). The total polymer concentration before swelling increased from 33 wt.% for P(AAm-*co*-AA)-0 to 36 wt.% for P(AAm-*co*-AA)-12. Therefore, changes in swelling due to increasing AA concentration may be masked by the changing initial polymer concentration.

7.3.2 Hydrogel Elastic Modulus & pH

The average reduced elastic modulus, *E**, for the P(AAm-*co*-AA) hydrogels at each pH were obtained through microindentations along three different positions and averaged across three separate samples (**Figure 7.3b**). Prouvé *et al.* demonstrated that the elastic modulus of P(AAm-*co*-AA) hydrogels decreased with increasing AA concentration due to an increase in swelling.[73] Therefore, the elastic modulus should be dependent on swelling and decrease with increasing water content.

For the P(AAm-*co*-AA) hydrogels at pH = 0.35, *E** increased from 134 ± 5 kPa at 0 wt.% AA to 218 ± 29 kPa at 12 wt.% AA. This can be attributed to an increase in hydrogen bonding between carboxylic acid (-COOH) and amide ($-CONH_2$) groups[290,300,301] due to a decrease in water content (87 ± 0.5% to 79 ± 0.2%). *E** stayed relatively constant with increasing AA wt.% (106 ± 21 – 119 ± 5 kPa) for the hydrogels at pH = 13.8, corresponding with their uniform water content (90-91%). However at pH = 7, *E** was approximately 200 kPa for the P(AAm-*co*-AA) hydrogels with 0 – 6 wt.% AA but decreased to *E** = 133 ± 36 kPa with 9 wt.% AA. This deviates from the swelling results where water content increased slightly with 1 wt.% AA and then monotonically decreased.

As expected, the gels in NaOH (pH = 13.8, *I* = 0.25 M) have a lower modulus than those in HCl (pH = 0.35, *I* = 0.25 M) for all AA concentrations due

to greater swelling. Hence, it is perplexing that the gels in DI water (pH = 7, I = 0 M) exhibited the highest moduli at low AA concentrations, despite experiencing similar swelling behavior as the NaOH samples. One possible explanation is the gels in DI water swelled so much due to electrostatic repulsion between carboxylate ions that the chains extended and became rigid, which has been observed for various polyelectrolyte hydrogels.[126,297,302,303] However in all of these studies, the gels exhibited this non-Gaussian behavior and extensibility at higher ionic molar ratios of the charged species (>15 mol.%) than those explored here. Additionally, we observe that E^* decreases with higher AA wt.% in DI water, so it is unlikely that chain stiffening due to electrostatic repulsion is occurring. Alternatively, others have hypothesized that effective crosslinking density decreases with increasing charge density for many polyelectrolyte hydrogels,[297,303] which may explain why we observe a decrease in E^* with increasing AA concentration. But if this were the case, the swelling results would have reflected this crosslinking density decrease by increasing in water content with AA wt.%, which is not what was observed.

Another factor that may be influencing the elastic modulus of these gels is degradation caused by the extremely corrosive conditions of 0.5 M HCl (pH = 0.35) and 0.5 M NaOH (pH = 13.8). As previously mentioned, the crosslinker may be susceptible to hydrolysis at pH 13.8, decreasing the effective crosslinking density. Not only would this reduce the modulus compared to those

in DI water, but it would also explain why there was not a significant change in E^* with increasing AA wt.% for the gels in NaOH. This hypothesis is plausible since it was observed that swelling significantly increased when the hydrogels equilibrated in basic conditions were placed in DI water (**Figure 7.12**), implying that crosslinks may have broken during the initial swelling in NaOH.

7.3.3 Superlubricity in Extreme Environments

The average friction coefficient for the P(AAm-*co*-AA) hydrogels were calculated over 25 sliding cycles at F_n = 4 mN. The effects of solution pH on the friction coefficients are shown in **Figure 7.4a**. By just altering the solution pH and AA concentration, the friction coefficients of the P(AAm-*co*-AA) hydrogels were tuned two orders of magnitude from $\mu = 0.17 \pm 0.01$ at pH = 0.35 (0 wt.% AA) to achieving superlubricity ($\mu = 0.005 \pm 0.001$) at pH = 7 (12 wt.% AA). In all pH conditions, the friction coefficients decreased with increasing AA concentration. The friction coefficients also decreased with increasing pH across all AA concentrations, except at 12 wt.% AA. These results are within the range of values found by Ma *et al.*, who observed tunable friction for pure polyacrylic acid nanohydrogel brushes.[295] At pH = 2, their PAA brushes exhibited friction coefficients $\mu = 0.3 – 0.4$, while low friction ($\mu < 0.01$) was observed at pH = 12.[295] Dehghani *et al.* also demonstrated similar pH-tunability for polyelectrolyte brushes [304]. However, we were able to demonstrate this tunability for a bulk

hydrogel in both extreme and neutral pH conditions and achieved superlubricity with just 12 wt.% AA. The effects of applied normal force and sliding velocity on the tribological properties of P(AAm-*co*-AA) hydrogels are described in **Section 7.6.9.**

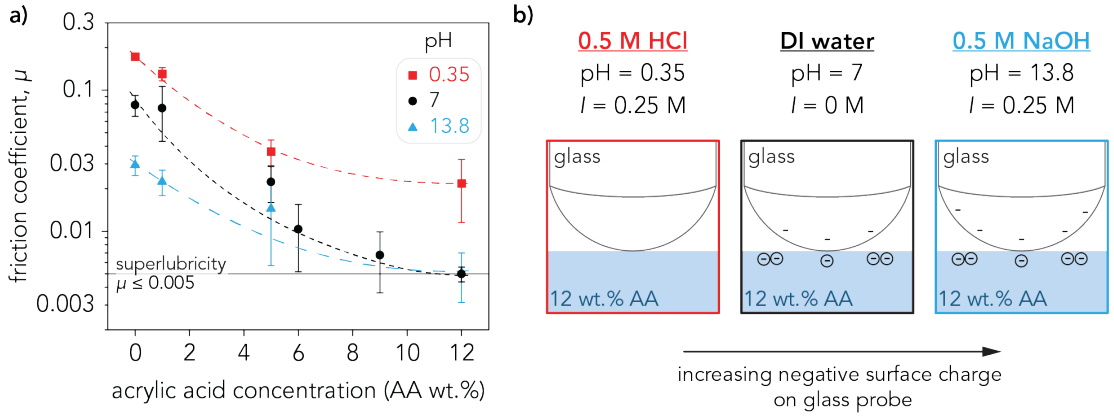

Figure 7.4 (a) Friction coefficient, μ, for the P(AAm-*co*-AA) hydrogels as a function of AA concentration plotted on a log–log scale. For all pH values, the friction coefficient decreased with increasing AA concentration. Friction was the highest at pH = 0.35 (red squares) with 0 wt.% AA (μ = 0.17 ± 0.009) and decreased to μ = 0.02 ± 0.01 at 12 wt.% AA. The hydrogels with low AA concentration (0 – 5 wt.% AA) had the lowest μ in NaOH (blue triangles), but μ was lower in DI water (black circles) at higher AA concentrations. Superlubricity was achieved for the P(AAm-*co*-AA)-12 hydrogel in DI water (μ = 0.005 ± 0.0006) and NaOH (μ = 0.005 ± 0.002). The dashed lines are guidelines and not meant to indicate a fit. Each data point is an average of three samples (n = 3) with the error bars as the standard deviation. **(b)** Schematic depicting the surface charge of the glass probe at pH = 0.35, 7, and 13.8. Since the friction coefficient is a systems property and not an intrinsic material property, μ depends on the properties of the countersurface as well as the substrate. The surface charge of glass increases with increasing pH, and the electrostatic repulsion between the carboxylate ions in the P(AAm-*co*-AA) hydrogels and SiO^- ions in the glass probe may be contributing to the lower friction exhibited in DI water and NaOH.

For charge-neutral hydrogels, such as polyacrylamide, there is a strong correlation between the friction coefficient and mesh size, which is influenced by water content. Scaling concepts[137] and recent experimental investigations of charge-neutral aqueous gels[112] suggest that the elastic modulus (E) decreases

with increasing swelling due to an increase in the mesh size (ξ) where $E \sim \xi^{-3}$; it is therefore expected that less swollen hydrogels have greater stiffness due to a smaller mesh size.[150] Additionally, previous reports have demonstrated that the friction coefficient scales with the mesh size as $\mu \sim \xi^{-1}$ for PAAm hydrogels tested in a self-mated, Gemini configuration (where both the substrate and countersurface are composed of PAAm).[150] However as demonstrated by the swelling, modulus, and friction coefficient results herein, these scaling relationships do not extend to P(AAm-*co*-AA) hydrogels.

For charged polyelectrolyte hydrogels like P(AAm-*co*-AA), the correlation between water content and friction coefficient is not as clear. Liu *et al.* demonstrated that the friction coefficient of pure poly(acrylic acid) hydrogels decreased with increasing water content.[305] Conversely, Gong *et al.* postulated that the friction coefficient of strongly charged polyelectrolyte gels swollen in water has no dependence on water content.[124] This is shown in our own results across all pH conditions, where there is no clear trend between E^* or μ with water content (**Figure 7.14** and **Figure 7.15**). At pH = 0.35, μ decreased with increasing AA concentration despite the water content decreasing and stiffness increasing with AA wt.%. Consequently, high water content and low elastic modulus do not necessarily indicate low friction, and other mechanisms need to be considered to understand the tribological behavior of the P(AAm-*co*-AA) hydrogel.

7.4 Possible Mechanisms of Superlubricity

7.4.1 Contributions of Electrostatics to Superlubricity

Electrostatic interactions have long been known to influence the tribological properties of polyelectrolyte hydrogels. Gong *et al.* demonstrated that the friction coefficients of polyelectrolyte hydrogels depend on their charge density and the charge of the sliding countersurface.[124,306,307] When the countersurface and hydrogel have the same charge, friction decreases with increasing surface charge density due to greater electrostatic repulsion between the two sliding interfaces and the formation of a solvent layer.[124,272,306–309] Models have been developed to predict the thickness of this fluid layer, which depend on variables such as contact pressures and swelling ratios.[124,310–314]

For our experiments, borosilicate glass was used as the sliding countersurface (**Figure 7.4b**). Previous studies have demonstrated that glass has a negative surface charge density in water[315] and that surface charge density increases with increasing pH.[177,316] Since friction is a systems property and is dependent on the countersurface material, having a negatively charged countersurface such as glass will lead to electrostatic interactions between the charged hydrogel surfaces.[309] At pH = 0.35, neither the glass probe nor P(AAm-*co*-AA) hydrogel should have any charge, justifying the high friction coefficients. Conversely, at pH = 7 both the probe and hydrogel should be negatively charged. Repulsion between these sliding interfaces would explain the reduction

in friction across all AA concentrations. Therefore, the superlubricity and low friction coefficients exhibited by P(AAm-*co*-AA) hydrogels in water may be attributed to greater electrostatic repulsion between the glass probe and hydrogel surface due to increasing negative surface charge with increasing AA concentration. The further reduction in friction at pH = 13.8 can be rationalized by the increase in negative surface charge on the glass probe due to the increase in pH. However, crosslink degradation may be the dominant driving force for the low friction coefficients exhibited by the P(AAm-*co*-AA) hydrogels in NaOH (**Figure 7.16**). This would clarify why the P(AAm-*co*-AA) hydrogels with 0 wt.% AA at pH = 13.8 possessed lower E^* and μ than their counterparts at pH = 7 supposedly being pH-insensitive due to lack of ionizable functional groups.[129,135] However, this still does not explain the behavior of P(AAm-*co*-AA) at pH = 0.35, which had the highest μ across all AA concentrations. Therefore, other mechanisms such as hydrogel microstructure may be contributing to the tribological behavior of these P(AAm-*co*-AA) hydrogels.

7.4.2 Influence of Hydrogel Microstructure on Superlubricity

As demonstrated herein, solution pH plays an important role in the swelling behavior, mechanics, and tribological properties of P(AAm-*co*-AA) hydrogels by altering the protonation state of AA. Conversely, the pH of the pre-polymerized solution significantly impacts the microstructure of copolymerized hydrogels.

There have been many studies examining the effects of pH on the reactivity ratios of acrylamide and acrylic acid monomers.[317–321] While the actual values of these reactivity ratios are highly dependent on the reaction conditions (e.g., temperature, pH, ionic concentration, monomer concentration, etc.), the overarching trend is that the reactivity ratio of AAm (r_{AAm}) increases while the reactivity ratio of AA (r_{AA}) decreases with increasing pH.[317,319,320]

Since the pre-polymerized solution was not buffered, we observed that the pH decreased with increasing AA concentration (**Figure 7.17**). Rintoul and Wandrey predicted that $r_{AAm} < 1$ and $r_{AA} > 1$ for the pH range of the pre-polymerized solution (pH = 2.7 – 3.6).[320] Because the reactivity ratio of AA is greater than unity, there may have been preferential clustering of AA during copolymerization. Therefore, these P(AAm-*co*-AA) hydrogels likely do not have a homogeneous distribution of AA monomers throughout the network and instead may contain microscale regions of high AA concentration, which could lead to heterogeneous charge distributions within the hydrogel (**Figure 7.5**).

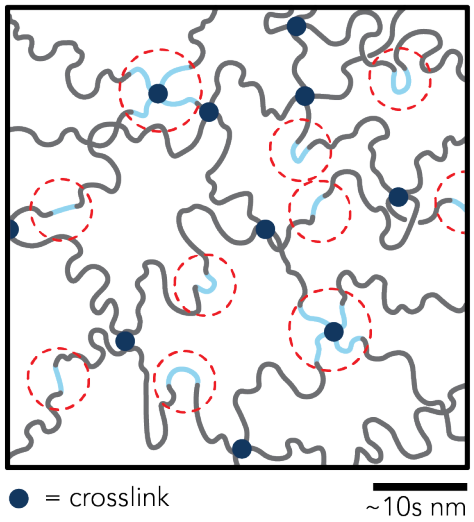

Figure 7.5 Illustration depicting possible clustering of AA (blue chains) within the P(AAm-*co*-AA)-12 hydrogel network. Due to low pH during polymerization, the reactivity ratio of acrylamide is less than unity, and the reactivity ratio of acrylic acid is greater than unity. Therefore, it is possible that AA-rich regions formed within the hydrogel network during polymerization leading to clusters of negatively charged domains, which may be partially responsible for superlubricity. Regions circled in red represent possible regions of counterion condensation and entrapment.

Others have noted microstructural inhomogeneities even in homopolymerized hydrogels.[109] Zeldovich *et al.* developed a model for inhomogeneous polyelectrolyte hydrogels with a heterogeneous distribution of charges. They posited that this inhomogeneous clustering of charge leads to counterion entrapment, prevents the counterions from contributing to the osmotic pressure and becoming "osmotically passive".[298] If clusters of AA regions within the P(AAm-*co*-AA) hydrogel formed, counterions may have gathered around these AA pockets and become osmotically passive, possibly clarifying the swelling behavior of the gels in NaOH. Recent investigations by Deptula *et al.* for P(AAm-*co*-AA) hydrogels with 8 wt.% total monomer concentration and > 20 wt.% AA demonstrated that AA-rich and AAm-rich

domains formed under confinement,[322] further supporting this hypothesis. The potential for AA clusters to exist in the network presents opportunities for future investigations using advanced microscopic and spectroscopic techniques. The contributions of potential AA cluster formation on the tribological properties of P(AAm-*co*-AA) hydrogels remain to be established, yet we postulate that negative charge clustering may lead to local repulsion between the hydrogel surface and the glass probe and interesting tribological properties that require further exploration.

7.4.3 Hydration Lubrication Often Leads to Superlubricity

For charged systems, hydration lubrication is often cited as a potential mechanism for the observed low friction. Hydration lubrication is a lubrication regime that can occur between charged, aqueous systems due to the formation of hydration layers surrounding the charges.[191–193,272,323] While the water molecules within the hydration layer are strongly attached to their charges, they are also dynamic, with the dipoles constantly fluctuating and the water molecules within the hydration shell rapidly exchanging with those within the bulk. Due to this mobility, these hydration shells fluidly shear when the applied shear rates are less than the relaxation rates of the hydration shells.[191,193] Coupled with the repulsion that occurs between hydration layers when in contact, hydration lubrication leads to extremely low friction coefficients. Counterions can also play

a role in friction reduction due to the short-range repulsion of their own hydration shells.

Many of the studies observing hydration lubrication were accomplished with mica substrates, which are molecularly smooth, coated with charged polymer brushes under confinement. When the separation distance between two charged polymer brush layers is smaller than the radius of gyration of the polymer chains, shear occurs across the hydration layers rather than the brush interface, reducing friction.[191,323] A more recent paper by Wang *et al.* also attributed the superlubricity of their bulk polyelectrolyte hydrogel to hydration layers.[272]

However, it has also been shown that anions are not as hydrated as cations and are not as effective at providing hydration lubrication.[191] Additionally, studies of hyaluronan – aggrecan complexes that possess COO^- groups and OSO_3^- groups have also shown that they have weak hydration layers that are not strongly bound and are not efficient at hydration lubrication.[324] Similarly, the P(AAm-*co*-AA) hydrogels have COO^- charged groups. Therefore, it is plausible that hydration lubrication may be one aspect contributing to the superlubricity demonstrated in our P(AAm-*co*-AA) hydrogels but not the only component.

7.5 Concluding Remarks

We demonstrated that poly(acrylamide-*co*-acrylic acid) (P(AAm-*co*-AA)) hydrogels achieved superlubricity by tuning the acrylic acid (AA) concentration (0 – 12 wt.%), solution pH (0.35, 7, 13.8), and ionic strength (I = 0 or 0.25 M). The swelling behavior and mechanical and tribological properties of these P(AAm-*co*-AA) hydrogels were characterized.

In 0.5 M HCl (pH = 0.35, I = 0.25 M), the carboxylic acid groups remain fully protonated, and the gels had the lowest water content and highest friction coefficients across all AA concentrations due to hydrogen bonding between carboxylic acid and amide groups. In 0.5 M NaOH (pH = 13.8, I = 0.25 M), the carboxylic acids groups are fully deprotonated, and the gels had the highest water content, lowest moduli, and lowest friction coefficients with 0 – 5 wt.% AA. This molarity of NaOH was chosen to ensure complete deprotonation of the AA, but extremely basic conditions may have had adverse effects on crosslinking concentration through the hydrolysis of amides in the crosslinker. Hydrogels equilibrated in unbuffered DI water exhibited the highest moduli despite having high water content. The friction coefficient generally decreased with increasing AA and increasing solution pH, as expected. Superlubricity was achieved with 12 wt.% AA in DI water and NaOH. The pH of the pre-polymerized solution may affect the microstructure of the P(AAm-*co*-AA) hydrogels, and AA clusters may form and induce inhomogeneous charge distributions. The contribution of this

inhomogeneity to the tribological properties has yet to be explored, but we postulate that tunable lubricity arises from changes in the protonation state of acrylic acid and electrostatic interactions between the glass probe and hydrogel surface.

7.6 Appendix

7.6.1 Swelling Measurements

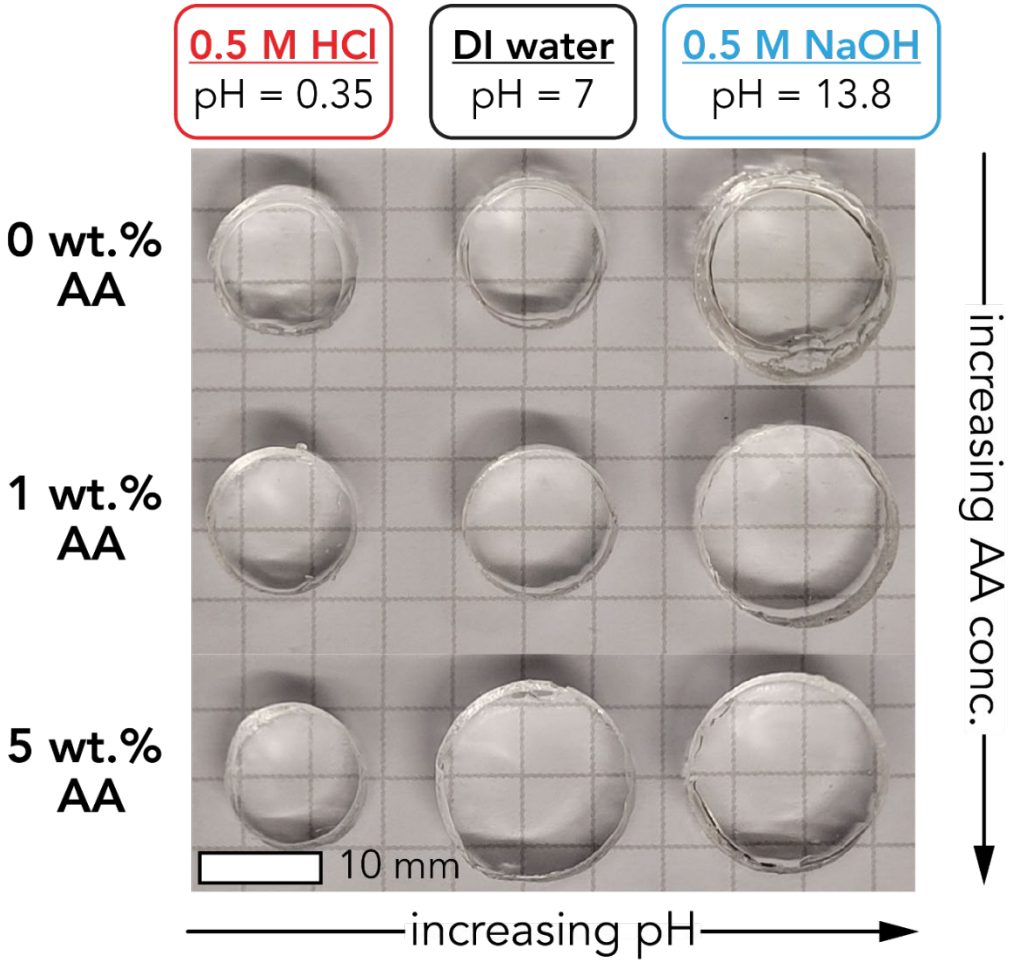

Figure 7.6 Comparison of P(AAm-*co*-AA) hydrogels with varying AA concentrations swollen in 0.5 M HCl (pH = 0.35, I = 0.25 M), unbuffered DI water (pH = 7, I = 0 M), or 0.5 M NaOH (pH = 13.8, I = 0.25 M) after reaching equilibrium swelling (4 days). Before swelling, all hydrogels had a diameter of 10 mm. Scale bar: 10 mm.

7.6.2 Optical Profilometry of Glass Probe

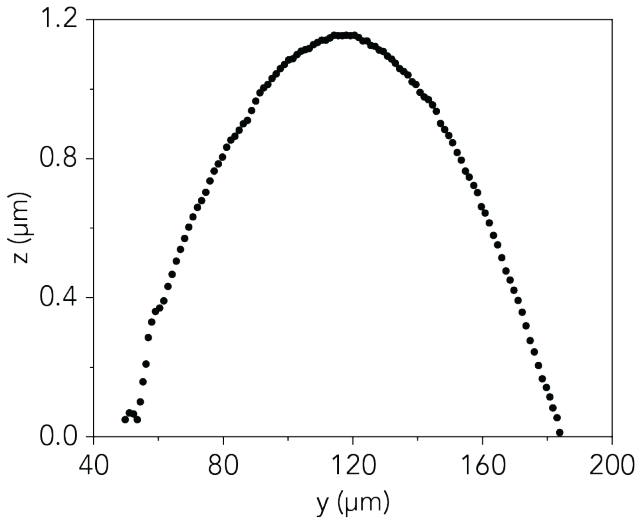

Figure 7.7 Optical profilometer trace of the hemispherical glass probe with radius of curvature R = 2 mm used during microindentation and friction experiments for the hydrogels in NaOH and HCl.

7.6.3 Microindentation Curves

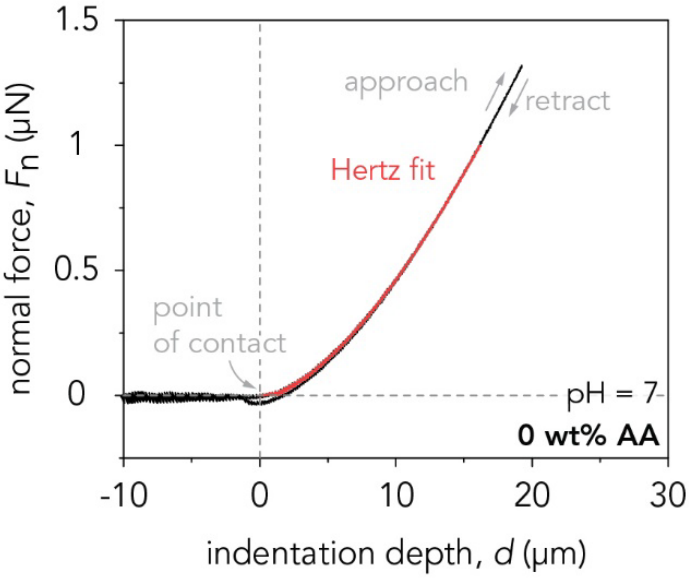

Figure 7.8 Microindentation curve for the P(AAm-*co*-AA)-0 hydrogel swollen in DI water with the approach and retraction parts of the curve labeled along with the point of contact. The Hertzian contact mechanics model (red) is fit to the approach curve up to F_n = 1 mN.

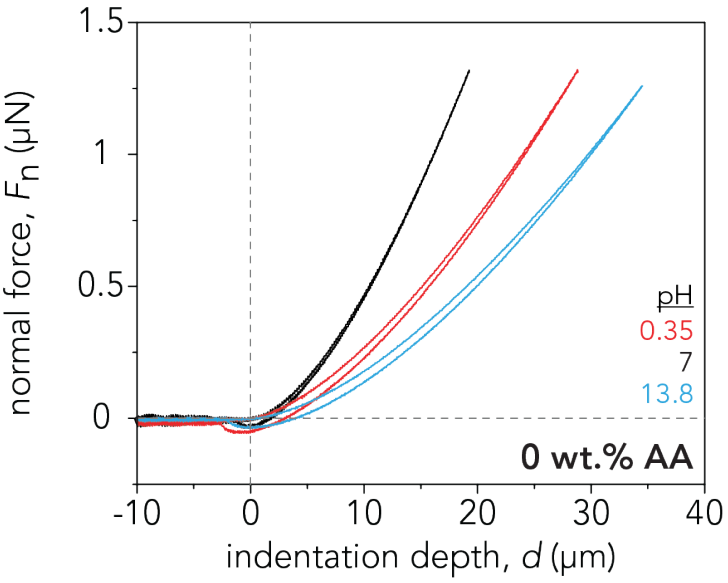

Figure 7.9 Representative indentation curves comparing the P(AAm-*co*-AA)-0 hydrogels at pH = 0.35 (red), pH = 7 (black), and pH = 13.8 (blue). There is not a monotonic decrease in the modulus with increasing pH.

7.6.4 Minimum Film Thickness Calculations

To ensure that the friction coefficients were measured within the boundary lubrication regime rather than the EHL regime, the sliding speed of v = 100 μm/s and normal force of F_n = 4 mN were carefully chosen. Using soft-elastohydrodynamic lubrication theory developed by Hamrock and Dowson as discussed in **Section 3.1**,[173] the minimum fluid film thickness, h_{min}, for soft-EHL lubrication was estimated to be between 9 – 17 nm using **Eqn. 3.2**, which was lower than the combined surface roughness of the probe and hydrogel surface. The minimum fluid film thickness was calculated by using the viscosity of water (η_o = 8.9 x 10^{-4} Pa·s), v = 100 μm/s, F_n = 1 and 4 mN, and E^* = 100 and 240 kPa

(the minimum and maximum measured E^* for the P(AAm-*co*-AA) hydrogels). **Table 7.1** displays the resulting h_{min} values.

Table 7.1 Minimum fluid film thickness values for the P(AAm-*co*-AA) hydrogels with the lowest and highest reduced elastic moduli at the lowest and highest applied normal force.

	E^* = 100 kPa	E^* = 240 kPa
F_n = 1 mN	17 nm	12 nm
F_n = 4 mN	13 nm	9 nm

Since h_{min} was less than the estimated surface roughness of the hydrogels ($R_a \approx 20$ nm), there was likely contact between the hydrogel surface and probe, indicating boundary-like lubrication. If h_{min} was significantly greater than the surface roughness of the hydrogel, then the measured superlubricity would be more likely due to a thick fluid film layer rather than the chemical composition of the hydrogel surface. At an applied normal force of 4 mN, the maximum pressure during sliding ranged between 9 – 15 kPa, depending on E^* of the P(AAm-*co*-AA) hydrogel. Since E^* scales with osmotic pressure and the applied contact pressures are much lower than E^*, it is unlikely that fluid flow or draining occurred, suggesting that the friction coefficients measured are not due to fluid flow or soft-EHL.[137]

The track length was chosen so the distance was at least 4 times the contact area diameter to ensure that the probe moved out of its initial contact area zone when sliding. **Table 7.2** shows the minimum track length necessary for applied normal forces of 1 mN and 4 mN for hydrogels with reduced elastic moduli of

100 kPa and 240 kPa. Hertzian contact mechanics was used to estimate the contact area diameter, d (**Eqn. 4.6**).

Table 7.2 Minimum track length required to ensure that the sliding path is at least four times the contact area diameter, assuming Hertzian contact mechanics.

	E^* = 100 kPa	E^* = 240 kPa
F_n = 1 mN	2.3 mm	1.7 mm
F_n = 4 mN	3.6 mm	2.7 mm

7.6.5 Friction Loops

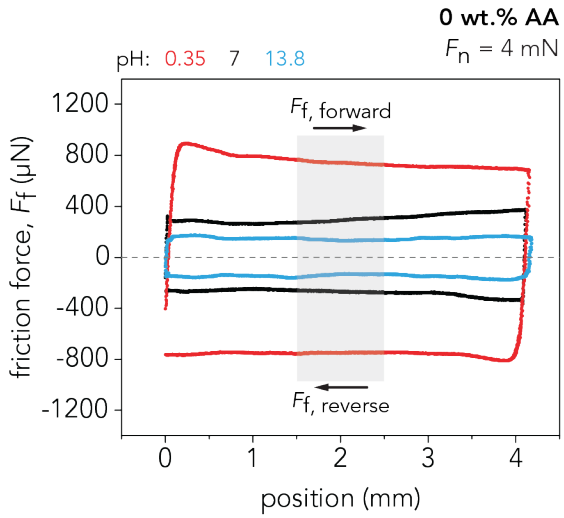

Figure 7.10 Comparison of representative friction force loops as a function of pH for the P(AAm-*co*-AA)-0 hydrogels. The forward and reverse directions of the friction loop are labeled. The middle 25% of the loop (gray area) is used to calculate the friction coefficient. As pH increases, the friction force decreases.

7.6.6 Henderson-Hasselbalch Equation

Rearranging the Henderson-Hasselbalch equation, the ratio of deprotonated acrylic acid (A^-) to protonated acrylic acid (HA) is as follows:

$$R = \frac{[A^-]}{[HA]} = 10^{(pH - \mathrm{p}K_a)} \qquad \text{Eqn. 7.3}$$

The fraction of protonated AA can be estimated as f_{HA} = 1/(1+R) while the fraction of deprotonated AA can be estimated as f_{A^-} = R/(1+R). With a pK_a = 4.5, f_{HA} = 0 and f_{A^-} = 1 when pH = 13.8 (0.5 M NaOH). When pH = 0.35 (0.5 M HCl), f_{HA} = 1 and f_{A^-} = 0. Therefore, it is expected that the AA is fully protonated in the HCl solution and deprotonated in the NaOH solution.

7.6.7 Degradation of Crosslinks

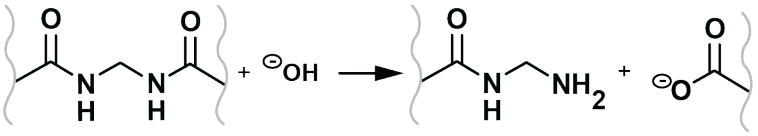

Figure 7.11 Possible hydrolysis of *N,N'*-methylenebisacrylamide leading to crosslink degradation within the hydrogel network.

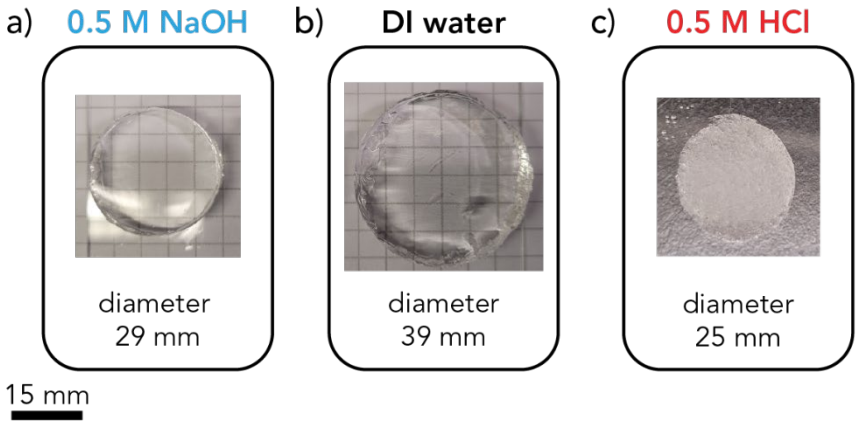

Figure 7.12 Comparison of the P(AAm-*co*-AA)-9 hydrogels swollen in various solutions. Scale bar: 15 mm **(a)** When placed in 0.5 M NaOH right after polymerization, the hydrogel reached equilibrium swelling. In this case, the hydrogel swelled to a diameter of 29 mm from a starting diameter of 16 mm. **(b)** When transferred directly from the NaOH solution into pure DI water, the hydrogel swelled to a diameter of 39 mm after three days, indicating that crosslinks might have been potentially broken while swelling in NaOH. **(c)** Within hours of being transferred from DI water into a 0.5 M HCl solution, the hydrogel collapsed and became brittle.

7.6.8 Hydrogel Synthesis

Table 7.3 Mass of each component in the pre-polymerized hydrogel solutions, where T represents the total polymer content and C represents the crosslinker concentration.

AA: AAm (molar ratio)	AA/ AAm molar ratio	T (wt%)	C (wt%)	AAm (mg)	AA (mg)	MBAm (mg)	TEMED (mg)	APS (mg)	MilliQ water (mg)
0	0/100	33.4	1.1	2500	0	27.1	20.4	20.1	5000
0.01	1/99	33.6	1.1	2500	25.3	27.4	20.4	20.1	5000
0.02	2/98	33.8	1.1	2500	50.7	27.7	20.4	20.1	5000
0.05	5/95	34.5	1.1	2500	126.7	28.5	20.4	20.1	5000
0.07	6/94	34.9	1.1	2500	169	28.9	20.4	20.1	5000
0.10	9/91	35.6	1.1	2500	253.4	29.8	20.4	20.1	5000
0.13	12/88	36.3	1.1	2500	337.9	30.7	20.4	20.1	5000

The total polymer content (T, wt.%) and crosslinker concentration (C, wt.%) were calculated with **Eqn. 2.1** and **Eqn. 2.2**.

7.6.9 Sliding Speed and Normal Force Effects on Friction

It has been demonstrated by Gong and others that the friction coefficient for charge-neutral and polyelectrolyte hydrogels is highly dependent on the testing conditions, including sliding speed and applied normal load.[176,177,272,325] Urueña *et al.* demonstrated that the friction coefficient of charge-neutral polyacrylamide hydrogels decreased with increasing applied normal force[176] while Gong *et al.* corroborated this trend for several other charge-neutral and polyelectrolyte hydrogels.[177] Similar results were found for copolymerized zwitterionic hydrogels within the hydrodynamic lubrication regime.[272] For the P(AAm-*co*-AA) hydrogels, the effects of applied force on the friction coefficient varied depending on AA concentration and pH (**Figure 7.13**). At pH = 13.8 and

lower AA concentrations (0 – 5 wt.%), the friction coefficient decreased with increasing force. But for the gels at lower pH (pH = 0.35 and 7) across all AA concentrations and for the gels at pH = 13.8 at 12 wt%, the friction coefficient stayed relatively constant with increasing force. The friction coefficient of hydrogels also has a dependence on sliding speed and can either increase[98,325] or exhibit Stribeck-like behavior.[272] For polyelectrolytes, friction increases with sliding velocity due to changes in the water layer at the interface caused by the electrostatic repulsion between the electric double layers.[307] While the sliding speed was not varied in our experiments, it can be postulated that the friction coefficient of these P(AAm-*co*-AA) hydrogels would increase with sliding speed.

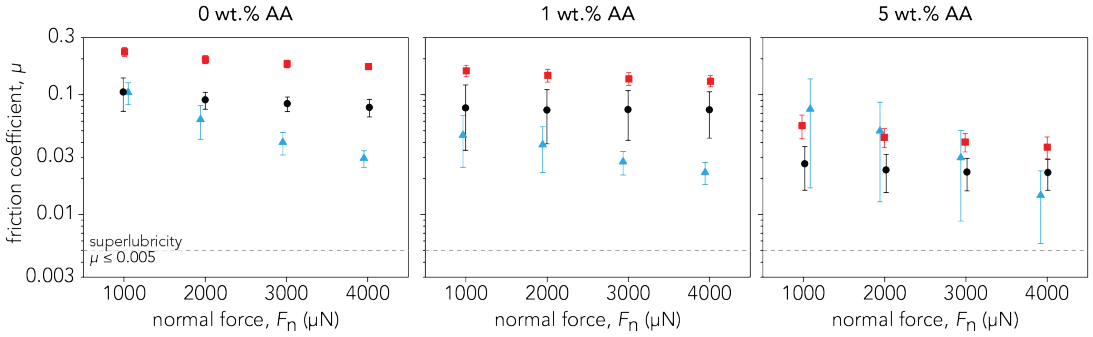

Figure 7.13 Friction coefficient, μ, as a function of applied normal force, F_n for P(AAm-*co*-AA) hydrogels at three AA concentrations (0, 1, and 5 wt.% AA). The effects of normal force on the friction coefficient varied depending on pH. The friction coefficient for the gels at pH = 13.8 (blue triangles) noticeably decreased with increasing force. For the gels at pH = 0.35 (red squares) and pH = 7 (black circles), the friction coefficient slightly decreased with increasing force or stayed relatively constant.

7.6.10 Water Content, Elastic Modulus, and Friction

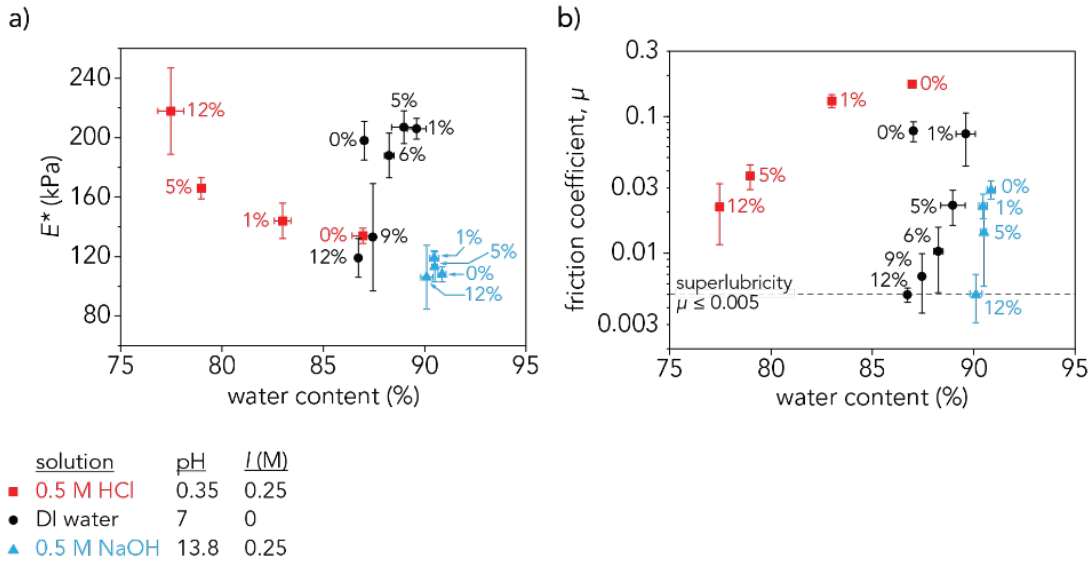

Figure 7.14 (a) Reduced elastic modulus, E^*, and **(b)** friction coefficient, μ, as a function of water content (%). Each data point is labeled with the AA wt.%. There is no clear trend between water content and E^* or μ. The modulus and the friction coefficient do not predictably decrease with increasing water content.

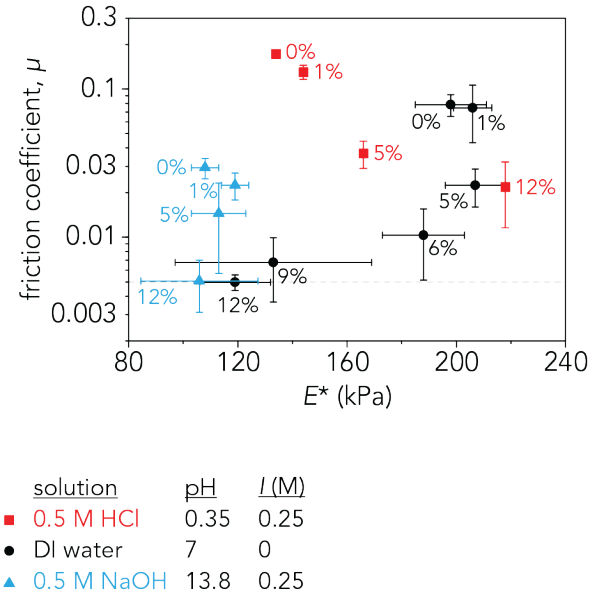

Figure 7.15 Friction coefficient, μ, as a function of reduced elastic modulus, E^*. Each data point is labeled with the AA wt.%. There is no clear trend between hydrogel stiffness and friction.

7.6.11 Impact of Mechanical Degradation

P(AAm-*co*-AA) hydrogels with 0 wt.% and 12 wt.% were characterized before and after one freeze-thaw cycle. After swelling for at least three days in DI water, the gels were characterized via microindentations and sliding experiments and then placed in -18°C without any excess liquid for at least 12 h. The gels were then left to thaw at room temperature (23°C) and then characterized again. This freeze-thaw cycle mechanically degraded the gels, physically breaking crosslinks to simulate the potential chemical degradation experienced by the hydrogels at pH = 13.8 through hydrolysis. At 0 wt.% AA, E^* and μ both decreased after mechanical degradation, but at 12 wt.% AA, E^* decreased while μ stayed the same. This may explain why the gels at pH = 13.8 had lower μ than the gels at pH = 7 at lower AA wt.% (0 – 5 wt.%). Any potential electrostatic interactions, or lack thereof, were trivial compared to crosslink degradation via hydrolysis.

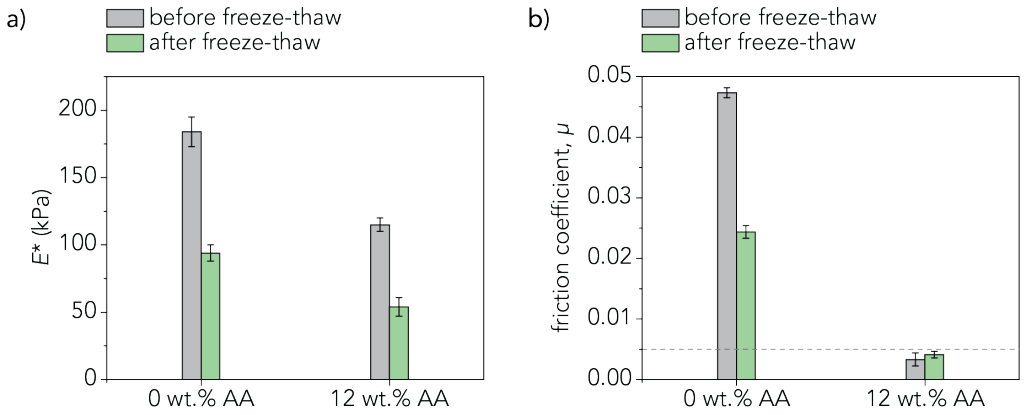

Figure 7.16 (a) Reduced elastic modulus, E^*, and **(b)** friction coefficient, μ, of P(AAm-*co*-AA) hydrogels at 0 wt.% and 12 wt.% before and after one freeze-thaw cycle. For P(AAm-*co*-AA)-0,

*E** and μ decreased after mechanical degradation of the gel through freeze-thaw. For P(AAm-*co*-AA)-12, *E** decreased but μ stayed the same.

7.6.12 Influence of pH on Reactivity Ratios

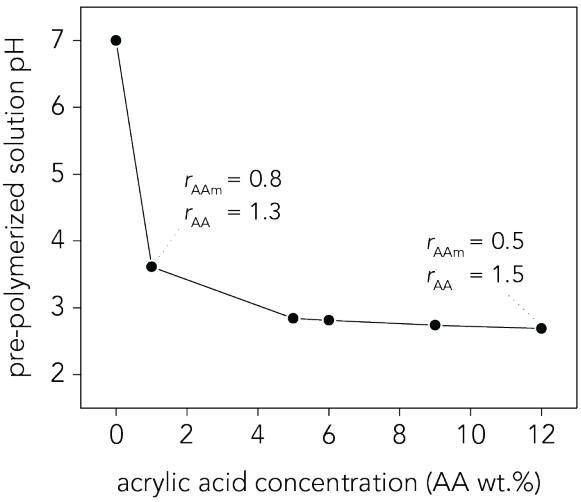

Figure 7.17 Pre-polymerized solution pH as a function of AA concentration labeled with reactivity ratios of AAm (r_{AAm}) and AA (r_{AA}) from Ref. [320]. While there is a slight decrease in the reactivity ratio for AAm and increase for AA with increasing AA concentration, the general trend of $r_{AAm} < 1$ and $r_{AA} > 1$ stays consistent.

8 CHAPTER 8: PH-RESPONSIVENESS OF NON-IONIC HYDROGELS

Polyacrylamide is typically considered a non-ionic hydrogel. Yet, it has been shown to demonstrate pH-responsive tribological behavior, as demonstrated in the previous chapter (0 wt.% AA). To determine the origins of this pH-responsiveness, we prepared polyacrylamide hydrogels with two different initiating chemistries: a reduction-oxidation (redox)-initiated system using ammonium persulfate (APS) and *N,N,N'N'*-tetramethylethylenediamine (TEMED) and a UV-initiated system with 2-hydroxy-4'-(2-hydroxyethoxy)-2-methylpropiophenone (Irgacure 2959). Hydrogel swelling, mechanical properties, and tribological behavior were investigated in response to solution pH (ranging from ≈ 0.34 to 13.5). For polyacrylamide hydrogels in sliding contact with glass hemispherical probes, friction coefficients decreased from $\mu = 0.07 \pm 0.02$ to $\mu = 0.002 \pm 0.002$ (redox-initiated) and from $\mu = 0.05 \pm 0.03$ to $\mu = 0.003 \pm 0.003$ (UV-initiated) with increasing solution pH. With hemispherical polytetrafluoroethylene (PTFE) probes, friction coefficients of redox-initiated hydrogels similarly decreased from $\mu = 0.06 \pm 0.01$ to $\mu = 0.002 \pm 0.001$ with increasing pH. Raman spectroscopy measurements demonstrated hydrolysis and the conversion of amide groups to carboxylic acid in basic conditions. We therefore propose that the mechanism for pH-responsive friction in polyacrylamide hydrogels may be credited to hydrolysis-driven swelling through the conversion of side chain amide groups into carboxylic groups and/or

crosslinker degradation. Our results could assist in the rational design of hydrogel-based tribological pairs for biomedical applications from acidic to alkaline conditions.

This chapter was reproduced in part with permission from:[326]

Chau, A.L., Pugsley, C.D., Miyamoto, M.E., Tang, Y., Eisenbach, C.D., Mates, T.E., Hawker, C.J., Valentine, M.T., and Pitenis, A.A., pH-Dependent Friction of Polyacrylamide Hydrogels. *Tribology Letters,* **71**, 2023.

Table of Contents

8.1 Introduction

The consensus in literature is that polyacrylamide is non-ionic, and its swelling properties are pH-independent due to the lack of ionizable functional groups.[129,327,328] To create pH-responsive hydrogels, acrylamide is often copolymerized with monomers containing ionizable groups, such as gelatin[129] or acrylic acid.[73,130,135,287,322] These ionizable groups deprotonate when solution pH exceeds the pK_a of the hydrogel, increasing negative charge within the network.[293] Our recent investigations of the tribological behavior of polyacrylamide gels copolymerized with acrylic acid have revealed pH-responsiveness; friction coefficients of the copolymerized gels decreased with increasing pH.[111] This pH-dependent friction behavior was attributed to the protonation state of the acrylic acid and electrostatic interactions between the hydrogel and glass probe. Surprisingly, the friction coefficient of charge neutral polyacrylamide hydrogels – without any acrylic acid – also decreased with increasing pH.[111] While the existence of local charges along polyacrylamide chains has been proposed to account for adhesion to colloidal probes during nanoindentation,[329] systematic studies have not yet been conducted to investigate the effects of pH on the mechanical or tribological properties of polyacrylamide hydrogels. In this study, 33 wt.% polyacrylamide hydrogels were synthesized via free-radical polymerization at room temperature with two different initiating chemistries. Reduction-oxidation (redox)-initiated hydrogels

using ammonium persulfate (APS) and *N,N,N'N'*-tetramethylethylenediamine (TEMED) as the initiator and catalyst respectively were compared to UV-initiated hydrogels with 2-hydroxy-4'-(2-hydroxyethoxy)-2-methylpropiophenone (Irgacure 2959) as the photoinitiator. Hydrogels were swollen in solutions with varying pH, and their swelling behavior and elastic modulus were compared. Their tribological behavior was investigated using glass and polytetrafluorethylene (PTFE) countersurfaces, and the mechanism behind this pH-responsive behavior was explored with Raman spectroscopy.

8.2 Materials & Methods

8.2.1 Hydrogel Synthesis

Polyacrylamide disks (pre-swollen dimensions: 4 mm thickness, 26 mm diameter) were prepared with two different initiating systems. The first set of gels were prepared with a reduction-oxidation (redox)-initiating system using ammonium persulfate (APS, Sigma-Aldrich, Product #A3678) as the initiator and *N,N,N',N'*-tetramethylethylenediamine (TEMED, Sigma-Aldrich Product #T9281) as the catalyst, as shown in **Figure 8.1a**. The second set of gels were prepared using 2-hydroxy-4'-(2-hydroxyethoxy)-2-methylpropiophenone (Irgacure 2959, Sigma-Aldrich, Product #410896) as the photoinitiator (**Figure 8.1b**). The mechanism of free-radical generation for these initiating systems is detailed in Wilems *et al*.[65] Stock solutions of acrylamide (AAm, Sigma-Aldrich

Product #A9099) (1 g/mL), *N,N'*-methylenebisacrylamide (MBAm, Sigma-Aldrich Product #M7279) (25 mg/mL), APS (50 mg/mL), and TEMED (50 mg/mL) were prepared in ultrapure water. The final AAm concentration in both the redox- and UV-initiated gels was 0.5 g/mL (≈ 33 wt.%) and molar ratio of monomer:crosslinker was 200:1 (≈ 0.4 wt.%). Gels were cast between two flat and smooth polystyrene sheets (average surface roughness, R_a < 20 nm), and reactions were conducted in ambient conditions (20°C). A thermocouple (Fluke 51 II Thermometer Type-K) was used to monitor the temperature of the solution during polymerization. For the redox-initiated hydrogels, the molar ratios of monomer:catalyst and monomer:initiator were 200:1 and 400:1 (both ≈ 0.3 wt.%), respectively. For the UV-initiated hydrogels, a molar ratio of 3,200:1 (≈ 0.03 wt.%) monomer:photoinitiator was used. Redox-initiated gels polymerized within 5 minutes, whereas UV-initiated gels polymerized under UV light for 22 minutes.

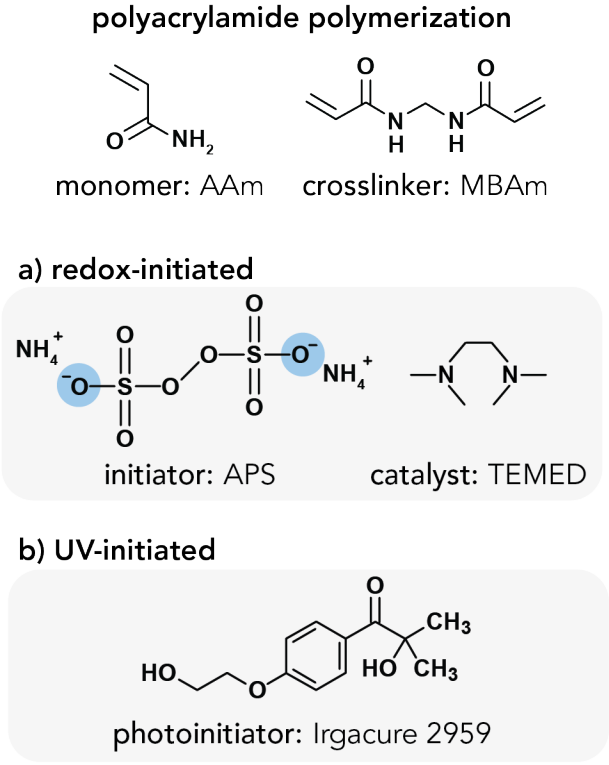

Figure 8.1 Chemical structures of the acrylamide monomer and *N,N'*-methylenebisacrylamide crosslinker. For all polyacrylamide hydrogels, the final monomer concentration was ≈ 33 wt.% and molar ratio of monomer:crosslinker was 200:1 (≈ 0.4 wt.%). The chemical components of the **(a)** redox-initiated and **(b)** UV-initiated systems. Blue circles highlight negative charge.

A 26 mm diameter circular punch was used to section the gels, which were swollen in solutions of varying pH (see **Table 8.1**). With the exception of DI water, solution pH was determined using a Mettler Toledo FiveEasy pH meter. For DI water, which has exceptionally low ion content, the pH was measured with litmus paper (Whatman pH indicator papers, CF strips, pH range = 0 – 14, Cat. No. 2613-991), which indicated that fresh unbuffered MilliQ water had a pH ≈ 6 – 7, consistent with the measured resistivity of 18.2 MΩ·cm. The pH is reported as an approximate ≈ 7 in this case.

Table 8.1 Solution concentrations, ionic strengths, and pH values for the polyacrylamide hydrogels.

Solution	Ionic Strength	pH
0.5 M HCl	0.5 M	0.34
0.001 M HCl	0.001 M	2
unbuffered DI water (18.2 MΩ·cm)	0 M	≈ 7
0.001 M NaOH	0.001 M	10
0.5 M NaOH	0.5 M	13.5

8.2.2 Swelling Behavior

Hydrogel water content was calculated following the methods described in **Section 7.2.2**.[111] Briefly, hydrogels were equilibrated in solutions ranging from pH = 0.34 to pH = 13.5 (**Table 8.1**) for at least one week before their swollen mass (m_s) was measured with a Mettler Toledo XPR105DR analytical balance. The dried mass (m_d) was obtained after drying the samples in an oven for 10 days at 60°C, and the water content (%) was calculated using **Eqn. 7.2.** The volume change (%) was also calculated using **Eqn. 6.1** following the methods described in **Section 6.2.2**.[69] The reported water content and volume change values herein are the averages and standard deviations from three independent hydrogel samples (n = 3).

8.2.3 Micromechanical Analysis & Friction Measurements

Tribological experiments and microindentations were conducted as outlined in **Section 4.3** and **Section 4.4.** For the tribological experiments, a hemispherical borosilicate glass probe (Type 1 Class A; radius of curvature,

R = 2.6 mm) and polytetrafluoroethylene (PTFE) probe (radius of curvature, R = 3.2 mm) were used as sliding countersurfaces. Probe surface roughness analyses are included in **Section 8.5.1**. Representative Hertzian fits of the approach curve can be found **Section 4.4.**

8.2.4 Raman Spectroscopy

Polyacrylamide and poly(acrylamide-*co*-acrylic acid) (P(AAm-*co*-AA)) hydrogels were prepared for Raman spectroscopy to determine changes in functional groups over different pH environments. Redox-initiated hydrogels were swollen in pH = 0.34, pH ≈ 7, or pH = 13.5 for 10 days and then equilibrated in DI water for two weeks. The P(AAm-*co*-AA) hydrogels were synthesized following the protocol in Chau *et al.*[111] and swollen in DI water for two weeks. For all samples, the solution was exchanged daily to ensure that no unreacted monomer or excess NaOH or HCl would interfere with the measurements. Laser Raman spectroscopy was then conducted at room temperature on swollen polyacrylamide and P(AAm-*co*-AA) hydrogels using a confocal Raman microscope (Horiba Jobin Yvon T64000) with an excitation wavelength of 488 nm and laser power of 400 mW. Samples were gently dried with lens paper to remove excess liquid and then placed on a fused quartz microscope slide before measurements. During spectra acquisition, the laser light was focused with a 50x objective lens 10 μm below the sample surface, and

spectra data was obtained with a resolution of 0.66 cm^{-1}. Three spectra were obtained at separate locations per sample, and each spectrum was the average of 25 eight-second measurements at the same location. Using the Spectragryph software, spectra data were smoothed using a 3rd-order Savitsky-Golay filter with an interval of 30, and spectra baselines were removed using the adaptive baseline subtraction tool with a coarseness of 15. For quantitative analyses, the deconvolution of peaks was carried out in Origin with details described in Section 8.5.4.

8.3 Results & Discussion

8.3.1 Observations of pH-Responsive Behavior

The mechanical and tribological properties of redox-initiated polyacrylamide hydrogels were compared to UV-initiated hydrogels to determine the source of their pH-responsiveness. As shown in Figure 8.2a, the friction coefficient decreased with increasing pH for both the redox-initiated and UV-initiated polyacrylamide hydrogels. This trend held for both sliding configurations: glass-on-gel and PTFE-on-gel.

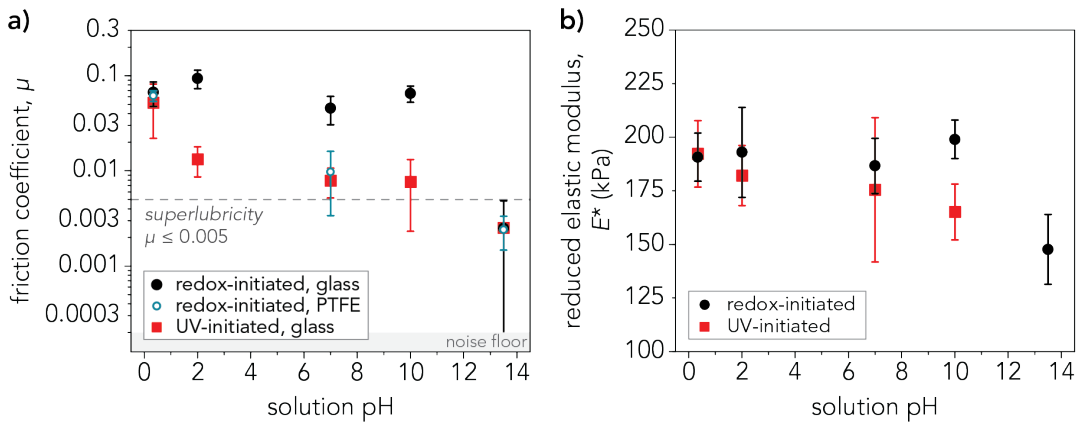

Figure 8.2 The tribological and mechanical properties of redox-initiated (black circle) and UV-initiated (red squares) hydrogels. **(a)** Friction coefficient, μ (semi-log plot) and **(b)** reduced elastic modulus, E^*, of polyacrylamide hydrogels (≈ 33 wt.% polymer) as a function of solution pH. The friction coefficients obtained with the PTFE-on-gel sliding configuration (open blue circles) for the redox-initiated hydrogels follow the same trend as the glass-on-gel sliding configuration (filled black circles), where μ decreases with increasing pH. Each data point is an average of three independent samples (n = 3) with error bars as the standard deviation, except for the UV-initiated gels at pH = 13.5, where n = 2. The experimental noise floor for the tribometer is μ = 0.0002, calculated following the methods in Chau *et al.*[111]

The friction coefficient was sensitive to initiator selection; redox-initiated polyacrylamide hydrogels exhibited higher friction coefficients than photoinitiated samples with identical polymer composition. The friction coefficient of redox-initiated hydrogels against a glass countersurface drastically decreased from μ = 0.07 ± 0.02 (pH = 0.34) to μ = 0.002 ± 0.002 (pH = 13.5). For UV-initiated hydrogels, friction coefficient decreased from μ = 0.05 ± 0.03 (pH = 0.34) to μ = 0.003 ± 0.003 (pH = 13.5). In both cases, the decrease in friction coefficient surpassed superlubricity ($\mu \leq 0.005$). Even with a PTFE countersurface, friction coefficients for the redox-initiated hydrogels decreased with increasing pH, from μ = 0.06 ± 0.01 in acid to μ = 0.002 ± 0.001 in base. The reduced elastic modulus followed a similar trend to the tribological

behavior, with redox-initiated gels maintaining relatively consistent E^* (186 ± 11 kPa) until pH = 13.5 when it decreased to E^* = 146 ± 16 kPa. For UV-initiated gels, reduced elastic modulus gradually decreased from E^* = 192 ± 15 kPa to E^* = 165 ± 13 kPa with increasing pH (**Figure 8.2b**).

Surprisingly, water content (%) was virtually pH-independent, with redox- and UV-initiated hydrogels maintaining 85 ± 3% water across all pH conditions (**Fig. 3a**). Previous swelling studies comparing completely dried and swollen hydrogels also reported pH-independent swelling behavior.[73,129,130,328] However, hydrogels in alkaline conditions were noticeably larger than those swollen in acidic and neutral solutions. Moreover, elastic modulus typically scales with swelling,[114,137,330] with lower elastic moduli corresponding to greater swelling.[129,137] Therefore, as a comparison to water content, which is one of the many approaches that involves hydrogel desiccation (**Section 2.3**, **Table 2.1**), we evaluated volume change, which allowed the hydrogels to remain hydrated. Here, the volumes of the redox-initiated hydrogels immediately after polymerization were compared to their fully swollen volumes (**Eqn. 6.1**). When calculating volume change rather than water content, the gels exhibited pH-dependent swelling and significantly increased in volume (457 ± 32%) at pH = 13.5 (**Figure 8.3b**), in agreement with the reduced elastic moduli trends (**Figure 8.2b**).

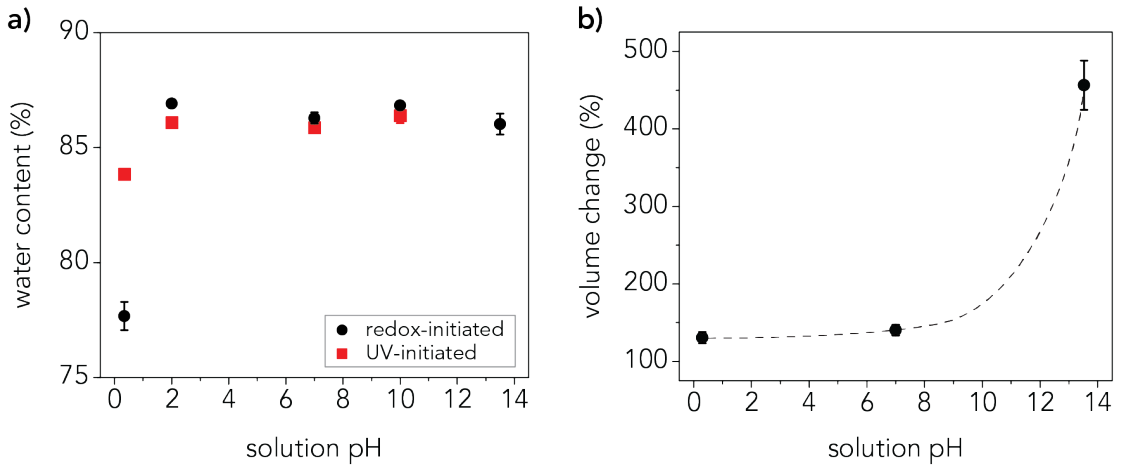

Figure 8.3 (a) Hydrogel water content (%) and **(b)** volume change (%) as a function of solution pH for redox-initiated (black circles) and UV-initiated (red squares) polyacrylamide hydrogels. Water content did not fully capture the swelling difference between the gels in acidic, neutral, and basic solutions, so volume change was used to represent the size change observed for the redox-initiated gels when swollen in basic solution. The dashed line is a guideline and not meant to indicate a fit. Each data point is an average of three samples (n = 3) with error bars as the standard deviation.

8.3.2 Effects of Free-Radical Initiators on Mechanical Properties

Redox- and UV-initiated polyacrylamide hydrogels slid against glass probes exhibit different friction coefficients and reduced elastic moduli despite having the same acrylamide concentration (≈ 33 wt.% before swelling) and molar ratio of monomer to crosslinker (200:1, corresponding to ≈ 0.4 wt.% before swelling). We observe somewhat lower elastic moduli for UV-initiated gels compared to redox-initiated gels across all pH solutions (**Figure 8.2b**) and significant reduction in friction coefficient with the glass countersurface, especially at higher pH (**Figure 8.2a**). One explanation for the differences in mechanical and tribological properties is the initiator selection. In previous studies of poly(ethylene glycol) (PEG) hydrogels, initiator selection impacted the

mechanical properties due to variations in gelation kinetics, which led to structural differences;[65] the redox-initiated PEG hydrogels had higher elastic moduli than the UV-initiated PEG hydrogels due to smaller mesh sizes. N-alkyl acrylamide/acrylic acid copolymer nanoparticles have also been reported to have differences in network structure due to the initiating chemistry.[106] Another possibility is initiator concentration, which has been shown to influence the swelling ratio, with increasing concentration leading to greater swelling.[331] Here, the redox-initiated hydrogels had a monomer:initiator molar ratio of 400:1 (≈ 0.3 wt.%), while the UV-initiated hydrogels had a molar ratio of 3,200:1 monomer:photoinitiator (≈ 0.03 wt.%). It is possible that the network structure is different since the UV-initiated hydrogels had a lower initiator concentration due to the low solubility limit of Irgacure 2959 in water (< 2%).[104] In both cases, the gels were cast against polystyrene sheets while exposed to atmospheric oxygen, which has been postulated to create a loosely crosslinked surface layer.[215,216,332] With lower concentration of photoinitiator, UV-initiated gels took longer to polymerize than redox-initiated gels, exposing them to oxygen longer, which could potentially lead to a more open network at the surface. While the difference in network structure may be indicated by the friction coefficient, it is not reflected in the elastic modulus or water content, indicating that it may be confined to the surface.

For redox-initiated polyacrylamide hydrogels in self-mated tribological contact, Urueña *et al*. demonstrated that friction coefficients decreased with increasing mesh size.[150] As our redox-initiated gels tested with PTFE probes exhibited similar friction coefficients to the UV-initiated gels tested with glass probes, our results suggest that the pH-responsiveness is indeed a function of the hydrogel. The difference in friction behavior between redox-initiated and UV-initiated gels against glass countersurfaces may suggest differences in mesh size since the same probe material was used. It is possible that our UV-initiated hydrogels have a larger *surface* mesh size than the redox-initiated hydrogels due to a combination of gelation kinetic differences and initiator concentration, with similar bulk properties, although further experimentation is needed.

8.3.3 Contributions of Probe-Mediated Electrostatics to Friction

The mechanism of hydrogel lubricity for polyelectrolyte hydrogels with charged sliding countersurfaces is often attributed to hydration lubrication[191–193,272,323] or electrostatic interactions.[124,306,307] By introducing charge to the hydrogel network via hydrolysis, electrostatic interactions between polyacrylamide hydrogels and smooth (S_a < 100 nm) glass probes may explain the decrease in friction coefficient with increasing pH. Redox-initiated polyacrylamide hydrogels exhibited similar trends in tribological behavior when slid against rough (S_a ≈ 1 μm) PTFE probes (**Figure 8.2a, Figure 8.7**). Although

PTFE is a well-known hydrophobic and inert material, its surface properties depend on solution pH and ionic strength. Its pH-dependent behavior arises from an interfacial water layer that accumulates OH^- ions at pH > 4 and H_3O^+ ions at lower pH values.[333] Since glass and PTFE are both pH-responsive, electrostatics may impact the resulting friction coefficients in both cases. **Figure 8.4** illustrates our predicted friction coefficient trend for polyacrylamide hydrogels with increasing pH if electrostatics was the main contributor.

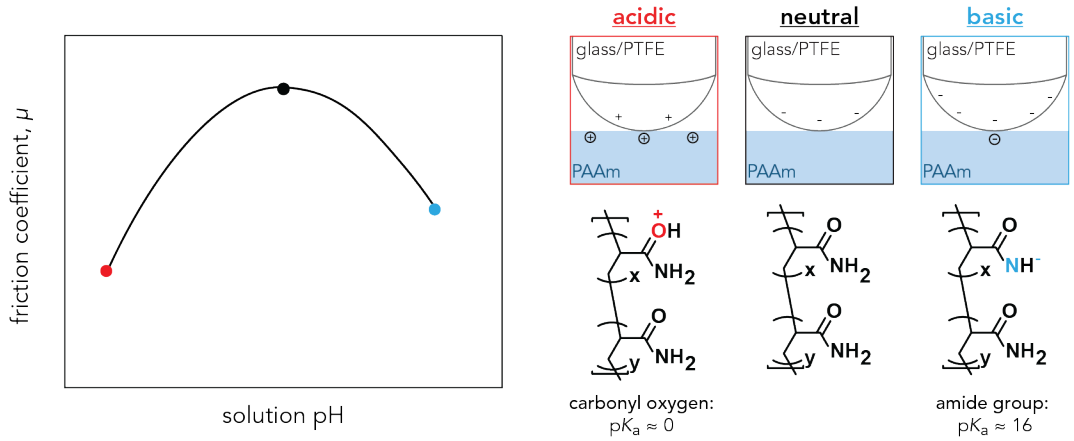

Figure 8.4 Predicted friction coefficient trend for the polyacrylamide hydrogels with varying pH if electrostatic interactions were the driving force behind the pH-dependent tribological behavior. Due to electrostatic repulsion between the probe and hydrogel surface in acidic and basic solutions, the friction coefficient would decrease, leading to a parabolic-like friction behavior, with the highest friction exhibited in neutral pH.

In acidic conditions, both glass and PTFE can be positively charged; conversely, in basic conditions they can be negatively charged.[315,333] For polyacrylamide hydrogels, the carbonyl oxygen, which has a $pK_a \approx 0$,[334] could become protonated in extremely acidic conditions, creating a positive charge. In extremely basic conditions, the amide group, with a $pK_a \approx 16$,[334] could

potentially deprotonate, although this is unlikely. Therefore, in acidic and basic conditions, electrostatic repulsion between the probe and hydrogel surface could lead to lower friction coefficients whereas in the neutral solution, only the probe would be negatively charged. However, our friction coefficients do not follow this predicted trend (Figure 8.2a) and decrease with increasing pH.

One limitation to our study is the lack of systematic control of the ionic strengths of our solutions, which ranged between 0 (pH ≈ 7), 0.001 M (pH = 2 and 10), and 0.5 M (pH = 0.34 and 13.5). Since ionic strength was not kept constant across pH solutions, it is difficult to draw definitive conclusions about the effects of electrostatics on the tribological behavior of our hydrogels. Despite the lack of control of ionic strength, friction coefficients were still the lowest at pH = 13.5, where ionic strength is the highest. Therefore, electrostatics may not be the sole mechanism driving the pH-responsive behavior of the polyacrylamide hydrogels. We propose that the dominant mechanism of friction reduction at high pH is hydrolysis-induced swelling resulting from deprotonated carboxylic acid pendant groups and/or crosslinker degradation, which is discussed further in Sections 8.3.4 and 8.3.5.

8.3.4 Base-Induced Amide Hydrolysis

We initially hypothesized that the pH-sensitivity of redox-initiated polyacrylamide hydrogels may be due to the incorporation of negatively-

charged sulfate groups at the chain ends of the network structure. These negatively-charged functionalities may lead to lower friction coefficients at high pH due to electrostatic repulsion between the glass probe and hydrogel and higher friction coefficients at low pH due to the protonation of the sulfate groups. While x-ray photoelectron spectroscopy (XPS) confirmed the presence of sulfate groups incorporated into the network (**Section 8.5.2**), it does not explain the pH-dependent friction behavior of the UV-initiated hydrogels, which use a charge-neutral photoinitiator (**Figure 8.1**). If the pH-dependence was solely due to negative charges from sulfate groups, the friction coefficient should stay constant across all pH solutions for the UV-initiated hydrogels, which was not observed (**Figure 8.2a**). Therefore, another mechanism is likely responsible for the pH-dependent friction behavior of polyacrylamide hydrogels.

The pH-sensitivity of polyacrylamide may be due to side chain and crosslinker hydrolysis through the conversion of the amide groups into ionizable carboxyl groups, as shown in the following reaction scheme for basic conditions.

$$R\text{-}CONH_2 + OH^- \rightarrow R\text{-}COO^- + NH_3$$

Typically, hydrolysis is intentionally performed on polyacrylamide at elevated temperatures (>40°C) in acidic[327,335,336] or basic environments[299,335–337] to form copolymerized poly(acrylamide-*co*-acrylic acid). In acidic conditions, complete conversion from polyacrylamide to poly(acrylic acid) can be achieved[335] while conversion is limited to 67% in basic conditions due to the

increase of negative charge built up along the backbone.[299,335] Hydrolysis can even occur at neutral pH under elevated temperatures (75 – 150°C).[70,338] However, Tanaka *et al*. demonstrated that polyacrylamide hydrolysis was also possible in alkaline conditions at room temperature, and even used TEMED (pH = 12) to partially hydrolyze polyacrylamide hydrogels.[337,339] Other studies have similarly shown that using TEMED as the catalyst in the polymerization reaction was enough to trigger hydrolysis due to its high pH.[103,132,158] Similarly, Ilavský *et al*. demonstrated that almost 6 mol.% of amide groups converted to carboxyl groups in polyacrylamide hydrogels swollen in a basic solution (pH ≈ 8 – 9) at room temperature over the course of 103 days. For the redox- and UV-initiated hydrogels in this study, the aging time ranged between 10 – 70 days and 7 – 15 days, respectively. Within this timeframe, Ilavský *et al*. observed 1 – 4 mol.% conversion.[133] Therefore, it is possible for hydrolysis to have occurred in our polyacrylamide hydrogels while they equilibrated over 7 – 70 days in acidic and basic solutions at room temperature. Our hydrolysis hypothesis is supported by the volume change of the redox-initiated hydrogels, which swelled dramatically at pH = 13.5 (**Figure 8.3b**). Others have noted increased swelling in hydrolyzed polyacrylamide hydrogels due to increased polymer chain repulsion caused by the conversion of amide groups ($-NH_2$) into deprotonated carboxylic acid groups ($-COO^-$) at high pH.[103,123,132,133,158,290–293,340]

To confirm the possibility of hydrolysis, Raman spectroscopy (**Figure 8.5, Figure 8.9 – Figure 8.12**) was conducted on redox-initiated hydrogels swollen at pH = 0.34 (0.5 M HCl), pH ≈ 7 (unbuffered DI water), and pH = 13.5 (0.5 M NaOH) for 10 days. These spectra were compared to the measured spectra of poly(acrylamide-*co*-acrylic acid) (P(AAm-*co*-AA)) hydrogels with varying amounts of acrylic acid (1, 5, 6, 9, and 12 wt.%) swollen in water. Raman peak assignments can be found in **Figure 8.10**. The polyacrylamide gels herein at neutral pH had peaks that corresponded to polyacrylamide spectra in literature,[41,341] including peaks at 1428 cm^{-1} (C-N stretching, or Amide III), 1617 cm^{-1} (-NH_2 bending, or Amide II), and 1670 cm^{-1} (C-O stretching, or Amide I) (**Figure 8.5a**). For the P(AAm-*co*-AA) gels, the peaks associated with the carboxyl group near 1555 cm^{-1} and 1716 cm^{-1} increased in intensity and merged with the two amide peaks near 1617 cm^{-1} and 1670 cm^{-1} with increasing acrylic acid concentration. Correspondingly, the normalized amide peak near 1428 cm^{-1} reduced in intensity, in agreement with the reduced portion of amide groups (**Figure 8.5b**). Remarkably, the spectra of the polyacrylamide gels swollen in NaOH are very similar to the spectra of P(AAm-*co*-AA) gels with high AA concentrations, with carboxyl peaks appearing as well as the emergence of a new peak near 1412 cm^{-1} which corresponded to sodium carboxylate.[342] These spectroscopic results suggest the formation of carboxyl groups in polyacrylamide gels swollen in NaOH due to hydrolysis at room temperature. In comparison, the spectra of

polyacrylamide gels swollen in HCl have almost identical spectra to the gels swollen in water but with a very small carboxyl peak near 1716 cm^{-1}, suggesting minimal hydrolysis occurred at low pH (**Figure 8.5a**).

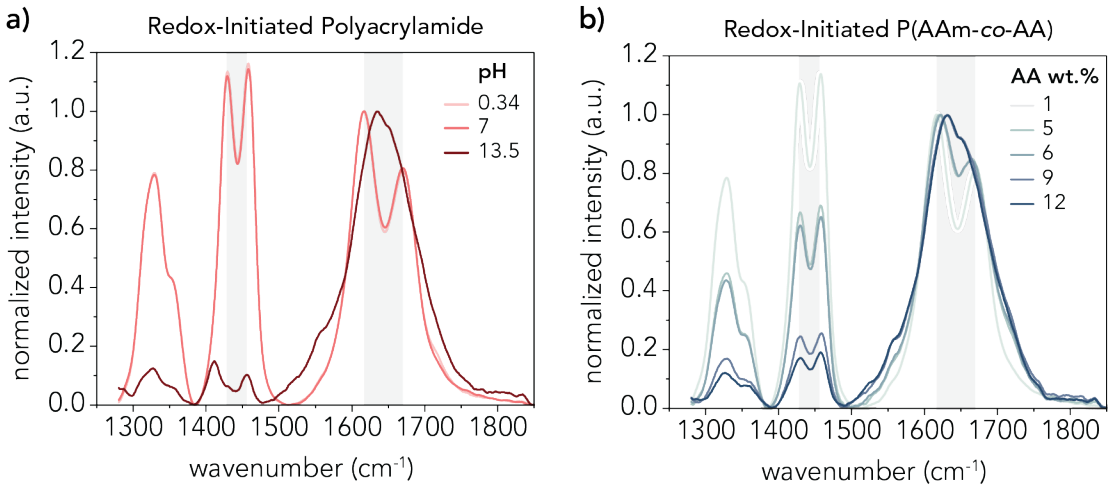

Figure 8.5 Averaged Raman spectra of redox-initiated **(a)** polyacrylamide and **(b)** P(AAm-*co*-AA) hydrogels, with intensity normalized to the peak near 1617 cm^{-1}. At pH = 0.34 (light pink) and pH ≈ 7 (pink), the spectra of the polyacrylamide gels almost overlap. At pH = 13.5 (dark pink), the amide peaks of polyacrylamide gels near 1428 cm^{-1} decreased in intensity and the carboxyl peaks near 1555 and 1716 cm^{-1} increased. In comparison, for P(AAm-*co*-AA) hydrogels swollen in water, the amide peaks near 1428 cm^{-1} decreased in intensity while the carboxyl peaks increased with increasing acrylic acid concentration (from 1 to 12 wt.%, light to dark blue, respectively).

To estimate the amount of amide groups hydrolyzed for redox-initiated polyacrylamide hydrogels, the Raman spectra were deconvoluted into individual bands (**Figure 8.11**), and linear calibration curves were established from the P(AAm-*co*-AA) gels based on the normalized peak areas and AA concentrations (**Figure 8.12**). From this analysis, about 12.7 mol.% and 0.3 mol.% of the amide groups were hydrolyzed after 10 days for the redox-initiated polyacrylamide hydrogels swollen at pH = 13.5 and pH = 0.34, respectively. Although it should

be noted that the accuracy of these values may be subject to potential uncertainties during baseline removal, Raman band deconvolution, curve fitting processes, and peak area normalization processes, the results indicate that a significant degree of hydrolysis occurred for the redox-initiated polyacrylamide hydrogels swollen at pH = 13.5. These values are slightly higher than those found by Ilavský *et al.*,[133] but during polymerization of the redox- and UV-initiated polyacrylamide hydrogels, temperatures reached a maximum of 88°C and 48°C, respectively. While longer reaction times and higher polymerization temperatures typically increase amide to carboxylic acid conversion,[103] it is unlikely that this transient temperature rise during polymerization led to greater hydrolysis since the redox-initiated gels polymerized within 5 minutes. Rather our gels may have exhibited greater hydrolysis due to the high pH of our solution (pH = 13.5 as opposed to pH ≈ 8 – 9).

Since *N,N'*-methylenebisacrylamide (MBAm) is used as the crosslinker, amide hydrolysis of the crosslinker may have occurred in addition to side chain hydrolysis. One indication of possible crosslinker degradation is that gels initially swollen in base and transferred to acid decreased in elastic modulus (**Figure 8.13**). However, it is difficult to distinguish from the Raman spectra whether the side chain primary amides were more susceptible to attack than the crosslinker secondary amides. Nevertheless, these results suggest that significant

polyacrylamide hydrolysis can occur at room temperature over the course of days when gels are swollen in extremely basic solutions.

8.3.5 Impact of Hydrolysis on Hydrogel Friction

Raman spectroscopy confirmed hydrolysis of polyacrylamide hydrogels in both acidic and basic environments over the course of 10 days at room temperature (**Figure 8.5a**), while swelling measurements indicated a volume increase with increasing pH (**Figure 8.3b**). This swelling increase could be due to the deprotonation of the carboxylic acid pendant group and/or the breakage of crosslinks, both of which would influence the friction coefficient. **Figure 8.6** illustrates our predicted trend of friction coefficient for polyacrylamide hydrogels with increasing pH if hydrolysis was the driving mechanism.

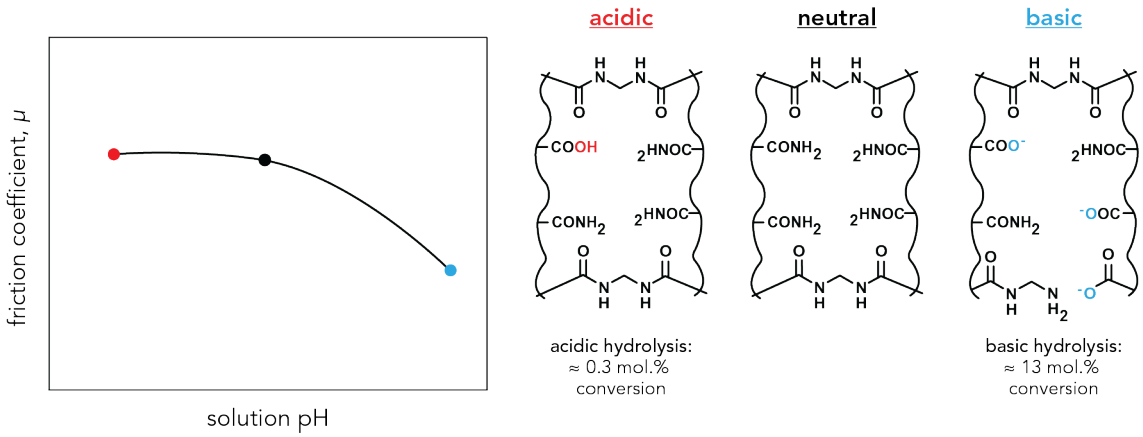

Figure 8.6 Predicted trend for polyacrylamide hydrogels if hydrolysis was the driving mechanism behind the pH-dependent friction. At low pH, hydrolysis of the pendant amide groups would not greatly impact swelling due to the protonation of the carboxylic acid, leading to charge neutrality. At high pH, hydrolysis of the pendant and crosslinker amide groups would lead to increased swelling and decreased friction coefficient.

At low pH, acid hydrolysis of the pendant amide groups is possible but the conversion is low. In contrast, conversion of the pendant and crosslinker amide groups to carboxylic acid is greater at high pH. Additionally, the carboxylic acid groups will deprotonate as long as the pH > pK_a, creating negative charges along the polymer chains, leading to increased electrostatic repulsion between chains and greater swelling. This increase in swelling could lead to a decrease in friction coefficient. While our tribological measurements do not completely follow this trend (Figure 8.2a), we still see a general decrease in friction coefficient with increasing pH, rather than the parabolic-like trends that would be expected if electrostatic repulsion between the probe and hydrogel were the predominant mechanism. Therefore, it is likely that the mechanism behind the pH-dependent behavior of the polyacrylamide hydrogels is driven by hydrolysis. Studies investigating the kinetics of hydrolysis at room temperature and its effects on the tribological properties of polyacrylamide hydrogels are outside the scope of this paper but would greatly benefit the tribological community.

8.4 Concluding Remarks

For tribological investigations of hydrogel lubricity in biological environments or biomedical applications where pH must be well-controlled, it is important to consider the possibility of pH-dependent friction behavior of polyacrylamide networks. In this work, the friction coefficients of both redox- and

UV-initiated polyacrylamide hydrogels decreased with increasing pH against glass and PTFE countersurfaces, with redox-initiated gels achieving superlubricity at pH = 13.5 (μ = 0.002 ± 0.002). This pH dependence may be due to hydrolysis within 10 days of swelling, which was confirmed by Raman spectroscopy for redox-initiated polyacrylamide hydrogels. Our measurements indicated a high degree (approximately 12.7 mol.%) of amide to carboxylic acid conversion at pH = 13.5 and a minimal degree (about 0.3 mol.%) of conversion at pH = 0.34. Additional evidence of hydrolysis was given by increased swelling (volume change = 457 ± 32%) and decreased modulus (E^* = 146 ± 86 kPa) at pH = 13.5 for redox-initiated hydrogels. Our results suggest that polyacrylamide hydrogels equilibrated in highly basic conditions, even at mild temperatures, are subject to hydrolysis, which can reduce friction coefficient and elastic modulus.

8.5 Appendix

8.5.1 Probe Surface Roughness Measurements

Due to the transparency of the glass probe, the surface roughness was unable to be measured. However, throughout the experiments there were no noticeable changes in transparency, indicating that the surface roughness did not appreciably change. Based on the mirror finish, we estimate that the average surface roughness was less than 100 nm. For the polytetrafluoroethylene (PTFE) probe, a laser scanning confocal M-scope (Olympus LEXT OLS4000 3D Laser

Measuring Microscope) was utilized to obtain a surface topography map of the probe surface. The curvature was flattened to determine the arithmetical mean height (S_a) and root mean square height (S_q).

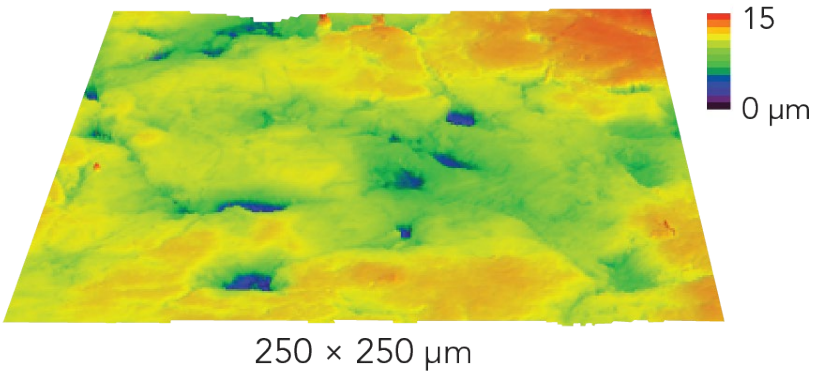

Figure 8.7 Surface topography map of the polytetrafluoroethylene (PTFE) probe surface taken with a laser scanning confocal M-scope. The color scale represents the z-direction and goes from 0 µm (purple) to 15 µm (red). Entire image is 250 µm x 250 µm. S_q = 1.57 µm and S_a = 1.16 µm.

8.5.2 X-Ray Photoelectron Spectroscopy of Hydrogels

X-ray photoelectron spectroscopy (XPS) was conducted on redox-initiated dehydrated polyacrylamide hydrogels using a Thermo Scientific ESCALAB™ Xi +. Hydrogel samples were dried in an oven at 60°C for two weeks prior to spectroscopy. A monochromatic Al/K_α x-ray radiation with a pass energy of 100 eV, dwell time of 50 ms, and spot size of 650 µm was used. Spectra were obtained after 105 s of etching using a 6 kV Ar1000+ cluster ion source.

XPS indicated the presence of sulfate within the hydrogel structure through the position of 2s and 2p peaks at 232 eV and 168 eV, respectively (**Figure 8.8a, c, d**). This chemical signature demonstrates a well-known maxim of the polymer

synthesis community: initiating fragments can be incorporated at various levels into the polymer chain backbone. In this case, the functional sulfate units derived from the ammonium persulfate initiator were incorporated into the hydrogel network, most likely at the chain ends (**Figure 8.8b**).[343]

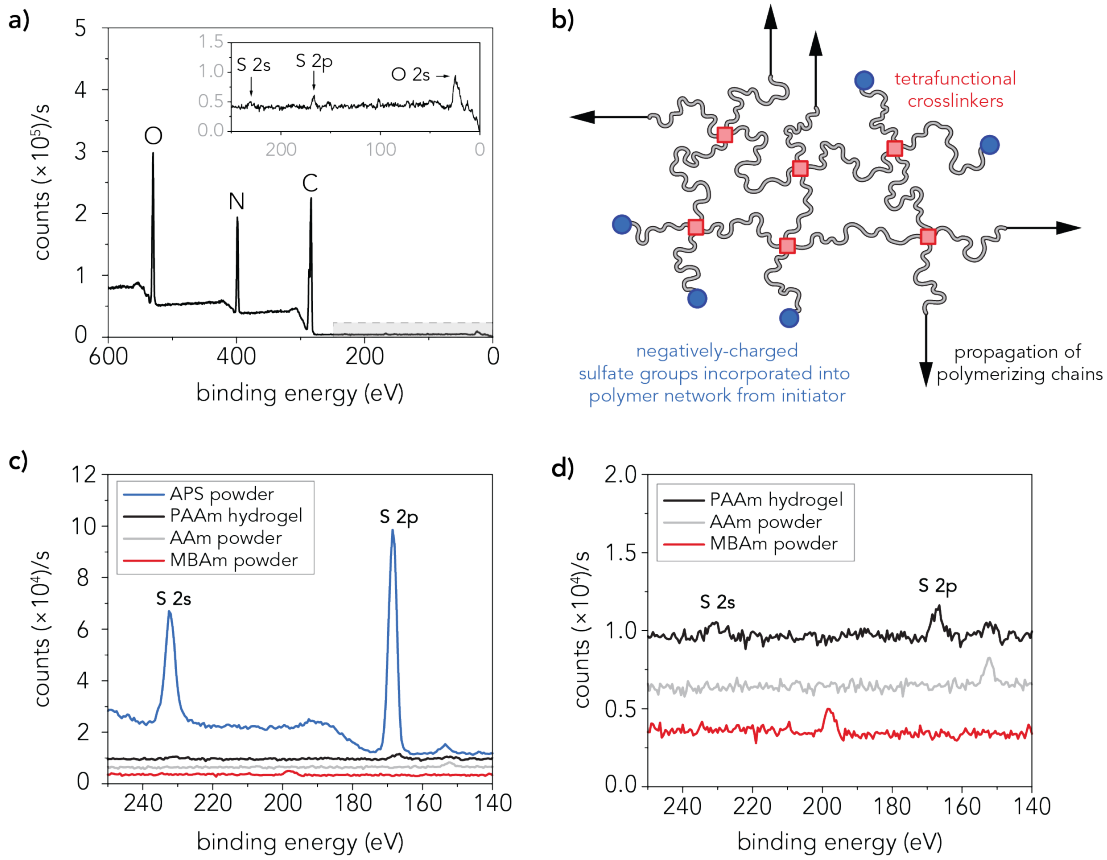

Figure 8.8 (a) XPS survey spectrum of the dehydrated redox-initiated polyacrylamide hydrogel after 105 s of cluster etching. The peaks corresponding to oxygen (O), nitrogen (N), carbon (C), and sulfur (S) are labeled. The inset expands the 0 – 250 eV binding energy range (gray box) to display the sulfur peaks. Specific atomic orbitals (2s and 2p) are indicated. The sulfur peaks indicate the presence of sulfate, which comes from the ammonium persulfate initiator. **(b)** Schematic of sulfate incorporation into the polyacrylamide hydrogel network. **(c)** XPS spectra comparing the dehydrated polyacrylamide hydrogel (PAAm, black) to the acrylamide (AAm, gray), *N,N'*-methylenebisacrylamide (MBAm, red), and ammonium persulfate (APS, blue) powders. The spectra are shifted by the following counts (x10^4)/s: 0.7 (APS powder), 0.55 (PAAm hydrogel), and 0.3 (AAm powder). Specific atomic orbitals (2s and 2p) are indicated. The sulfur peaks present in the polyacrylamide hydrogel indicate the presence of sulfate, which comes from the ammonium persulfate initiator. **(d)** XPS spectra of the dehydrated polyacrylamide hydrogel (black), AAm powder (gray), and MBAm powder (red) to highlight the sulfur peaks.

8.5.3 Raman Spectroscopy Analysis

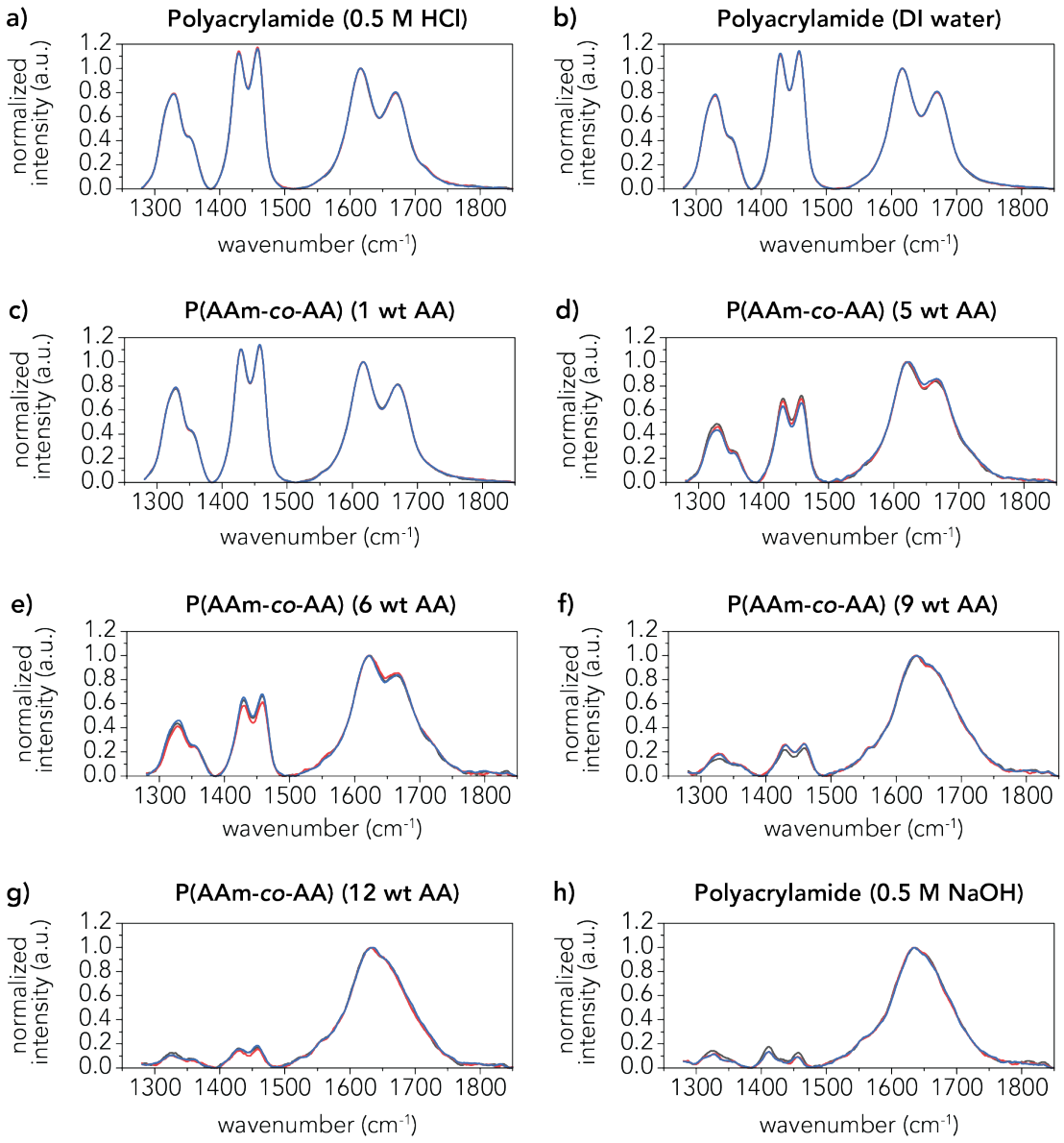

Figure 8.9 Three overlaid Raman spectra from three positions of the **(a)** polyacrylamide hydrogels swollen in 0.5 M HCl (pH = 0.34), **(b)** polyacrylamide hydrogels swollen in unbuffered DI water (pH ≈ 7), **(c-g)** P(AAm-*co*-AA) hydrogels with 1, 5, 6, 9, and 12 wt.% AA, respectively, swollen in water, and **(h)** polyacrylamide hydrogels swollen in 0.5 M NaOH (pH = 13.5).

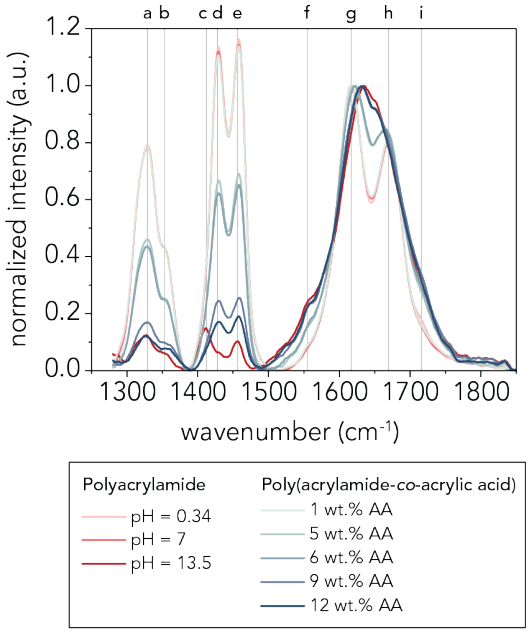

	Peak wavenumber (cm^{-1})	Assignment
a)	1329	$-CH_2$ bending
b)	1353	$-CH_2$ wagging
c)	1412	$-COO^-$
d)	1428	C-N stretching (Amide III)
e)	1456	$-CH_2$ bending
f)	1555	-COOH
g)	1617	$-NH_2$ bending (Amide II)
h)	1670	C-O stretching (Amide I)
i)	1716	C=O stretching

Figure 8.10 Averaged Raman spectra of the polyacrylamide and P(AAm-co-AA) hydrogels with the measured peaks labeled according to supplementary references.[41,341,342]

8.5.4 Quantitative Analysis of Raman Spectra

The measured Raman spectrum was deconvoluted into distinct bands based on peak wavenumbers shown in **Figure 8.10**, using the peak analyzer tool in the Origin software (**Figure 8.11**). Gaussian functions were employed to fit all bands except for the bands with peak wavenumbers near 1617 cm^{-1} and 1670 cm^{-1}, which were fitted based on Voigt functions (a combination of Gaussian and Lorentzian functions). To ensure that the width of the fitted peaks remained relatively consistent across the different spectra, during the curve fitting process, the full width at half-maximum (FWHM) of the same Raman band across different spectra was kept within a ±5% difference of each other.

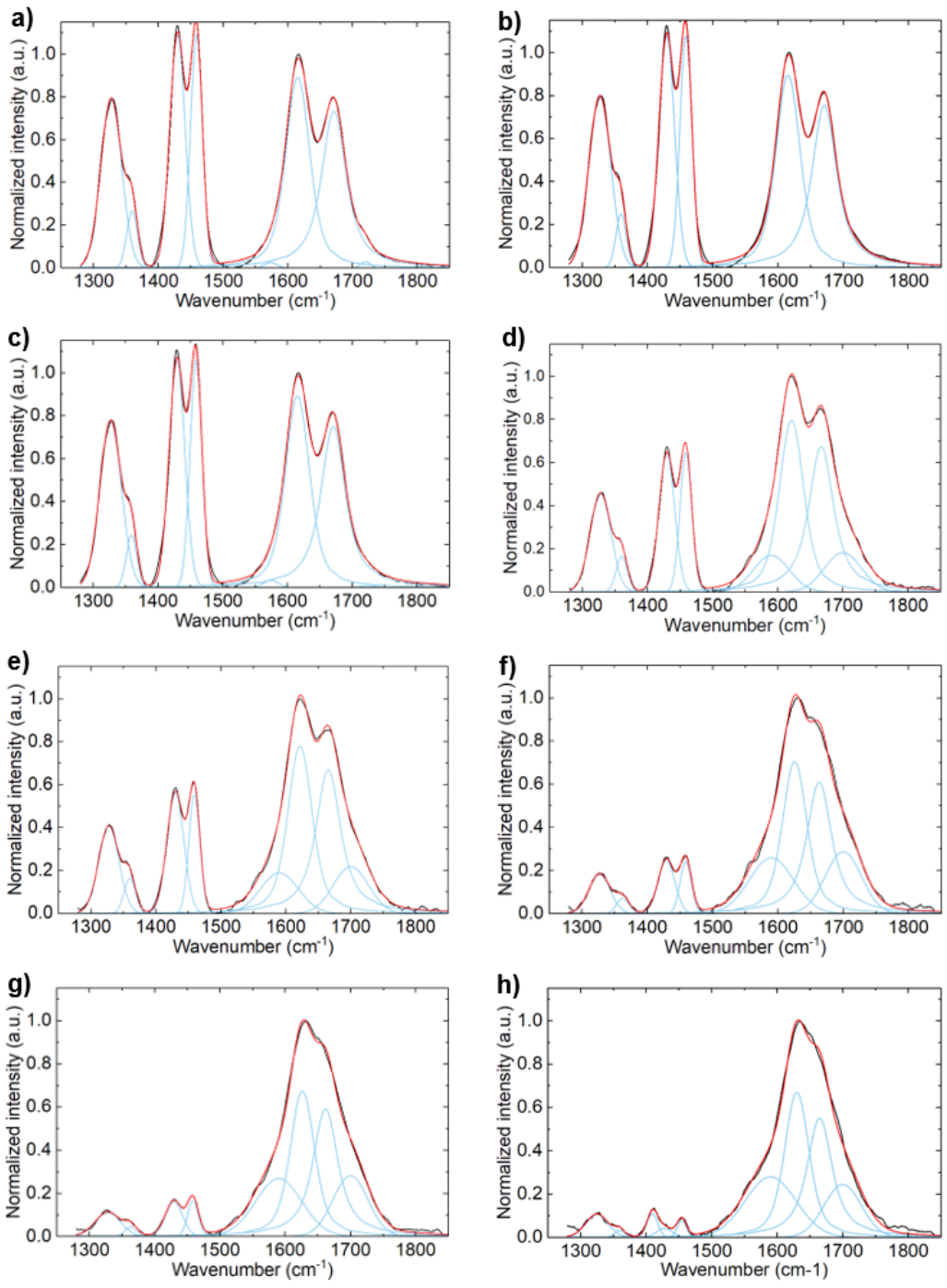

Figure 8.11 Typical results of Raman band deconvolution via curve fitting for **(a)** polyacrylamide hydrogels swollen in 0.5 M HCl (pH = 0.34), **(b)** polyacrylamide hydrogels swollen in unbuffered DI water (pH ≈ 7), **(c-g)** P(AAm-*co*-AA) hydrogels with 1, 5, 6, 9, and 12 wt.% AA, respectively, swollen in water, and (h) polyacrylamide hydrogels swollen in 0.5 M NaOH (pH = 13.5). The black curves are the measurements, the blue curves are the deconvoluted bands determined by curve fitting, and the red curves are the summation of the fitted bands.

After band deconvolution, quantitative analysis was conducted to estimate the degree of hydrolysis. The area of the 1555 cm^{-1} Raman band (associated with the carboxyl group of AA) was normalized by the combined area of 1670 cm^{-1} and 1716 cm^{-1} carbonyl bands (associated with both the amide and carboxyl groups) and plotted against the mole concentration of AA (**Figure 8.12a**). A linear relationship was established from the measured spectra of the P(AAm-*co*-AA) copolymer gels and polyacrylamide gels swollen in water allowing the determination of the carboxylic group concentration in the acid and base treated polyacrylamide gels. Following this relationship, from the normalized peak areas, we estimate that about 12.7 ± 0.6 and 0.34 ± 0.08 mol.% of amide groups have been hydrolyzed in polyacrylamide hydrogels swollen in 0.5 M NaOH (pH = 13.5) and 0.5 M HCl (pH = 0.34), respectively. Other peak area normalization methods result in similar values. For example, we normalized the area of the 1555 cm^{-1} Raman band (associated with the carboxyl group) by the area of the 1617 cm^{-1} band (associated with the amide group) and plotted against the mole ratio of AA and NH_2 (**Figure 8.12b**). In a similar manner, it was calculated that about 12.8 ± 0.3 and 0.25 ± 0.06 mol.% of amide groups have been hydrolyzed in polyacrylamide hydrogels swollen in 0.5 M NaOH and 0.5 M HCl, respectively.

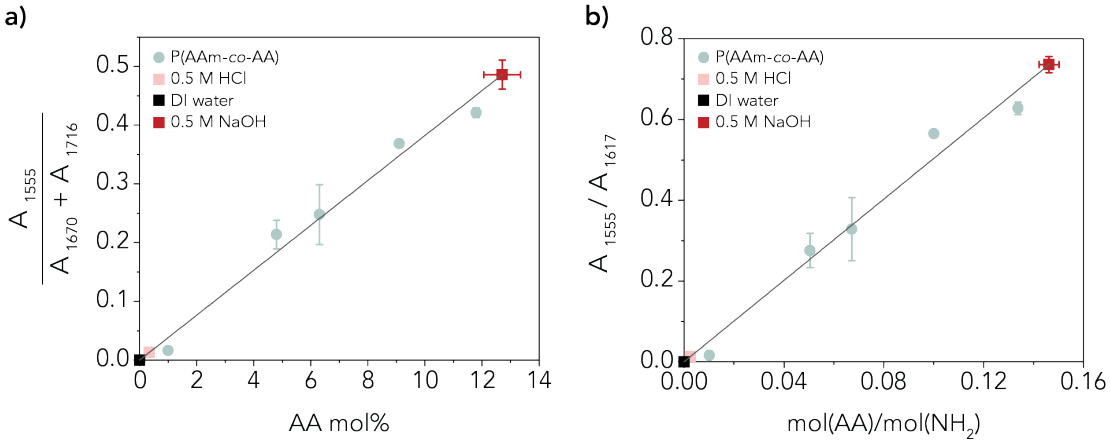

Figure 8.12 Linear calibration curves for estimating the degree of hydrolysis of polyacrylamide hydrogels swollen in 0.5 M NaOH (pH = 13.5) (dark red square) and 0.5 M HCl (pH = 0.34) (light pink square) using the P(AAm-*co*-AA) copolymer gels (light blue circles) and polyacrylamide gels swollen in DI water (black square). Error bars indicate standard deviation. **(a)** Raman peak area ratio between the carboxyl band associated with AA (near 1555 cm^{-1}) and the combined peak areas of both amide and carboxyl bands (near 1670 and 1716 cm^{-1}) versus the AA mol.%. The linear fit has a slope of 0.038 and goodness of fit, R^2 = 0.982. **(b)** Raman peak area ratio between the carboxyl group (near 1555 cm^{-1}) and the amide group (near 1617 cm^{-1}) versus their mole ratio. The linear fit has a slope of 5.035 and goodness of fit, R^2 = 0.978.

8.5.5 Switchable Friction

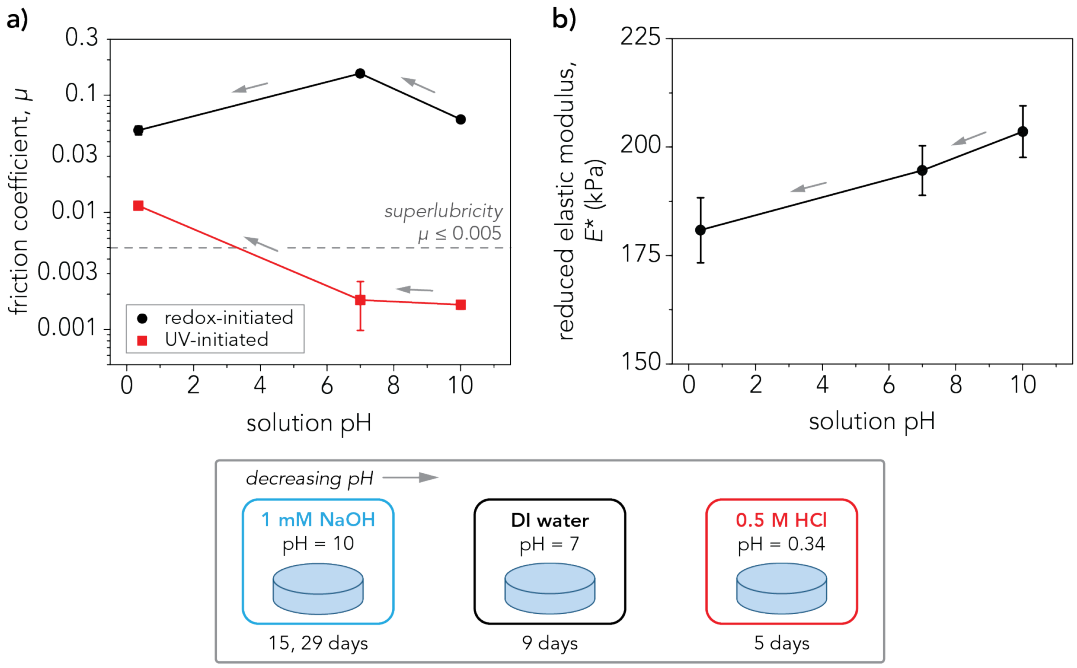

Figure 8.13 (a) Friction coefficient as a function of solution pH demonstrating the tunability of the friction coefficient for the redox-initiated (black circle) and UV-initiated (red square) polyacrylamide hydrogels against a glass probe. The gels were initially swollen in 0.001 M NaOH (pH = 10) for 29 and 15 days for the redox-initiated and UV-initiated hydrogels, respectively. After measuring their friction coefficient, the gels were swollen in DI water for nine days. In both cases, the friction coefficient increased. Finally, the gels were swollen in 0.5 M HCl (pH = 0.34) for five days. For the redox-initiated gels, the friction coefficient decreased. However, for the UV-initiated gels, the friction coefficient increased one order of magnitude. Each data point is the average and standard deviation of 25 cycles. **(b)** Reduced elastic modulus as a function of solution pH for the redox-initiated hydrogels. As pH decreased, E^* decreased. These results indicate that hydrolysis of the crosslinker may play a role in the friction and modulus decrease at lower pH for the redox-initiated gels due to the longer swelling time in base. However, further experiments are required to fully investigate this hypothesis.

9 CHAPTER 9: PHOTORESPONSIVE GELS

Spiropyran is a photoswitchable molecule that undergoes photoisomerization in response to light. It has been shown that the incorporation of spiropyran into hydrogel networks leads to the regulation of gel swelling. However, there are no studies on the tribological properties of these stimuli-responsive hydrogels. This chapter discusses the development and tribological characterization of photoresponsive hydrogels through the copolymerization of spiropyran-methacrylate (SP-MA) into poly(*N*-isopropylacrylamide) (pNIPAAm) networks.

Table of Contents

9.1 Introduction

Stimuli-responsive hydrogels, including poly(*N*-isopropylacrylamide) (pNIPAAm), are broadly used in biomedical applications (*e.g.*, drug delivery, soft robotics, cell culture) due to their tunable mechanical properties and swelling behavior in response to external stimuli such as temperature or pH. Recently, light has been used to alter hydrogel mechanics through the incorporation of azobenzene- or spiropyran-derived photoswitches, which isomerize in response to light. Spiropyran is a t-type photoswitch that undergoes pericyclic isomerization in response to light irradiation and exchanges between the hydrophilic merocyanine (MC) (ring-open) form and the hydrophobic spiropyran (SP) (ring-closed form) when exposed to 470 nm light, resulting in bulk hydrogel shrinking. By copolymerizing spiropyran into hydrogel networks, light-induced swelling and deswelling can be achieved, along with spatially controlled actuation and bending.[344–347] Although previous works have investigated the swelling behavior of these photoswitchable hydrogels, the tribological behavior (*e.g.*, friction and lubrication) remains largely unexplored.

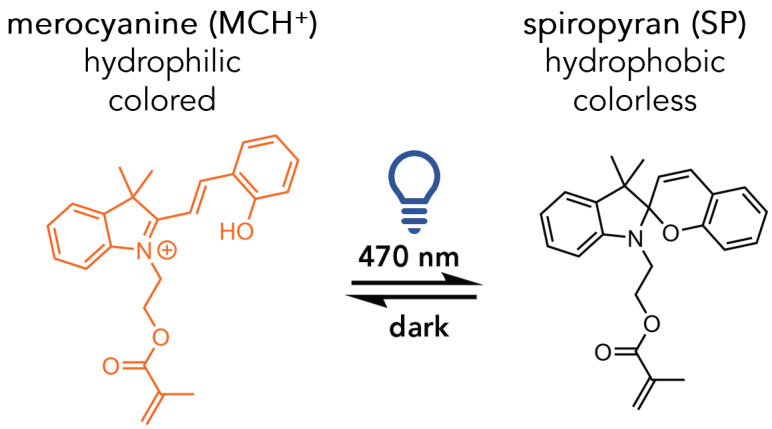

Figure 9.1 Schematic of spiropyran-methacrylate isomerization.

In this work, pNIPAAm-based gel lubricity was controlled using light as the external stimulus. Spiropyran-methacrylate (SP-MA) was conjugated with *N*-isopropylacrylamide (NIPAAm) and crosslinked with *N,N'*-methylenebisacrylamide (MBAm) to form a copolymerized hydrogel network (p(NIPAAm-*co*-SP-MA)). The elastic modulus, adhesion, and friction coefficient of the gels before and after irradiation were characterized, and the kinetics of switching between the MCH^+ and SP form was also evaluated. We hypothesized that the hydrogels would have lower friction when the SP-MA was in the MCH^+ form and higher friction in the SP form due to an increase in hydrophobicity, leading to hydrogel deswelling.

9.2 Materials & Methods

9.2.1 Hydrogel Synthesis

N-isopropylacrylamide (NIPAAm) (8.6 wt.%) was copolymerized with spiropyran-methacrylate (SP-MA) and crosslinked with *N,N'*-

methylenebisacrylamide (MBAm) (0.35 wt.%) via free-radical polymerization to form p(NIPAAm-*co*-SP-MA) gels. *N*,*N*,*N*',*N*'-tetramethylethylenediamine (TEMED) and ammonium persulfate (APS) were used as the catalyst and initiator, respectively. NIPAAm, SP-MA, and MBAm were dissolved in a 4:1 v/v mixture of dioxane and water and bubbled with nitrogen for 1 h to form gels with either 0.8 wt.% or 1.7 wt.% SP-MA. TEMED and a 10 wt.% APS solution in water were added, and the gels were polymerized between two glass slides ~ 3.5 mm apart for 2 h. Afterwards, the gels were swollen in methanol for 2 h to get rid of any unreacted monomers and then transferred to a 3:1 v/v solution of methanol and 5 mM HCl overnight in the dark to ensure that the SP-MA was in the merocyanine form. A 470 nm light source (30 mW/cm^2) was used to irradiate the hydrogel for 2 h and drive the SP-MA to the spiropyran form (SP).

9.2.2 Hydrogel Characterization

Microindentation and tribological sliding experiments were conducted to obtain the reduced elastic modulus (E^*) and force of adhesion (F_{adh}) of the photo-responsive hydrogels in the MC and SP form as described in **Section 4.4**. A hemisphere glass probe (radius of curvature, R = 2.6 mm) mounted to a double-leaf cantilever with normal and tangential spring constants of K_n = 222 μN/μm and K_f = 92 μN/μm was used to indent hydrogels at a maximum force of F_n = 1.5 mN at an indentation velocity of v_{ind} = 10 μm/s. Approach curves were fit with the Hertz contact mechanics model (**Eqn. 4.3**).

Tribological experiments were also performed as discussed in Section 4.3 to determine the friction coefficients of the hydrogels. While the samples were fully submerged in liquid, F_n = 2 mN was applied at a sliding velocity of 500 μm/s across a sliding path length of 4 mm. For each gel, 30 cycles were averaged to obtain the friction coefficient. UV-vis spectroscopy data demonstrated that SP-MA molecules in solution photoisomerized from MCH^+ to SP within minutes and thermally relaxed in the dark to MCH^+ within hours. To ensure that the gels were fully swollen and in the MCH^+ form, indentation and sliding experiments were conducted in the dark one day after polymerization. The gels were then irradiated with 470 nm light for 2 h to drive the SP-MA to the SP form, and indentation and sliding experiments were conducted again. Afterwards, the gels were allowed to equilibrate and reswell in the dark overnight before the characterization the next day.

9.3 Results & Discussion

9.3.1 Tuning Friction Coefficients with Light

The tribological behavior of p(NIPAAm-*co*-SP-MA)) hydrogels was observed before and after illumination with 470 nm light. Friction coefficients increased after light irradiation for hydrogels with 0.8 wt.% (Figure 9.2a) and 1.7 wt.% SP-MA (Figure 9.2b).

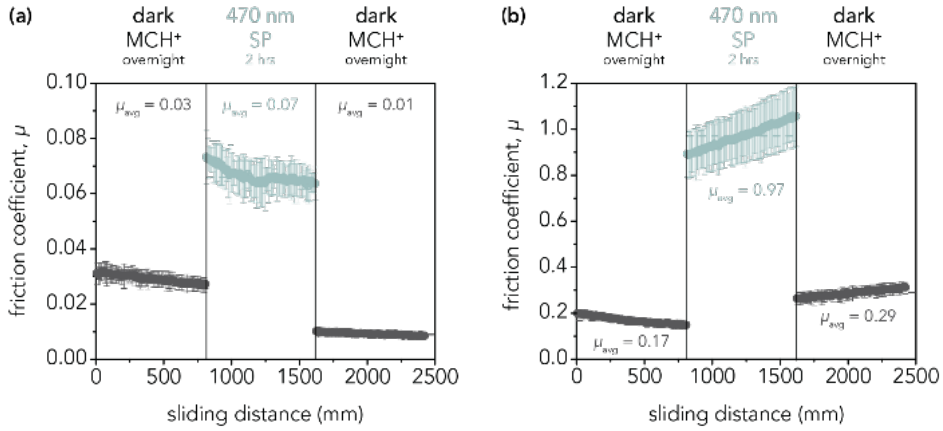

Figure 9.2 Friction coefficient as a function of distance for p(NIPAAm-*co*-SP-MA) hydrogels with **(a)** 0.8 wt.% and **(b)** 1.7 wt.% SP-MA. Gels in the MCH^+ form equilibrated overnight in the dark before sliding while gels in the SP form were irradiated with 470 nm light for 2 h before sliding.

For the 0.8 wt.% SP-MA hydrogels, friction more than doubled after 2 h of light irradiation, increasing from μ_{MCH+} = 0.03 to μ_{SP} = 0.07. After thermally relaxing overnight in the dark, the friction coefficient decreased to μ_{MCH} = 0.01 (**Figure 9.2a**). When the SP-MA concentration was doubled to 1.7 wt.%, friction increased 5-fold from μ_{MCH+} = 0.17 to μ_{SP} = 0.97 with light and then decreased to μ_{MCH+} = 0.29.

The initial increase in friction coefficient in the MCH^+ form with increasing SP-MA concentration is due to the hydrophobicity of SP-MA compared to NIPAAm. Likewise, there was a greater increase in friction coefficient after light irradiation for the gels with 1.7 wt.% SP-MA due to a greater change in hydrophobicity after MCH^+ to SP isomerization with light.

9.3.2 Effects of Light on Elastic Modulus & Adhesion

For the 1.7 wt.% SP-MA gels, a slight change in elastic modulus was observed upon 2 h of light irradiation, with the reduced elastic modulus increasing to E^*_{SP} = 13 kPa from an initial value of E^*_{MCH+} = 12 kPa (**Figure 9.3**). Additionally, the adhesion force vanished when the gels were irradiated with 470 nm light ($F_{adh,\ MCH+} \approx$ -250 μN to $F_{adh,\ SP} \approx$ 0 μN).

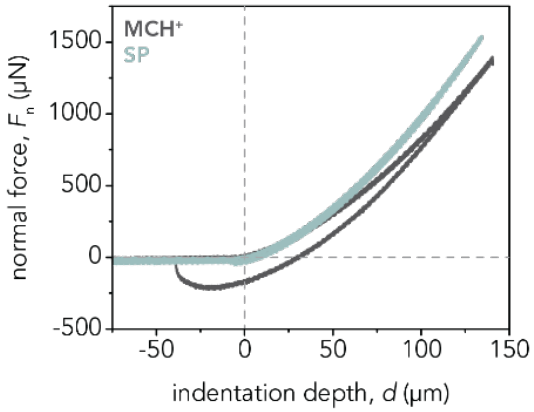

Figure 9.3 Representative indentation curves for the p(NIPAAm-*co*-SP-MA) hydrogels with 1.7 wt.% SP-MA in the MCH$^+$ (black) and SP (blue) form.

The minor increase in E^* with light irradiation was surprising considering the drastic increase in friction coefficient. If hydrogel deswelling was the main mechanism behind the change in friction coefficient, a greater increase in elastic modulus would be expected. Since this was not observed, another mechanism is responsible for the friction coefficient increase, which is currently under investigation.

Typically, adhesion and friction are proportional – with increased adhesion, friction increases. Here, adhesion was observed in the MCH$^+$ form, which

exhibited lower friction, but not in the SP state. This adhesive switch can be explained by hydrogen bonding interactions between the glass probe and hydrogel surface. When SP-MA is in the MCH^+ state, hydrogen bonding is possible. However, when irradiated with light, the ring closes to the SP form and hydrogen bonding no longer occurs.

9.4 Conclusion

Our findings demonstrate that light-tunable friction and adhesion was achieved with p(NIPAAm-*co*-SP-MA)) hydrogels with varying amounts of SP-MA. Hydrogels with low friction but high adhesion were formed when the gels were in the MCH^+ form while high friction but low adhesion was achieved in the SP state. The mechanism behind this interesting trend is still being investigated, but these gels hold promise as photoswitchable materials.

10 CHAPTER 10: CONCLUSIONS

In this dissertation, I have demonstrated several ways to tune hydrogel friction and have investigated the various mechanisms instigating these changes. Chapter 1 introduced the biological motivation behind studying hydrogel friction. The basics of hydrogel synthesis and structure were discussed in Chapter 2 and hydrogel tribology was explored in Chapter 3 along with several proposed lubrication mechanisms. Chapter 4 summarized the techniques used to characterize the mechanical and tribological properties of the hydrogel systems that I designed.

In Chapter 5, environmental oxygen was used to alter the surface structure of polyacrylamide hydrogels by exploiting the oxygen inhibition of free-radical polymerized systems. With increasing oxygen concentration, the surface structure was more loosely crosslinked, had lower polymer concentration, and a thicker surface gel layer. This led to decreasing friction coefficients and a lower reduced elastic modulus at the top surface of the gel. A reaction-kinetics model was developed to predict the thickness and polymer concentration gradient of the surface gel layer and could be used to design hydrogels with specific surface characteristics.

Chapter 6 investigated the solvophilic behavior of amphiphilic poly(2-hydroxyethyl methacrylate) (pHEMA) hydrogels. By regulating the ratio of ethanol and water in solution, the friction and adhesion were controlled. With

moderates amount of ethanol, both friction and adhesion increased an order of magnitude due to molecular scale rearrangements within the polymer network.

The friction behavior of charged hydrogel systems was investigated in Chapter 7 by making poly(acrylamide-*co*-acrylic acid) (p(AAm-*co*-AA)) hydrogels with varying amounts of acrylic acid (0 – 12 wt.%). By controlling solution pH and AA concentration, the friction coefficients were tuned two orders of magnitude. In Chapter 8, the surprising pH-dependent behavior of non-ionic polyacrylamide hydrogels was investigated. It was shown that basic hydrolysis led to the unintentional formation of copolymerized p(AAm-*co*-AA) through the conversion of amide groups to carboxylic acid, demonstrating another way to control hydrogel friction.

Chapter 9 introduced the design of photoswitchable gels through the incorporation of spiropyran-methacrylate (SP-MA), a molecule that photoisomerizes under 470 nm light, into a poly(*N*-isopropylacrylamide) network. By controlling the swelling and deswelling of the gel through the transition of hydrophilic merocyanine to hydrophobic spiropyran, friction increased two- to five-fold depending on the SP-MA concentration.

With the design principles and structure-property relationships discussed herein, the use of stimuli-responsive hydrogels in conjunction with 3D printing holds great promise for the development of soft robotics and material systems that better mimic the human body. I leave this exploration to future studies.

11 REFERENCES

1. Sophia Fox, A. J.; Bedi, A.; Rodeo, S. A. The Basic Science of Articular Cartilage: Structure, Composition, and Function. *Sports Health* 2009, **1** (6), 461–468. https://doi.org/10.1177/1941738109350438
2. Wagner, C. E.; Wheeler, K. M.; Ribbeck, K. Mucins and Their Role in Shaping the Functions of Mucus Barriers. *Annu Rev Cell Dev Biol* 2018, **34** (1), 189–215. https://doi.org/10.1146/annurev-cellbio-100617-062818
3. Bansil, R.; Turner, B. S. The Biology of Mucus: Composition, Synthesis and Organization. *Adv Drug Deliv Rev* 2018, **124**, 3–15. https://doi.org/10.1016/j.addr.2017.09.023
4. Werlang, C.; Cárcarmo-Oyarce, G.; Ribbeck, K. Engineering Mucus to Study and Influence the Microbiome. *Nat Rev Mater* 2019, **4** (2), 134–145. https://doi.org/10.1038/s41578-018-0079-7
5. Shoaib, T.; Yuh, C.; Wimmer, M. A.; Schmid, T. M.; Espinosa-Marzal, R. M. Nanoscale Insight into the Degradation Mechanisms of the Cartilage Articulating Surface Preceding OA. *Biomater Sci* 2020, **8** (14), 3944–3955. https://doi.org/10.1039/D0BM00496K
6. Pawaskar, S. S.; Fisher, J.; Jin, Z. Robust and General Method for Determining Surface Fluid Flow Boundary Conditions in Articular Cartilage Contact Mechanics Modeling. *J Biomech Eng* 2010, **132**, 1–8. https://doi.org/10.1115/1.4000869
7. Lin, W.; Liu, Z.; Kampf, N.; Klein, J. The Role of Hyaluronic Acid in Cartilage Boundary Lubrication. *Cells* 2020, **9** (7), 1–14. https://doi.org/10.3390/cells9071606
8. Yuh, C.; Laurent, M. P.; Espinosa-Marzal, R. M.; Chubinskaya, S.; Wimmer, M. A. Transient Stiffening of Cartilage during Joint Articulation: A Microindentation Study. *J Mech Behav Biomed Mater* 2021, **113**, 104113. https://doi.org/10.1016/j.jmbbm.2020.104113
9. de Boer, G. N.; Raske, N.; Soltanahmadi, S.; Dowson, D.; Bryant, M. G.; Hewson, R. W. A Porohyperelastic Lubrication Model for Articular Cartilage in the Natural Synovial Joint. *Tribol Int* 2020, **149**, 105760. https://doi.org/10.1016/j.triboint.2019.04.044
10. Klein, J. Repair or Replacement- A Joint Perspective. *Science* 2009, **323** (5910), 47–48. https://doi.org/10.1126/science.1166753
11. Wang, Y.; Liu, L.; Le, Z.; Tay, A. Analysis of Nanomedicine Efficacy for Osteoarthritis. *Adv Nanobiomed Res* 2022, **2** (12), 2200085. https://doi.org/10.1002/anbr.202200085

12. Jahn, S.; Seror, J.; Klein, J. Lubrication of Articular Cartilage. *Annu Rev Biomed Eng* 2016, **18**, 235–258. https://doi.org/10.1146/annurev-bioeng-081514-123305
13. Wagner, C. E.; Turner, B. S.; Rubinstein, M.; Mckinley, G. H.; Ribbeck, K. A Rheological Study of the Association and Dynamics of MUC5AC Gels. *Biomacromolecules* 2017, **18**, 3654–3664. https://doi.org/10.1021/acs.biomac.7b00809
14. Meldrum, O. W.; Yakubov, G. E.; Bonilla, M. R.; Deshmukh, O.; McGuckin, M. A.; Gidley, M. J. Mucin Gel Assembly Is Controlled by a Collective Action of Non-Mucin Proteins, Disulfide Bridges, Ca2+ -Mediated Links, and Hydrogen Bonding. *Sci Rep* 2018, **8** (1), 1–16. https://doi.org/10.1038/s41598-018-24223-3
15. Kayal, A. The Physiology of Tear Film. In *Dry Eye Syndrome - Modern Diagnostic Techniques and Advanced Treatments*; Ferreri, F. M., Ed.; 2022. https://doi.org/10.5772/intechopen.98945
16. Pitenis, A. A.; Urueña, J. M.; Hormel, T. T.; Bhattacharjee, T.; Niemi, S. R.; Marshall, S. L.; Hart, S. M.; Schulze, K. D.; Angelini, T. E.; Sawyer, W. G. Corneal Cell Friction: Survival, Lubricity, Tear Films, and Mucin Production over Extended Duration in Vitro Studies. *Biotribology* 2017, **11**, 77–83. https://doi.org/10.1016/j.biotri.2017.04.003
17. Efron, N. Contact Lens Wear Is Intrinsically Inflammatory. *Clin Exp Optom* 2017, **100**, 3–19. https://doi.org/10.1111/cxo.12487
18. Cao, X.; Bansil, R.; Bhaskar, K. R.; Turner, B. S.; LaMont, J. T.; Niu, N.; Afdhal, N. H. PH-Dependent Conformational Change of Gastric Mucin Leads to Sol-Gel Transition. *Biophys J* 1999, **76** (3), 1250–1258. https://doi.org/10.1016/S0006-3495(99)77288-7
19. Ruiz-Pulido, G.; Medina, D. I. An Overview of Gastrointestinal Mucus Rheology under Different PH Conditions and Introduction to PH-Dependent Rheological Interactions with PLGA and Chitosan Nanoparticles. E*uropean Journal of Pharmaceutics and Biopharmaceutics* 2021, **159**, 123–136. https://doi.org/10.1016/j.ejpb.2020.12.013
20. Schomig, V.; Kasdorf, B. T.; Scholz, C.; Bidmon, K.; Lieleg, O.; Berensmeier, S. An Optimized Purification Process for Porcine Gastric Mucin with Preservation of Its Native Functional Properties. *RSC Adv* 2016, **6**, 44932–44943. https://doi.org/10.1039/c6ra07424c
21. Celli, J. P.; Turner, B. S.; Afdhal, N. H.; Ewoldt, R. H.; Mckinley, G. H.; Bansil, R.; Erramilli, S. Rheology of Gastric Mucin Exhibits a pH-Dependent Sol -

Gel Transition. *Biomacromolecules* 2007, **8**, 1580–1586. https://doi.org/10.1021/bm0609691

22. Røn, T.; Patil, N. J.; Ajalloueian, F.; Rishikesan, S.; Zappone, B.; Chronakis, I. S.; Lee, S. Gastric Mucus and Mucuslike Hydrogels: Thin Film Lubricating Properties at Soft Interfaces. *Biointerphases* 2017, **12** (5). https://doi.org/10.1116/1.5003708
23. Bonyadi, S. Z.; Demott, C. J.; Grunlan, M. A.; Dunn, A. C. Cartilage-like Tribological Performance of Charged Double Network Hydrogels. *J Mech Behav Biomed Mater* 2021, **114**, 104202. https://doi.org/10.1016/j.jmbbm.2020.104202
24. Spencer, N. D. Cartilage-Inspired Lubrication with Polymer Brushes and Gels. In *World Tribology Congress Abstract*; 2021; p 6767.
25. Lin, W.; Kluzek, M.; Iuster, N.; Shimoni, E.; Kampf, N.; Goldberg, R.; Klein, J. Cartilage-Inspired, Lipid-Based Boundary-Lubricated Hydrogels. *Science* 2020, **370** (6514), 335–338. https://doi.org/10.1126/science.aay8276
26. Liu, M.; Zeng, X.; Ma, C.; Yi, H.; Ali, Z.; Mou, X.; Li, S.; Deng, Y.; He, N. Injectable Hydrogels for Cartilage and Bone Tissue Engineering. *Bone Res* 2017, **5** (1), 17014. https://doi.org/10.1038/boneres.2017.14
27. Gadjanski, I. Recent Advances on Gradient Hydrogels in Biomimetic Cartilage Tissue Engineering. *F1000Res* 2018, **6**, 2158. https://doi.org/10.12688/f1000research.12391.2
28. Sasaki, S.; Murakami, T.; Suzuki, A. Frictional Properties of Physically Cross-Linked PVA Hydrogels as Artificial Cartilage. *Biosurf Biotribol* 2016, **2** (1), 11–17. https://doi.org/10.1016/j.bsbt.2016.02.002
29. Pan, Y.; Xiong, D. Friction Properties of Nano-Hydroxyapatite Reinforced Poly(Vinyl Alcohol) Gel Composites as an Articular Cartilage. *Wear* 2009, **266** (7–8), 699–703. https://doi.org/10.1016/j.wear.2008.08.012
30. Pan, Y. S.; Xiong, D. S.; Ma, R. Y. A Study on the Friction Properties of Poly(Vinyl Alcohol) Hydrogel as Articular Cartilage against Titanium Alloy. *Wear* 2007, **262** (7–8), 1021–1025. https://doi.org/10.1016/j.wear.2006.10.005
31. Crouzier, T.; Boettcher, K.; Geonnotti, A. R.; Kavanaugh, N. L.; Hirsch, J. B.; Ribbeck, K.; Lieleg, O. Modulating Mucin Hydration and Lubrication by Deglycosylation and Polyethylene Glycol Binding. *Adv Mater Interfaces* 2015, **2**, 1500308. https://doi.org/10.1002/admi.201500308
32. Vinod, A.; Reddy Bhimavarapu, Y. V.; Hananovitz, M.; Stern, Y.; Gulec, S.; Jena, A. K.; Yadav, S.; Gutmark, E. J.; Patra, P. K.; Tadmor, R. Mucus-

Inspired Tribology, a Sticky Yet Flowing Hydrogel. *ACS Appl Polym Mater* 2022, **4** (11), 8527–8535. https://doi.org/10.1021/acsapm.2c01434
33. Wang, Z.; Sun, Z.; Ye, X.; Li, X. P.; Tan, W. Research on Bio-Tribological Properties of Intestinal Mucous and Its Mechanism Analysis. *Monatsh Chem* 2017, **148** (7), 1295–1299. https://doi.org/10.1007/s00706-016-1870-z
34. Freeman, M. E.; Furey, M. J.; Love, B. J.; Hampton, J. M. Friction, Wear, and Lubrication of Hydrogels as Synthetic Articular Cartilage. *Wear* 2000, **241** (2), 129–135. https://doi.org/10.1016/S0043-1648(00)00387-2
35. Denisin, A. K.; Pruitt, B. L. Tuning the Range of Polyacrylamide Gel Stiffness for Mechanobiology Applications. *ACS Appl Mater Interfaces* 2016, **8** (34), 21893–21902. https://doi.org/10.1021/acsami.5b09344
36. Wichterle, O.; Lim, D. Hydrophilic Gels for Biological Use. *Nature* 1960, **185**, 117–118. https://doi.org/10.1038/185117a0
37. Correa, S.; Grosskopf, A. K.; Lopez Hernandez, H.; Chan, D.; Yu, A. C.; Stapleton, L. M.; Appel, E. A. Translational Applications of Hydrogels. *Chem Rev* 2021, **121** (18), 11385–11457. https://doi.org/10.1021/acs.chemrev.0c01177
38. Rennie, A. C.; Dickrell, P. L.; Sawyer, W. G. Friction Coefficient of Soft Contact Lenses: Measurements and Modeling. *Tribol Lett* 2005, **18** (4), 499–504. https://doi.org/10.1007/s11249-005-3610-0
39. Dunn, A. C.; Urueña, J. M.; Huo, Y.; Perry, S. S.; Angelini, T. E.; Sawyer, W. G. Lubricity of Surface Hydrogel Layers. *Tribol Lett* 2013, **49** (2), 371–378. https://doi.org/10.1007/s11249-012-0076-8
40. Rizwan, M.; Yahya, R.; Hassan, A.; Yar, M.; Azzahari, A. D.; Selvanathan, V.; Sonsudin, F.; Abouloula, C. N. pH Sensitive Hydrogels in Drug Delivery: Brief History, Properties, Swelling, and Release Mechanism, Material Selection and Applications. *Polymers* 2017, **9** (4). https://doi.org/10.3390/polym9040137
41. Dai, H.; Chen, Q.; Qin, H.; Guan, Y.; Shen, D.; Hua, Y.; Tang, Y.; Xu, J. A Temperature-Responsive Copolymer Hydrogel in Controlled Drug Delivery. *Macromolecules* 2006, **39** (19), 6584–6589. https://doi.org/10.1021/ma060486p
42. Ravichandran, P.; Shantha, K. L.; Panduranga Rao, K. Preparation, Swelling Characteristics and Evaluation of Hydrogels for Stomach Specific Drug Delivery. *Int J Pharm* 1997, **154** (1), 89–94. https://doi.org/10.1016/S0378-5173(97)00131-2

43. Bazban-Shotorbani, S.; Hasani-Sadrabadi, M. M.; Karkhaneh, A.; Serpooshan, V.; Jacob, K. I.; Moshaverinia, A.; Mahmoudi, M. Revisiting Structure-Property Relationship of pH-Responsive Polymers for Drug Delivery Applications. *Journal of Controlled Release* 2017, **253**, 46–63. https://doi.org/10.1016/j.jconrel.2017.02.021
44. Ferreira, L.; Vidal, M. M.; Gil, M. H. Evaluation of Poly(2-Hydroxyethyl Methacrylate) Gels as Drug Delivery Systems at Different pH Values. *Int J Pharm* 2000, **194** (2), 169–180. https://doi.org/10.1016/S0378-5173(99)00375-0
45. Hoffman, A. S. Hydrogels for Biomedical Applications. *Adv Drug Deliv Rev* 2002, **64**, 18–23. https://doi.org/10.1016/j.addr.2012.09.010
46. Sant, S.; Hancock, M. J.; Donnelley, J. P.; Iyer, D.; Khademhosseini, A. Biomimetic Gradient Hydrogels for Tissue Engineering. *Can J Chem Eng* 2010, **88** (6), 899–911. https://doi.org/10.1002/cjce.20411
47. George, J.; Hsu, C. C.; Nguyen, L. T. B.; Ye, H.; Cui, Z. Neural Tissue Engineering with Structured Hydrogels in CNS Models and Therapies. *Biotechnol Adv* 2020, **42**, 1–17. https://doi.org/10.1016/j.biotechadv.2019.03.009
48. Caló, E.; Khutoryanskiy, V. V. Biomedical Applications of Hydrogels: A Review of Patents and Commercial Products. *Eur Polym J* 2015, **65**, 252–267. https://doi.org/10.1016/j.eurpolymj.2014.11.024
49. Mitura, S.; Sionkowska, A.; Jaiswal, A. Biopolymers for Hydrogels in Cosmetics: Review. *J Mater Sci Mater Med* 2020, **31** (6). https://doi.org/10.1007/s10856-020-06390-w
50. Leblanc, K. J.; Niemi, S. R.; Bennett, A. I.; Harris, K. L.; Schulze, K. D.; Sawyer, W. G.; Taylor, C.; Angelini, T. E. Stability of High Speed 3D Printing in Liquid-Like Solids. *ACS Biomater Sci Eng* 2016, **2** (10), 1796–1799. https://doi.org/10.1021/acsbiomaterials.6b00184
51. Xie, R.; Mukherjee, S.; Levi, A. E.; Reynolds, V. G.; Wang, H.; Chabinyc, M. L.; Bates, C. M. Room Temperature 3D Printing of Super-Soft and Solvent-Free Elastomers. *Sci Adv* 2020, **6** (46), 1–11. https://doi.org/10.1126/sciadv.abc6900
52. Xu, C.; Dai, G.; Hong, Y. Recent Advances in High-Strength and Elastic Hydrogels for 3D Printing in Biomedical Applications. *Acta Biomater* 2019, **95**, 50–59. https://doi.org/10.1016/j.actbio.2019.05.032
53. Rehor, I.; Maslen, C.; Moerman, P. G.; Van Ravensteijn, B. G. P.; Van Alst, R.; Groenewold, J.; Eral, H. B.; Kegel, W. K. Photoresponsive Hydrogel

Microcrawlers Exploit Friction Hysteresis to Crawl by Reciprocal Actuation. *Soft Robot* 2021, **8** (1), 10–18. https://doi.org/10.1089/soro.2019.0169
54. Ying, B.; Liu, X. Skin-like Hydrogel Devices for Wearable Sensing, Soft Robotics and Beyond. *iScience* 2021, **24** (11), 103174. https://doi.org/10.1016/j.isci.2021.103174
55. Jacchetti, E.; Emilitri, E.; Rodighiero, S.; Indrieri, M.; Gianfelice, A.; Lenardi, C.; Podestà, A.; Ranucci, E.; Ferruti, P.; Milani, P. Biomimetic Poly(Amidoamine) Hydrogels as Synthetic Materials for Cell Culture. *J Nanobiotechnology* 2008, **6**, 1–15. https://doi.org/10.1186/1477-3155-6-14
56. Tannouri, P.; Arafeh, K. M.; Krahn, J. M.; Beaupré, S. L.; Menon, C.; Branda, N. R. A Photoresponsive Biomimetic Dry Adhesive Based on Doped PDMS Microstructures. *Chemistry of Materials* 2014, **26** (15), 4330–4333. https://doi.org/10.1021/cm502222c
57. Cohen, Y.; Ramon, O.; Kopelman, I. J.; Mizrahi, S. Characterization of Inhomogeneous Polyacrylamide Hydrogels. *J Polym Sci B Polym Phys* 1992, **30** (9), 1055–1067. https://doi.org/10.1002/polb.1992.090300913
58. Baselga, J.; Llorente, M. A.; Hernández-Fuentes, I.; Piérola, I. F. Network Defects in Polyacrylamide Gels. *Eur Polym J* 1989, **25** (5), 471–475. https://doi.org/10.1016/0014-3057(89)90188-2
59. Baselga, J.; Llorente, M. A.; Nieto, J. L.; Hernández-Fuentes, I.; Piérola, I. F. Polyacrylamide Networks. Sequence Distribution of Crosslinker. *Eur Polym J* 1988, **24** (2), 161–165. https://doi.org/10.1016/0014-3057(88)90145-0
60. Yang, T.-H. Recent Applications of Polyacrylamide as Biomaterials. *Recent Patents on Materials Science* 2012, **1** (1), 29–40. https://doi.org/10.2174/1874464810801010029
61. Baselga, J.; Llorente, M. A.; Hernández-Fuentes, I.; Piérola, I. F. Polyacrylamide Gels. Process of Network Formation. *Eur Polym J* 1989, **25** (5), 477–480. https://doi.org/10.1016/0014-3057(89)90189-4
62. Naghash, H. J.; Okay, O. Formation and Structure of Polyacrylamide Gels. *J Appl Polym Sci* 1996, **60**, 971–979. https://doi.org/10.1002/(SICI)1097-4628(19960516)60:7<971::AID-APP7>3.0.CO;2-J
63. Datta, A. Characterization of Polyethylene Glycol Hydrogels for Biomedical Applications. *Louisiana State University Master's Thesis;* 2007.
64. Offeddu, G. S.; Axpe, E.; Harley, B. A. C.; Oyen, M. L. Relationship between Permeability and Diffusivity in Polyethylene Glycol Hydrogels. *AIP Adv* 2018, **8**, 105006. https://doi.org/10.1063/1.5036999

65. Wilems, T. S.; Lu, X.; Kurosu, Y. E.; Khan, Z.; Lim, H. J.; Smith Callahan, L. A. Effects of Free Radical Initiators on Polyethylene Glycol Dimethacrylate Hydrogel Properties and Biocompatibility. *J Biomed Mater Res A* 2017, **105** (11), 3059–3068. https://doi.org/10.1002/jbm.a.36160
66. Krutkramelis, K.; Xia, B.; Oakey, J. Monodisperse Polyethylene Glycol Diacrylate Hydrogel Microsphere Formation by Oxygen-Controlled Photopolymerization in a Microfluidic Device. *Lab Chip* 2016, **16** (8), 1457–1465. https://doi.org/10.1039/C6LC00254D
67. Zare, M.; Bigham, A.; Zare, M.; Luo, H.; Rezvani Ghomi, E.; Ramakrishna, S. PHEMA: An Overview for Biomedical Applications. *Int J Mol Sci* 2021, **22** (12). https://doi.org/10.3390/ijms22126376
68. Passos, M. F.; Dias, D. R. C.; Bastos, G. N. T.; Jardini, A. L.; Benatti, A. C. B.; Dias, C. G. B. T.; Maciel Filho, R. PHEMA Hydrogels: Synthesis, Kinetics and in Vitro Tests. *J Therm Anal Calorim* 2016, **125** (1), 361–368. https://doi.org/10.1007/s10973-016-5329-6
69. McGhee, E. O.; Chau, A. L.; Cavanaugh, M. C.; Rosa, J. G.; Davidson, C. L. G.; Kim, J.; Urueña, J. M.; Sumerlin, B. S.; Pitenis, A. A.; Sawyer, W. G. Amphiphilic Gel Lubrication and the Solvophilic Transition. *Biotribology* 2021, **26**, 100170. https://doi.org/10.1016/j.biotri.2021.100170
70. Kheradmand, H.; François, J.; Plazanet, V. Hydrolysis of Polyacrylamide and Acrylic Acid-Acrylamide Copolymers at Neutral PH and High Temperature. *Polymer* 1988, **29** (5), 860–870. https://doi.org/10.1016/0032-3861(88)90145-0
71. Sennakesavan, G.; Mostakhdemin, M.; Dkhar, L. K.; Seyfoddin, A.; Fatihhi, S. J. Acrylic Acid/Acrylamide Based Hydrogels and Its Properties - A Review. *Polym Degrad Stab* 2020, **180**, 109308. https://doi.org/10.1016/j.polymdegradstab.2020.109308
72. Tomar, R. S.; Gupta, I.; Singhal, R.; Nagpal, A. K. Synthesis of Poly(Acrylamide-Co-Acrylic Acid)-Based Super-Absorbent Hydrogels by Gamma Radiation: Study of Swelling Behaviour and Network Parameters. *Des Monomers Polym* 2007, **10** (1), 49–66. https://doi.org/10.1163/156855507779763685
73. Prouvé, E.; Drouin, B.; Chevallier, P.; Rémy, M.; Durrieu, M. C.; Laroche, G. Evaluating Poly(Acrylamide-Co-Acrylic Acid) Hydrogels Stress Relaxation to Direct the Osteogenic Differentiation of Mesenchymal Stem Cells. *Macromol Biosci* 2021, **21** (6), 1–12. https://doi.org/10.1002/mabi.202100069

74. Deng, Y.; Sun, J.; Ni, X.; Yu, B. Tribological Properties of Hierarchical Structure Artificial Joints with Poly Acrylic Acid (AA) - Poly Acrylamide (AAm) Hydrogel and Ti6Al4V Substrate. *Journal of Polymer Research* 2020, **27** (6). https://doi.org/10.1007/s10965-020-02143-z
75. Gredyukhina, I. V.; Plotnikova, L. V.; Balbekin, N. S.; Kulya, M. S.; Petrov, N. V.; Nechiporenko, A. P.; Uspenskaya, M. V. Influence of the Degree of Neutralization of Acrylic Acid and Cross-Linking Agent on Optical Properties and Swelling of Sodium Polyacrylate. *Opt Spectrosc* 2017, **122** (6), 877–879. https://doi.org/10.1134/S0030400X1706008X
76. Zhao, Z. X.; Li, Z.; Xia, Q. B.; Bajalis, E.; Xi, H. X.; Lin, Y. S. Swelling/Deswelling Kinetics of PNIPAAm Hydrogels Synthesized by Microwave Irradiation. *Chemical Engineering Journal* 2008, **142** (3), 263–270. https://doi.org/10.1016/j.cej.2007.12.009
77. Ziminska, M.; Wilson, J. J.; McErlean, E.; Dunne, N.; McCarthy, H. O. Synthesis and Evaluation of a Thermoresponsive Degradable Chitosan-Grafted PNIPAAm Hydrogel as a "Smart" Gene Delivery System. *Materials* 2020, **13** (11), 1–21. https://doi.org/10.3390/ma13112530
78. Guilherme, M. R.; Da Silva, R.; Rubira, A. F.; Geuskens, G.; Muniz, E. C. Thermo-Sensitive Hydrogels Membranes from PAAm Networks and Entangled PNIPAAm: Effect of Temperature, Cross-Linking and PNIPAAm Contents on the Water Uptake and Permeability. *React Funct Polym* 2004, **61** (2), 233–243. https://doi.org/10.1016/j.reactfunctpolym.2004.06.004
79. Refojo, M. F. Hydrophobic Interaction in Poly(2-Hydroxyethyl Methacrylate) Homogeneous Hydrogel. *J Polym Sci A1* 1967, **5** (12), 3103–3113. https://doi.org/10.1002/pol.1967.150051211
80. Andersson, M.; Axelsson, A.; Zacchi, G. Swelling Kinetics of Poly(N-Isopropylacrylamide) Gel. *Journal of Controlled Release* 1998, **50** (1–3), 273–281. https://doi.org/10.1016/S0168-3659(97)00151-X
81. Saikia, A. K.; Aggarwal, S.; Mandal, U. K. Swelling Dynamics of Poly(NIPAM-Co-AMPS) Hydrogels Synthesized Using PEG as Macroinitiator: Effect of AMPS Content. *Journal of Polymer Research* 2013, **20** (1). https://doi.org/10.1007/s10965-012-0031-2
82. Bischofberger, I.; Calzolari, D. C. E.; Trappe, V. Co-Nonsolvency of PNiPAM at the Transition between Solvation Mechanisms. *Soft Matter* 2014, **10** (41), 8288–8295. https://doi.org/10.1039/c4sm01345j
83. Meacham, R.; Liu, M.; Guo, J.; Zehnder, A. T.; Hui, C. Y. Effect of Hydration on Tensile Response of a Dual Cross-Linked PVA Hydrogel. *Exp Mech* 2020, **60**, 1161–1165. https://doi.org/10.1007/s11340-020-00598-1

84. Wahab, A. H. A.; Saad, A. P. M.; Harun, M. N.; Syahrom, A.; Ramlee, M. H.; Sulong, M. A.; Kadir, M. R. A. Developing Functionally Graded PVA Hydrogel Using Simple Freeze-Thaw Method for Artificial Glenoid Labrum. *J Mech Behav Biomed Mater* 2019, **91**, 406–415. https://doi.org/10.1016/j.jmbbm.2018.12.033
85. Wu, G.; Jin, K.; Liu, L.; Zhang, H. A Rapid Self-Healing Hydrogel Based on PVA and Sodium Alginate with Conductive and Cold-Resistant Properties. *Soft Matter* 2020, **16** (13), 3319–3324. https://doi.org/10.1039/c9sm02455g
86. Grinnell, F.; Petroll, W. M. Cell Motility and Mechanics in Three-Dimensional Collagen Matrices. *Annu Rev Cell Dev Biol* 2010, **26** (1), 335–361. https://doi.org/10.1146/annurev.cellbio.042308.113318
87. Chung, K. H.; Chen, A. K.; Anderton, C. R.; Bhadriraju, K.; Plant, A. L.; Bush, B. G.; Cook, R. F.; Delrio, F. W. Frictional Properties of Native and Functionalized Type I Collagen Thin Films. *Appl Phys Lett* 2013, **103** (14). https://doi.org/10.1063/1.4824685
88. Hopkins, E.; Valois, E.; Stull, A.; Le, K.; Pitenis, A. A.; Wilson, M. Z. An Optogenetic Platform to Dynamically Control the Stiffness of Collagen Hydrogels. *ACS Biomater Sci Eng* 2021, **7** (2), 408–414. https://doi.org/10.1021/acsbiomaterials.0c01488
89. Baumberger, T.; Caroli, C.; Ronsin, O. Self-Healing Slip Pulses and the Friction of Gelatin Gels. *European Physical Journal E* 2003, **11** (1), 85–93. https://doi.org/10.1140/epje/i2003-10009-7
90. Czerner, M.; Fellay, L. S.; Suárez, M. P.; Frontini, P. M.; Fasce, L. A. Determination of Elastic Modulus of Gelatin Gels by Indentation Experiments. *Procedia Materials Science* 2015, **8**, 287–296. https://doi.org/10.1016/j.mspro.2015.04.075
91. Roberts, J. J.; Earnshaw, A.; Ferguson, V. L.; Bryant, S. J. Comparative Study of the Viscoelastic Mechanical Behavior of Agarose and Poly(Ethylene Glycol) Hydrogels. *J Biomed Mater Res B* 2011, **99B** (1), 158–169. https://doi.org/10.1002/jbm.b.31883
92. Hafezi, M.; Qin, L.; Mahmoodi, P.; Dong, G. Osmosis Effect on Protein Sustained Release of Agarose Hydrogel for Anti-Friction Performance. *Tribol Int* 2019, **132**, 108–117. https://doi.org/10.1016/j.triboint.2018.12.013
93. Wu, C.; Li, X.; Wu, C.; Yang, Q.; Long, S. Low-Velocity Super-Lubrication of Sodium-Alginate/Polyacrylamide Ionic-Covalent Hybrid Double-Network

Hydrogels. *Soft Matter* 2015, **11** (15), 3022–3033. https://doi.org/10.1039/c4sm02783c
94. Lee, K. Y.; Mooney, D. J. Alginate: Properties and Biomedical Applications. *Progress in Polymer Science* 2012, **37** (1), 106–126. https://doi.org/10.1016/j.progpolymsci.2011.06.003
95. Caccavo, D.; Cascone, S.; Lamberti, G.; Barba, A. A. Hydrogels: Experimental Characterization and Mathematical Modelling of Their Mechanical and Diffusive Behaviour. *Chem Soc Rev* 2018, **47**, 2357. https://doi.org/10.1039/c7cs00638a
96. Tsihlis, N. D.; Murar, J.; Kapadia, M. R.; Ahanchi, S. S.; Oustwani, C. S.; Saavedra, J. E.; Keefer, L. K.; Kibbe, M. R. Hydrogels: Methods of Preparation. *J Vasc Surg* 2010, **51** (5), 1248–1259. https://doi.org/10.1016/j.jvs.2009.12.028
97. Gull, N.; Khan, S. M.; Islam, A.; Butt, M. T. Z. Hydrogels Used for Biomedical Applications. In *Bio Monomers for Green Polymeric Composite Materials*; 2019; pp 175–199. https://doi.org/10.1002/9781119301714.ch9
98. Pitenis, A. A.; Schulze, K. D.; Nixon, R. M.; Dunn, A. C.; Krick, B. A.; Sawyer, W. G.; Angelini, T. E. Polymer Fluctuation Lubrication in Hydrogel Gemini Interfaces. *Soft Matter* 2014, **10**, 8955–8962. https://doi.org/10.1039/C4SM01728E
99. Bashir, S.; Hina, M.; Iqbal, J.; Rajpar, A. H.; Mujtaba, M. A.; Alghamdi, N. A.; Wageh, S.; Ramesh, K.; Ramesh, S. Fundamental Concepts of Hydrogels: Synthesis, Properties, and Their Applications. *Polymers* 2020, **12** (11), 1–60. https://doi.org/10.3390/polym12112702
100. Chan, E. P.; Deeyaa, B.; Johnson, P. M.; Stafford, C. M. Poroelastic Relaxation of Polymer-Loaded Hydrogels. *Soft Matter* 2012, **8** (31), 8234–8240. https://doi.org/10.1039/c2sm25363a
101. Chang, S.; Kim, M.; Oh, S.; Min, J. H.; Kang, D.; Han, C.; Ahn, T.; Koh, W. G.; Lee, H. Multi-Scale Characterization of Surface-Crosslinked Superabsorbent Polymer Hydrogel Spheres. *Polymer* 2018, **145**, 174–183. https://doi.org/10.1016/j.polymer.2018.04.073
102. Orakdogen, N.; Okay, O. Influence of the Initiator System on the Spatial Inhomogeneity in Acrylamide-Based Hydrogels. *J Appl Polym Sci* 2007, **103** (5), 3228–3237. https://doi.org/10.1002/app.24977
103. Takata, S. I.; Norisuye, T.; Shibayama, M. Preparation Temperature Dependence and Effects of Hydrolysis on Static Inhomogeneities of

Poly(Acrylamide) Gels. *Macromolecules* 1999, **32** (12), 3989–3993. https://doi.org/10.1021/ma990188a

104. Tomal, W.; Ortyl, J. Water-Soluble Photoinitiators in Biomedical Applications. *Polymers* 2020, **12** (5), 1073. https://doi.org/10.3390/polym12051073
105. Strachota, B.; Matějka, L.; Zhigunov, A.; Konefał, R.; Spěváček, J.; Dybal, J.; Puffr, R. Poly(N-Isopropylacrylamide)–Clay Based Hydrogels Controlled by the Initiating Conditions: Evolution of Structure and Gel Formation. *Soft Matter* 2015, **11** (48), 9291–9306. https://doi.org/10.1039/c5sm01996f
106. Ahmed, M. A.; Erdőssy, J.; Horváth, V. The Role of the Initiator System in the Synthesis of Acidic Multifunctional Nanoparticles Designed for Molecular Imprinting of Proteins. *Periodica Polytechnica Chemical Engineering* 2020, **65** (1), 28–41. https://doi.org/10.3311/PPch.15414
107. Oyen, M. L. Mechanical Characterisation of Hydrogel Materials. *International Materials Reviews* 2014, **59** (1), 44–59. https://doi.org/10.1179/1743280413Y.0000000022
108. Johnson, C. L.; Dunn, A. C. Composition Controls Soft Hydrogel Surface Layer Dimensions and Contact Mechanics. *Biointerphases* 2022, **17** (6), 061002. https://doi.org/10.1116/6.0002047
109. Gombert, Y.; Roncoroni, F.; Sánchez-Ferrer, A.; Spencer, N. D. The Hierarchical Bulk Molecular Structure of Poly(Acrylamide) Hydrogels: Beyond the Fishing Net. *Soft Matter* 2020, **16** (42), 9789–9798. https://doi.org/10.1039/d0sm01536a
110. Shannon, D. P.; Moon, J. D.; Barney, C. W.; Sinha, N. J.; Yang, K.-C.; Jones, S. D.; Garcia, R. V.; Helgeson, M. E.; Segalman, R. A.; Valentine, M. T.; Hawker, C. J. Modular Synthesis and Patterning of High-Stiffness Networks by Postpolymerization Functionalization with Iron–Catechol Complexes. *Macromolecules* 2023, **56** (6), 2268–2276. https://doi.org/10.1021/acs.macromol.2c02561
111. Chau, A. L.; Getty, P. T.; Rhode, A. R.; Bates, C. M.; Hawker, C. J.; Pitenis, A. A. Superlubricity of pH-Responsive Hydrogels in Extreme Environments. *Front Chem* 2022, **11**. https://doi.org/10.3389/fchem.2022.891519
112. Pedro, D. I.; Nguyen, D. T.; Trachsel, L.; Rosa, J. G.; Chu, B.; Eikenberry, S.; Sumerlin, B. S.; Sawyer, W. G. Superficial Modulus, Water-Content, and Mesh-Size at Hydrogel Surfaces. *Tribol Lett* 2021, **69** (4), 1–9. https://doi.org/10.1007/s11249-021-01538-3

113. Flory, P. J.; Rehner, J. Statistical Mechanics of Cross - Linked Polymer Networks II. Swelling. *Journal of Chemical Physics* 1943, **11**, 521–526. https://doi.org/10.1063/1.1723792
114. Flory, P. J. *Principles of Polymer Chemistry*; Cornell University Press: Ithaca, 1953.
115. Li, J.; Hu, Y.; Vlassak, J. J.; Suo, Z. Experimental Determination of Equations of State for Ideal Elastomeric Gels. *Soft Matter* 2012, **8** (31), 8121–8128. https://doi.org/10.1039/c2sm25437a
116. Fennell, E.; Huyghe, J. M. Chemically Responsive Hydrogel Deformation Mechanics: A Review. *Molecules* 2019, **24** (19), 1–22. https://doi.org/10.3390/molecules24193521
117. Horkay, F. Polyelectrolyte Gels: A Unique Class of Soft Materials. *Gels* 2021, **7** (3). https://doi.org/10.3390/gels7030102
118. Collins, M. N.; Birkinshaw, C. Investigation of the Swelling Behavior of Crosslinked Hyaluronic Acid Films and Hydrogels Produced Using Homogeneous Reactions. *J Appl Polym Sci* 2008, **109** (2), 923–931. https://doi.org/10.1002/app.27631
119. Lopez, C. G.; Richtering, W. Does Flory-Rehner Theory Quantitatively Describe the Swelling of Thermoresponsive Microgels? *Soft Matter* 2017, **13** (44), 8271–8280. https://doi.org/10.1039/c7sm01274h
120. Brannon-Peppas, L.; Peppas, N. A. *The Equilibrium Swelling Behavior of Porous and Non-Porous Hydrogels,* 2nd ed.; Elsevier Inc., 1990; Vol. 8. https://doi.org/10.1016/b978-0-444-88654-5.50009-1
121. Chen, G. Thermodynamics of Hydrogels for Applications in Atmospheric Water Harvesting, Evaporation, and Desalination. Ph*ysical Chemistry Chemical Physics* 2022, **24** (20), 12329–12345. https://doi.org/10.1039/D2CP00356B
122. Aalaie, J.; Vasheghani-Farahani, E. Swelling Behavior of Sulfonated Polyacrylamide Nanocomposite Hydrogels in Electrolyte Solutions: Comparison of Theoretical and Experimental Results. *Iranian Polymer Journal (English Edition)* 2012, **21** (3), 175–183. https://doi.org/10.1007/s13726-012-0016-3
123. Li, W.; Zhao, H.; Teasdale, P. R.; John, R.; Zhang, S. Synthesis and Characterisation of a Polyacrylamide-Polyacrylic Acid Copolymer Hydrogel for Environmental Analysis of Cu and Cd. *React Funct Polym* 2002, **52** (1), 31–41. https://doi.org/10.1016/S1381-5148(02)00055-X

124. Gong, J. P.; Kagata, G.; Osada, Y. Friction of Gels. 4. Friction on Charged Gels. *Journal of Physical Chemistry B* 1999, **103** (29), 6007–6014. https://doi.org/10.1021/jp9902553
125. Okay, O.; Sariisik, S. B. Swelling Behavior of Poly(Acrylamide-Co-Sodium Acrylate) Hydrogels in Aqueous Salt Solutions: Theory versus Experiments. *Eur Polym J* 2000, **36** (2), 393–399. https://doi.org/10.1016/S0014-3057(99)00058-0
126. Horkay, F.; Han, M. H.; Han, I. S.; Bang, I. S.; Magda, J. J. Separation of the Effects of pH and Polymer Concentration on the Swelling Pressure and Elastic Modulus of a pH-Responsive Hydrogel. *Polymer* 2006, **47** (21), 7335–7338. https://doi.org/10.1016/j.polymer.2006.08.037
127. Borzacchiello, A.; Ambrosio, L.; Netti, P. A.; Nicolais, L.; Peniche, C.; Gallardo, A.; San Roman, J. Chitosan-Based Hydrogels: Synthesis and Characterization. *J Mater Sci Mater Med* 2001, **12** (10–12), 861–864. https://doi.org/10.1023/A:1012851402759
128. Biomedical Applications of Hydrogels Handbook; Ottenbrite, R. M., Park, K., Okano, T., Eds.; Springer, 2008.
129. Martínez-Ruvalcaba, A.; Becerra-Bracamontes, F.; Sánchez-Díaz, J. C.; González-Álvarez, A. Polyacrylamide-Gelatin Polymeric Networks: Effect of pH and Gelatin Concentration on the Swelling Kinetics and Mechanical Properties. *Polymer Bulletin* 2009, **62** (4), 539–548. https://doi.org/10.1007/s00289-008-0037-4
130. Nesrinne, S.; Djamel, A. Synthesis, Characterization and Rheological Behavior of PH Sensitive Poly(Acrylamide-Co-Acrylic Acid) Hydrogels. *Arabian Journal of Chemistry* 2017, **10** (4), 539–547. https://doi.org/10.1016/j.arabjc.2013.11.027
131. Peppas, N. A.; Moynihan, H. J.; Lucht, L. M. The Structure of Highly Crosslinked Poly(2-hydroxyethyl Methacrylate) Hydrogels. *J Biomed Mater Res* 1985, **19** (4), 397–411. https://doi.org/10.1002/jbm.820190405
132. Patel, S. K.; Rodriguez, F.; Cohen, C. Mechanical and Swelling Properties of Polyacrylamide Gel Spheres. *Polymer* 1989, **30** (12), 2198–2203. https://doi.org/10.1016/0032-3861(89)90249-8
133. Ilavský, M.; Hrouz, J.; Stejskal, J.; Bouchal, K. Phase Transition in Swollen Gels. 6. Effect of Aging on the Extent of Hydrolysis of Aqueous Polyacrylamide Solutions and on the Collapse of Gels. *Macromolecules* 1984, **17** (12), 2868–2874. https://doi.org/10.1021/ma00142a072
134. Lai, Y.; Hu, Y. Probing the Swelling-Dependent Mechanical and Transport Properties of Polyacrylamide Hydrogels through AFM-Based Dynamic

Nanoindentation. *Soft Matter* 2018, **14** (14), 2619–2627. https://doi.org/10.1039/c7sm02351k
135. Turan, E.; Çaykara, T. Swelling and Network Parameters of pH-Sensitive Poly(Acrylamide-Co-Acrylic Acid) Hydrogels. *J Appl Polym Sci* 2007, **106** (3), 2000–2007. https://doi.org/10.1002/app.26848
136. McGhee, E. O.; Manuel, J.; Angela, U.; Gregory, A. P. W. Temperature Dependent Friction of Gemini Hydrogels. *Tribol Lett* 2019, **67** (4), 1–7. https://doi.org/10.1007/s11249-019-1229-9
137. de Gennes, P. G. *Scaling Concepts in Polymer Physics*; Cornell University Press: Ithaca, 1979.
138. Cuccia, N. L.; Pothineni, S.; Wu, B.; Méndez-Harper, J.; Burton, J. C.; Méndez Harper, J.; Burton, J. C. Pore-Size Dependence and Slow Relaxation of Hydrogel Friction on Smooth Surfaces. *Proceedings of the National Academy of Sciences* 2020, **117** (21), 11247–11256. https://doi.org/10.1073/pnas.1922364117
139. Amsden, B. G. Hydrogel Mesh Size and Its Impact on Predictions of Mathematical Models of the Solute Diffusion Coefficient. *Macromolecules* 2022, **55** (18), 8399–8408. https://doi.org/10.1021/acs.macromol.2c01443
140. Teraoka, I. *Polymer Solutions: An Introduction to Physical Properties*; Wiley-Interscience: New York, NY, 2002.
141. Ganji, F.; Vasheghani-Farahani, S.; Vasheghani-Farahani, E. Theoretical Description of Hydrogel Swelling: A Review. Ir*anian Polymer Journal (English Edition)* 2010, **19** (5), 375–398.
142. Peppas, N. A.; Hilt, J. Z.; Khademhosseini, A.; Langer, R. Hydrogels in Biology and Medicine: From Molecular Principles to Bionanotechnology. *Advanced Materials* 2006, **18** (11), 1345–1360. https://doi.org/10.1002/adma.200501612
143. Flory, P. J.; Rehner, J. Statistical Mechanics of Cross-Linked Polymer Networks I. Rubberlike Elasticity. *J Chem Phys* 1943, **11** (11), 512–520. https://doi.org/10.1063/1.1723791
144. Tsuji, Y.; Li, X.; Shibayama, M. Evaluation of Mesh Size in Model Polymer Networks Consisting of Tetra-Arm and Linear Poly(Ethylene Glycol)s. *Gels* 2018, **4** (50). https://doi.org/10.3390/gels4020050
145. Treloar, L. R. G. *The Physics of Rubber Elasticity*, 3rd ed.; Oxford University Press, 1975.
146. Pincus, P. Excluded Volume Effects and Stretched Polymer Chains. *Macromolecules* 1976, **9** (3), 386–388. https://doi.org/10.1021/ma60051a002

147. Kotsmar, C.; Sells, T.; Taylor, N.; Liu, D. E.; Prausnitz, J. M.; Radke, C. J. Aqueous Solute Partitioning and Mesh Size in HEMA/MAA Hydrogels. *Macromolecules* 2012, **45**, 9177–9187. https://doi.org/10.1021/ma3018487
148. Wen, J. H.; Vincent, L. G.; Fuhrmann, A.; Choi, Y. S.; Hribar, K. C.; Taylor-Weiner, H.; Chen, S.; Engler, A. J. Interplay of Matrix Stiffness and Protein Tethering in Stem Cell Differentiation. *Nat Mater* 2014, **13** (10), 979–987. https://doi.org/10.1038/nmat4051
149. Burla, F.; Sentjabrskaja, T.; Pletikapic, G.; van Beugen, J.; Koenderink, G. H. Particle Diffusion in Extracellular Hydrogels. *Soft Matter* 2020, **16**, 1366–1376. https://doi.org/10.1039/c9sm01837a
150. Urueña, J. M.; Pitenis, A. A.; Nixon, R. M.; Schulze, K. D.; Angelini, T. E.; Sawyer, W. G. Mesh Size Control of Polymer Fluctuation Lubrication in Gemini Hydrogels. *Biotribology* 2015, **1–2**, 24–29. https://doi.org/10.1016/j.biotri.2015.03.001
151. Waters, D. J.; Engberg, K.; Parke-Houben, R.; Hartmann, L.; Ta, C. N.; Toney, M. F.; Frank, C. W. Morphology of Photopolymerized End-Linked Poly (Ethylene Glycol) Hydrogels by Small-Angle X-Ray Scattering. *Macromolecules* 2010, **43**, 6861–6870. https://doi.org/10.1021/ma101070s
152. De Molina, P. M.; Lad, S.; Helgeson, M. E. Heterogeneity and Its Influence on the Properties of Difunctional Poly(Ethylene Glycol) Hydrogels: Structure and Mechanics. *Macromolecules* 2015, **48** (15), 5402–5411. https://doi.org/10.1021/acs.macromol.5b01115
153. Horkay, F.; Basser, P. J.; Hecht, A. M.; Geissler, E. Osmotic and SANS Observations on Sodium Polyacrylate Hydrogels in Physiological Salt Solutions. *Macromolecules* 2000, **33** (22), 8329–8333. https://doi.org/10.1021/ma000972r
154. Shoaib, T.; Heintz, J.; Lopez-Berganza, J. A.; Muro-Barrios, R.; Egner, S. A.; Espinosa-Marzal, R. M. Stick-Slip Friction Reveals Hydrogel Lubrication Mechanisms. *Langmuir* 2018, **34** (3), 756–765. https://doi.org/10.1021/acs.langmuir.7b02834
155. Shibayama, M. Spatial Inhomogeneity and Dynamic Fluctuations of Polymer Gels. *Macromol Chem Phys* 1998, **199** (1), 1–30. https://doi.org/10.1002/(SICI)1521-3935(19980101)199:1<1::AID-MACP1>3.0.CO;2-M

156. Shibayama, M.; Okamoto, M. Dynamic Light Scattering Study on Gelatin Aqueous Solutions and Gels. *Journal of Chemical Physics* 2001, **115** (9), 4285–4291. https://doi.org/10.1063/1.1391257
157. Lehmann, M.; Krause, P.; Miruchna, V.; von Klitzing, R. Tailoring PNIPAM Hydrogels for Large Temperature-Triggered Changes in Mechanical Properties. *Colloid Polym Sci* 2019, **297**, 633–640. https://doi.org/10.1007/s00396-019-04470-0
158. Kizilay, M. Y.; Okay, O. Effect of Hydrolysis on Spatial Inhomogeneity in Poly(Acrylamide) Gels of Various Crosslink Densities. *Polymer* 2003, **44** (18), 5239–5250. https://doi.org/10.1016/S0032-3861(03)00494-4
159. Pitenis, A. A.; Sawyer, W. G. Lubricity of High Water Content Aqueous Gels. *Tribol Lett* 2018, **66** (3), 1–7. https://doi.org/10.1007/s11249-018-1063-5
160. Schulze, K. D.; Hart, S. M.; Marshall, S. L.; O'Bryan, C. S.; Urueña, J. M.; Pitenis, A. A.; Sawyer, W. G.; Angelini, T. E. Polymer Osmotic Pressure in Hydrogel Contact Mechanics. *Biotribology* 2017, **11**, 3–7. https://doi.org/10.1016/j.biotri.2017.03.004
161. Canal, T.; Peppas, N. A. Correlation between Mesh Size and Equilibrium Degree of Swelling of Polymeric Networks. *J Biomed Mater Res* 1989, **23** (10), 1183–1193. https://doi.org/10.1002/jbm.820231007
162. Wang, Q. M.; Mohan, A. C.; Oyen, M. L.; Zhao, X. H. Separating Viscoelasticity and Poroelasticity of Gels with Different Length and Time Scales. *Acta Mechanica Sinica* 2014, **30** (1), 20–27. https://doi.org/10.1007/s10409-014-0015-z
163. Hu, Y.; Suo, Z. Viscoelasticity and Poroelasticity in Elastomeric Gels. *Acta Mechanica Solida Sinica* 2012, **25** (5), 441–458. https://doi.org/10.1016/S0894-9166(12)60039-1
164. Biot, M. A. General Theory of Three-Dimensional Consolidation. *J Appl Phys* 1941, **12**, 155–164. https://doi.org/10.1063/1.1712886
165. Galli, M.; Comley, K. S. C.; Shean, T. A. V.; Oyen, M. L. Viscoelastic and Poroelastic Mechanical Characterization of Hydrated Gels. *J Mater Res* 2009, **24** (3), 973–979. https://doi.org/10.1557/jmr.2009.0129
166. Kalcioglu, Z. I.; Mahmoodian, R.; Hu, Y.; Suo, Z.; Van Vliet, K. J. From Macro- to Microscale Poroelastic Characterization of Polymeric Hydrogels via Indentation. *Soft Matter* 2012, **8** (12), 3393–3398. https://doi.org/10.1039/c2sm06825g
167. Degen, G. D.; Chen, Y.; Chau, A. L.; Månsson, L. K.; Pitenis, A. A. Poroelasticity of Highly Confined Hydrogel Films Measured with a Surface

Forces Apparatus. *Soft Matter* 2020, **16**, 8096–8100. https://doi.org/10.1039/d0sm01312a
168. Faghihnejad, A.; Zeng, H. Fundamentals of Surface Adhesion, Friction, and Lubrication. In *Polymer Adhesion, Friction, and Lubrication*; John Wiley & Sons, Inc, 2013; pp 1–58.
169. Pitenis, A. A.; Dowson, D.; Gregory Sawyer, W. Leonardo Da Vinci's Friction Experiments: An Old Story Acknowledged and Repeated. *Tribol Lett* 2014, **56** (3), 509–515. https://doi.org/10.1007/s11249-014-0428-7
170. Gong, J. P. Friction and Lubrication of Hydrogels - Its Richness and Complexity. *Soft Matter* 2006, **2** (7), 544–552. https://doi.org/10.1039/b603209p
171. Stribeck, R. Kugellager Für Beliebige Belastungen. *Zeitschrift des Vereins Deutscher Ingenieure* 1901, **45**.
172. Murakami, T. Importance of Biotribology. *Biotribology of Natural and Artificial Joints* 2023, 1–27. https://doi.org/10.1016/b978-0-12-823669-7.00007-7
173. Hamrock, B. J.; Dowson, D. Elastohydrodynamic Lubrication of Elliptical Contacts for Materials of Low Elastic Modulus I — Fully Flooded Conjunction. *Transactions of the ASME* 1978, **100**, 236–244.
174. Kurokawa, T.; Tominaga, T.; Katsuyama, Y.; Kuwabara, R.; Furukawa, H.; Osada, Y.; Gong, J. P. Elastic-Hydrodynamic Transition of Gel Friction. *Langmuir* 2005, **21** (19), 8643–8648. https://doi.org/10.1021/la050635h
175. Hamrock, B. J.; Schmid, S. R.; Jacobson, B. O. *Fundamentals of Fluid Film Lubrication*, 2nd ed.; CRC Press, 2004. https://doi.org/10.1201/9780203021187
176. Urueña, J. M.; McGhee, E. O.; Angelini, T. E.; Dowson, D.; Sawyer, W. G.; Pitenis, A. A. Normal Load Scaling of Friction in Gemini Hydrogels. *Biotribology* 2018, **13**, 30–35. https://doi.org/10.1016/j.biotri.2018.01.002
177. Gong, J. P.; Iwasaki, Y.; Osada, Y. Friction of Gels. 3. Friction on Solid Surfaces. *Journal of Physical Chemistry B* 1999, **103**, 6001–6006. https://doi.org/10.1021/jp9902553
178. Chang, D. P.; Dolbow, J. E.; Zauscher, S. Switchable Friction of Stimulus-Responsive Hydrogels. *Langmuir* 2007, **23** (1), 250–257. https://doi.org/10.1021/la0617006
179. Shoaib, T.; Espinosa-Marzal, R. M. Insight into the Viscous and Adhesive Contributions to Hydrogel Friction. *Tribol Lett* 2018, **66** (3), 1–14. https://doi.org/10.1007/s11249-018-1045-7

180. Dunn, A. C.; Sawyer, W. G.; Angelini, T. E. Gemini Interfaces in Aqueous Lubrication with Hydrogels. *Tribol Lett* 2014, **54**, 59–66. https://doi.org/10.1007/s11249-014-0308-1
181. Simič, R.; Yetkin, M.; Zhang, K.; Spencer, N. D. Importance of Hydration and Surface Structure for Friction of Acrylamide Hydrogels. *Tribol Lett* 2020, **68** (64). https://doi.org/10.1007/s11249-020-01304-x
182. Shoaib, T.; Espinosa-Marzal, R. M. Advances in Understanding Hydrogel Lubrication. *Colloids and Interfaces* 2020, **4** (54), 1–24. https://doi.org/10.3390/colloids4040054
183. Bonyadi, S. Z.; Hasan, M. M.; Kim, J.; Mahmood, S.; Schulze, K. D.; Dunn, A. C. Review: Friction and Lubrication with High Water Content Crosslinked Hydrogels. *Tribol Lett* 2020, **68** (4), 1–15. https://doi.org/10.1007/s11249-020-01352-3
184. Reale, E. R.; Dunn, A. C. Poroelasticity-Driven Lubrication in Hydrogel Interfaces. *Soft Matter* 2017, **13**, 428–435. https://doi.org/10.1039/c6sm02111e
185. Delavoipière, J.; Tran, Y.; Verneuil, E.; Heurtefeu, B.; Hui, C. Y.; Chateauminois, A. Friction of Poroelastic Contacts with Thin Hydrogel Films. *Langmuir* 2018, **34** (33), 9617–9626. https://doi.org/10.1021/acs.langmuir.8b01466
186. Moore, A. C.; Burris, D. L. An Analytical Model to Predict Interstitial Lubrication of Cartilage in Migrating Contact Areas. *J Biomech* 2014, **47** (1), 148–153. https://doi.org/10.1016/j.jbiomech.2013.09.020
187. Gong, J.; Osada, Y. Gel Friction: A Model Based on Surface Repulsion and Adsorption. *Journal of Chemical Physics* 1998, **109** (18), 8062–8068. https://doi.org/10.1063/1.477453
188. Kagata, G.; Gong, J. P.; Osada, Y. Friction of Gels. 6. Effects of Sliding Velocity and Viscoelastic Responses of the Network. *Journal of Physical Chemistry B* 2002, **106** (18), 4596–4601. https://doi.org/10.1021/jp012380w
189. Schallamach, A. How Does Rubber Slide? *Wear* 1971, **17** (4), 301–312. https://doi.org/10.1016/0043-1648(71)90033-0
190. Baumberger, T.; Caroli, C.; Ronsin, O. Self-Healing Slip Pulses along a Gel/Glass Interface. *Phys Rev Lett* 2002, **88** (7), 4. https://doi.org/10.1103/PhysRevLett.88.075509
191. Klein, J. Hydration Lubrication. *Friction* 2013, **1** (1), 1–23. https://doi.org/10.1007/s40544-013-0001-7

192. Lin, W.; Klein, J. Hydration Lubrication in Biomedical Applications: From Cartilage to Hydrogels. *Acc Mater Res* 2022, **3** (2), 213–223. https://doi.org/10.1021/accountsmr.1c00219
193. Gaisinskaya, A.; Ma, L.; Silbert, G.; Sorkin, R.; Tairy, O.; Goldberg, R.; Kampf, N.; Klein, J. Hydration Lubrication: Exploring a New Paradigm. *Faraday Discuss* 2012, **156**, 217–233. https://doi.org/10.1039/c2fd00127f
194. Mees, J.; Simič, R.; Connor, T. C. O.; Spencer, N. D.; Pastewka, L. Molecular Mechanisms of Self mated Hydrogel Friction. *Tribol Lett* 2023, **71** (3), 1–7. https://doi.org/10.1007/s11249-023-01746-z
195. Urueña, J. M.; Hart, S. M.; Hood, D. L.; McGhee, E. O.; Niemi, S. R.; Schulze, K. D.; Levings, P. P.; Sawyer, W. G.; Pitenis, A. A. Considerations for Biotribometers: Cells, Gels, and Tissues. *Tribol Lett* 2018, **66** (4), 1–7. https://doi.org/10.1007/s11249-018-1094-y
196. Chau, A. L.; Edwards, C. E. R.; Helgeson, M. E.; Pitenis, A. A. Designing Superlubricious Hydrogels from Spontaneous Peroxidation Gradients. *ACS Appl Mater Interfaces* 2023, **15** (36), 43075–43086. https://doi.org/10.1021/acsami.3c04636
197. Mow, V. C.; Ratcliffe, A.; Robin Poole, A. Cartilage and Diarthrodial Joints as Paradigms for Hierarchical Materials and Structures. *Biomaterials* 1992, **13** (2), 67–97. https://doi.org/10.1016/0142-9612(92)90001-5
198. Sunyer, R.; Jin, A. J.; Nossal, R.; Sackett, D. L. Fabrication of Hydrogels with Steep Stiffness Gradients for Studying Cell Mechanical Response. *PLoS One* 2012, **7** (10), 1–9. https://doi.org/10.1371/journal.pone.0046107
199. Lavrentieva, A.; Fleischhammer, T.; Enders, A.; Pirmahboub, H.; Bahnemann, J.; Pepelanova, I. Fabrication of Stiffness Gradients of GelMA Hydrogels Using a 3D Printed Micromixer. *Macromol Biosci* 2020, **20** (7), 2000107. https://doi.org/10.1002/mabi.202000107
200. Zinkovska, N.; Pekar, M.; Smilek, J. Gradient Hydrogels—Overview of Techniques Demonstrating the Existence of a Gradient. *Polymers* 2022, **14** (5). https://doi.org/10.3390/polym14050866
201. Zinkovska, N.; Smilek, J.; Pekar, M. Gradient Hydrogels—The State of the Art in Preparation Methods. *Polymers* 2020, **12** (4), 966. https://doi.org/10.3390/polym12040966
202. Pitenis, A. A.; Manuel Urueña, J.; Nixon, R. M.; Bhattacharjee, T.; Krick, B. A.; Dunn, A. C.; Angelini, T. E.; Gregory Sawyer, W. Lubricity from Entangled Polymer Networks on Hydrogels. *J Tribol* 2016, **138** (4), 1–4. https://doi.org/10.1115/1.4032889

203. Pedron, S.; Peinado, C.; Bosch, P.; Benton, J. A.; Anseth, K. S. Microfluidic Approaches for the Fabrication of Gradient Crosslinked Networks Based on Poly(Ethylene Glycol) and Hyperbranched Polymers for Manipulation of Cell Interactions. *J Biomed Mater Res A* 2011, **96A** (1), 196–203. https://doi.org/10.1002/jbm.a.32974
204. Diederich, V. E. G.; Studer, P.; Kern, A.; Lattuada, M.; Storti, G.; Sharma, R. I.; Snedeker, J. G.; Morbidelli, M. Bioactive Polyacrylamide Hydrogels With Gradients in Mechanical Stiffness. *Biotechnol Bioeng* 2013, **110** (5), 1508–1519. https://doi.org/10.1002/bit.24810
205. Lee, D.; Golden, K.; Rahman, M. M.; Moran, A.; Gonzalez, B.; Ryu, S. Fabrication of Hydrogels with a Stiffness Gradient Using Limited Mixing in the Hele-Shaw Geometry. *Exp Mech* 2019, **59** (9), 1249–1259. https://doi.org/10.1007/s11340-018-0416-1
206. Shu, Y.; Chan, H. N.; Guan, D.; Wu, H.; Ma, L. A Simple Fabricated Thickness-Based Stiffness Gradient for Cell Studies. *Sci Bull (Beijing)* 2017, **62** (3), 222–228. https://doi.org/10.1016/j.scib.2016.12.012
207. Wong, J. Y.; Velasco, A.; Rajagopalan, P.; Pham, Q. Directed Movement of Vascular Smooth Muscle Cells on Gradient-Compliant Hydrogels. *Langmuir* 2003, **19** (5), 1908–1913. https://doi.org/10.1021/la026403p
208. Tse, J. R.; Engler, A. J. Preparation of Hydrogel Substrates with Tunable Mechanical Properties. *Curr Protoc Cell Biol* 2010, **47** (1). https://doi.org/10.1002/0471143030.cb1016s47
209. Kloxin, A. M.; Benton, J. A.; Anseth, K. S. In Situ Elasticity Modulation with Dynamic Substrates to Direct Cell Phenotype. *Biomaterials* 2010, **31**, 1–8. https://doi.org/10.1016/j.biomaterials.2009.09.025
210. Zhang, N.; Milleret, V.; Thompson-Steckel, G.; Huang, N.-P.; Vörös, J.; Simona, B. R.; Ehrbar, M. Soft Hydrogels Featuring In-Depth Surface Density Gradients for the Simple Establishment of 3D Tissue Models for Screening Applications. *SLAS Discovery* 2017, **22** (5), 635–644. https://doi.org/10.1177/2472555217693191
211. Simona, B. R.; Hirt, L.; Demkó, L.; Zambelli, T.; Vörös, J.; Ehrbar, M.; Milleret, V. Density Gradients at Hydrogel Interfaces for Enhanced Cell Penetration. *Biomater Sci* 2015, **3**, 586–591. https://doi.org/10.1039/c4bm00416g
212. Kii, A.; Xu, J.; Gong, J. P.; Osada, Y.; Zhang, X. Heterogeneous Polymerization of Hydrogels on Hydrophobic Substrate. *Journal of Physical Chemistry B* 2001, **105**, 4565–4571. https://doi.org/10.1021/jp003242u

213. Gong, J. P.; Kurokawa, T.; Narita, T.; Kagata, G.; Osada, Y.; Nishimura, G.; Kinjo, M. Synthesis of Hydrogels with Extremely Low Surface Friction. *J Am Chem Soc* 2001, **123** (23), 5582–5583. https://doi.org/10.1021/ja003794q
214. Gong, J. P.; Kii, A.; Xu, J.; Hattori, Y.; Osada, Y. A Possible Mechanism for the Substrate Effect on Hydrogel Formation. *Journal of Physical Chemistry B* 2001, **105** (20), 4572–4576. https://doi.org/10.1021/jp003244e
215. Meier, Y. A.; Zhang, K.; Spencer, N. D.; Simic, R. Linking Friction and Surface Properties of Hydrogels Molded Against Materials of Different Surface Energies. *Langmuir* 2019, **35** (48), 15805–15812. https://doi.org/10.1021/acs.langmuir.9b01636
216. Simič, R.; Mandal, J.; Zhang, K.; Spencer, N. D. Oxygen Inhibition of Free-Radical Polymerization Is the Dominant Mechanism behind the "Mold Effect" on Hydrogels. *Soft Matter* 2021, **17** (26), 6394–6403. https://doi.org/10.1039/D1SM00395J
217. Menter, P. Acrylamide Polymerization- A Practical Approach. *Electrophoresis* 2000, 1156.
218. Studer, K.; Decker, C.; Beck, E.; Schwalm, R. Overcoming Oxygen Inhibition in UV-Curing of Acrylate Coatings by Carbon Dioxide Inerting: Part II. *Prog Org Coat 2003*, **48** (1), 101–111. https://doi.org/10.1016/S0300-9440(03)00149-8
219. Chawla, C. P.; Dupre, J. Oxygen and Radical Photopolymerization in Films. In *ACS Symposium Series*; 2003; pp 165–175.
220. Bowman, C. N.; Kloxin, C. J. Toward an Enhanced Understanding and Implementation of Photopolymerization Reactions. *AIChE Journal* 2008, **54** (11). https://doi.org/10.1002/aic.11678
221. Dendukuri, D.; Panda, P.; Haghgooie, R.; Kim, J. M.; Hatton, T. A.; Doyle, P. S. Modeling of Oxygen-Inhibited Free Radical Photopolymerization in a PDMS Microfluidic Device. *Macromolecules* 2008, **41**, 8547–8556. https://doi.org/10.1021/ma801219w
222. Ligon, S. C.; Husár, B.; Wutzel, H.; Holman, R.; Liska, R. Strategies to Reduce Oxygen Inhibition in Photoinduced Polymerization. *Chem Rev* 2014, **114** (1), 557–589. https://doi.org/10.1021/cr3005197
223. Cao, H.; Currie, E.; Tilley, M.; Jean, Y. C. Oxygen Inhibition Effect on Surface Properties of UV-Curable Acrylate Coatings. In *ACS Symposium Series*; 2003; pp 152–164. https://doi.org/10.1021/bk-2003-0847.ch013
224. Studer, K.; Decker, C.; Beck, E.; Schwalm, R. Overcoming Oxygen Inhibition in UV-Curing of Acrylate Coatings by Carbon Dioxide Inerting,

Part I. *Prog Org Coat* 2003, **48** (1), 92–100. https://doi.org/10.1016/S0300-9440(03)00120-6

225. Pierrel, J.; Ibrahim, A.; Croutxé-Barghorn, C.; Allonas, X. Effect of the Oxygen Affected Layer in Multilayered Photopolymers. *Polym Chem* 2017, **8** (31), 4596–4602. https://doi.org/10.1039/c7py00974g
226. Whitely, M. E.; Robinson, J. L.; Stuebben, M. C.; Pearce, H. A.; McEnery, M. A. P.; Cosgriff-Hernandez, E. Prevention of Oxygen Inhibition of PolyHIPE Radical Polymerization Using a Thiol-Based Cross-Linker. *ACS Biomater Sci Eng* 2017, **3** (3), 409–419. https://doi.org/10.1021/acsbiomaterials.6b00663
227. Decker, C.; Jenkins, A. D. Kinetic Approach of O2 Inhibition in Ultraviolet and Laser-Induced Polymerizations. *Macromolecules* 1985, **18** (6), 1241–1244. https://doi.org/10.1021/ma00148a034
228. Courtecuisse, F.; Karasu, F.; Allonas, X.; Croutxé-Barghorn, C.; van der Ven, L. Confocal Raman Microscopy Study of Several Factors Known to Influence the Oxygen Inhibition of Acrylate Photopolymerization under LED. *Prog Org Coat* 2016, **92**, 1–7. https://doi.org/10.1016/j.porgcoat.2015.11.020
229. O'Brien, A. K.; Bowman, C. N. Modeling the Effect of Oxygen on Photopolymerization Kinetics. *Macromol Theory Simul* 2006, **15** (2), 176–182. https://doi.org/10.1002/mats.200500056
230. Courtecuisse, F.; Dietlin, C.; Croutxé Barghorn, C.; Van Der Ven, L. G. J. Depth Characterization of Photopolymerized Films by Confocal Raman Microscopy Using an Immersion Objective. *Appl Spectrosc* 2011, **65** (10), 1126–1132. https://doi.org/10.1366/11-06299
231. Lin, J.-T.; Liu, H.-W.; Chen, K.-T.; Cheng, D.-C. Modeling the Kinetics, Curing Depth, and Efficacy of Radical-Mediated Photopolymerization: The Role of Oxygen Inhibition, Viscosity, and Dynamic Light Intensity. *Front Chem* 2019, **7**, 1–14. https://doi.org/10.3389/fchem.2019.00760
232. Guvendiren, M.; Yang, S.; Burdick, J. A. Swelling-Induced Surface Patterns in Hydrogels with Gradient Crosslinking Density. *Adv Funct Mater* 2009, **19**, 3038–3045. https://doi.org/10.1002/adfm.200900622
233. Guvendiren, M.; Burdick, J. A.; Yang, S. Kinetic Study of Swelling-Induced Surface Pattern Formation and Ordering in Hydrogel Films with Depth-Wise Crosslinking Gradient. *Soft Matter* 2010, **6** (9), 2044. https://doi.org/10.1039/b927374c

234. Gombert, Y.; Simič, R.; Roncoroni, F.; Dübner, M.; Geue, T.; Spencer, N. D. Structuring Hydrogel Surfaces for Tribology. *Adv Mater Interfaces* 2019, **6** (22), 1901320. https://doi.org/10.1002/admi.201901320
235. Pitenis, A. A.; Urueña, J. M.; Cooper, A. C.; Angelini, T. E.; Sawyer, W. G. Superlubricity in Gemini Hydrogels. *J Tribol* 2016, **138** (4), 21–23. https://doi.org/10.1115/1.4032890
236. Simič, R.; Spencer, N. D. Controlling the Friction of Gels by Regulating Interfacial Oxygen During Polymerization. *Tribol Lett* 2021, **69** (3), 86. https://doi.org/10.1007/s11249-021-01459-1
237. Itagaki, N.; Kawaguchi, D.; Oda, Y.; Nemoto, F.; Yamada, N. L.; Yamaguchi, T.; Tanaka, K. Surface Effect on Frictional Properties for Thin Hydrogel Films of Poly(Vinyl Ether). *Macromolecules* 2019, **52** (24), 9632–9638. https://doi.org/10.1021/acs.macromol.9b01786
238. Johnson, C. L.; Dunn, A. C. Tribological Characterization of Gradient-Density Polyacrylamide Hydrogel Surfaces. *Exp Mech* 2021, **61** (5), 829–842. https://doi.org/10.1007/s11340-021-00704-x
239. Bonyadi, S. Z.; Atten, M.; Dunn, A. C. Self-Regenerating Compliance and Lubrication of Polyacrylamide Hydrogels. *Soft Matter* 2019, **15** (43), 8728–8740. https://doi.org/10.1039/c9sm01607d
240. Chau, A. L.; Cavanaugh, M. K.; Chen, Y. T.; Pitenis, A. A. A Simple Contact Mechanics Model for Highly Strained Aqueous Surface Gels. *Exp Mech* 2021, **61** (4), 699–703. https://doi.org/10.1007/s11340-021-00699-5
241. Hasan, M. M.; Johnson, C. L.; Dunn, A. C. Soft Contact Mechanics with Gradient-Stiffness Surfaces. *Langmuir* 2022, **38** (31), 9454–9465. https://doi.org/10.1021/acs.langmuir.2c00296
242. Sudre, G.; Hourdet, D.; Cousin, F.; Creton, C.; Tran, Y. Structure of Surfaces and Interfaces of Poly(N,N-Dimethylacrylamide) Hydrogels. *Langmuir* 2012, **28** (33), 12282–12287. https://doi.org/10.1021/la301417x
243. Yoffe, E. H. Modified Hertz Theory for Spherical Indentation. *Philosophical Magazine A* 1984, **50** (6), 813–828. https://doi.org/10.1080/01418618408237539
244. Bahrami, M.; Le Houérou, V.; Rühe, J. Lubrication Mechanism of Surface-Attached Hydrogel Layers in Sliding Contact. *Adv Mater Interfaces* 2022, **9** (33). https://doi.org/10.1002/admi.202201581
245. Kontomaris, S. V; Malamou, A. Hertz Model or Oliver & Pharr Analysis? Tutorial Regarding AFM Nanoindentation Experiments on Biological Samples. *Mater Res Express* 2020, **7** (3), 033001. https://doi.org/10.1088/2053-1591/ab79ce

246. Nieto, J. L.; Baselga, J.; Hernandez-Fuentes, I.; Llorente, M. A.; Piérola, I. F. Polyacrylamide Networks. Kinetic and Structural Studies by High Field 1H-NMR with Polymerization in Situ. *Eur Polym J* 1987, **23** (7), 551–555. https://doi.org/10.1016/0014-3057(87)90111-X
247. Garcia, M.; Schulze, K. D.; O'Bryan, C. S.; Bhattacharjee, T.; Sawyer, W. G.; Angelini, T. E. Eliminating the Surface Location from Soft Matter Contact Mechanics Measurements. *Tribology - Materials, Surfaces & Interfaces* 2017, **11** (4), 187–192. https://doi.org/10.1080/17515831.2017.1397908
248. Klein, J.; Kamiyama, Y.; Yoshizawa, H.; Israelachvili, J. N.; Fredrickson, G. H.; Pincus, P.; Fetters, L. J. Lubrication Forces between Surfaces Bearing Polymer Brushes. *Macromolecules* 1993, **26** (21), 5552–5560. https://doi.org/10.1021/ma00073a004
249. Fredrickson, G. H.; Ajdari, A.; Leibler, L.; Carton, J. P. Surface Modes and Deformation Energy of a Molten Polymer Brush. *Macromolecules* 1992, **25** (11), 2882–2889. https://doi.org/10.1021/ma00037a015
250. Giz, A.; Çatalgil-Giz, H.; Alb, A.; Brousseau, J. L.; Reed, W. F. Kinetics and Mechanisms of Acrylamide Polymerization from Absolute, Online Monitoring of Polymerization Reaction. *Macromolecules* 2001, **34** (5), 1180–1191. https://doi.org/10.1021/ma000815s
251. Wang, D. W.; Thomas, W. M. *Encyclopedia of Polymer Science and Engineering*; Wiley-Interscience: New York, 1991.
252. Fuxman, A. M.; McAuley, K. B.; Schreiner, L. J. Modeling of Free-Radical Crosslinking Copolymerization of Acrylamide and N,N′-Methylenebis(Acrylamide) for Radiation Dosimetry. *Macromol Theory Simul* 2003, **12** (9), 647–662. https://doi.org/10.1002/mats.200350050
253. Kulichikhin, S. G.; Malkin, A. Y.; Polushkina, O. M.; Kulichikhin, V. G. Rheokinetics of Free-Radical Polymerization of Acrylamide in an Aqueous Solution. *Polym Eng Sci* 1997, **37** (8), 1331–1338. https://doi.org/10.1002/pen.11779
254. Hepworth, S. J.; Leach, M. O.; Doran, S. J. Dynamics of Polymerization in Polyacrylamide Gel (PAG) Dosimeters: (II) Modelling Oxygen Diffusion. *Phys. Med. Biol.* 1999, **44** (8), 1875–1884. https://doi.org/10.1088/0031-9155/44/8/302
255. Chang, H.; Li, C.; Huang, R.; Su, R.; Qi, W.; He, Z. Amphiphilic Hydrogels for Biomedical Applications. *J Mater Chem B* 2019, **7** (18), 2899–2910. https://doi.org/10.1039/c9tb00073a

256. Patrickios, C. S.; Georgiou, T. K. Covalent Amphiphilic Polymer Networks. *Curr Opin Colloid Interface Sci* 2003, **8** (1), 76–85. https://doi.org/10.1016/S1359-0294(03)00005-0
257. Walker, P. S.; Dowson, D.; Longfield, M. D.; Wright, V. "Boosted Lubrication" in Synovial Joints by Fluid Entrapment and Enrichment. *Ann Rheum Dis* 1968, **27** (6), 512–520. https://doi.org/10.1136/ard.27.6.512
258. Bonnevie, E. D.; Baro, V. J.; Wang, L.; Burris, D. L. In Situ Studies of Cartilage Microtribology: Roles of Speed and Contact Area. *Tribol Lett* 2011, **41** (1), 83–95. https://doi.org/10.1007/s11249-010-9687-0
259. Moore, A. C.; Burris, D. L. Tribological Rehydration of Cartilage and Its Potential Role in Preserving Joint Health. *Osteoarthritis Cartilage* 2017, **25** (1), 99–107. https://doi.org/10.1016/j.joca.2016.09.018
260. Bonnevie, E. D.; Baro, V. J.; Wang, L.; Burris, D. L. Fluid Load Support during Localized Indentation of Cartilage with a Spherical Probe. *J Biomech* 2012, **45** (6), 1036–1041. https://doi.org/10.1016/j.jbiomech.2011.12.019
261. Seror, J.; Zhu, L.; Goldberg, R.; Day, A. J.; Klein, J. Supramolecular Synergy in the Boundary Lubrication of Synovial Joints. *Nat Commun* 2015, 6. https://doi.org/10.1038/ncomms7497
262. Jay, G. D.; Waller, K. A. The Biology of Lubricin: Near Frictionless Joint Motion. *Matrix Biology* 2014, **39**, 17–24. https://doi.org/10.1016/j.matbio.2014.08.008
263. Jung, S.; Petelska, A.; Beldowski, P.; Augé, W. K.; Casey, T.; Walczak, D.; Lemke, K.; Gadomski, A. Hyaluronic Acid and Phospholipid Interactions Useful for Repaired Articular Cartilage Surfaces—a Mini Review toward Tribological Surgical Adjuvants. *Colloid Polym Sci* 2017, **295** (3), 403–412. https://doi.org/10.1007/s00396-017-4014-z
264. Smith, P.; Ziolek, R. M.; Gazzarrini, E.; Owen, D. M.; Lorenz, C. D. On the Interaction of Hyaluronic Acid with Synovial Fluid Lipid Membranes. *Physical Chemistry Chemical Physics* 2019, **21** (19), 9845–9857. https://doi.org/10.1039/c9cp01532a
265. McGhee, E. O.; Hart, S. M.; Urueña, J. M.; Sawyer, W. G. Hydration Control of Gel-Adhesion and Muco-Adhesion. *Langmuir* 2019, **35**, 15769–15775. https://doi.org/10.1021/acs.langmuir.9b02816
266. Khattab, I. S.; Bandarkar, F.; Amin, M.; Fakhree, A.; Jouyban, A. Density, Viscosity, and Surface Tension of Water+ethanol Mixtures from 293 to 323 K. *Korean Journal of Chemical Engineering* 2012, **29** (6), 812–817. https://doi.org/10.1007/s11814-011-0239-6

267. Weaver, J. V. M.; Bannister, I.; Robinson, K. L.; Armes, S. P.; Smallridge, M.; Mckenna, P. Stimulus-Responsive Water-Soluble Polymers Based on 2-Hydroxyethyl Methacrylate. *Macromolecules* 2004, **37** (7), 2395–2403. https://doi.org/10.1021/ma0356358
268. Li, A.; Ramakrishna, S. N.; Kooij, E. S.; Espinosa-Marzal, R. M.; Spencer, N. D. Poly(Acrylamide) Films at the Solvent-Induced Glass Transition: Adhesion, Tribology, and the Influence of Crosslinking. *Soft Matter* 2012, **8** (35), 9092–9100. https://doi.org/10.1039/c2sm26222c
269. Lorenz, B.; Rodriguez, N.; Mangiagalli, P.; Persson, B. N. J. Role of Hydrophobicity on Interfacial Fluid Flow: Theory and Some Applications. *European Physical Journal E* 2014, **37** (6), 1–14. https://doi.org/10.1140/epje/i2014-14057-6
270. Hirano, M.; Shinjo, K. Superlubricity and Frictional Anisotropy. *Wear* 1993, **168** (1–2), 121–125. https://doi.org/10.1016/0043-1648(93)90207-3
271. Baykara, M. Z.; Vazirisereshk, M. R.; Martini, A. Emerging Superlubricity: A Review of the State of the Art and Perspectives on Future Research. *Appl Phys Rev* 2018, **5** (4). https://doi.org/10.1063/1.5051445
272. Wang, Z.; Li, J.; Liu, Y.; Luo, J. Macroscale Superlubricity Achieved Between Zwitterionic Copolymer Hydrogel and Sapphire in Water. *Mater Des* 2020, 188, 108441. https://doi.org/10.1016/j.matdes.2019.108441
273. Martin, J. M.; Erdemir, A. Superlubricity: Friction's Vanishing Act. *Phys Today* 2018, **71** (4), 40–45. https://doi.org/10.1063/PT.3.3897
274. Liu, Y. Approaching Superlubricity under Liquid Conditions and Boundary Lubrication— Superlubricity of Biomaterials. In *Superlubricity*; Erdemir, Ali., Martin, J. M., Luo, J., Eds.; Elsevier B.V.: Cambridge, MA, 2021; pp 405–437. https://doi.org/10.1016/b978-0-444-64313-1.00021-1
275. Yong, Y.; Qiao, M.; Chiu, A.; Fuchs, S.; Liu, Q.; Pardo, Y.; Worobo, R.; Liu, Z.; Ma, M. Conformal Hydrogel Coatings on Catheters to Reduce Biofouling. *Langmuir* 2019, **35** (5), 1927–1934. https://doi.org/10.1021/acs.langmuir.8b03074
276. Banquy, X.; Burdyńska, J.; Lee, D. W.; Matyjaszewski, K.; Israelachvili, J. Bioinspired Bottle-Brush Polymer Exhibits Low Friction and Amontons-like Behavior. *J Am Chem Soc* 2014, **136** (17), 6199–6202. https://doi.org/10.1021/ja501770y
277. Briscoe, W. H.; Titmuss, S.; Tiberg, F.; Thomas, R. K.; McGillivray, D. J.; Klein, J. Boundary Lubrication under Water. *Nature* 2006, **444**, 191–194. https://doi.org/10.1038/nature05196

278. Yan, W.; Ramakrishna, S. N.; Romio, M.; Benetti, E. M. Bioinert and Lubricious Surfaces by Macromolecular Design. *Langmuir* 2019, **35** (42), 13521–13535. https://doi.org/10.1021/acs.langmuir.9b02316
279. Chen, M.; Briscoe, W. H.; Armes, S. P.; Klein, J. Lubrication at Physiological Pressures by Polyzwitterionic Brushes. *Science* 2009, **323** (5922), 1698–1701. https://doi.org/10.1126/science.1169399
280. Ohsedo, Y.; Takashina, R.; Gong, J. P.; Osada, Y. Surface Friction of Hydrogels with Well-Defined Polyelectrolyte Brushes. *Langmuir* 2004, **20** (16), 6549–6555. https://doi.org/10.1021/la036211+
281. Zhang, K.; Simič, R.; Spencer, N. D. Imparting Ultralow Lubricity to Double-Network Hydrogels by Surface-Initiated Controlled Radical Polymerization under Ambient Conditions. *Biotribology* 2021, **26**, 100161. https://doi.org/10.1016/j.biotri.2021.100161
282. Rudy, A.; Kuliasha, C.; Urueña, J. M.; Rex, J.; Schulze, K. D. Lubricous Hydrogel Surface Coatings on Polydimethylsiloxane (PDMS). *Tribol Lett* 2017, **65** (3). https://doi.org/10.1007/s11249-016-0783-7
283. Johnson, B. D.; Beebe, D. J.; Crone, W. C. Effects of Swelling on the Mechanical Properties of a pH-Sensitive Hydrogel for Use in Microfluidic Devices. *Materials Science and Engineering C* 2004, **24** (4), 575–581. https://doi.org/10.1016/j.msec.2003.11.002
284. Choi, J.; Kung, H. J.; Maclas, C. E.; Muratoglu, O. K. Highly Lubricious Poly(Vinyl Alcohol)-Poly(Acrylic Acid) Hydrogels. *J Biomed Mater Res B Appl Biomater* 2012, **100B** (2), 524–532. https://doi.org/10.1002/jbm.b.31980
285. Lopez-Ureta, L. C.; Orozco-Guareño, E.; Cruz-Barba, L. E.; Gonzalez-Alvarez, A.; Bautista-Rico, F. Synthesis and Characterization of Acrylamide/Acrylic Acid Hydrogels Crosslinked Using a Novel Diacrylate of Glycerol to Produce Multistructured Materials. *J Polym Sci A Polym Chem* 2008, **46** (8), 2667–2679. https://doi.org/10.1002/pola.22598
286. Jing, Z.; Xu, A.; Liang, Y. Q.; Zhang, Z.; Yu, C.; Hong, P.; Li, Y. Biodegradable Poly(Acrylic Acid-Co-Acrylamide)/ Poly(Vinyl Alcohol) Double Network Hydrogels with Tunable Mechanics and High Self-Healing Performance. *Polymers* 2019, **11** (6). https://doi.org/10.3390/polym11060952
287. Thakur, A.; Wanchoo, R. K.; Singh, P. Structural Parameters and Swelling Behavior of pH Sensitive Poly(Acrylamide-Co-Acrylic Acid) Hydrogels. *Chem Biochem Eng Q* 2011, **25** (2), 181–194.

288. Heidari, S.; Esmaeilzadeh, F.; Mowla, D.; Ghasemi, S. Synthesis of an Efficient Copolymer of Acrylamide and Acrylic Acid and Determination of Its Swelling Behavior. *J Pet Explor Prod Technol* 2018, **8** (4), 1331–1340. https://doi.org/10.1007/s13202-017-0428-x
289. Mahon, R.; Balogun, Y.; Oluyemi, G.; Njuguna, J. Swelling Performance of Sodium Polyacrylate and Poly(Acrylamide co acrylic Acid) Potassium Salt. *SN Appl Sci* 2019, **2** (117), 1–15. https://doi.org/10.1007/s42452-019-1874-5
290. Garces, F. O.; Sivadasan, K.; Somasundaran, P.; Turro, N. J. Interpolymer Complexation of Poly(Acrylic Acid) and Polyacrylamide: Structural and Dynamic Studies by Solution- and Solid-State NMR. *Macromolecules* 1994, **27** (1), 272–278. https://doi.org/10.1021/ma00079a040
291. Zhou, X.; Weng, L.; Chen, Q.; Zhang, J.; Shen, D.; Li, Z.; Shao, M.; Xu, J. Investigation of pH Sensitivity of Poly(Acrylic Acid-Co-Acrylamide) Hydrogel. *Polym Int* 2003, **52** (7), 1153–1157. https://doi.org/10.1002/pi.1207
292. Çaykara, T.; Akçakaya, I. Synthesis and Network Structure of Ionic Poly(N,N-Dimethylacrylamide-Co-Acrylamide) Hydrogels: Comparison of Swelling Degree with Theory. *Eur Polym J* 2006, **42** (6), 1437–1445. https://doi.org/10.1016/j.eurpolymj.2006.01.001
293. Sheikh, N.; Jalili, L.; Anvari, F. A Study on the Swelling Behavior of Poly(Acrylic Acid) Hydrogels Obtained by Electron Beam Crosslinking. *Radiation Physics and Chemistry* 2010, **79** (6), 735–739. https://doi.org/10.1016/j.radphyschem.2009.12.013
294. Han, L.; Yin, J.; Wang, L.; Chia, K. K.; Cohen, R. E.; Rubner, M. F.; Ortiz, C.; Boyce, M. C. Tunable Stimulus-Responsive Friction Mechanisms of Polyelectrolyte Films and Tube Forests. *Soft Matter* 2012, **8** (33), 8642–8650. https://doi.org/10.1039/c2sm25503k
295. Ma, S.; Scaraggi, M.; Lin, P.; Yu, B.; Wang, D.; Dini, D.; Zhou, F. Nanohydrogel Brushes for Switchable Underwater Adhesion. *Journal of Physical Chemistry C* 2017, **121** (15), 8452–8463. https://doi.org/10.1021/acs.jpcc.7b01305
296. Arens, L.; Weißenfeld, F.; Klein, C. O.; Schlag, K.; Wilhelm, M. Osmotic Engine: Translating Osmotic Pressure into Macroscopic Mechanical Force via Poly(Acrylic Acid) Based Hydrogels. *Advanced Science* 2017, **4** (9). https://doi.org/10.1002/advs.201700112

297. Okay, O.; Durmaz, S. Charge Density Dependence of Elastic Modulus of Strong Polyelectrolyte Hydrogels. *Polymer* 2002, **43** (4), 1215–1221. https://doi.org/10.1016/S0032-3861(01)00723-6
298. Zeldovich, K. B.; Khokhlov, A. R. Osmotically Active and Passive Counterions in Inhomogeneous Polymer Gels. *Macromolecules* 1999, **32** (10), 3488–3494. https://doi.org/10.1021/ma9815298
299. Zeynali, M. E.; Rabbii, A. Alkaline Hydrolysis of Polyacrylamide and Study on Poly(Acrylamide-Co-Sodium Acrylate) Properties. *Iranian Polymer Journal* 2002, **11** (4), 269–275.
300. Owens, D. E.; Jian, Y.; Fang, J. E.; Slaughter, B. v.; Chen, Y.; Peppas, N. A. Thermally Responsive Swelling Properties of Polyacrylamide/Poly(Acrylic Acid) Interpenetrating Polymer Network Nanoparticles. *Macromolecules* 2007, **40** (20), 7306–7310. https://doi.org/10.1021/ma071089x
301. Yang, M.; Liu, C.; Li, Z.; Gao, G.; Liu, F. Temperature-Responsive Properties of Poly(Acrylic Acid-Co-Acrylamide) Hydrophobic Association Hydrogels with High Mechanical Strength. *Macromolecules* 2010, **43** (24), 10645–10651. https://doi.org/10.1021/ma1022555
302. Orakdogen, N.; Boyaci, T. Finite Extensibility and Deviation from Gaussian Elasticity of Dimethylacrylamide-Based Gels with Different Charge Density: Insight into pH/Solvent-Dependent Swelling and Surfactant Interactions. *Polymer* 2017, **132**, 306–324. https://doi.org/10.1016/j.polymer.2017.11.013
303. Orakdogen, N.; Boyaci, T. Non-Gaussian Elasticity and Charge Density-Dependent Swelling of Strong Polyelectrolyte Poly(N-Isopropylacrylamide-Co-Sodium Acrylate) Hydrogels. *Soft Matter* 2017, **13** (47), 9046–9059. https://doi.org/10.1039/c7sm01866e
304. Dehghani, E. S.; Ramakrishna, S. N.; Spencer, N. D.; Benetti, E. M. Controlled Crosslinking Is a Tool To Precisely Modulate the Nanomechanical and Nanotribological Properties of Polymer Brushes. *Macromolecules* 2017, **50** (7), 2932–2941. https://doi.org/10.1021/acs.macromol.6b02409
305. Liu, X.; Nanao, H.; Li, T.; Mori, S. A Study on the Friction Properties of PAAc Hydrogel under Low Loads in Air and Water. *Wear* 2004, **257** (7–8), 665–670. https://doi.org/10.1016/j.wear.2004.02.005
306. Ahmed, J.; Guo, H.; Yamamoto, T.; Kurokawa, T.; Takahata, M.; Nakajima, T.; Gong, J. P. Sliding Friction of Zwitterionic Hydrogel and Its Electrostatic Origin. *Macromolecules* 2014, **47** (9), 3101–3107. https://doi.org/10.1021/ma500382y

307. Oogaki, S.; Kagata, G.; Kurokawa, T.; Kuroda, S.; Osada, Y.; Gong, J. P. Friction between Like-Charged Hydrogels - Combined Mechanisms of Boundary, Hydrated and Elastohydrodynamic Lubrication. *Soft Matter* 2009, **5** (9), 1879–1887. https://doi.org/10.1039/b815102d
308. Yoo, M. K.; Sung, Y. K.; Cho, C. S.; Lee, Y. M. Effect of Polymer Complex Formation on the Cloud-Point of Poly(N-Isopropyl Acrylamide) (PNIPAAm) in the Poly(NIPAAm-Co-Acrylic Acid): Polyelectrolyte Complex between Poly(Acrylic Acid) and Poly(Allylamine). *Polymer* 1997, **38** (11), 2759–2765. https://doi.org/10.1016/s0032-3861(97)85612-1
309. Osaheni, A. O.; Ash-Shakoor, A.; Gitsov, I.; Mather, P. T.; Blum, M. M. Synthesis and Characterization of Zwitterionic Polymer Brush Functionalized Hydrogels with Ionic Responsive Coefficient of Friction. *Langmuir* 2020, **36** (14), 3932–3940. https://doi.org/10.1021/acs.langmuir.9b03566
310. Sokoloff, J. B. Theory of Lubrication Due to Polyelectrolyte Hydrogels with Arbitrary Salt Concentration and Degree of Compression. *Journal of Chemical Physics* 2013, **139** (8). https://doi.org/10.1063/1.4818873
311. Erbaş, A.; Olvera De La Cruz, M. Interactions between Polyelectrolyte Gel Surfaces. *Macromolecules* 2016, **49** (23), 9026–9034. https://doi.org/10.1021/acs.macromol.6b01416
312. Tai, F. I.; Sterner, O.; Andersson, O.; Ekblad, T.; Ederth, T. Interaction Forces on Polyampholytic Hydrogel Gradient Surfaces. *ACS Omega* 2019, **4** (3), 5670–5681. https://doi.org/10.1021/acsomega.9b00339
313. Sokoloff, J. B. Theory of the Effects of Surface Roughness on Fluid Lubrication of Hydrogels. *Soft Matter* 2012, **8** (31), 8164–8170. https://doi.org/10.1039/c2sm25414j
314. Sokoloff, J. B. Theory of Hydrostatic Lubrication for Two Like-Charge Polymer Hydrogel Coated Surfaces. *Soft Matter* 2010, **6** (16), 3856–3862. https://doi.org/10.1039/c000252f
315. Behrens, S. H.; Grier, D. G. The Charge of Glass and Silica Surfaces. *Journal of Chemical Physics* 2001, **115** (14), 6716–6721. https://doi.org/10.1063/1.1404988
316. Shah, G.; Dubin, P. L.; Kaplan, J. I.; Newkome, G. R.; Moorefield, C. N.; Baker, G. R. Size-Exclusion Chromatography of Carboxyl-Terminated Dendrimers as a Model for Permeation of Charged Particles into like-Charged Cavities. *J Colloid Interface Sci* 1996, **183** (2), 397–407. https://doi.org/10.1006/jcis.1996.0562

317. Riahinezhad, M.; Kazemi, N.; McManus, N.; Penlidis, A. Optimal Estimation of Reactivity Ratios for Acrylamide/Acrylic Acid Copolymerization. *J Polym Sci A Polym Chem* 2013, **51** (22), 4819–4827. https://doi.org/10.1002/pola.26906
318. Ezenwajiaku, I. H.; Hutchinson, R. A. Effect of Ionization on Aqueous Phase Radical Copolymerization of Acrylic Acid and Cationic Monomers. *Ind Eng Chem Res* 2021, **60** (29), 10511–10521. https://doi.org/10.1021/acs.iecr.1c00193
319. Cabaness, W. R.; Yen-Chin Lin, T.; Parkanyi, C. Effect of pH on the Reactivity Ratios in the Copolymerization of Acrylic Acid and Acrylamide. *Journal of Polymer Science: Part A-1* 1971, **9**, 2155–2170. https://doi.org/10.1002/pol.1971.150090805
320. Rintoul, I.; Wandrey, C. Polymerization of Ionic Monomers in Polar Solvents: Kinetics and Mechanism of the Free Radical Copolymerization of Acrylamide/Acrylic Acid. *Polymer* 2005, **46** (13), 4525–4532. https://doi.org/10.1016/j.polymer.2005.04.005
321. Haque, M. A Kinetic Study of Acrylamide/Acrylic Acid Copolymerization. *University of Waterloo Master's Thesis;* 2010.
322. Deptula, A.; Wade, M.; Rogers, S. A.; Espinosa-Marzal, R. M. Charge-Induced Structural Changes of Confined Copolymer Hydrogels for Controlled Surface Morphology, Rheological Response, Adhesion, and Friction. *Adv Funct Mater* 2022, **32** (10), 2111414. https://doi.org/10.1002/adfm.202111414
323. Raviv, U.; Giasson, S.; Kampf, N.; Gohy, J. F.; Jéröme, R.; Klein, J. Lubrication by Charged Polymers. *Nature* 2003, **425** (6954), 163–165. https://doi.org/10.1038/nature01970
324. Seror, J.; Merkher, Y.; Kampf, N.; Collinson, L.; Day, A. J.; Maroudas, A.; Klein, J. Normal and Shear Interactions between Hyaluronan-Aggrecan Complexes Mimicking Possible Boundary Lubricants in Articular Cartilage in Synovial Joints. *Biomacromolecules* 2012, **13** (11), 3823–3832. https://doi.org/10.1021/bm301283f
325. Gong, J. P.; Higa, M.; Iwasaki, Y.; Katsuyama, Y.; Osada, Y. Friction of Gels. *Journal of Physical Chemistry B* 1997, **101**, 5487–5489. https://doi.org/10.1021/jp9713118
326. Chau, A. L.; Pugsley, C. D.; Miyamoto, M. E.; Tang, Y.; Eisenbach, C. D.; Mates, T. E.; Hawker, C. J.; Valentine, M. T.; Pitenis, A. A. pH-Dependent Friction of Polyacrylamide Hydrogels. *Tribol Lett* 2023, **71** (4), 1–12. https://doi.org/10.1007/s11249-023-01779-4

327. Xiong, B.; Loss, R. D.; Shields, D.; Pawlik, T.; Hochreiter, R.; Zydney, A. L.; Kumar, M. Polyacrylamide Degradation and Its Implications in Environmental Systems. *NPJ Clean Water* 2018, **1** (1), 17. https://doi.org/10.1038/s41545-018-0016-8
328. Zhao, Q.; Sun, J.; Lin, Y.; Zhou, Q. Study of the Properties of Hydrolyzed Polyacrylamide Hydrogels with Various Pore Structures and Rapid PH-Sensitivities. *React Funct Polym* 2010, **70** (9), 602–609. https://doi.org/10.1016/j.reactfunctpolym.2010.04.010
329. Nalam, P. C.; Gosvami, N. N.; Caporizzo, M. A.; Composto, R. J.; Carpick, R. W. Nano-Rheology of Hydrogels Using Direct Drive Force Modulation Atomic Force Microscopy. *Soft Matter* 2015, **11** (41), 8165–8178. https://doi.org/10.1039/C5SM01143D
330. Hoshino, K. I.; Nakajima, T.; Matsuda, T.; Sakai, T.; Gong, J. P. Network Elasticity of a Model Hydrogel as a Function of Swelling Ratio: From Shrinking to Extreme Swelling States. *Soft Matter* 2018, **14** (47), 9693–9701. https://doi.org/10.1039/c8sm01854e
331. Awasthi, S.; Singhal, R. Mathematical Modeling for the Prediction of the Overall Swelling Profile from Poly (AM-Co-AA-Co-HEA) Hydrogels: Effect of Glycidyl Methacrylate and Ammonium per Sulphate. *International Journal of Plastics Technology* 2015, **19** (2), 241–262. https://doi.org/10.1007/s12588-015-9124-1
332. Kiyama, R.; Yoshida, M.; Nonoyama, T.; Sedlačík, T.; Jinnai, H.; Kurokawa, T.; Nakajima, T.; Gong, J. P. Nanoscale TEM Imaging of Hydrogel Network Architecture. *Advanced Materials* 2023, **35** (1), 1–11. https://doi.org/10.1002/adma.202208902
333. Preočanin, T.; Selmani, A.; Lindqvist-Reis, P.; Heberling, F.; Kallay, N.; Lützenkirchen, J. Surface Charge at Teflon/Aqueous Solution of Potassium Chloride Interfaces. *Colloids Surf A Physicochem Eng Asp* 2012, **412** (20), 120–128. https://doi.org/10.1016/j.colsurfa.2012.07.025
334. Bruice, P. Y. *Organic Chemistry*, 8th ed.; Pearson/Prentice Hall: Upper Saddle River, 2017.
335. Muller, G.; Fenyo, J. C.; Selegny, E. High Molecular Weight Hydrolyzed Polyacrylamides. III. Effect of Temperature on Chemical Stability. *J Appl Polym Sci* 1980, **25** (4), 627–633. https://doi.org/10.1002/app.1980.070250409
336. Ma, Q.; Shuler, P. J.; Aften, C. W.; Tang, Y. Theoretical Studies of Hydrolysis and Stability of Polyacrylamide Polymers. *Polym Degrad Stab* 2015, **121**, 69–77. https://doi.org/10.1016/j.polymdegradstab.2015.08.012

337. Tanaka, T.; Sun, S. T.; Nishio, I.; Swislow, G.; Shah, A. Phase Transitions In Ionic Gels. *Phys Rev Lett* 1980, **30** (1), 97. https://doi.org/10.1080/00150198008209494
338. Xiong, C.; Wei, F.; Li, W.; Liu, P.; Wu, Y.; Dai, M.; Chen, J. Mechanism of Polyacrylamide Hydrogel Instability on High-Temperature Conditions. *ACS Omega* 2018, **3** (9), 10716–10724. https://doi.org/10.1021/acsomega.8b01205
339. Tanaka, T. Collapse of Gels and the Critical Endpoint. *Phys Rev Lett* 1978, **40** (12), 820–823. https://doi.org/10.1103/PhysRevLett.40.820
340. Zhou, Y.; Jin, L. Hydrolysis-Induced Large Swelling of Polyacrylamide Hydrogels. *Soft Matter* 2020, **16** (24), 5740–5749. https://doi.org/10.1039/d0sm00663g
341. Gupta, M. K.; Bansil, R. Laser Raman Spectroscopy of Polyacrylamide. *Journal of Polymer Science. Part A-2, Polymer Physics* 1981, **19** (2), 353–360. https://doi.org/10.1002/pol.1981.180190214
342. Koda, S.; Nomura, H.; Nagasawa, M. Raman Spectroscopic Studies on the Interaction between Counterion and Polyion. *Biophys Chem* 1982, **15** (1), 65–72. https://doi.org/10.1016/0301-4622(82)87017-8
343. Satoh, T.; Sumaru, K.; Takagi, T.; Kanamori, T. Fast-Reversible Light-Driven Hydrogels Consisting of Spirobenzopyran- Functionalized Poly(N-Isopropylacrylamide). *Soft Matter* 2011, **7** (18), 8030–8034. https://doi.org/10.1039/c1sm05797a
344. Francis, W.; Dunne, A.; Delaney, C.; Florea, L.; Diamond, D. Spiropyran Based Hydrogels Actuators—Walking in the Light. *Sens Actuators B Chem* 2017, **250**, 608–616. https://doi.org/10.1016/j.snb.2017.05.005
345. Li, C.; Iscen, A.; Palmer, L. C.; Schatz, G. C.; Stupp, S. I. Light-Driven Expansion of Spiropyran Hydrogels. *J Am Chem Soc* 2020, **142** (18), 8447–8453. https://doi.org/10.1021/jacs.0c02201
346. Aggarwal, A.; Li, C.; Stupp, S. I.; Olvera de la Cruz, M. Controlling the Shape Morphology of Origami-Inspired Photoresponsive Hydrogels. *Soft Matter* 2022, **18** (11), 2193–2202. https://doi.org/10.1039/d1sm01751a